NUMERICAL AND EXPERIMENTAL ANALYSIS OF THE WIND FORCES ACTING ON A HIGH-SPEED CATAMARAN

by

Saeid Amani

Australian Maritime College | College of Science and Engineering

Submitted in fulfilment of the requirements for the degree of Master of Philosophy (Maritime Engineering)

University of Tasmania January, 2019

Declaration of Originality and Authority of Access

This thesis contains no material which has been accepted for a degree or diploma by the University or any other institution, except by way of background information and duly acknowledged in the thesis, and to the best of my knowledge and belief no material previously published or written by another person except where due acknowledgement is made in the text of the thesis, nor does the thesis contain any material that infringes copyright.

This thesis is not to be made available for loan or copying for two years following the date this statement was signed. Following that time, the thesis may be made available for loan and limited copying and communication in accordance with the Copyright Act 1968.

Saeid Amani

Acknowledgements

I would like to express my appreciation and thanks to my supervisors, Professor Jonathan Binns and Dr Alan Henderson for their ongoing support and guidance. Thank you for all your useful comments, remarks and engagement through the learning process of this master project.

I would also like to thank Dr Zhi Leong for his support and encouragement while he was part of the supervisory team and later as the project advisor. Thank you for all your help.

I would like to thank Dr Jason Mc Vicar for continually answering my questions and for discussions which forced me to look further and think deeper in my research. Thank you for being so patient and being happy to share your knowledge.

I would like to thank Incat Tasmania and Revolution Design for giving me the opportunity to study one of their 112m high-speed Catamaran ships. My special thanks to Robert Clifford, Gary Davidson, Tim Roberts, Pierre Denneulin, Mark Redon, Tony Clifford, Dennis Baker, Trevor Hard staff and Jenny Self for their support and for giving me a chance to further my study during my employment at Incat and Revolution Design.

I also would like to thank Andrew Bylett and the other staff member of the University of Tasmania workshop for fabrication and assembly of the test area and load cell for my wind tunnel experiment. My special thanks to his "Royal majesty" Sir Calverly Gerard for the calibration of the load cell and writing a high quality, bespoke program for it to use in any experiments. I also like to thank Laurie Burke, Heather Mitchell and Jillian Smith for their help.

I am grateful to all of those in Revolution Design with whom I have had the pleasure to work during this thesis. Thank you all for sharing your knowledge and putting up with me and my silly questions.

Finally, I must express my very profound gratitude to my family and to my partner Tracey for providing me with unfailing support and continuous encouragement throughout my years of study and through the process of researching and writing this thesis. This accomplishment would not have been possible without you. I am grateful to my boys Eric and Ryan who have provided me moral and emotional support in my life.

Thank you

Abstract

The influence of wind on a ship's manoeuvring performance has always been an important issue, particularly in harbour environments, and during the ship's docking or disembarking. Strong wind can force a ship to drift from its intended course of travel which could end in a dramatic accident. The effect of wind loads is even more noticeable on high-speed catamarans which are in general much lighter than conventional ships of a similar size. These types of ships have a relatively shallow draft and a smaller cross-sectional area below the waterline compared with their above waterline area. Therefore, the motion of high-speed wave piercing catamarans due to wind forces can be significant.

This research presents 3D steady Reynolds-Averaged Navier-Stocks (RANS) CFD simulations of wind loads on a high speed wave piercing catamaran and validation of the CFD analysis against a new wind tunnel experimental test. It demonstrates, how Computational Fluid Dynamics (CFD) and experimental methods can be used to complement each other in quantifying the magnitude and effects of wind loading on a high-speed catamaran.

For the validation, CFD simulations are performed to replicate the experimental test which were performed in the University of Tasmania's wind tunnel. This experiment were carried out on a scale model of a 112m catamaran. The geometrical features of the CFD computational domain were made to be precisely the same as the dimensions of the wind tunnel test section. Preliminary CFD analysis was conducted to determine how the atmospheric boundary layer could be best generated in the experimental test. It was determined the model should be placed on a raised platform allowing the boundary layer profile to be controlled by varying the distance between the model and the leading edge of the platform. This also removed any blockage effects caused by the domain boundaries of the wind tunnel. The experiment was followed by an extensive set of CFD analyses to replicate the experiment. The three-dimensional steady equations were solved with the commercial CFD code Star CCM+.

It is shown that the results from the wind tunnel experiment correspond well with the CFD computations. From the analysis results, the required coefficients of wind loading on the 112m high speed wave piercing catamaran were determined which can be used in station keeping analysis of the ship. Agreement between the experiment and CFD simulations shows that CFD is a viable tool for the calculation of wind loading on a full-scale high-speed wave piercing catamaran.

Content

Nomenclature

	units	
CFD	-	computational fluid dynamics
m	kg	mass
P	Pa	pressure
C_X	-	longitudinal force coefficient
C_Y	-	lateral force coefficient
C_N	-	yaw moment coefficient
F_x	N	longitudinal force component parallel to the lateral area of the ship
F_y	N	lateral force component perpendicular to the lateral area of the ship
∇	m^3	displacement volume
β	Radians	the angle of drift motion
N	N/m	yaw moment
M_Z	N/m	moment around z axis
U_W	m/s	wind velocity
U_S	m/s	model drift velocity
C_D	-	drift resistance coefficient
L_{OA}	m	overall length of the ship
B	m	beam
H	m	height
S_F	m^2	frontal projected wind area of the ship
S_L	m^2	lateral projected wind area of the ship
R_n	-	Reynolds number
y^+	-	non-dimensional wall distance
ρ_a	kg/m^3	air density
ρ_W	kg/m^3	water density
RANS	-	Reynolds-averaged-Navier–Stokes equations
k	m^2/s^2	turbulent kinetic energy
ε	1/s	turbulent dissipation rate
ω	1/s	the specific dissipation rate
CFL	-	Courant-Friedrichs-Levy
HRIC	-	high-resolution interface capturing
T	sec	period
θ	degrees	wind angle from the bow
β	degrees	drift angle
δ	degrees	helm angle
S_{HL}	m^2	lateral projected area of the submerged demi-hull
S_{WT}	m^2	projected front area above waterline
S_{WL}	m^2	projected lateral area above waterline
LCG	m	longitudinal centre of gravity
VCG	m	vertical centre of gravity
TCG	m	transversal centre of gravity

List of Figures

List of Tables

Chapter 1 Introduction

Catamarans, in general, have a large superstructure above the waterline compared with their relatively shallow draft. The shallow draft gives catamarans the advantage of being able to travel in places where the depth of the water is not greater than a few metres. Their shallow draft also helps in reducing the overall resistance of these ships, helping them to achieve higher speed with less fuel consumption than their single hulled counterparts. The ships not having that much of their structure below the waterline often experience difficulties with course keeping in rough seas, particularly when they face strong winds or currents. They also have similar problems when they are travelling at low speeds, particularly when they are manoeuvring for berthing. This problem is worse if they have to remain stationary for a period of time in rough seas such as, during the transfer of a ship's crew to or from oil rigs at sea. The current market demands that catamaran ships become larger in size and travel faster with increased fuel efficiency. These ships have to carry larger loads and operate in places where they are constantly facing strong winds and currents. The behaviour of these ships in such conditions affects the safety of the passengers, crew, cargo and the ship itself.

Figure 1: 112m catamaran built by Incat Tasmania (Luttrell 2017)

Currently, most of the large catamarans are still using their own primary propulsion system (water jets) for berthing or disembarking. Waterjets improve the station keeping of these vessels compared with propeller driven ships. It may be true that catamarans have superior station keeping compared with monohulls due to there being a larger distance between their waterjets which are located in two separate hulls. Nevertheless, even catamarans with waterjets may not have sufficient station keeping for the wind speeds at which they are operated, especially in harbour when they have to travel at a much lower speed (Sadovnikov 2009).

Sadovnikov explains that there is a chance of an increased risk of losing control over the vessel because they are normally operated on short routes, with having several departures and approaches per day at low speed. Travelling at low speed for berthing or disembarking when strong wind is present can cause collisions with other vessels or marine structures, for example piers, break waves, and so on (Sadovnikov 2009).

The global economic crisis in last few decades has caused many problems for ship manufacturers. It has forced a number of them to close down or restructure their businesses. Those manufacturers whose businesses survived soon learnt that the only way for them to stay afloat and live through this period was to become more competitive. Similarly, the fast ferry catamaran manufacturers have suffered during time. An increase in the price of oil and base materials has made manufacturers learn that the only way to secure a new contract is to incorporate new and innovative design ideas that make their ships better, faster, cheaper, safer, more fuel efficient and more environmentally than their competitors. It has become crucial for the ship builders to improve the efficiency of their ships in any way possible.

Wind loads on ships and offshore structures play an important part in almost any operation at sea. The function and safety of floating vessels are dependent upon an accurate prediction of the wind loads at the design stage. Wind loads on ships are of special importance in relation to manoeuvrability at low speed, when the hydrodynamic forces on the underwater hull are small and difficult to control. Consequently, accurate wind load data are of great importance for the programming of ship manoeuvring simulators. The wind overturning roll moment is the determining factor for the dynamic stability of ships (Aage *et al.* 1997).

The importance of having accurate knowledge of the wind loads on ships for better station keeping ability, fuel efficiency, comfort and safety of the passengers has been discussed in a number of studies such as Aage *et al.* (1997), Oura and Ikeda (2007), Sadovnikov (2009), Andersen (2012a), Janssen *et al.* (2017). Anderson discusses how much effort is put into measures that can improve ships' fuel efficiency by even a few per cent. All ships experience air and wind resistance while under way at sea, and they may experience adverse effects of wind while manoeuvring in harbours and confined waterways (Andersen 2012b). Matsomoto reports that wind force acting on a tanker sailing in 14m/s relative wind speed can reach 15% of the total resistance while, PCC (pure car carriers) can sail in 10m/s wind and reach22% (Matsumoto 2003). Molland explains the significance of the shape of the superstructure and the hull above the waterline can represent up to 5% to 10% of the total resistance of a catamaran while travelling at high speed at sea (Molland & Barbeau 2003).

In the harbour it is very important to consider the effect of wind on a ship’s motions in order to avoid the risk of collision and grounding. In this manner, knowing the influence of wind is very important for a ship’s operation in the ocean and in the harbour (Nihei, Li, Nakashima, *et al.* 2010). A lack of sufficient control over the wind or strong currents has forced many pilots to abort docking completely in order to avoid an accident, resulting in the loss of time and resources. Some captains of such high speed passenger ships say that, in strong winds in the oblique bow direction, manoeuvring is very difficult due to fluctuations in a ship’s motion (Tasumi & Ikeda 1999).

Therefore, manufacturers need to employ fast and accurate methods to obtain new design data for their engineers, when they are designing new ships. For this purpose, all new designs need to be tested. This is to obtain a reliable full-scale prediction of the wind forces on catamarans. However, due to the cost and limitations of conducting full scale tests, the majority of the new design data for design engineers has traditionally been collected from model testing in towing

tanks and a few by wind tunnel testing on scale models. In recent years, Computational Fluid Dynamics (CFD) modelling is proving that it can also provide fast and reliable data for engineering design. The idea of using CFD is becoming more attractive as the results can be available in the early stage of a ship's design at a greatly reduced cost. However, the weakness of CFD is that the credibility of the CFD predictions needs to be demonstrated before it can be considered reliable for engineering purposes. Current practices necessitate that the CFD model be validated (for example, via experimental measurements or empirical data) prior to extending the model for further use.

In this study, it is shown how CFD can be used as an alternative to other experimental or analytical methods for calculating the aerodynamic forces acting on catamaran ships. It will be discussed that the study of making a ship more aerodynamic and more fuel efficient can be continued more economically and efficiently by using CFD. Advancing a design to the next level can be achieved after building a computational domain for aerodynamic analysis and after validation of CFD results, with changes made to the shape or parts of the ship at minimal cost.

"The CFD method is based on the finite volume principle, in which the flow domain is divided into a very large number of small fluid volumes or cells, each being governed by a set of dynamic and kinematic equations, interacting with its neighbouring elements and with the flow domain boundaries. The investigated structure, for example, a ship or an offshore platform, will act as one of these boundaries. When the large system of equations and boundary conditions is solved, one of the results is the total mapping of the pressures upon the surface of the investigated structure. By integrating the pressures over the vessel's surface, the wind loads (that is, the forces and moments) can be found as providing the most important result in this context" (Aage *et al.* 1997).

The physical test conditions can be easily manipulated in CFD and the ship's design can be evaluated in all different conditions with minimal time and cost. The original design can then be quickly changed, modified and retested. Performing CFD analysis can give quick and inexpensive results to engineers who are designing a new ship, while their design is in the very early stages. There is not the additional cost of making a test model for use in a towing tank. The cost of employing experts and technicians for conducting the tank test will also be eliminated. All other overhead costs related to towing tank maintenance and operation will be eliminated. CFD can also give a broader view about the effect of wind on different parts of the ship. Therefore, decisions can be made in advance about the location of the towers, mufflers and so on.

Both research on and applications of aerodynamic forces on high speed wave piercing catamarans are currently limited. The number of published research papers which give detailed information about the effect of wind forces on the station keeping of catamarans is very minimal. Therefore, the focus of this research project is to inspect the effect of aerodynamic forces on the performance of catamarans and to find a reliable method for prediction of the station keeping ability of catamarans.

Calculation of the wind forces on full scale ships is very difficult and expensive. There are hardly any full scale data from aerodynamic forces on ships being published. Generally, the prediction of aerodynamic forces for the purpose of studying the station keeping ability of ships is determined by using either an analytical method such as Fujiwara *et al.* (1998), Sadovnikov (2009), or an experimental method, such as Oura and Ikeda (2007), Tasumi and Ikeda (1999) using the towing tank test and Andersen (2012a), Janssen *et al.* (2017), or the study of (Molland & Barbeau 2003) which were on aerodynamic drag of the superstructures of fast catamarans, using wind tunnel experiment.

The limitations in experimental testing can be summarised as uncertainty of the wind profile, reducing the movement of the model in the water and the need for the extrapolation of the results from experimental testing to full scale. In recent years, the Computational Fluid Dynamics or CFD methods have been developed to a stage in which they offer a realistic computational alternative to the experimental methods (Aage *et al.* 1997). Once a CFD model is validated, it can be used to replace the restrictive process of building scale models and then assessing their performance in towing tanks and wind tunnels. CFD also demonstrates its value in identifying and addressing design and performance issues that otherwise might not have been evident until much later in the design and build of a vessel. As such, it can help avoid expensive modifications having to be made at some point in the future.

The usual way to produce a prediction of full-scale power is by model testing, followed by an extrapolation of the results to full scale. Of course, model manufacturing and testing are expensive and time-consuming; using CFD only might be more practical. But there are also some simplifications in the model testing approach that could be introduced using CFD. In particular the extrapolation procedure is largely empirical. It assumes that the viscous resistance is unaffected by wave making (Froude number independent), an assumption that is not necessary for today's CFD methods that solve RANS equations with free surface. Hull form features that may affect the scale effect, such as immersed transoms, bulbous bows close to the still water surface, or wave-induced flow separation, play no role in the extrapolation but do so in CFD computations. Evidently CFD computations in principle could provide more accurate and more reliable full-scale power predictions, if not separate from any model test, then as a complement to model testing to provide a more precise scale effect estimate (Raven *et al.* 2006). However, before this method can be used on its own with confidence, many validation studies specific to the type of analysis are required to build confidence about the numerical code and the details of modelling the various types of problems (Wnęk *et al.* 2010).

Computational Fluid Dynamics (CFD) has progressed rapidly in the past fifty years. It has been used in many industrial fields and plays an irreplaceable role in engineering design and scientific research. However, due to the existence of free surface and complex ship geometry. Ship CFD has fallen behind its counterparts in other industrial fields. But with the recent breakthrough in ship CFD technology, practical applications of CFD in analysing and predicting ship performance now become possible (Zhang *et al.* 2006). A number of recent studies used computer solution, finite volume CFD for validation of their studies on different type of ships such as trimarans, LNG or container carriers etc. A few examples of them are Martin (1980), Aage *et al.* (1997), Sezer-Uzol *et al.* (2005), (Ikeda 2008), Nihei, Li,

Nakashima, *et al.* (2010), Wnęk *et al.* (2010),(Nihei, Li & Ikeda 2010) , (Broglia *et al.* 2011), (Zha *et al.* 2015),(Van He *et al.* 2016) , (Aktas *et al.* 2017), (Janssen *et al.* 2017).

Most of studies which are performed in towing tanks or basins are mainly focused on determining ships hydrodynamic resistance. There are only a few studies on aerodynamics of ships and very few specifically on current commercial high speed wave piercing catamarans. Detail of many of these wind tunnel studies are not public open resources and the results of those tests are mostly kept confidential. Therefore, it is impossible to find out if boundary constraints such as proximity of side walls and their effects on flow field around the model or modelling the atmospheric boundary layer have been correctly considered. Exceptions are for studies such as (Andersen 2012a) and (Janssen *et al.* 2017) on container ships. They have managed to successfully model the effect of the atmospheric boundary layer in their experimental tests. However, they failed to eliminate the effect of the wind tunnel side walls on flow field around the ship model in their experiments.

This study details how CFD is used to identify the potential limitations of a wind tunnel test prior to the experimental test and how CFD assisted in locating the scale model in the wind tunnel test section so the scaled model experiences the same boundary profile as a full scale ship does on ocean. Also, it is shown that how CFD is used to ensure the side walls of the wind tunnel have minimal effect on the flow filed around the model.

Thus, the research question of this project is:

> *How CFD can assist effectively as a tool to correctly perform and then to validate the results of an experimental test which is set to obtain a reliable prediction of the wind forces and their effects on performance of current commercial high speed wave piercing catamaran?*

1.1 Objective statement

The objective of this research is to increase CFD as the primary approach to quantify the magnitudes of wind forces and moments on a high-speed catamaran as it enables predictions at both model scale and full scale.

There are several research goals in this project:

- The objective of the thesis is to develop and validate a RANS based numerical model from a scaled wind-tunnel experiment.
- Provide more detailed analysis and more design scenarios, to calculate the wind forces on wave piercing catamarans by using CFD instead of experimental model testing in towing tanks, wind tunnels or other empirical methods;
- Demonstrate CFD ability as an effective tool in preliminary stage design for engineers, and
- Show the capabilities of CFD in identifying potential problems in design by allowing the visualisation of the fluid flow around the model and the effect of the boundary conditions on final results.

Ultimately, this research is hoping to provide a quicker, more accurate and more cost-effective method of study the station keeping ability of the catamarans which assists in several areas:

- increasing the safety and manoeuvrability of the catamaran ships at low or zero speeds against wind and current;
- a safer departure and docking for catamaran ships, and
- increasing the station keeping ability of the catamaran ships.

1.2 Thesis outline

The research and work carried out in this paper is structured into chapters and sections as shown below:

- **Chapter 1**_ Introduction
- **Chapter 2**_ Verification and validation of CFD simulations against Oura and Ikeda (2007)
- **Chapter 3**_ Wind tunnel test design
- **Chapter 4**_ Preparation for the wind tunnel test
- **Chapter 5**_ Velocity profile
- **Chapter 6**_ CFD simulation of the wind tunnel test
- **Chapter 7**_ Conclusion
- **Chapter 8**_ Recommendations
- References

Chapter 2 Verification and validation of CFD simulations against Oura and Ikeda (2007)

One aspect of this research is to show how CFD can be used as an alternative to experimental methods (towing tank or wind tunnel test) in the study of the station keeping of catamaran ships. The weakness of CFD is that the credibility of its predictions needs to be demonstrated before it can be considered reliable for engineering purposes. This means that all results from CFD analysis should be verified and validated against the results from an experimental test on either a full scale or scale model of a ship. Details of many experimental studies are not public open resources and cannot be used for validation of CFD simulations. At the time of starting this research, the most comprehensive study which contained enough information to use for validation of CFD analysis, was the paper which was published by Ikeda and Oura (Oura & Ikeda 2007). Their experiment was on a 1/80 scale model of a 112m fast ferry catamaran and here will be used as a benchmark for validation of CFD simulations.

2.1 Summary of Ikeda and Oura's experiment

In 2007 Takuya Oura and Yoshiho Ikeda performed an experiment on one of the latest catamaran ships, built by Incat Tasmania. For their experiment a 1/80 scale model of an Incat 112m wave piercing catamaran was used. The test was performed in the towing tank of the Osaka Prefecture University in Japan. Their study was focused on the manoeuvrability of a high- speed catamaran at low speed while the ship is subjected to strong wind. They compared the results of their experimental test with the results from a theoretical calculation method suggested by Fujiwara (Fujiwara *et al.* 1998). The result from their experiment showed that the longitudinal force coefficient (C_X) is asymmetrical and smaller in a head wind than in a following wind. They explained that this difference may be caused by the catamaran's shape with a tunnel but no further explanation is provided (Oura & Ikeda 2007). The principal particulars of this vessel are shown in Table 1.

Gross tonnage	L OA	Length of demi hull	Width of the demi hull	Breadth	Draft	Maximum speed	Main Engine	Water jets thrust (x4)
8000 Ton	112.6 m	105.6 m	5.8 m	30.50 m	3.7 m	40 knots	9000 KW/ 1000 RPM (x4)	303 KN (x4)

Table 1: Principal particulars of the 112m WPC which was built by Incat Tasmania ship building company. The 1/80 scale model of this ship was used by Ikeda and Oura for their experiment (Oura & Ikeda 2007)

2.2 CFD analysis

To demonstrate that CFD can be used to supplement experimental methods in quantifying the magnitude and effect of wind loading on a high speed catamaran, it is necessary to show that it can replicate the experimental results. STAR CCM$^+$ is used for CFD modelling of their research. This software has the capability of modelling both water and air regions, including their interface, by using a feature named VOF (volume of fluid).

The published paper by Ikeda and Oura contains most of the required information for performing a CFD simulation. There is, however, more key information to be determined such as, the mass of the model test and its draft waterline, the wind profile at inlet, the closeness of the model test to the towing tank side walls (boundary conditions), and the effect of the generated wind on the water surface of the towing tank (if any waves were formed). Professor Ikeda, in one of his correspondences, confirmed that the 1/80 scale model which was used in their experimental test had a total mass of 5.86 kg. However, further investigations were required to find answers to the rest of the questions above.

2.2.1 Identifying the correct waterline

To be able to measure the wind force coefficients on the ship, the correct windage area of the ship structure above the waterline should be calculated. Therefore, hydrostatic analysis (sinkage and trim) is performed to identify the correct draft waterline. For this purpose, a computational domain was created in Star CCM$^+$ with the following dimensions:

Length (L) 23.6m (18L),

Width (W) 23.6m (18L),

Height above waterline, (HAWL) 4.5m (4L),

Height below waterline (HBWL) 4.5m (4L)

The computational domain and its coordinate system are shown in Figure 2.

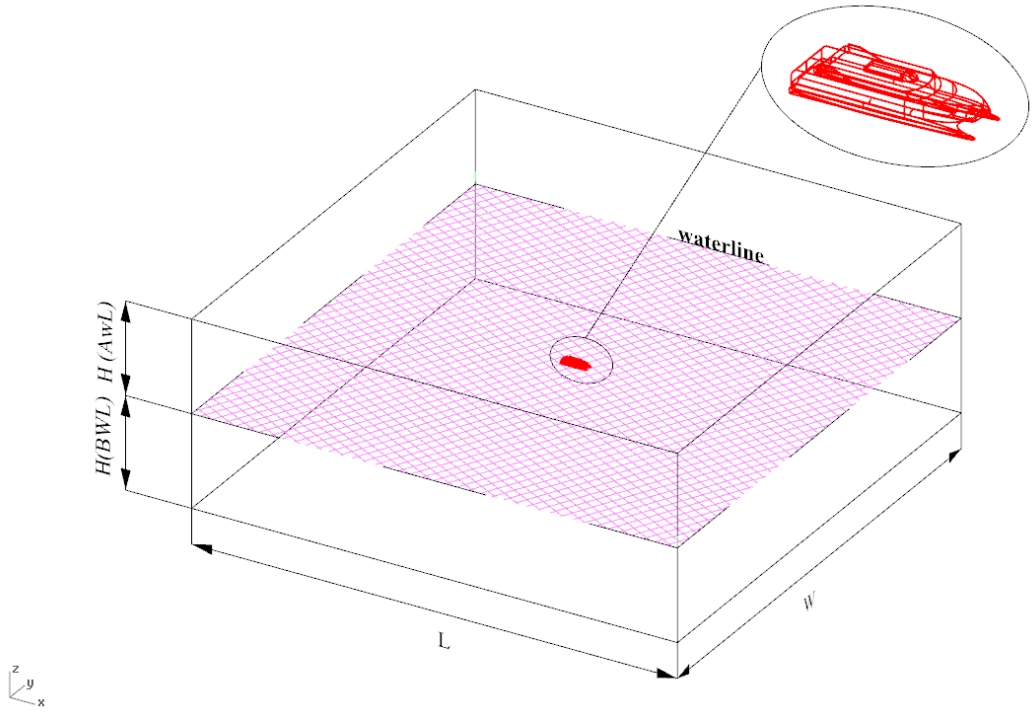

Figure 2: The computational domain created for sinkage and trim analysis. The intersection point of the transom at the centreline of the model test and the water surface, is set to be the origin of this domain (0,0,0). The length and width of the domain is influenced by the wave damping length.

For the mesh, trimmer mesh with two prism layers, for the turbulence model, Realisable K-epsilon with two layers with all wall y^+ wall treatment as an initial setting and to model the interface of the water and the air VOF (volume of fluid), were used. The results of this analysis showed that the correct waterline for the 1/80 scale model of the 112m catamaran, with the total mass of 5.86 kg, is 0.055m above base. By knowing the correct waterline, the frontal and side projected areas of the scale model were calculated in a CAD software.

Next, all analysis was repeated with higher mesh resolution and SST K-omega turbulence model, to show the above result is independent from the type of turbulence models and mesh settings. Then, by using a finite element model of the 112m ship (FEAMAP software) and more CFD analysis, the correct COG (at level trim) was determined to be at [0.526, 0.0, 0.112] m, m, m. (for more information see Appendix 1).

2.2.2 Boundary conditions

In Ikeda and Oura's paper, the distance between the wind generators (fans) and the location of the test model in the towing tank are not specified (Oura & Ikeda 2007). Moreover, the wind profile of the fans at inlet is unknown. In addition, the distance of the scale model to the side of the towing tank is not defined. Therefore, for initial CFD analysis, the assumption was made that all inlet and side walls are far enough from the model and have no effect on air flow in the domain and around the model, or on the final results. Domain size sensitivity analysis was also performed to ascertain whether changes in domain size could cause any changes in the final results (See Appendix 2 for more information about domain sensitivity analysis).

2.2.3 Performing CFD on Ikeda's experiment

In their experiment, Ikeda and Oura first mounted their scale model test on a rotating platform in a basin (assuming its correct waterline). The model was kept stationary in calm water (no current). The wind was generated by a wind generating device that was capable of producing constant wind at different velocities (assuming uniform flow). The attack angle of the wind was changed by 15° increments from 0 to 180°. They used a three-component load cell to measure the longitudinal and transverse forces plus the yaw moment (moment about the z-axis) about its mid ship position.

2.2.4 Definitions of loads and coordinate system in CFD

Figure 3 shows the ship's coordinate system, which has its origin on the ship centreline, halfway along the length between perpendiculars ($L_{pp}/2$); here it is based on the hull waterline. The axes are defined as follows:

–The x-axis is positive forward.
–The y-axis is positive to port.
–The z-axis is positive upward.

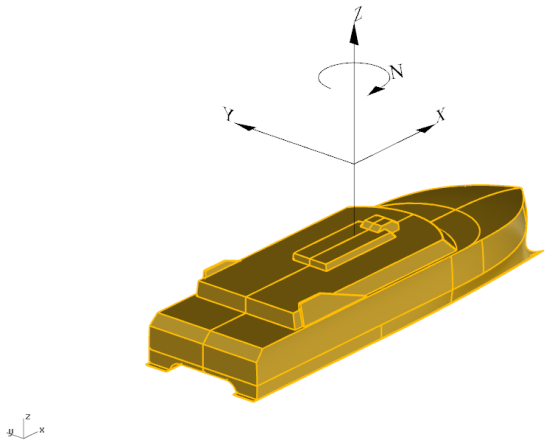

Figure 3: Definition of ship coordinate system. The ship coordinate system is not necessarily always the same as the CFD domain coordinate system.

For CFD modelling of this part of the experiment in Star CCM+ any of the two following methods can be used:

1.The multiphase regions in a domain (water and air)

This requires using VOF. For the region above the waterline, the wind velocity can be set as per that which Ikeda and Oura used in their experiment and for the region below waterline, the water current should be set to zero. This is when, in DFBI (dynamic fluid body interaction), no

translations or rotations are allowed. Steady simulation cannot be used for this method and convergence due to using unsteady solutions may take more time.

2.A single-phase region without modelling the water in domain

Since there is no current and the model test is kept stationary, it is possible to have a single-phase model (just air). This means that the section which was required to be modelled is the part above the waterline. Steady simulation can be employed which helps to achieve faster convergence. Choosing this method will also minimise the size of the domain and subsequently reduce the number of cells; this will lead to a solution more quickly. Therefore, it is easier to have a single-phase region and model the part of the domain which is above the waterline and ignore the section of the model which is below the waterline. It was also decided to perform CFD analysis for both slip and non-slip floor conditions, as the effect of the generated wind flow on the water surface of the towing tank was unknown.

2.2.5 Detail of CFD modelling (numerical simulation)

Domain size

The initial geometrical size of the computational domain was set as: L = 21.76 m, W = 21.76 m, H = 5.12 m (see Appendix 1 , 2 and 3 for more detail). The inlet boundary was set as the velocity inlet, the outlet as the pressure outlet and the condition of the floor first set as a slip wall. However, this does not allow any boundary layer to be formed on the floor of the CFD domain. (Later, the analysis was repeated with the floor condition as non-slip and results were compared.) All other walls were set as symmetry. For the grid, trimmer mesh with six prism layers and for turbulence model, a Realisable K-epsilon turbulence model with two layers, all y^+ wall treatment, were used. The wind angle of attack in the first model was set to 0°. (When the wind is directly blowing into the bow, the heading is 0°). This is shown in Figure 4. Next, CFD analyses were repeated, after changing the wind angle of attack by 15°. This step was replicated a number of times, until the wind angle of attack reached 180°. Figure 5 shows the computational domain with a section of the ship above the waterline. Figure 6 shows the mesh setting and grid resolution around the model. Details of the grid arrangement for this particular model are shown in Table 2.

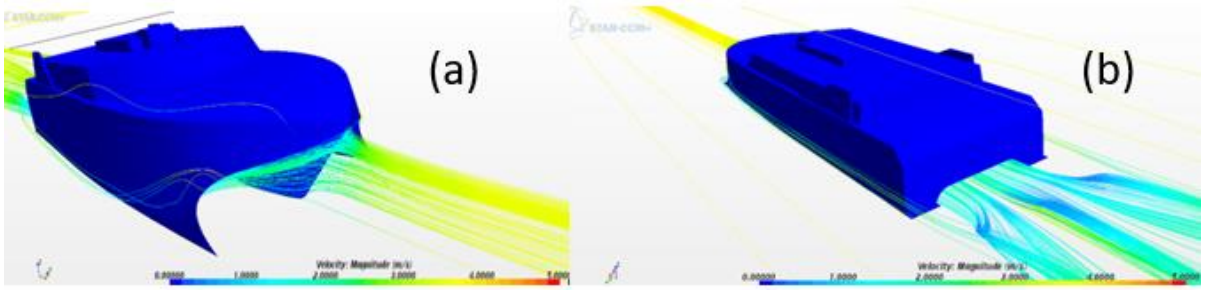

Figure 4: Wind is directly blowing into the bow at 0° angle of attack. Only the structure which is above the waterline is modelled and air is the only fluid in the domain. (a) isometric view, looking aft. (b) isometric view, looking forward

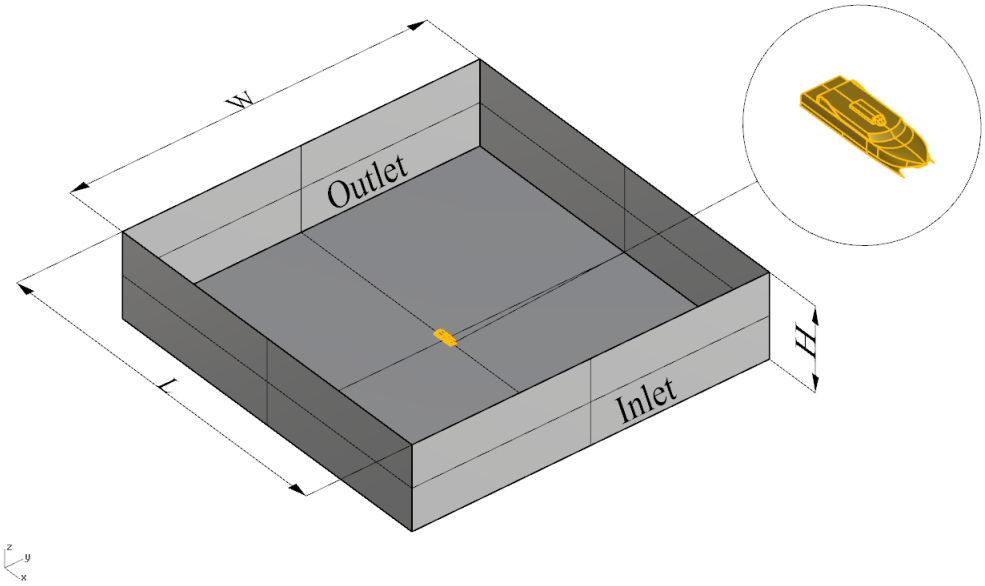

Figure 5: The computational domain only, above the waterline with the wind angle of attack set at zero 0°. The scale model is on the floor and at the centre of the domain. The point (0,0,0) is at midship and on the waterline which is on the floor of the domain.

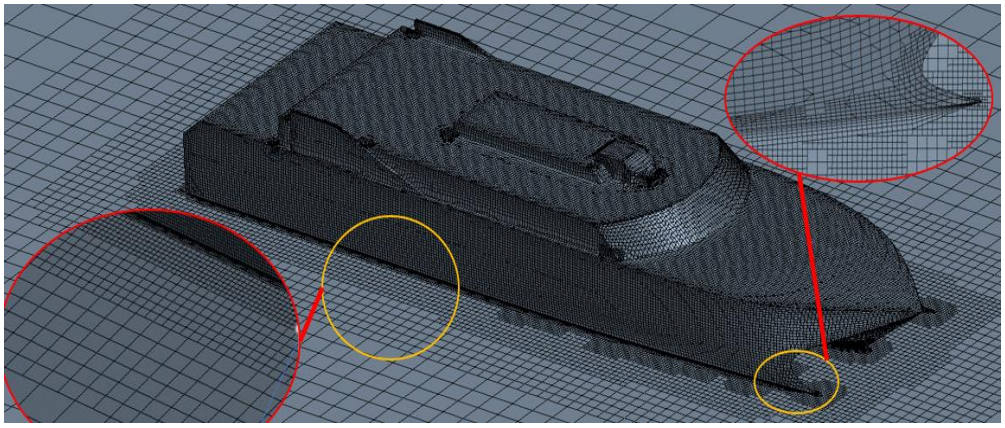

Figure 6: The progression of the mesh refinement from the prism layer (close to the model) to the core mesh and towards the boundary walls. Each time the mesh density changes by a factor of two. To show this, sections of the grid are partially magnified.

Type of mesh	Number of cells	Prism layer thickness	Number of layers	Prism layer stretching	Water density	Air density
trimmer	710,000 plus	14 mm	6	1.3	997.56 kg/m^3	1.184 kg/m^3

Table 2: Model specification when the wind angle of attack is 0° into the bow. The prism layer thickness is set in a way that ensures smooth transition between the prism and the core mesh

2.2.6 Results

The results from analysis showed that there are certain disagreements between CFD and Ikeda and Oura's experimental results. It is clear that there should not be any side load and yaw moment on the scale model when the wind is blowing directly into the bow (wind angle of

attack is zero degrees), as the scale model has a symmetrical shape. However, as is shown in Table 3, the results from Ikeda's experiment for this particular heading are showing values which are not zero. These errors could have been introduced from a misalignment of their model to the direction of the wind (not perfect zero) or a calibration of their load cell. More disagreements are also shown in the C_X coefficient plot in which the wind angle of attacks is changing from 150° to 180° in a following wind. Ikeda and Oura's estimated results are higher than that which is measured in CFD. Also, the measured transverse forces by Ikeda are lower than the calculated results in CFD. The summary of the results is plotted against Ikeda and Oura's experimental results and are shown in Figure 7, Figure 8 and Figure 9.

K_ zero		Cx	Cy	CN
	CFD	0.36	0.00	0.00
	Ikeda Experiment	0.44	0.02	0.01

Table 3: Comparison of the results between Ikeda's experiment and CFD. Wind angle of attack is 0° into the bow and wind velocity is 3.8 m/s

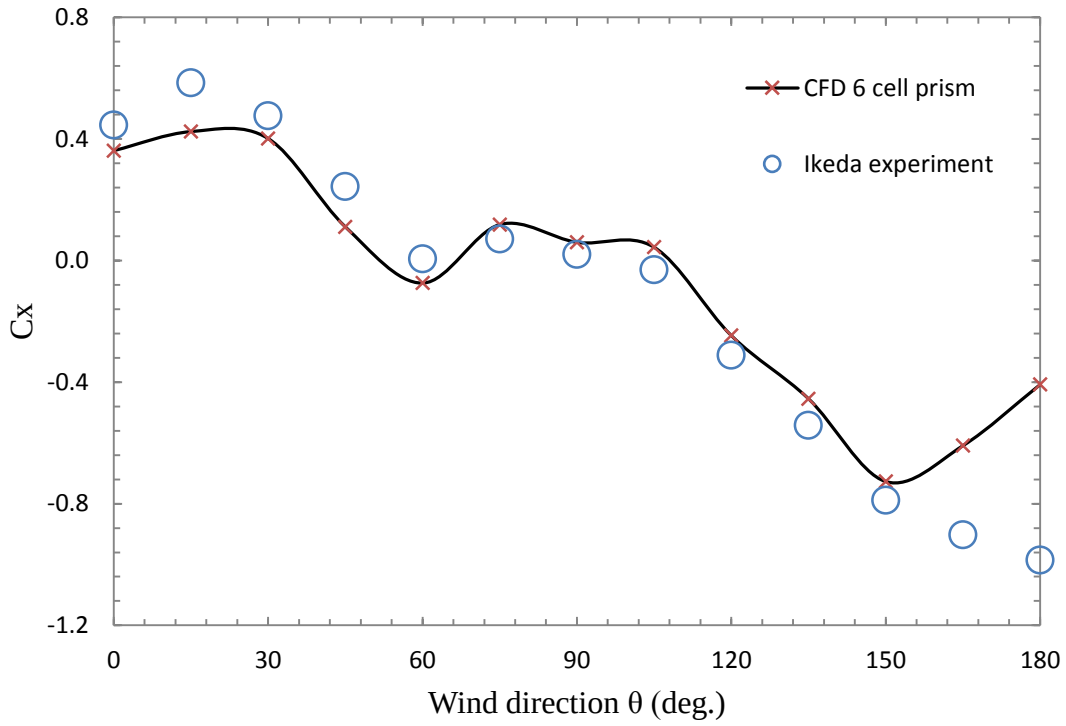

Figure 7: (1/80 scale model) CFD results vs experimental results (Cx). The CFD model has six cells in its prism layer and Realisable K-epsilon for turbulence model. There are significant differences between results when the wind angle of attack changes from 150° to 180°.

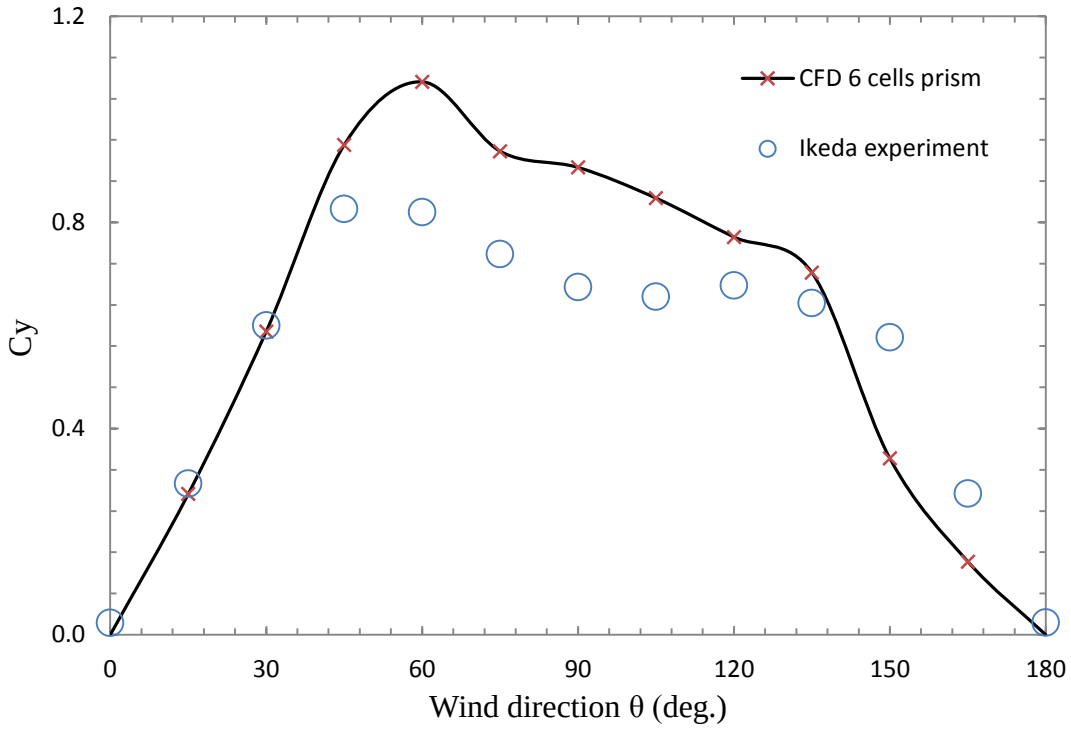

Figure 8: (1/80 scale model) CFD results vs experimental results (Cy). The CFD model has six cells in its prism layer and Realisable K-epsilon for turbulence model. The measured transverse forces, between 30° to 135°, are lower than those which the CFD results are showing

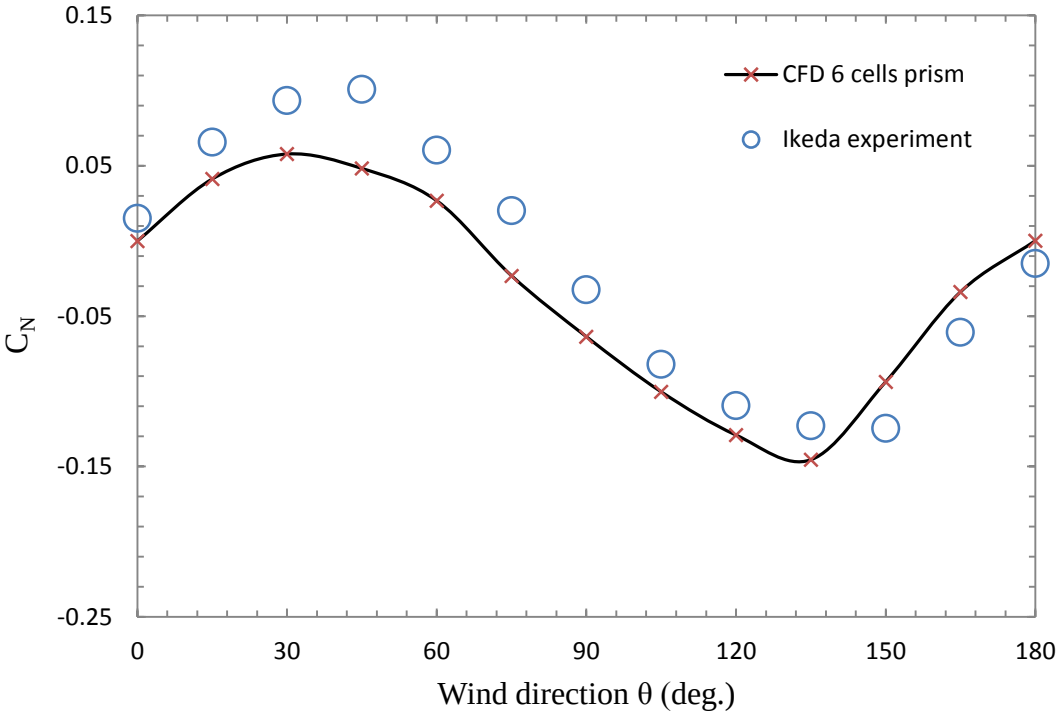

Figure 9: (1/80 scale model) CFD vs experimental results, yaw moment coefficient (C_N). The CFD model has six cells in its prism layer and Realisable K-epsilon for turbulence model. The calculated moment coefficients in Ikeda and Oura's experiment are generally higher than those which were measured in CFD.

2.2.7 Optimising the model (domain size, mesh settings, y^+ and turbulence models)

To show that the results from CFD analysis are independent from mesh settings in the near wall and in the core area, all CFD analysis was repeated after refining the mesh and changing the number of prism layers to achieve a better y^+ (see Appendix 4 for more details). To show that the results are independent from this type of turbulence modelling, all analysis was repeated with SST K- ω turbulence model with two layers, all y^+ wall treatment. Additionally, domain size sensitivity analysis was performed by changing the distance of the model to the side walls a number of times. This is to show that the changes in the domain size do not change the original results (see Appendix 2 for more details).

Finally, all analysis was once again repeated after changing the floor condition to be non-slip. Defining the floor condition as non-slip allows the boundary layer on the floor of the CFD domain to be shaped. This step was to ascertain whether the results of Ikeda's experiment were affected by the generated boundary layer on the towing tank's water surface. In addition, the results from this set of analyses did not show any agreement with Ikeda's experimental results. All CFD analysis was checked and it was confirmed that the original CFD results are correct and they are independent from any of the above changes. The only exception was when the floor of the domain was specified as non-slip which made the results deviate further from Ikeda and Oura's results. (Detail and results of the above analysis are shown and discussed in Appendix 4).

2.3 Discussion of results

It is shown that the results for both models with y^+ of ($5 < y^+ < 30$) using all y^+ wall treatment, and y^+ ($y^+ < 5$) for the above analysis, are the same. The results from all CFD analyses indicate that all results are independent from the grid density. It is also shown that both types of turbulent models, (Realisable K-epsilon and K-omega) can produce the same results as long as the computational domain has a good mesh transition between the coarse core mesh and the fine prism layer. The domain sensitivity analysis showed that all results are independent from the size of the domain. Reducing the size of the domain to 25% of its original size did not have any impact on the final results.

The results from CFD simulations did not support the results from Ikeda and Oura's experimental test. It is clear that there should not be any side load and yaw moment on the scale model when the wind is blowing directly into its bow (when the wind angle of attack is zero degrees), as the scale model has a symmetrical shape. However, it is shown that the results from Ikeda's experiment are showing force and moment which are not zero. The C_y plots show that Ikeda and Oura's results are generally below that which was measured in CFD. C_N plot is showing that the calculated moment from Ikeda's experiment is higher than the CFD results.

The calculated C_x results from CFD, especially between 150° and 180°, are totally different to that which was measured in the experiment by Ikeda and Oura.

The lack of similarity between CFD and Ikeda's experimental results does not prove that CFD is incapable of calculating the aerodynamics of the ship. Disagreements between those results only shows the possibility of some limitation in either Ikeda's experiment or some errors in CFD analysis. The disagreement between the results also questions Ikeda's conclusion with regards to the longitudinal force coefficient (Cx) being asymmetrical (smaller in a head wind than in a following wind. Ikeda concluded that this effect is due to the shape of the catamarans with tunnels) (Oura & Ikeda 2007).

Finally, due to uncertainty in the boundary layer in Ikeda and Oura's experiment all analysis was repeated after changing the condition of the domain floor to non-slip. Setting the floor of the domain as non-slip indicates that the generated wind in Ikeda's experiment was blowing right down to the water level, allowing the boundary profile to be formed on the water surface. The results from this set of analysis also, once again displayed even more disagreement to Ikeda's experimental results. Additional study was also performed to capture the effect of blockage due to proximity of side walls to the model by changing the domain size. The results from this study showed the impact on final results due to blockage affect if the model test get too close to side walls.

A few different environmental parameters could have existed between the experiment and CFD simulation which were not captured properly during setting the boundary conditions in CFD simulations. These could possibly be summarised as:

1. Where the fans were mounted and how far were they from the model?
2. Was the fan blowing directly at the water surface level or was it set slightly higher?
3. Were there any waves generated during the test? (It was confirmed by Professor Ikeda that during the experiment the water surface was undisturbed.)
4. Was the fan blowing a steady flow or perhaps the fan flow profile was not that steady and had some effect on the results?
5. What was the room temperature?
6. What was the density of the water?
7. What was the distance of the test model to the surrounding walls (the tank's sides) and were there any blockage effects?
8. How much were the misalignment of the model or calibration of the load cell affecting the results when the wind was blowing from different angles?
9. How was the load cell attached to the model test and where?

Finding answer to any of the above questions does not change the fact that the CFD results do not support the results from Ikeda and Oura's experimental test. It is clear that there is a need to find another experiment to use for validation of the results from CFD simulations. Therefore, the only possibility to validate the CFD results is to perform a new experiment. This is due to a lack of access to another experiment with comprehensive details and results. One of the possibilities is to perform this new experiment in the UTAS (University of Tasmania) wind tunnel.

Chapter 3 Wind tunnel test design

Performing a new wind tunnel test assists in finding a reliable source of information that can be used as a benchmark reference for full scale station keeping analysis of the ship and also for validation of the CFD results. Recreating Ikeda and Oura's experiment in a towing tank or basin does not seems to be necessary as the goal of the first part of Ikeda's experiment was to find wind force coefficients on a 112m catamaran. This part of their experiment can easily be recreated on a smaller scale model and in a wind tunnel. Performing the test in UTAS's wind tunnel has the advantage of providing a more controlled environment for an aerodynamic experiment, compared with a similar test in a towing tank; it is also more cost effective.

The results from the wind tunnel test can also be used to measure against Ikeda and Oura's test results, if the flow characteristics in both experiments are the same. This comparison could potentially show the reason for the different results between CFD and Ikeda and Oura's experiment. To achieve the same flow characteristics between the two experiments, both flows have to have the same Reynolds value. It is also important to make sure the flow characteristics and the boundary conditions are similar, by choosing the correct size for the model and locating it in an appropriate location in the wind tunnel. This is to avoid solid or wake blockage, and to eliminate the effect of the side wall on air flow around the model.

Finally, in order to use the results from the wind tunnel experiment in the station keeping of a full-scale ship, it is necessary to ensure that the measured mean velocity profile at the location of the scale model in the wind tunnel is similar to the velocity profile on the ocean surface. This is to ensure the turbulence characteristics of the flow are close to and similar to the full-scale condition (Cengel & Cimbala 2013).

3.1 Achieving similarity in Reynolds value

For validation of CFD results it is only necessary to compare the results from the wind tunnel experimental test with the results from similar CFD simulations. However, further comparison between Ikeda's towing test and the new wind tunnel test can be made, if the new experimental test is set to have the same Reynolds value as Ikeda and Oura's experimental test.

Due to the size of the (UTAS) School of Engineering's wind tunnel test area, the length of the ship model for the test in the wind tunnel must be much smaller than the length of the ship model that Ikeda and Oura used in their experiment. Therefore, to achieve the same Reynolds number, the velocity of the air for the wind tunnel test should be increased. Ikeda and Oura used a 1/80 scale model of a 112m Incat vessel with a wind velocity of 3.8 m/s for their experimental study in a towing tank. The calculated Reynolds number for the 1/80 scale model with the length of 1.32m and with kinematic viscosity of air as $1.567 \cdot 10^{-5}\ m^2/s$, is $3.20 \cdot 10^5$.

The wind tunnel in Hobart's UTAS is a closed type wind tunnel as shown in Figure 10. This wind tunnel is capable of producing wind flow within the range of 3 to 36 m/s. The test area

has an octagonal cross section. The wind tunnel has a glassed test section with the following dimensions:

L x W x H $(1.2 \text{ x } 0.715 \text{ x } 0.62\ m)$, with chamfered corners of 0.15m as shown in Figure 11.

The optimum size for the model ship which can be fitted in this wind tunnel is a 1/300 scale model of the same catamaran ship. This model has the total height of 59 mm which is measured from the top of the ship's bridge to the waterline. The calculated length for the model's scale is 0.352m. Therefore, to get the same Reynolds value ($3.02 \cdot 10^5$), the wind velocity should be set at 14.25 m/s. Table 4 shows the particulars of the 1/300 scale model.

$R_e = V \cdot L/\text{k}$, where:

V (m/s)	L (m)	K_ Visc (m^2/s)
14.25	0.352	$1.57 \cdot 10^{-5}$

Table 4: Wind tunnel setting parameters

Figure 10: The wind tunnel in the School of Engineering at the University of Tasmania (UTAS) (panaroma picture). This is a closed type wind tunnel.

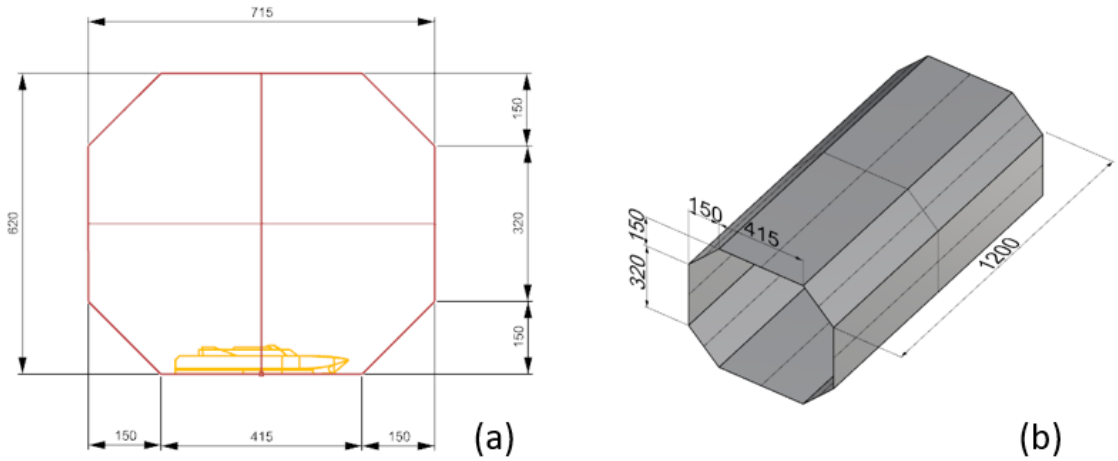

Figure 11: (a) Wind tunnel cross section. The test model is mounted on a rotating disc and located on the floor of the wind tunnel. (b)Isometric view of the wind tunnel test area.

3.2 The size of the model and solid blockage in the wind tunnel

It is important to ensure that the blockage ratio in the wind tunnel does not exceed the recommended value which is approximately 7.5% (Rae & Pope 1984). International Best Practice Guidelines suggest a maximal blockage ratio of 5% for wind tunnel research and 3% for CFD research (Frank *et al.* (2007), Tominaga *et al.* (2008). The side cross section area of the scale model (1/300) of the actual ship, when it is rotated and is perpendicular to the wind flow (90°), is equal to 16037 mm^2. The cross section of the wind tunnel has the area of 466225 mm^2. This gives a maximum blockage ratio of 3.4%.

A 1/300 scale model is the largest size that can be fitted on the floor of the wind tunnel. The length of the 1/300 scale model is 0.352m. When the model rotates to 90 degrees to the wind direction, the bow and stern of the model get very close to the chamfered sides of the wind tunnel. The closeness of the model to these walls could possibly affect the air flow around the model which in reality never exists. The proximity of the wind tunnel side walls to the model in the test area of the wind tunnel could impose the same limitations as previously experienced by Anderson and Jansen in their research (Andersen (2012b), Janssen *et al.* (2017). The closeness of the side wall boundaries to the model caused restrictions in flow around their models which affected the final results. The maximum blockage ratio in their experiment was also reported at 7.4%. Therefore, they also had to correct their results for the blockage effects using correction factors.

For the test in the UTAS wind tunnel, care must be taken to avoid excessive solid blockage and any effect from the side walls on air flow around the model. Figure 12 shows the proposed arrangement for the wind tunnel test.

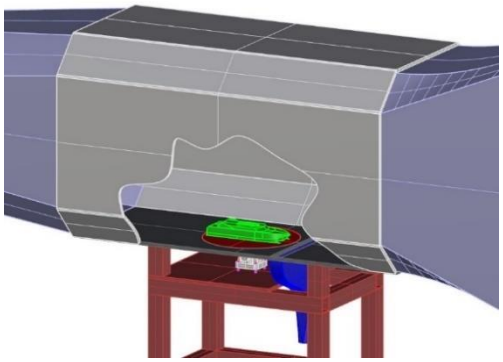

Figure 12: Initial proposal for the wind tunnel test. In this proposal the model is on the floor of the wind tunnel and is mounted on a rotating disc which is attached to a load cell.

3.3 Preliminary CFD analysis to explore the influence of the wind tunnel side walls on the flow field around the model

To ascertain the effect of the side walls on the air flow around the model ship, a new computational domain was created. The new CFD domain had the same geometrical shape (including the chamfered corners) and dimensions as the UTAS wind tunnel. The purpose of this simulation was to visualise the behaviour of the flow field in region around the model and to identify any other potential problems, before starting the actual test in the wind tunnel. Modelling the exact geometrical domain ensures that all results from CFD analysis are directly comparable with the experimental results.

The model was first positioned on the floor of the wind tunnel with its bow directly pointing into the wind tunnel inlet. The wind velocity was set at 14.25 m/s. CFD analysis was performed by rotating the model for 13 different wind angles of attack from 0° to 180° in 15° intervals. The model is symmetrical in respect of its longitudinal, centreline axes. Therefore, no more analysis is required for angles between 180° to 360°. Figure 13 shows the initial arrangements of the CFD domain.

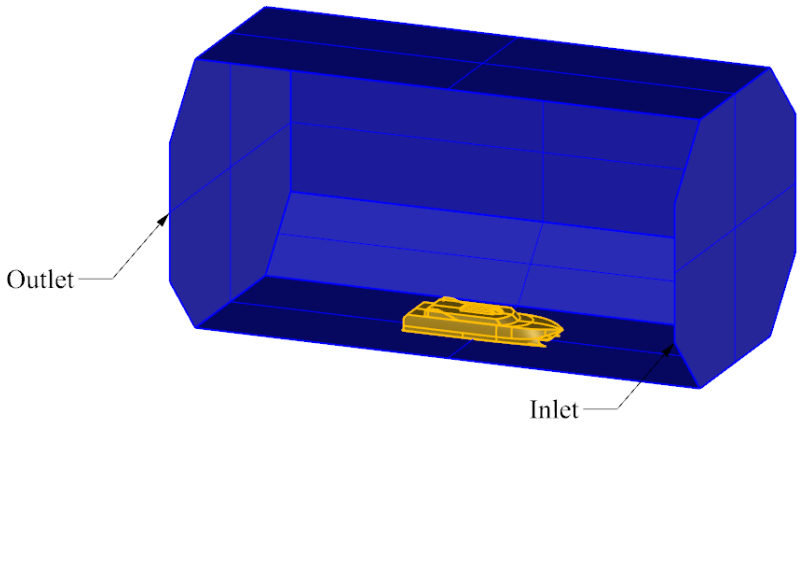

Figure 13: The initial CFD domain of the wind tunnel test. In this proposal the scale model of the ship is on the floor of the wind tunnel. The model is at zero° to the wind angle of attack. This is when the bow is directly pointing into the inlet. The length of the domain is equal to the glass section test area of the wind tunnel.

3.3.1 CFD model

Physics and mesh settings

For turbulence model, Realisable K-epsilon two layer all y^+ wall treatment with steady simulation and for the grid, the trimmer mesh with eight prism layers, are used. Local

refinement was undertaken to capture the complete behaviour of the fluid flow around the model. Table 5 shows the principal particulars of the CFD grid; the performed local refinement is shown in Figure 14. A complete analysis was performed while the model was rotating from 0 to 180°. The results from the CFD analysis displayed a potential problem in the flow field, especially when the model was at a 90° angle to the direction of the wind.

When the air is blowing across the wind tunnel floor and walls, a boundary layer forms along the wind tunnel's wall surfaces. The boundary layer arises due to relative velocity between the air and walls of the wind tunnel. This is most importantly characterised by a velocity profile within the boundary layer, increasing from zero on the floor to the free stream air velocity at some height above the floor, at a distance further downstream. This effectively means that the mass flow in the boundary layer per unit height is less than in the adjacent free stream. Therefore, objects that protrude into this boundary layer will experience a different force than objects not protruding into this region, due to lower mass flow rate (Lutz 1997). Figure 15 shows the interference of the generated boundary layer on the side wall of the wind tunnel and the scale model. This interference affects the air flow while it is passing the model. This effect gets larger during rotation of the model and is easier to be visualised at the time that the model is rotated to 90 degrees and is perpendicular to the wind flow.

Type of mesh	Number of cells	Prism layer thickness	Number of layers	Prism layer stretching	Air density
trimmer	3117228	1.25 mm	8	1.5	1.184 kg/m^3

Table 5: The principal particular of the CFD grid settings which is used to investigate the flow field inside the wind tunnel

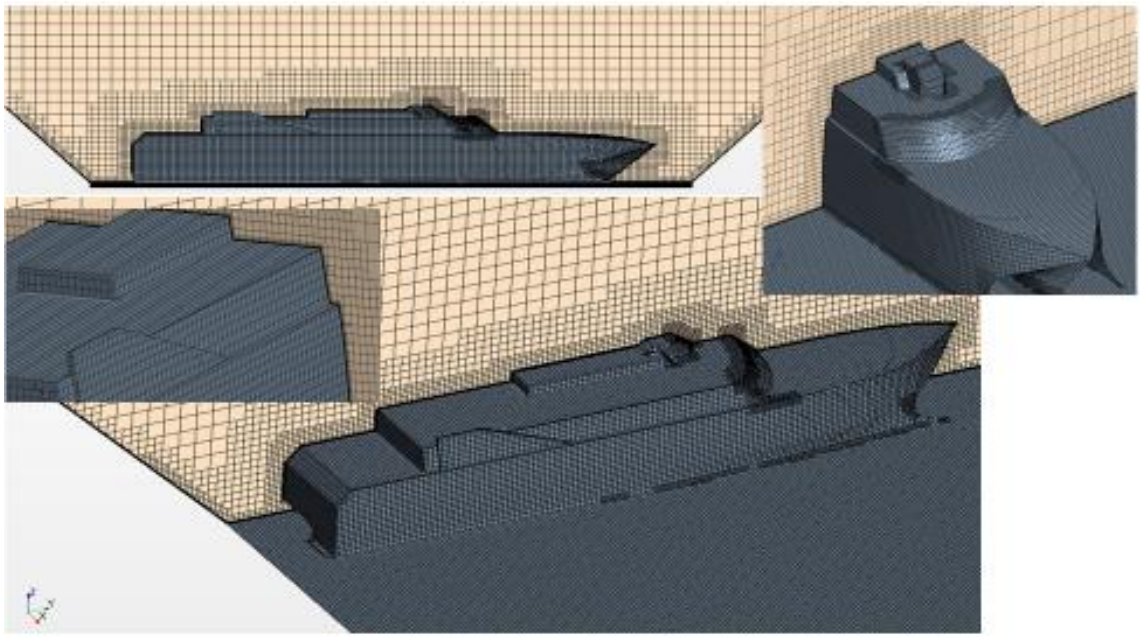

Figure 14: Mesh refinement and prism layer setting of the experiment. Sections of the domain are scaled up to display the transition of the mesh between the prism layer and the core mesh.

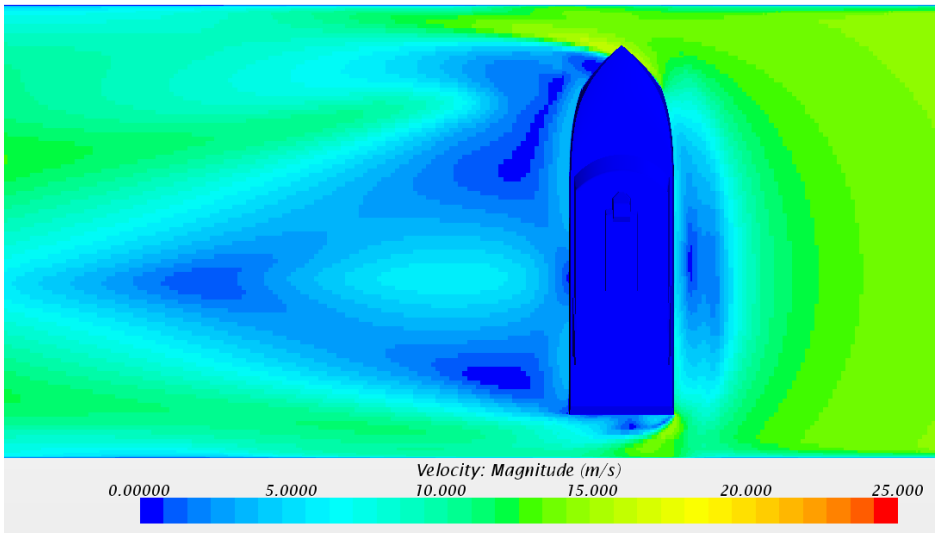

Figure 15: Simulated velocityfield of the wind tunnel experiment. The test model is set on the floor of the wind tunnel and is at a 90 degrees angle to the wind flow. The counotr plane is at ship's water level which is just above the wind tunnel floor.

To gain a better understanding of this problem, further refinement was undertaken. Changing the mesh density around the model and adjacent to the walls displayed a better image of this problem. Table 6 and Figure 16 are showing the level of refinement of the new model. The results from CFD analysis on the model with more refined mesh allowed a better visualisation of the problem. Figure 17 shows the impact of the proximity of the side walls on the wind flow while it is passing the model. It shows how the generated boundary layer on the ship's walls mixes with the boundary layer which is generated on the surface of the wind tunnel side walls, particularly at the ship's transom. This effect changes the mass flow in this region and also causes disturbance in the recirculation zone behind the ship (which in real life never exists) which consequently affects the final results.

Type of mesh	Number of cells	Prism layer thickness	Number of layers	Prism layer stretching	Air density
trimmer	12492067	1.25 mm	8	1.5	1.184 kg/m^3

Table 6: The principle particular of the CFD mesh with further refinement in the surrounding area of the test model and adjacent walls

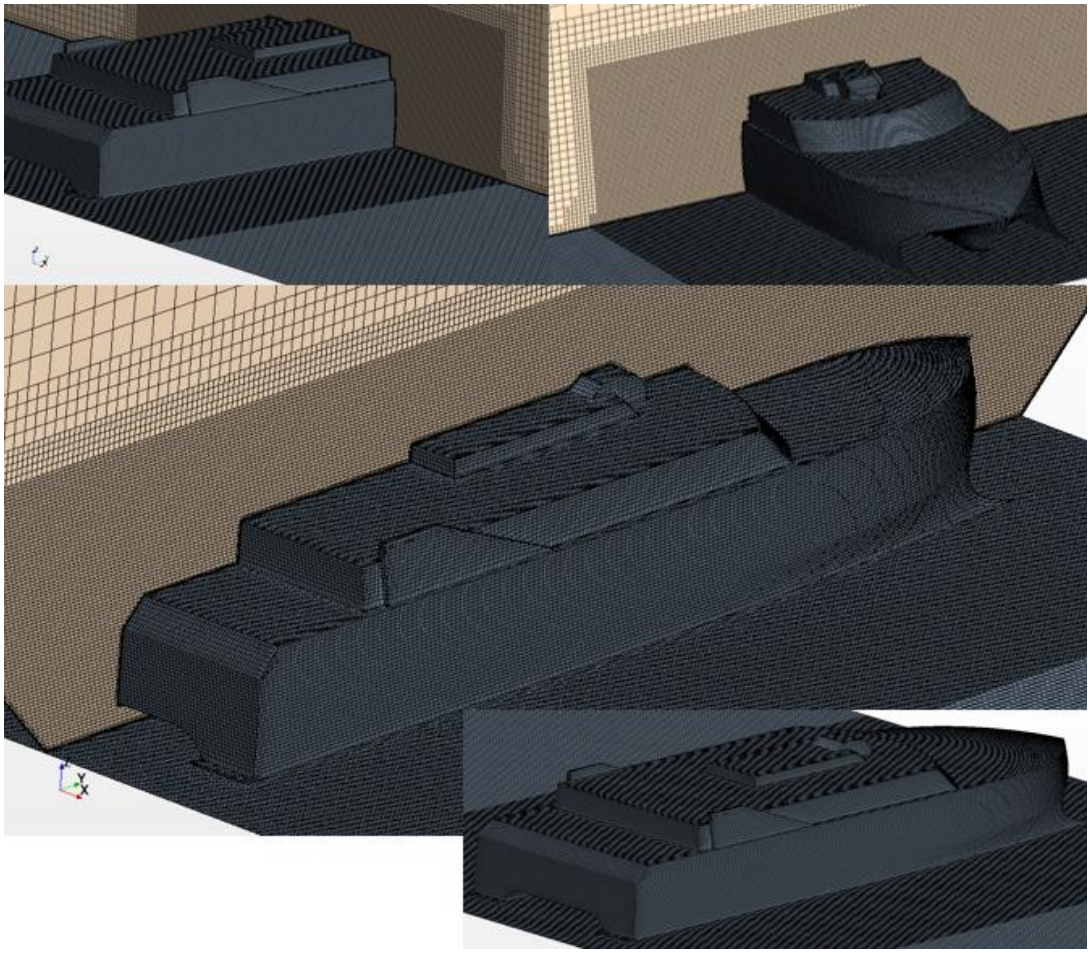

Figure 16: Mesh refinement around the model. The domain now has about 12.5 milion cells. This is to capture the effect of the side walls on the flow while the wind is passing through the test model.

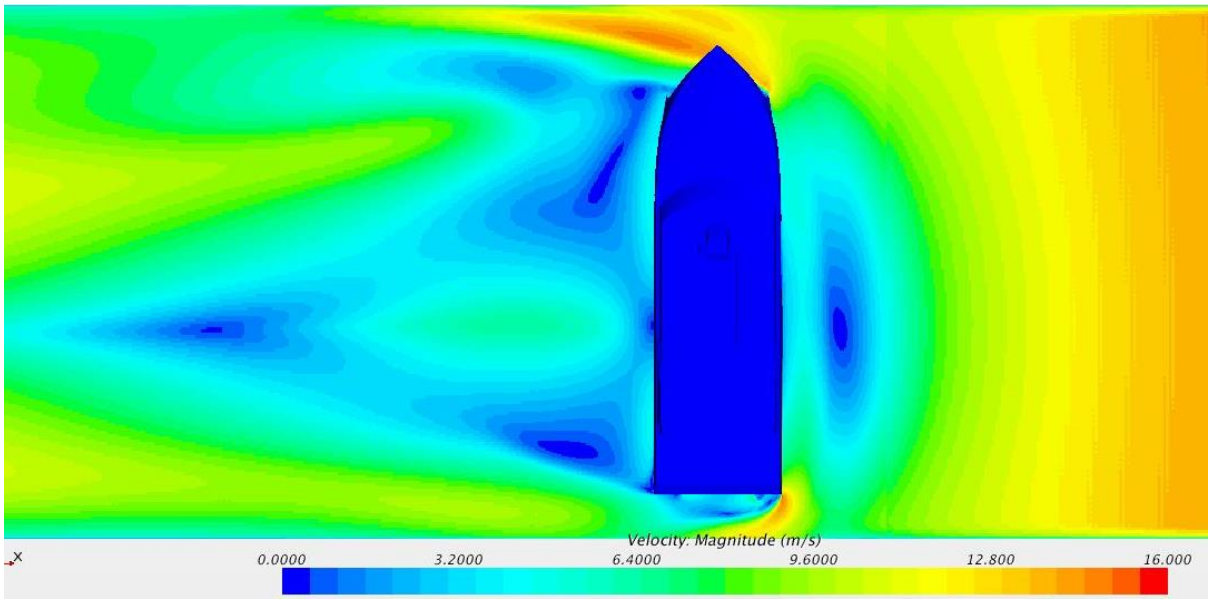

Figure 17: CFD velocity magnitude contour. The interference of the side wall on wind flow around the test model is noticeable. This interference causes the wind velocity to slow down while passing the ship. This makes the analysis results inaccurate.

One of the most important requirements of scale model testing is that the obtained results reflect an accurate picture of the prototype's behaviour. It is therefore of fundamental importance that scale model testing does not introduce any factors which could corrupt the test data (Lutz 1997).

It is clear that the side walls are affecting the flow in domain and consequently change the final results. Therefore, the proposed settings for the wind tunnel test should be modified to eliminate this problem. To remove the effect of the side walls on the air flow it is possible to either reduce the size of the test model or raise the model from the floor. Either way, the distance between the model and the side wall will increase and that could eliminate the effect of the side walls on the flow.

Hulls of the catamaran are connected by a bridging deck (tunnel). The distance between the underside of this deck, in a 1/300 scale model, to the waterline is only 7.68mm. Any further scaling down of the model could cause blockage in air flow through this tunnel which would introduce errors and compromise the accuracy of the final results. Therefore, the possibility of raising the model from the floor seems to be a better solution and should be considered.

Classical wind tunnel testing is characterised by a model resting on a balance supported by a sting and air is blown against the model. The model then experiences an array of forces; the wind tunnel balance measures these forces (Lutz 1997). Raising the model and mounting it on a sting or strut is not an option for performing tests on a ship as it allows the underside of the model ship to be exposed to the wind flow. This would induce additional lift and drag on the model which in real life never exist. (It should be noted that, in the previous arrangement, when the model was mounted on the floor of the wind tunnel, the floor was representing the ocean's surface. Therefore, the only part of the ship's structure which was above the waterline was experiencing the wind loads.)

To avoid this problem, one possibility is to mount the model on a rotating disc or table which eliminates the exposure of the ship's underside to the wind flow during the test. The rotating disc could represent the ocean's surface. This rotating disc needs to be connected to the load cell with a strut. The load cell will be fitted below and outside the test section of the wind tunnel. This is to stop the direct effect of air flow on the load cell. This concept is shown in Figure 18.

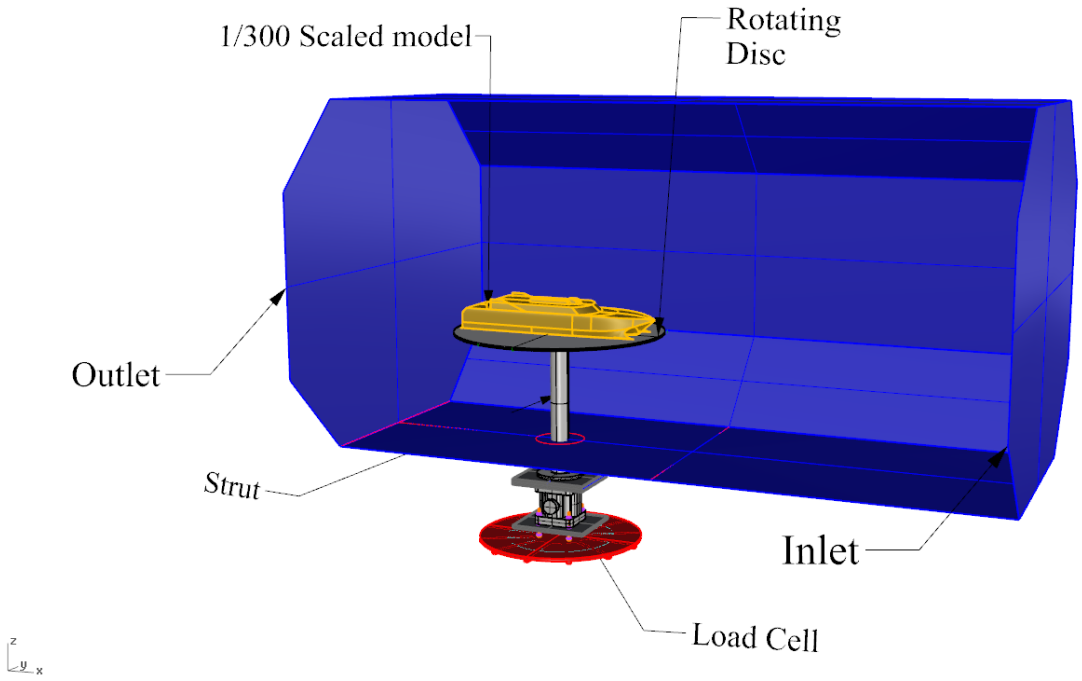

Figure 18: Initial concept of mounting the test model of the ship on a rotating disc which connects the model to the load cell via a strut. It is shown that the strut and the bottom surface of the rotating disc are exposed to the wind flow during the test.

However, in the above arrangement, the strut and the underside of the rotating disc are still exposed to direct wind flow which is transferring additional loads and moments to the load cell. Preliminary CFD analysis on the above concept also showed that the shape of the leading and trailing edges of the rotating disc have a great influence on flow separation inside the domain and they needed to be designed carefully. It is also clear that when the air flows over the ocean surface from any direction a natural boundary layer is formed. The effect of this boundary layer on the final results could be considerable and should not be neglected. However, in the above arrangement, the model only experiences a uniform flow as there is no chance of the development of any boundary layer on the top surface of the rotating disc. Other issues, such as the distance of the model from the inlet and outlet boundaries and the height of the model from the floor of the wind tunnel, also needed to be addressed. Performing more CFD analysis should assist in finding answers to all of the above questions.

3.3.2 Modifications to the test arrangements

To stop any unwanted wind force on the underside of the rotating disc, the rotating disc should be inserted inside a new platform. This new platform should extend to the side walls of the wind tunnel and divide the tunnel test area into two sections. The top surface of the rotating disc should be levelled to the top surface of the new platform. This should eliminate the need for any special design consideration for the rotating disc's leading and trailing edges. Instead, the leading and trailing edges of the platform are now the main concern and need to be designed carefully.

From a series of CFD studies, it was found that the leading and trailing edges of the new platform should have a shape similar to the shape of a NACA foil. This is to minimise any disturbance and flow separations in the flow field inside the wind tunnel. In addition, from further CFD analysis, it was concluded that the test model should be raised from the floor and mounted in the widest part of the wind tunnel. This is to minimise the effect of the side walls on the flow field. This location is just above the chamfered sides of the wind tunnel. To stop any unwanted force on the strut, the strut should be fitted inside a protective skin. This skin cover should be sealed at the top to the underside of the platform and in the base, to the floor of the wind tunnel. It should have the shape of NACA foil for the purpose of minimising any separation in air flow inside the test domain. The final design consideration for the wind tunnel test area is to find the longitudinal location of the model inside the wind tunnel (distance from the inlet boundary). The correct location ensures the atmospheric boundary layer is modelled properly and has the correct velocity profile and a turbulence characteristic similar to the full-scale condition. This allows the results from this test to be usable for full scale station keeping analysis (for more detail see Appendix 5). Figure 19 and Figure 20 are showing the proposed assembly for the wind tunnel test area.

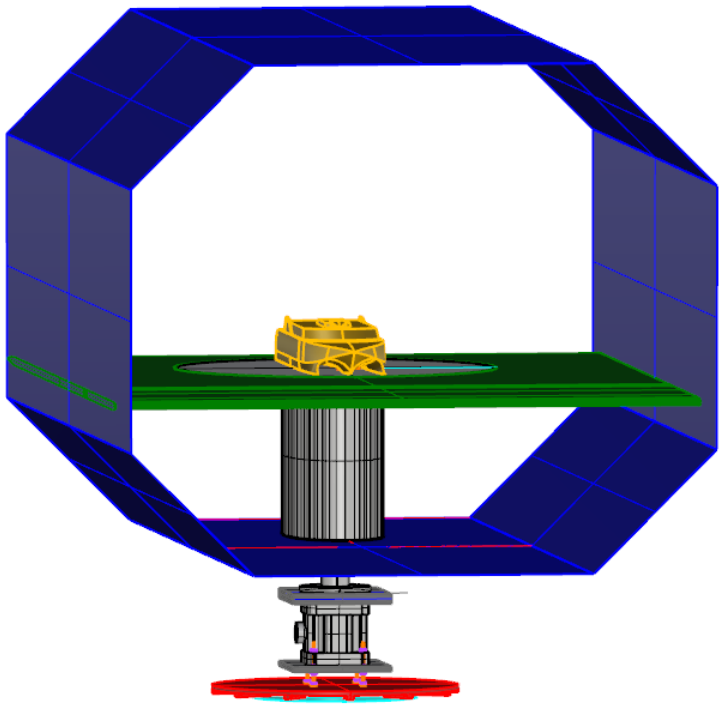

Figure 19: The final arrangement of the wind tunnel test assembly. The model is raised from the floor of the wind tunnel. A protective skin (strut cover) is fitted to stop the wind loading on the strut.

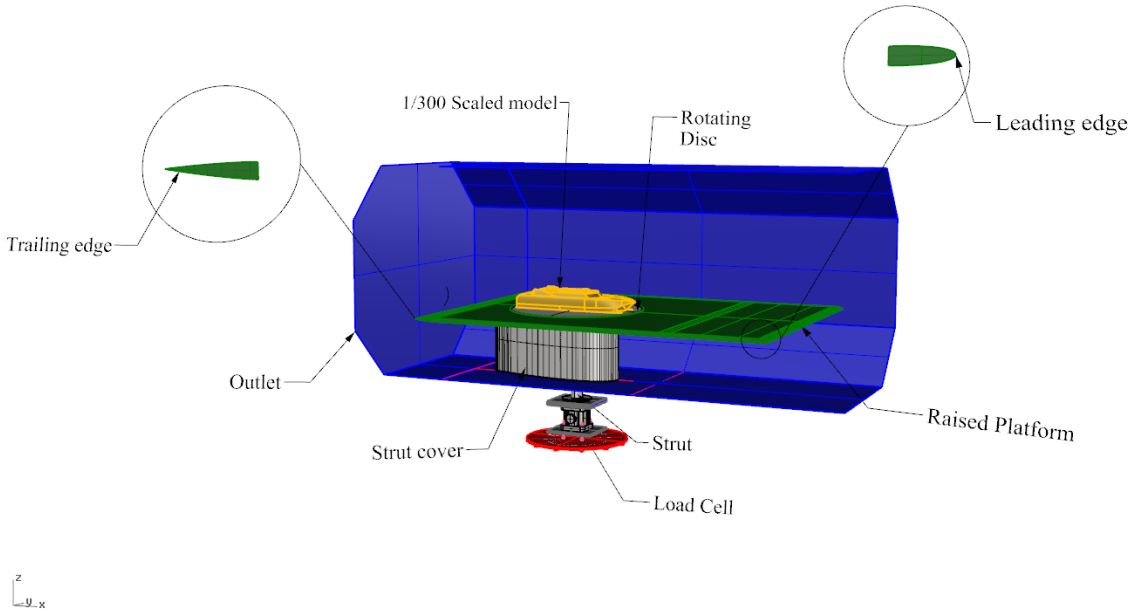

Figure 20: The isometric view of the wind tunnel assembly. Sections of the leading edge and the trailing edge are shown in a bigger scale to assist better visualisation. The figure above also shows how the skin cover is fitted between the floor of the wind tunnel and the underside of the raised platform to protect the strut from any wind loads. All the gaps on the top and bottom of this section are sealed with silicon.

3.3.3 Atmospheric boundary layer on ocean

A ship moving on a smooth sea and in still air experiences a resistance arising from the movement through the air of the part of the hull which is above the water. This resistance depends on the speed of the ship and on the area and shape of the upper structure.

When the air flows over the ocean surface from any direction, a natural boundary layer is formed. This means that the wind velocity at the surface is zero and increases with higher altitude. The local wind field caused by the movement of the ship does not have a boundary layer and is homogenous. The actual wind field encountered by the part of the ship above the water surface is thus a combination of the wind field with a boundary layer and the homogenous wind field caused by the ship's forward speed (Andersen 2012b). This is shown in Figure 21.

The wind resistance also depends on the wind speed and its relative direction. In addition, the wind generates waves which normally cause a further increase in resistance (Larsson *et al.* 2003). Locating wind forces are very important in a station keeping study of the ships. However, these wind forces can be noticeably overestimated if a constant wind speed is used in station keeping calculations, because the wind speed is reduced at lower elevations above the free surface (Sadovnikov 2009). This is why it is important to make sure the wind velocity profile over the ocean surface is taken into consideration as this improves the accuracy of analytical calculations.

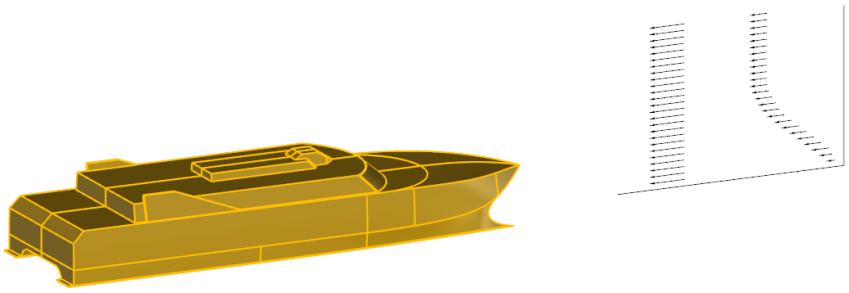

Figure 21: Combined local wind field caused by a ship's movement and the natural velocity profile over the ocean surface

3.3.4 Velocity profile in wind tunnel (CFD domain)

It has been shown in the literature that correctly reproducing the atmospheric boundary layer profile is essential for modelling accuracy (Polsky (2002), Forrest and Owen (2010), Vogt *et al.* (2017). The boundary layer within the wind tunnel should simulate the same turbulent characteristics found in the full-scale atmospheric boundary layer. It is important that the atmospheric boundary layer approaching the modelled region has the same characteristics as it does in full-scale. Otherwise, the changes in local velocity over the model will not be accurately simulated. The relationship between the mean velocity U and height above the surface z, for a boundary-layer of height δ and a mean velocity of U_∞ at height δ, is described by the power law:

$$\frac{U_z}{U_\infty} = \left(\frac{z}{\delta}\right)^{\alpha} \quad \text{(Cengel \& Cimbala 2013)} \qquad (3.1)$$

The power law exponent α defines the shape of the boundary layer velocity profile. Its value in the wind tunnel must closely match the full scale value of α. Generally, the value of α depends on the roughness of the terrain. Over open ocean $\alpha \approx 0.1$ (Hsu *et al.* (1994), Lubitz and White (2004). Reproducing the combined wind field (combination of the wind direction and the ship's wind field) is difficult to create in any wind tunnel and almost impossible in the UTAS wind tunnel (referring to the UTAS wind tunnel test area limitation in dimensions). Therefore, as an alternative, the aim should be, if possible, to do the tests in such a velocity profile similar to the natural atmospheric profile over the ocean.

The reference value for the wind speed on the ocean is usually at 10m height from the water surface (Larsson *et al.* 2003). 10m height corresponds to 33.3 mm in 1/300 scale model which is used in this wind tunnel experiment. The idea of locating the test model in the wind tunnel in such a position that the velocity profile is close to the natural velocity profile in the ocean was previously used by Andersen (2012a) and Janssen *et al.* (2017). They have measured the velocity profile at different locations of their wind tunnel to find the most suitable location to position their test models.

To measure the velocity profile on different locations of the platform, CFD analysis was performed on an empty tunnel. A new CFD domain was created in Star CCM+ which had all the proposed modifications for improving the flow field in the wind tunnel. Line probes were used to measure the vertical velocity profile at different distances from the inlet boundary. Figure 22 shows the CFD domain and the location of the line probes is shown in Figure 23.

Figure 24 shows the plot of the non-dimensionalised velocity profile which was measured by line probes at different distances from the inlet boundary. The target atmospheric velocity profile is also shown. For comparison of the velocity profiles with the atmospheric velocity profile, the best location to mount the model was found to be at 700mm from the leading edge of the platform. Due to the limitation in length of the UTAS wind tunnel test area, this location cannot be pushed any further away from the inlet boundary. Therefore, the midship of the model and the centre of the rotating table should be located at this point (Details of measured data from line probes are shown in Appendix 5).

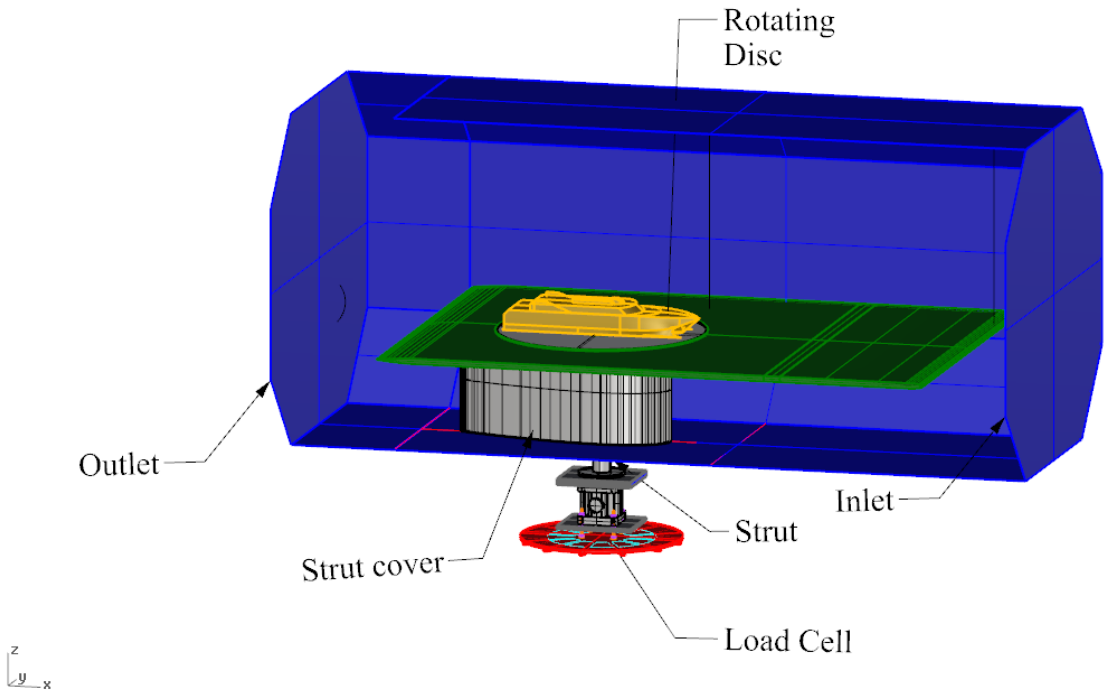

Figure 22: CFD domain which was created to measure the velocity profile on top surface of the platform. The outlet boundary is 200mm downstream of the trailing edge.

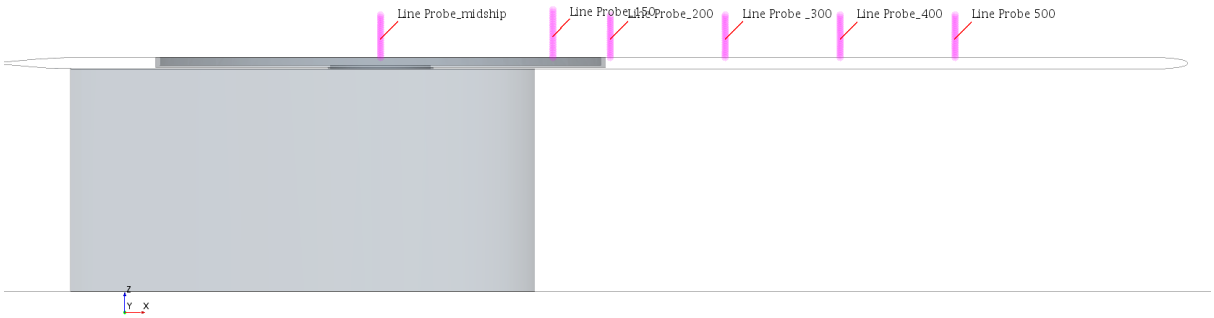

Figure 23: Cross section of the wind tunnel test area. Location of the line probes at different distances downstream of the leading edge of the platform is shown. The tunnel is empty.

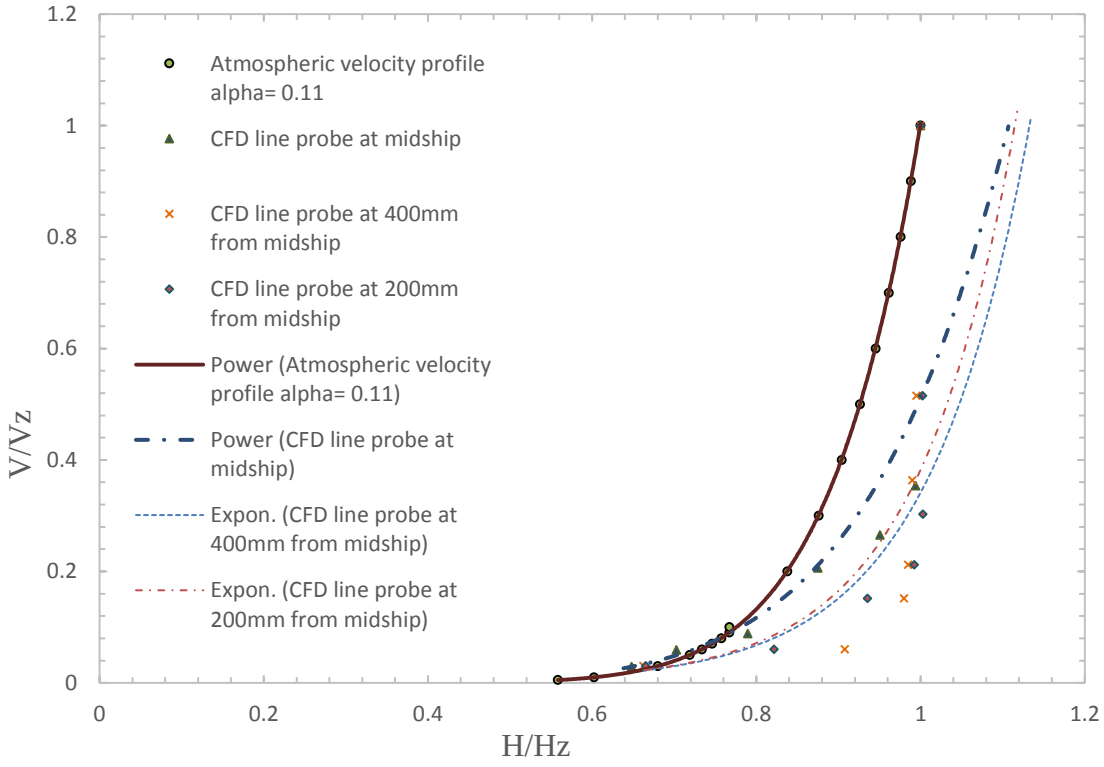

Figure 24: Velocity profile measured at different locations in the wind tunnel. The horizontal axis displays the non-dimensional velocity and the vertical axis displays the non-dimensional height.The target is the solid brown line which represents the atmospheric velocity profile on the ocean. The closest plot is from the line probe at midship at 700mm from the leading edge of the platform.

3.4 Checking the blockage ratio

The total cross section of the wind tunnel above the platform is 275801.9 mm^2 (when the model is fitted above the chamfered corners). The projected side cross section of the 1/300 scale model is 16037 mm^2. Therefore, the calculated blockage ratio is 5.8%

3.4.1 Results after raising the model from the wind tunnel floor

A new CFD domain with all the suggested modifications from the CFD results was created. In the new domain, the model was mounted at a distance of 700mm away from the leading edge of the platform and the analysis was repeated. The results showed a significant improvement in flow around the model. Figure 25 shows the new CFD domain in which the scale model of ship has been lifted from the floor of the wind tunnel to a new height just above the chamfered corners of the wind tunnel. The results from CFD analysis showed that, with this arrangement, the side walls had very little effect on air flow around the model. This is shown in Figure 26.

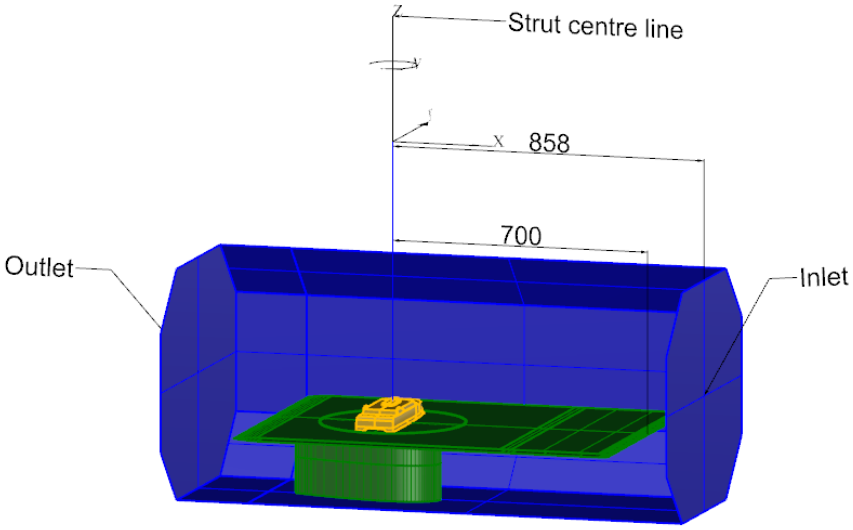

Figure 25: CFD domain when the model is set at 700mm downstream from the trailing edge of the platform. The wind angle of attack is 90°.

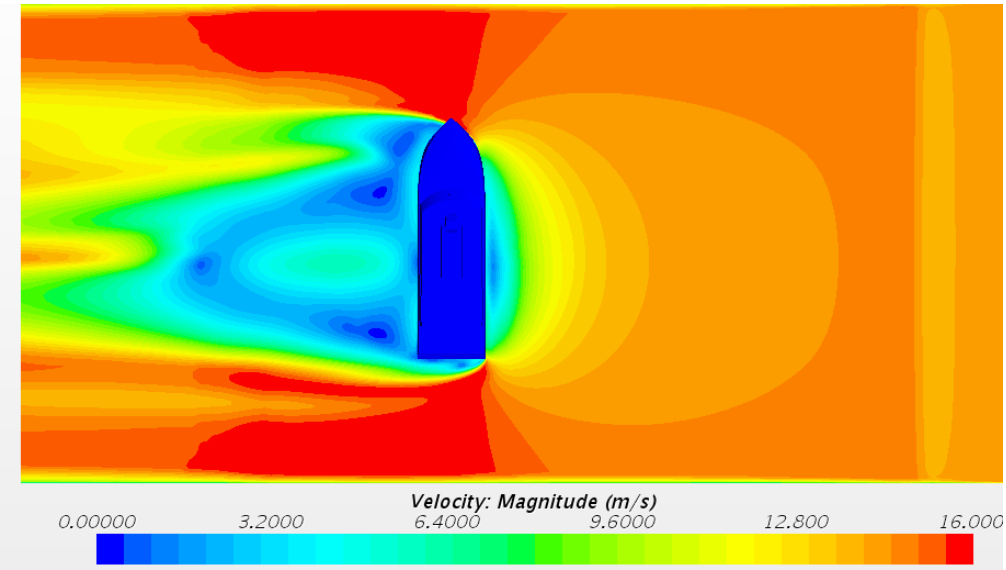

Figure 26: CFD velocity magnitude contour. The model is raised from the floor to a higher elevation in the domain where the side walls are far enough from the test model. The effect of the side wall on wind flow inside the domain is very small.

3.4.2 The effect of the side wall on results

Table 7 compares the results from CFD simulation when the model was mounted on the floor of the wind tunnel with the time when the model was raised to a new elevation above the chamfered corners of the wind tunnel.

	Model on the floor of the wind tunnel	Model on top of the platform	Percentage of error
Cx	0.15	0.13	15.3%
Cy	0.85	0.88	3.4%
CN	-0.06	-0.05	20%

Table 7: Comparison of force and moment coefficients measured from the results of CFD simulation when the model is mounted on the floor of the wind tunnel to when the model is mounted on the platform. Model is set at 90° heading into the wind. It is shown that the side wall effects on results could be considerable.

3.4.3 Location of the CFD domain outlet

The location of the domain outlet first was set at 200mm aft of the platform trailing edge. This was to allow the flow, after passing the model, to become fully developed before exiting the outlet boundary. It was also to avoid any reverse flow into the domain due to recirculation around the trailing edge of the platform. To ensure that the outlet boundary is far enough and does not have any effect on results, a sensitivity analysis was performed by moving the outlet boundary further downstream to 600mm from the trailing edge of the platform. The results remained unchanged. This shows that the original location at 200mm aft of the trailing edge was satisfactory and that there was no need to increase the length of the domain; this would increase the computational time. (For more detail see Appendix 7.)

3.5 Discussion of the results

It was shown that the preliminary CFD analysis assisted in visualising the effect of the side walls of the wind tunnel on air flow around the model. This assisted the understanding of the need to raise and mount the model to a new height where there is very little or no effect from the side walls on the air flow while passing the model. It is shown that the proximity of the side walls could introduce a 15% to 20% error to the final results.

Preliminary CFD simulations assisted in identifying the maximum wind forces acting on the model. This information was used to choose the correct strain gauges for the new load cell and to identify the maximum force and moment in defining the maximum expected deflection of the strut and rotating disc. This determines the size of the gap between the rotating disc and the platform.

It is shown that CFD is used as an effective tool in designing the best shape for the leading and trailing edges of the new platform, and a new structure to protect the strut which connects the rotating disc to the load cell. This protective cover has the shape of a NACA foil and it not only protects the strut against any direct wind force, but it also helps to avoid the possibility of the creation of vortex shedding behind the strut. The results from CFD analysis also assisted in determining the correct size of the scale model to suit the test in the wind tunnel to avoid blockage effects. In addition, the results from CFD analysis, assisted in finding the most suitable location for the test model (referring to the distance from the inlet of the test area to the scale model) in the test area of the wind tunnel where the velocity profile at that location was similar to the natural velocity profile on the ocean.

Chapter 4 Preparation for the wind tunnel test

From the results of CFD simulations in previous chapter, detail drawings with required instruction were provided for modification and preparation of the wind tunnel test area. Drawings were detailing the type of materials, methods of fabrication, machining and final order of assembly of the parts for the wind tunnel (See Appendix 9 for all drawings).

To be able to perform the experimental test in the wind tunnel, manufacture of the following parts was required:

- a platform, a rotating disc and a strut;
- a 1/300 scale model of the ship;
- a shell to protect the strut, and
- a load cell.

4.1 Fabricating the parts

The platform, rotating disc and strut are made from aluminium. These parts were machined and manufactured in the UTAS workshop. The cheapest and most accurate method to make the scale model for the wind tunnel test is to use a 3D resin printer. The scale model of the ship must have very accurate and detailed specifications which could only be achieved by using the resin printing.

The resin 3D printers are capable of printing models to within 0.1 mm of accuracy. Additive manufacturing is often referred to as 3D printing, as it works in a similar way to a laser printer. The technique builds a solid object from a series of layers – each one printed directly on top of the previous one. The machine operating software cuts the CAD model of the workpiece into slices, the thickness of which depends on the type of material employed. Additive layer manufacturing (ALM) uses 0.1mm for polymers and 30 microns for metals. A blade mounted on a moving arm sweeps an even layer of the powder on top of the work surface inside the chamber, then a laser – generally around 200W – scans back and forth over the surface, melting the powder in the shape of the first layer. The work surface then drops by the thickness of the layer and another layer of powder is distributed over the surface (Cummins 2010).

These printers generate less heat and, consequently, less distortion than normal PLA printing. The finished products for the model test are also much lighter than those manufactured by any other methods. Due to the limitations of the resin printer at the UTAS campus, the scale model of the ship needed to be printed in two segments and then joined together. The two segments of the scale model are shown in Figure 28. Finally, the two parts of the printed model were glued together as shown in Figure 29. All dimensions of the final assembly were inspected to ensure the accuracy of the scale model is thoroughly within 0.1 mm.

Another part which was made by the 3D printer was the skin cover for the strut. This part has a NACA foil cross section to minimise flow separation below the platform. For this part, PLA printing was utilised. PLA materials have the disadvantage of becoming distorted due to heat

generation while the model is being printed. This can be worse if the printed object is large and very thin. This part is fitted below the main platform and its role is to stop any wind load on the strut, during the test. The flow below the platform does not affect the flow above the platform because the platform is extended and sealed to the side wall of the wind tunnel. Therefore, any slight distortion in the final printing of this section would not have any effect on the results.

Figure 30 shows the skin cover which is prepared for protecting the strut using normal PLA plastic printing. This part is glued to both the underside of the platform and to the floor of the wind tunnel. This stops any unwanted wind load from the underside of the platform on both the rotating disc and the strut which connects the rotating disc to the load cell.

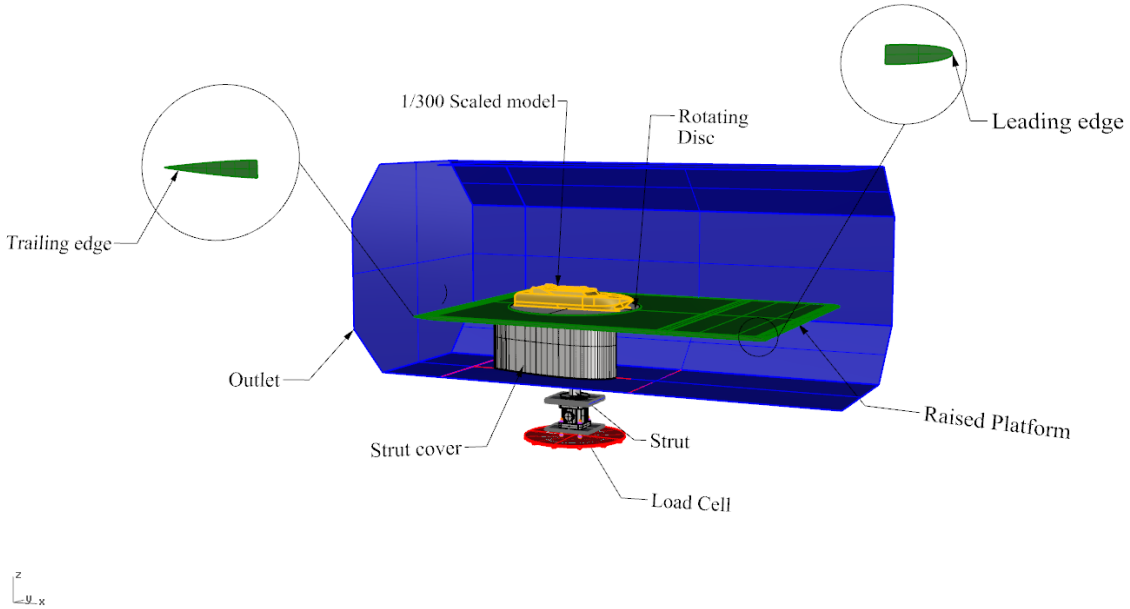

Figure 27: Isometric view of the wind tunnel assembly. Sections of the leading edge and the trailing edge are shown in a bigger scale to aid better visualisation. The figure above also shows that the the skin cover is fitted around the strut, from the floor of the wind tunnel to the underside of the raised platform. All the gaps on the top and bottom of this section are sealed with silicon to prevent any air or wind loading on the strut.

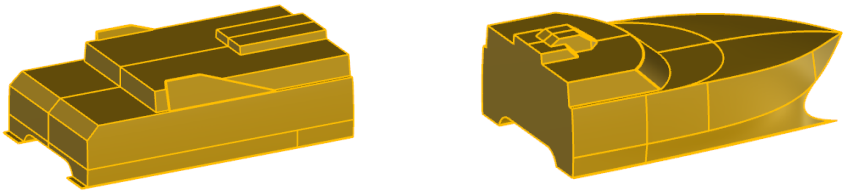

Figure 28: Due to the limitation of the 3D printer in printing large models, the scale model was divided into two sections for printing purposes. Those parts were then glued together to create the 1/300 scale model of the 112m high speed catamaran. Polymer material with an accuracy of 0.1mm was used.

Figure 29: The finished product of the 1/300 model ship using a 3D printer after glueing the parts together

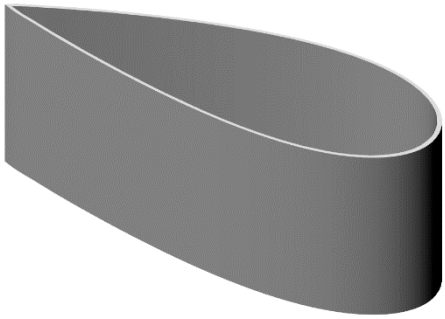

Figure 30: Protective cover which was printed in a 3D printer using PLA materials. This component will be fitted under the platform and around the strut to prevent any unwanted wind load on the load cell.

4.2 Manufacturing of a six component force balance

The load cell which was used in the experiment was designed and manufactured by UTAS staff. The total weight of the rotating disc, the strut and the ship model are estimated to be 1.3 kg. During the test, and while the model is subjected to wind force, the total force and moment on the load cell increases. The estimated total force on the strain gauges during the test are expected to be less than 1 kg (9.81 N). Therefore, using a minimum of 3kg strain gauges in the load cell is sufficient. The load cell was calibrated by a UTAS technician. Detail of the calibration process and the method of data acquisition is described in Appendix 11. Figure 31 shows isometric plots of the load cell.

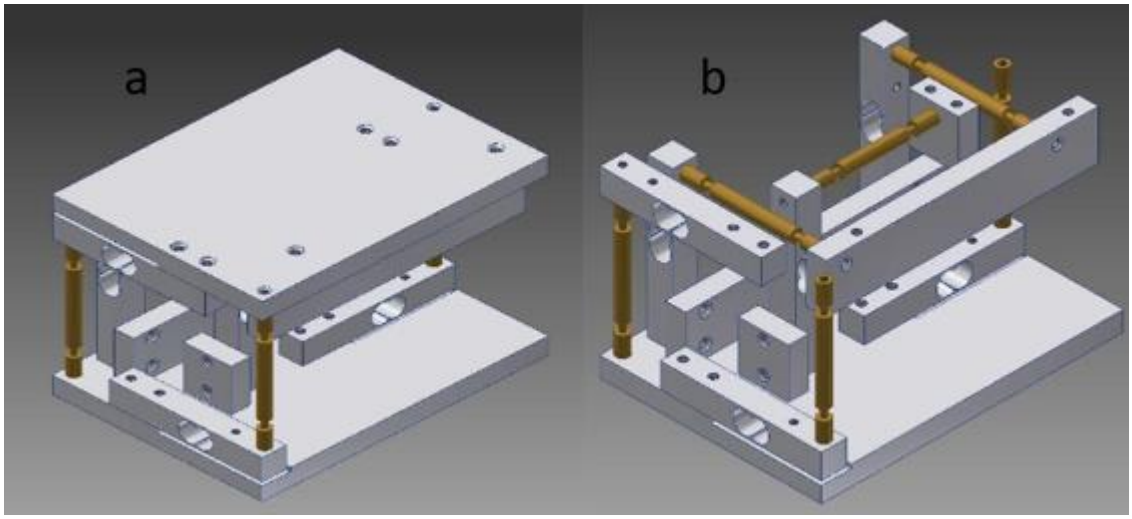

Figure 31: a) 3D plot of the six DOF load cells built in UTAS, Hobart, for the wind tunnel experiment. b) Top plate is removed to display the location of the strain gauges.

4.3 Final assembly of the parts for the wind tunnel test

All parts for the wind tunnel test were finally assembled as shown in Figure 32. The platform was fitted at its correct height, just above the chamfered corners of the wind tunnel. The gap between the platform and the side walls was made airtight. The rotating disc was inserted inside the platform and the top surface of the rotating disc was levelled with the top surface of the platform. All necessary inspection was undertaken to ensure that the top surface of the rotating disc remained at the same height and was perfectly level at all times during the rotation of the disc.

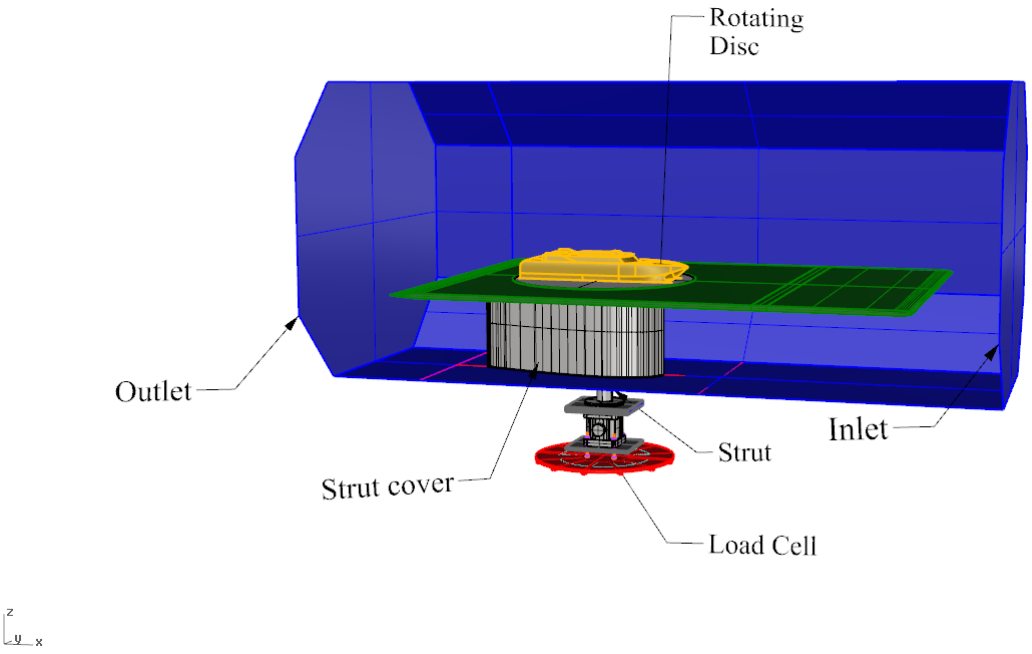

Figure 32: Final assembly of the platform and the test equipment before mounting the ship's model

Chapter 5 Velocity profile in wind tunnel

Prior to starting the experiment, the velocity profile at the location of the midship on the platform should be measured and compared with that which was measured previously in Chapter 3. This is to ensure that the model is experiencing a representative turbulent profile as in the full-scale atmospheric boundary-layer. It also ensures that all settings are correct and all equipment is properly calibrated.

Initially, the average velocity of the wind inside the wind tunnel test area was measured by pitot tubes at several locations. Hot wire was also used to ensure that the velocity readings of the load cell's computer software are correct. Final checks were made to ensure that the velocity at the inlet of the wind tunnel is the same as the value given by the pitot tube when it was set in free stream and above the test model. The software which is written for the load cell in the laboratory view is able to measure a number of variables such as pressure, temperature, air density, air velocity, force in x, y and z directions and moment on the load cell in all x, y and z-axes.

Next, the thickness of the boundary layer was measured at a point 700mm downstream of the leading edge of the platform by using a pitot tube, after setting the wind velocity of the wind tunnel at 14.25 m/s. This was undertaken by measuring the wind velocity while the tip of the pitot tube was resting on the top surface of the platform and then continuing to read the velocity after gradually raising the pitot tube until it reaches the free stream velocity. The total thickness of the boundary layer at a distance of 0.7m (this is midship) from the leading edge was measured at 16.25 mm. This is when the average wind velocity at the wind tunnel inlet was reported to be 14.29 m/s (See Appendix 10 for details).

The velocity magnitude of the free stream was first checked by a calibrated hand-held hot-wire anemometer (DT_8880 model) to ensure that the flow rate inside the wind tunnel was correct. Then the second hot-wire anemometer (TSI Veloci Calcs Plus model) was used to confirm that all readings were the same. The total thickness of the boundary layer was checked against the calculated theoretical value as shown below:

Theoretical value for the thickness of the boundary layer:

For a flat plate the expression for turbulent boundary layers on a smooth flat plate aligned parallel to a uniform stream is:

$$\frac{\delta}{x} = \frac{0.16}{(Re_x)^{1/7}}$$ (Cengel & Cimbala 2013) page 574 (5.1)

$$R_e = \frac{V \cdot x}{\vartheta}$$ when kinematic viscosity of air at 20°, $\boldsymbol{\nu}$ =1.516 · 10^{-5} m^2/s (5.2)

and x = 0.7m (midship) and V = 14.299m/s (*the wind velocity was set at 14.25 m/s at inlet. However, the averaged velocity was recorded at 14.299 m/s (Lab view software which is written for the load cell) after 20seconds. This variation is normal even in a wind tunnel with perfect settings*)

Then $R_e = 6.6 \cdot 10^5$ this indicates the flow is turbulent as it is greater than $R_{e,cr} = 5.0 \cdot 10^5$

Therefore: $\delta = \frac{0.16 \cdot 0.7}{(6.6 \cdot 10^5)^{1/7}}$ = 0.01651 m or 16.51 mm

(Note: repeating the calculation for kinematic viscosity of air at 22°, $\boldsymbol{\nu} = 1.5295 \cdot 10^{-5}$ m^2/s, also gives the value of δ =16.53 mm)

5.1 Velocity profile in wind tunnel

The test area of the UTAS wind tunnel was modified and upgraded to replicate all settings as in CFD analysis. An initial test was undertaken to measure the velocity profile at different locations of the platform, in order to verify that the chosen location for the centre of the rotating disc was correct. The velocity profile was measured by a pitot tube while the wind was blowing at a speed of 14.25 m/s. All the measured data from the use of the pitot tube in the wind tunnel is shown in Table 19, at the end of Appendix 5. Figure 33 shows the measured velocity profile at different locations on the platform inside the wind tunnel. For clarity, the measured velocity profile from the wind tunnel test at midship (700mm downstream from the leading edge of the platform) was compared with the measured velocity profile from CFD analysis at the same location. The measured flow velocities are plotted as a function of height above the platform surface and are shown in Figure 34. V_z is the reference value for the wind speed on the ocean which is usually at a 10m height from the water surface (Larsson *et al.* 2003). 10m height corresponds to 33.3 mm in 1/300 scale model (H_z) and is used in this wind tunnel experiment. The non-dimensional values of V/V_z and H/H_z of the measured atmospheric vertical velocity profile on the ocean surface and that which was measured in the wind tunnel and the CFD domain at the above reference points are plotted in Figure 35.

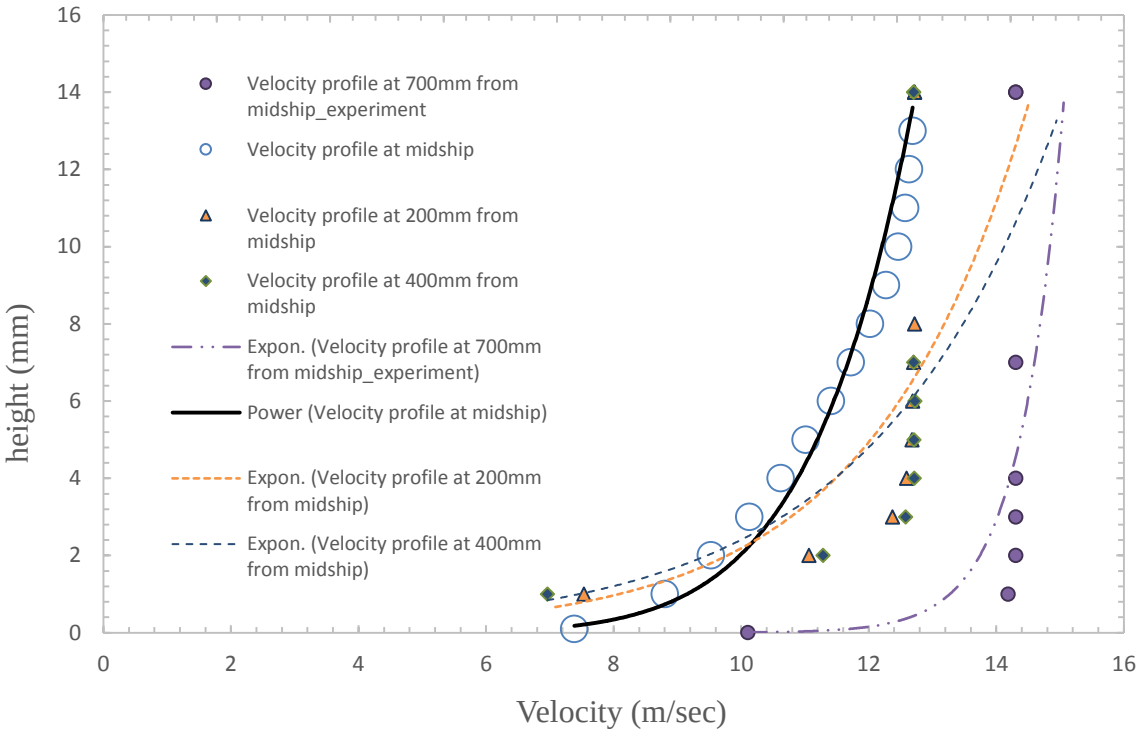

Figure 33: Velocity profile at different locations inside the wind tunnel. The velocity profile is measured by using a pitot tube. Final results are compared with CFD results at midship. The midship is 700mm downstream from the leading edge of the platform.

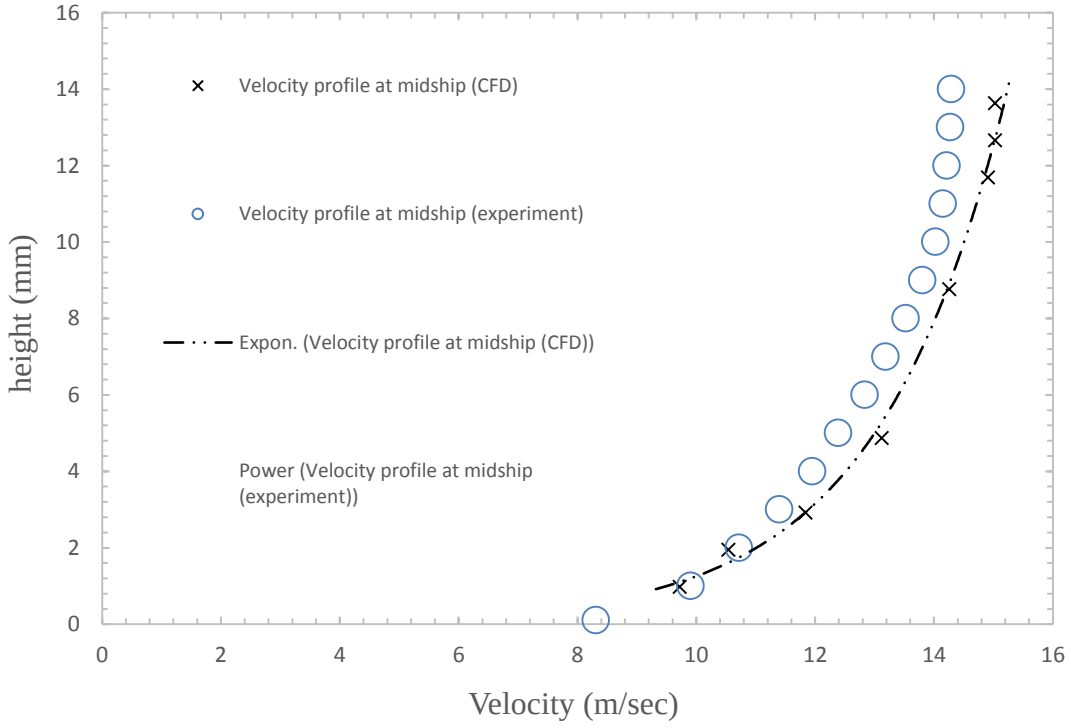

Figure 34: Comparing CFD and wind tunnel velocity profile at the distance of 700mm from the leading edge of the platform. Both tests were performed in an empty tunnel.

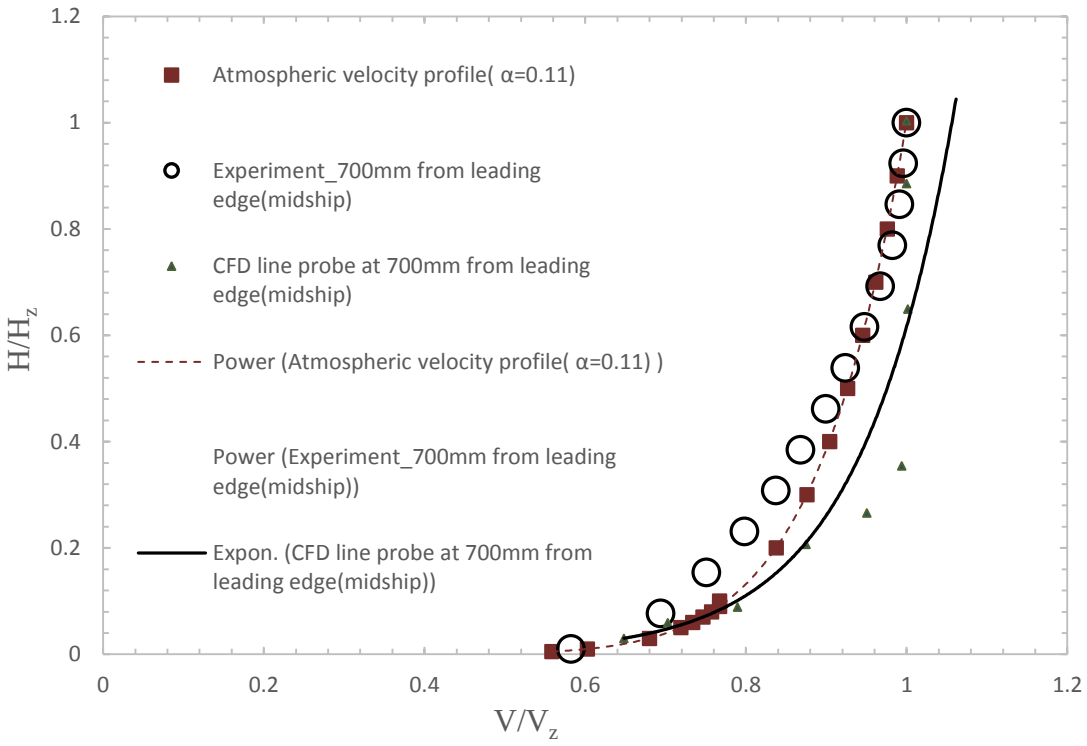

Figure 35: Comparing the velocity profile which is measured in the wind tunnel and CFD with the atmospheric velocity profile on the ocean. 10m is used as the reference height on the ocean. The location of the line probe in CFD and the data from experimental tests are taken at midship which is 700mm downstream from the leading edge of the platform.

5.2 Preparation for the wind tunnel set up

Finally, the scale model was fitted inside the test area. Care was taken in ensuring that the ship's model was fitted centreline of the platform and its midship was located at the centre of the rotating disc. At this point the longitudinal axis of the ship was aligned with the longitudinal axes of the wind tunnel and the bow was pointing into the inlet of the wind tunnel. The protective cover for the strut was already fitted into place and was glued to the underside of the platform at the top, and to the floor of the wind tunnel at its bottom edge, in order to stop wind flow from the underside of the platform, entering the top of the platform. Inspection was undertaken in order to ensure that the rotating disc and the strut were correctly inserted inside the platform and were securely attached to the load cell. Measurements were taken to ensure that the rotating disc was mounted level and aligned to the top surface of the platform while the disc rotates a complete 360° turn and the gap between the rotating disc and the platform remained unchanged. The calibration of the load cell was also checked once again.

Next, a preliminary test was performed to ensure that the model was mounted securely at the correct location on the platform so it could withstand the maximum wind loading during the experiment. Another task was to identify the correct 0° heading of the model in relation to the wind tunnel inlet. This is when the bow of the scale model points directly to the wind tunnel inlet and the load cell measures no side force and moment from the wind loading, as the model has a symmetrical shape. The next test was to set the wind velocity in the wind tunnel to its

maximum to ensure that an induced force does not make the rotating disc come into contact with the platform. More measurements were taken to ensure that the load cell was calibrated properly and working correctly at all times.

In the current arrangement of the wind tunnel, the ship and the rotating disc were glued together. Therefore, the load cell measures the total shear and pressure drag on both the model and the rotating disc as both these parts are experiencing wind loading. During the test and each time when the ship is rotating, the size and the intensity of the recirculation zone behind the scale model changes the effects of the magnitude of the force and moment on the rotating disc. Therefore, for validation of the CFD results, the measured forces and moments on both the ship's model and the rotating disc should be measured from CFD analysis and compared with similar measured forces given by the load cell during the wind tunnel test.

Figure 36 shows the scale model of the ship which is mounted on the rotating disc, inside the wind tunnel. The load cell is located below the wind tunnel and is mounted on a rotatory table. This table has the capability of rotating the load cell and the model from 0 to 180°. Figure 37 shows the coordinate axes of the load cell and the ship's model. The ship's coordinate axes are aligned with the wind tunnel axes but perpendicular to the load cell. The true zero heading of the ship's model is when the transverse force generated by the wind, blowing directly into the bow, is zero and the longitudinal force is at its maximum. The true zero heading was found by trial and error while rotating the model slightly to plus and minus of a few decimal degrees of zero to find the F_X, to be almost zero.

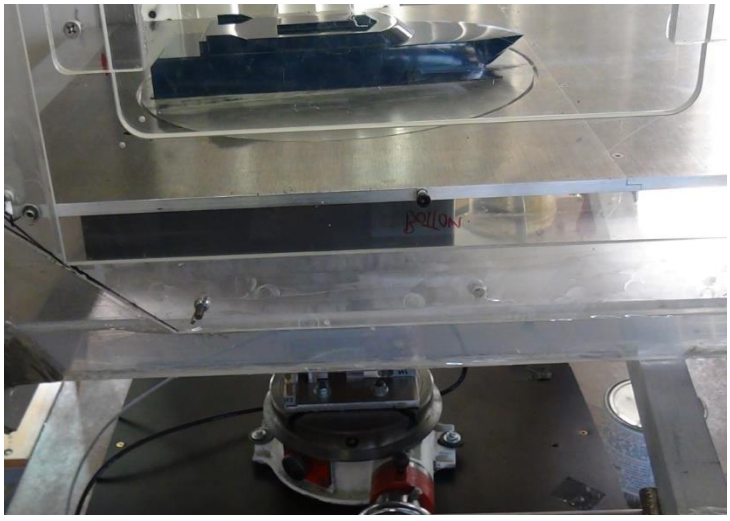

Figure 36: 1/300 scale model of the ship glued onto the top surface of the rotating disc. The rotating disc is inserted inside the platform. The ship's model is set at zero degrees when the wind is directly blowing into the bow.

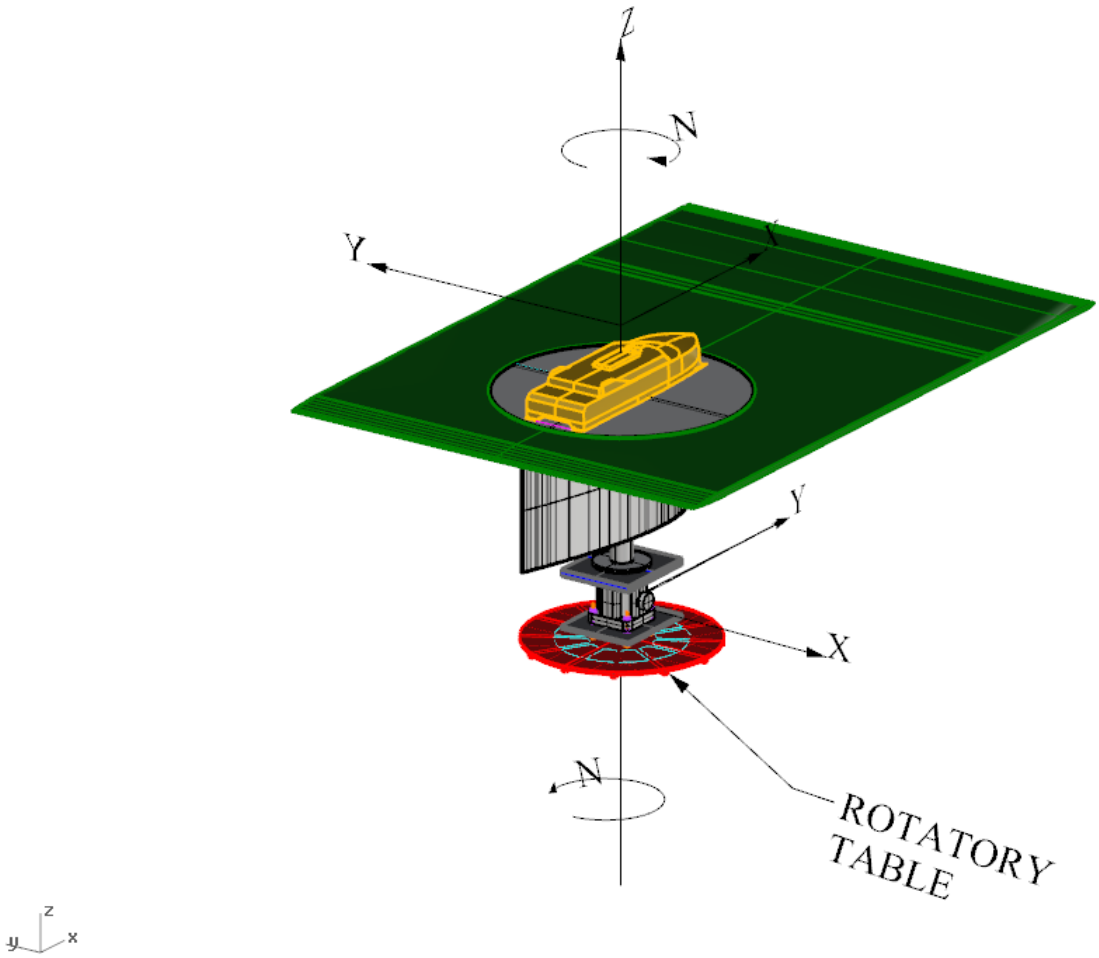

Figure 37: The coordinate system of the load cells which are at 90 degrees to the ship's coordinates. The positive x axis of the wind tunnel test area is from its outlet to the inlet.

5.3 Performing the test in the wind tunnel

The test started after ensuring that the load cell was reading zero transverse forces and moments while the wind was blowing directly from the inlet to the ship's bow (wind angle of attack is zero). The true zero heading was marked on the rotary table as a reference point. Next, the wind was generated (by starting the motor of the wind tunnel) and was set to 14.25 m/s. After the system was stabilised, the computer was set to save the first set of data. The duration for reading data for each angle of the ship's heading was 20 seconds. Every second the computer was measuring the relative density of the air, pressure, humidity, air velocity, forces on the load cell in x and y directions, moment and the room temperature. Then, all results were averaged and saved. The final averaged value of wind velocity, as measured by the computer, was within $\pm$ 0.8% of the initial setting. At this time the wind tunnel motor was turned off and all data was saved. Measurement was taken to ensure the wind velocity inside the wind tunnel test area was back to zero.

The next step was to rotate the model by 15 degrees from the true zero reference point. The motor was restarted and the wind velocity was set at 14.25 m/s, which was the same as before the data acquisition, after the system was stabilised and results were recorded. This process was repeated multiple times, by rotating the model for another 15 degrees, until the model had a full 180 degrees of rotation. The final results from this test are shown in Appendix 12. The wind tunnel experiment was repeated with a wind velocity of 28.5 m/s. The results from this experiment are also shown in Appendix 12.

5.4 Discussion of the results

By using analytical methods, it is shown that the calculated boundary layer thickness agrees with that which was measured in the wind tunnel. A slight variation between analytical and experimental results should always be expected. This could be explained by limitations in the equipment used for the wind tunnel test. One of the limitations was from the lack of accuracy of the velocity control unit on the control panel of the wind tunnel which was within 0.8% of the expected settings. Additionally, the variation in room temperature and the relative humidity of the air during the test could have introduced minor errors to the final results.

It is recommended that appropriate data is used in CFD simulations of the wind tunnel test. For example, when analysing the CFD model for 15 degrees, wind velocity should be set at 14.18 m/s and air density to 1.192 kg/m^3, the same as that which was measured in the wind tunnel test by computer. This is to ensure that the results from CFD analysis are comparable with wind tunnel results.

Chapter 6 CFD simulation of the wind tunnel test

A set of new CFD analyses was performed to replicate the wind tunnel experimental test. The aim of this was to validate the results from CFD against the results from the wind tunnel test. The CFD domain size was set to the same geometrical constraints as the test area of the UTAS wind tunnel. This computational domain is that which was described in the final preliminary design stage; this is detailed in Chapter 3.

Table 8 details the mesh settings of the CFD model while the boat is heading at 45° into the wind. Table 9 displays the principal particulars of the scale model. The general mesh and physics settings for this model are typical for all other angles. The number of cells varies slightly between each model. Realisable K-epsilon turbulence with two layer all y^+ wall treatment and steady model were chosen for turbulence modelling. It was shown in Chapter 1 that this model and the SST K-omega turbulence model both produce similar results. All other settings for this set of analyses was retained the same as for the other CFD models which were described comprehensively in Chapter 2.

CFD Model detail:

Type of mesh	Number of cells	Prism layer thickness	Number of layers	Prism layer stretching	Air density
trimmer	13465353	0.00125 m	8	1.5	1.184 kg/m^3

Table 8: Typical setting of the grid in CFD analysis for all CFD analyses. The number of cells varies slightly between each model.

Length		0.352	m
Breadth		0.101	m
Wind velocity		14.25	m/s
Wind attack angle		zero to 180°	degrees

Table 9: Principal particulars of CFD scale model

$$Re = V \cdot \frac{L}{\vartheta} \qquad (7.1)$$

When ϑ = k_ visc ($1.57 \cdot 10^{-5}$ m^2/s), V is Velocity (14.25 m/s) and L (0.352m) is the ship waterline. Therefore, Reynolds number (Re) is $3.20 \cdot 10^5$ and when the wind velocity is 28.5 m/s, the Reynolds number is $6.40 \cdot 10^5$. Figure 38 and Figure 39 are showing the general mesh refinement in the CFD domain.

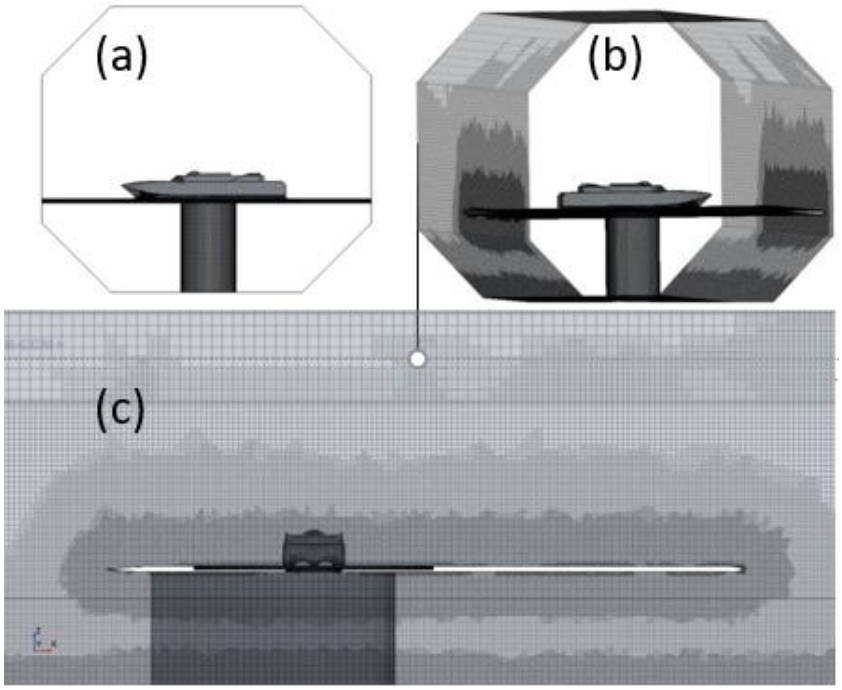

Figure 38: General mesh setting and refinement in the CFD domain. a) side elevation, b) isometric, c) front elevation

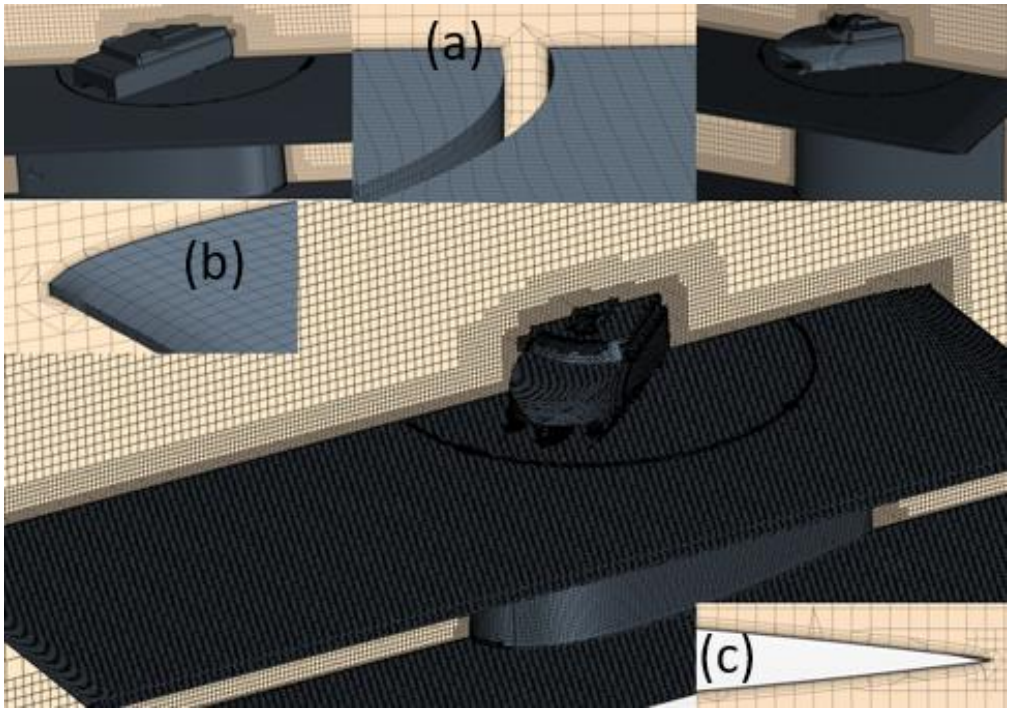

Figure 39: The mesh and prism layer setting for the CFD models while the test model is at 45 degreees heading into the wind. The transition of the mesh around the leading edge, the trailing edge and the gap between the rotating disc and platform are shown in larger scale for clarity. The model is cut through its centreline to show the mesh refinemnet in the CFD domain. The general settings are typical for all other ship headings, a) prism layer and mesh refinement in the vicinity of the gap between the rotating disc and the platform, b) prism layer and mesh refinement at the leading edge of the platform, c) prism layer and mesh refinement at the trailing edge of the platform.

6.1 Results

Figure 40 shows the model at 45 degrees heading into the wind. The streamline plot demonstrates the expected recirculation zone behind the ship's model. A low-pressure zone inside the tunnel, and behind the ship, forces the wind velocity to increase in those regions. Figure 41 shows the vector plots of the wind velocity. Part of the platform at the leading and trailing edges is magnified to assist visualisation of the transition of the wind flow. The design of the leading and trailing edges generates minimal disturbances in the flow field. The behaviour of the wind in the air wake of the ship (bluff body) has a very high level of turbulence coupled with large gradients of wind velocity. The plots also show the way in which the flow from below and above the platform surfaces are mixing at the trailing edge of the platform, before marching towards the outlet boundary.

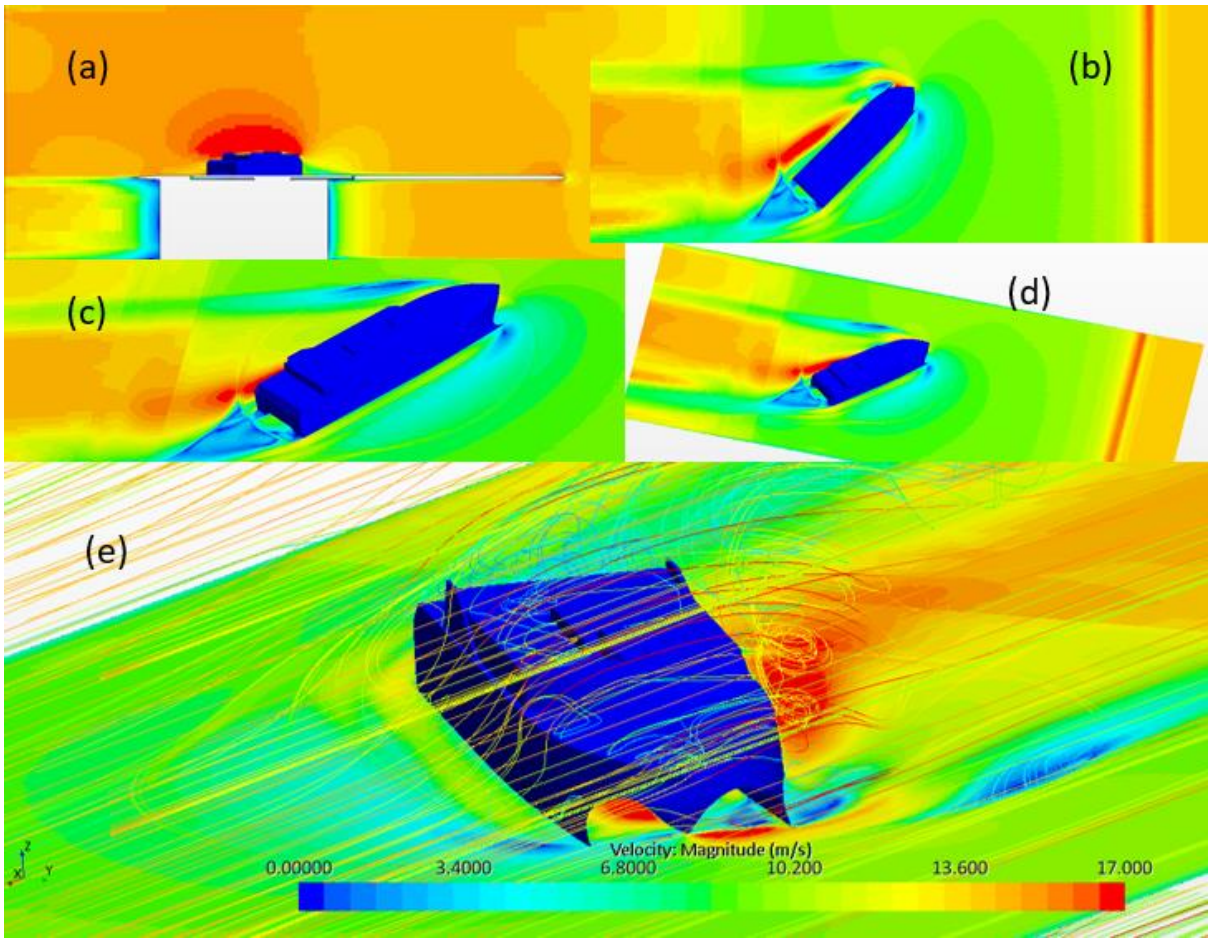

Figure 40: CFD velocity contours for the wind speed of 14.25 m/s. The wind angle of attack is 45°. A low pressure zone inside the tunnel, and also behind the vessel, causes the increase in the wind velocity in those regions and this results in an increase of the lift force on the ship. a) elevation at centreline of the domain, b) plan view at waterline level, c)isometric view (close up at transom), d) isometric view, e) isometric with wind streamline

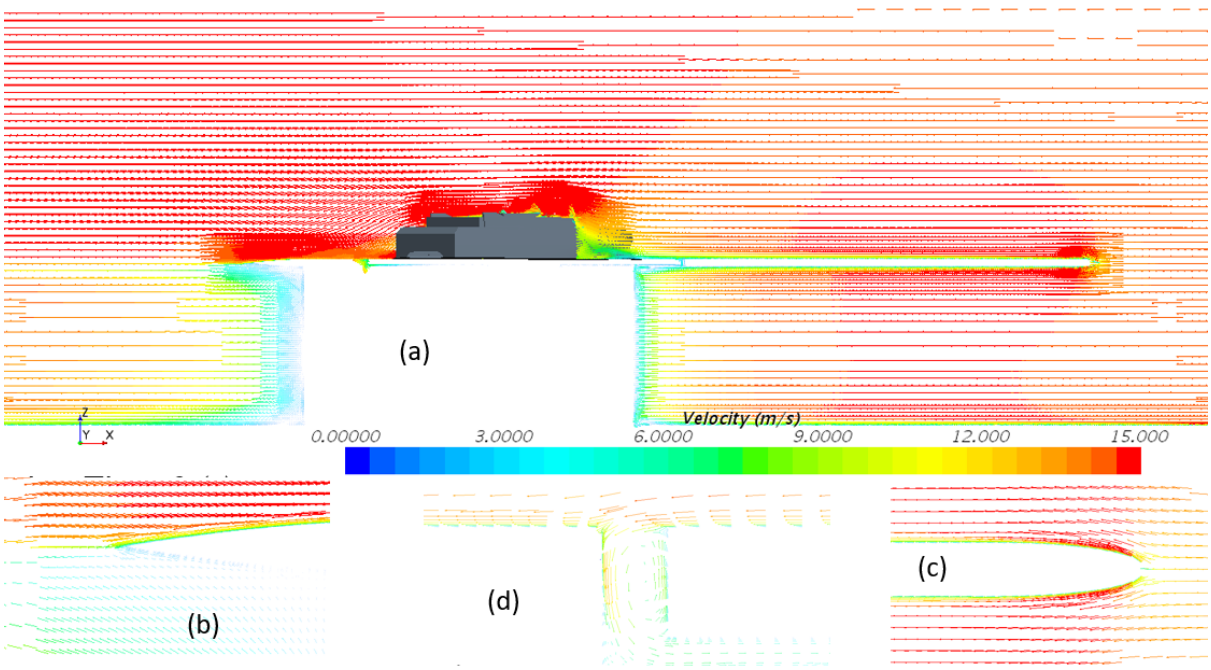

Figure 41: Vector plot of the velocity in the CFD domain. Wind velocity is 14.25 m/s and wind angle of attack is 45°. The plot shows that the separation in flow at the leading and trailing edges is minimal. A small amount of air flow enters the domain after travelling between the rotating disc and the platform. This causes minimal disturbance in the air flow inside the domain. a) vector plot elevation at centreline of the domain, b) vector plot at trailing edgeof the platform, c) vector plot at leading edge of the platform, d) vector plot showing the air entering the domain after travelling underside of the rotating disc

6.2 Velocity magnitude plots

Bluff bodies are defined as having a massive separated region in their wake at Reynolds number ranges of the order of 10^4 and greater (Bardera Mora 2012). With a crosswind, the flow topology becomes much more complex, with the recirculation zone intermittently 'spilling' and refilling in a highly unsteady manner (Greenwell & Barret 2006). This is shown in Figure 42. Similarly, when wind flows over a ship, a large recirculation region will be formed at its wake. In high speed catamarans, the incoming wind flow from its tunnel (the region between the demi hulls), adds to the complexity of the flow in this region. Figure 43 displays the complexity of the wind flow as it passes the model.

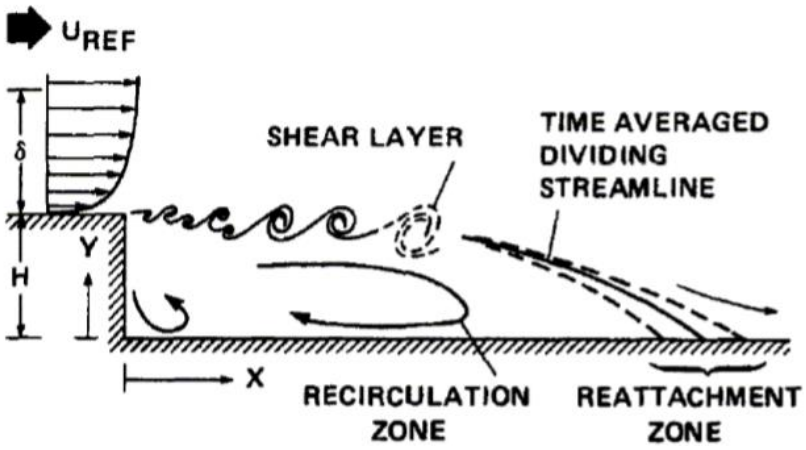

Figure 42: Two dimensional flow field of a bluff body (Greenwell & Barret 2006)

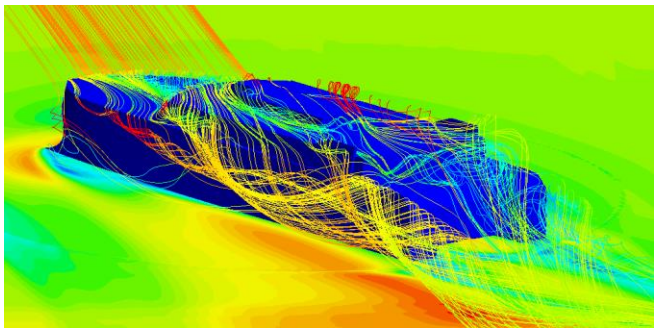

(a)

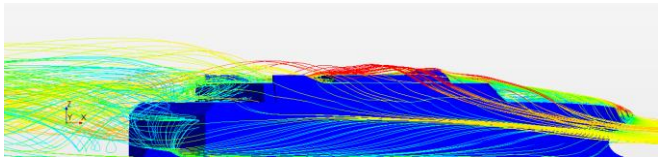

(b)

Figure 43: Velocity streamline displaying the complexity of the flow in the recirculation zone downstream of the ship. a) isometric, b) front elevation

The shape of a catamaran creates interesting behaviour of the wind flow in its wake region. The aerodynamic shape of the bow and the ship's demi hulls generate a low pressure zone with a high velocity in the ship's wake region. This behaviour is similar to that which is normally seen when the wind passes the sail of a sailing boat. This region generates a lift force which adds up to the total wind loadings acting on the ship.The size of this region does get larger as the wind angle of attack changes from 0 to 45°. When the wind angle of attack approaches 60°, the size of this region slowly decreases and, by the time the ship rotates to 75° into the wind, this high velocity zone completely disappears. Therefore, it should be expected that the maximum transverse force is at the time when the ship is heading into the wind at a 45° angle. Figure 129 to Figure 154 (section 6.3 Velocity and pressure plots) are showing the velocity and pressure plots of the catamaran in all the ship's headings.

It is also important to pay attention to the effect of the side walls on the flow field inside the computational domain. Raising the model from the floor of the wind tunnel and mounting it in a higher elevation, where the model is in the furthest possible distance from the side walls, minimises the effect of the side walls on the flow field around the model. However, this change does not completely eliminate the interference of the side walls on flow while passing the model. Ideally, the test should have been performed in a much larger wind tunnel. However, as is shown, even with all the limitations in length and width of the wind tunnel test area, the results from the experiment and replicated CFD analysis, are still showing agreement.

6.3 Velocity and pressure plots

The Velocity and pressure contours for the wind angle of attack at 0° is shown here. To see the velocity and pressure contours for all other ship's headings, see Appendix 12.

Velocity contours (wind velocity at 14.25 m/s; wind angle of attack 0°):

The x axis of the model is aligned with the wind tunnel's longitudinal axis when wind is blowing directly to the bow.

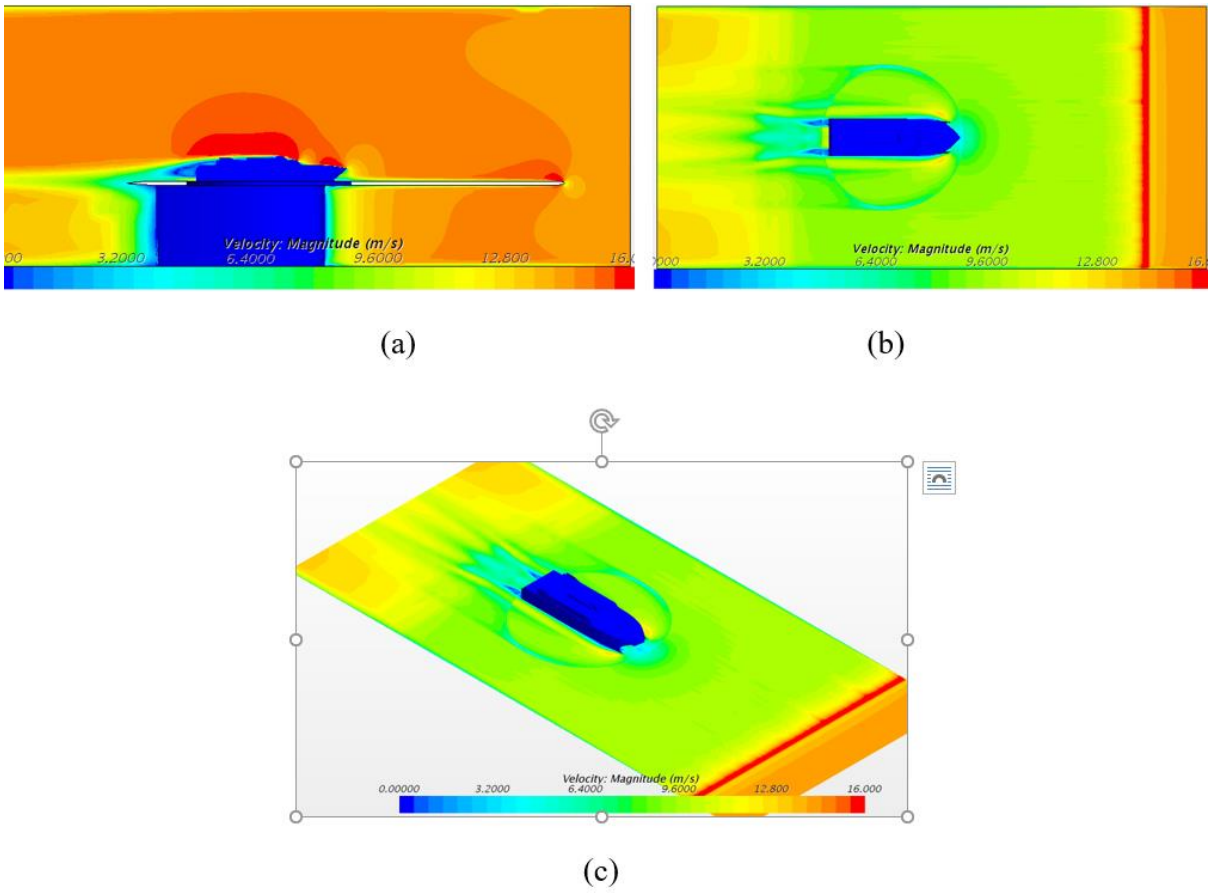

Figure 44: CFD velocity contours for a wind speed of 14.25 m/s and wind angle of attack at 0°. (a) elevation at centreline of the domain, (b) plan view at waterline level, (c) isometric view at waterline level

Pressure contours (wind velocity at 14.25 m/s; wind angle of attack is 0°):

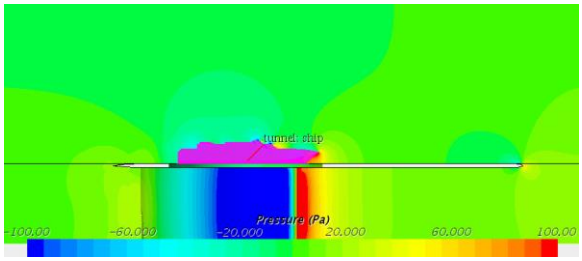

(d)

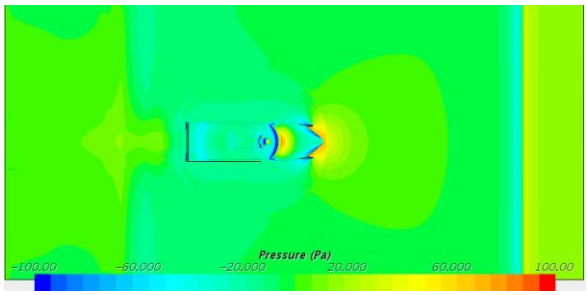

(e)

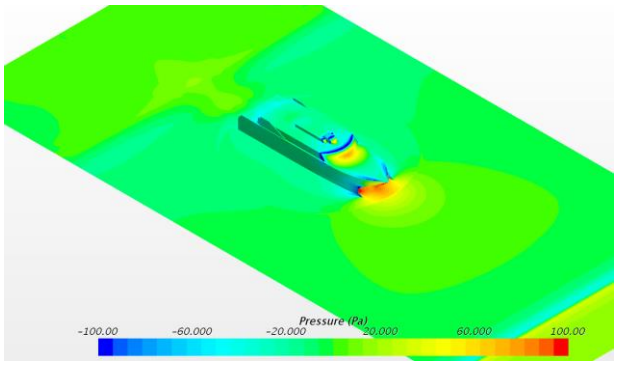

(f)

Figure 45: CFD pressure contours for a wind speed of 14.25 m/s and wind angle of attack at 0°. (a) elevation at centreline of the domain, (b) plan view at waterline level, (c) isometric view at waterline level

6.4 Validation of the CFD results

The load cell measures the total pressure and drag forces acting on both the model and the rotating disc. This is because the model is glued to the rotating disc. Each time the model rotates the behaviour of the air flow regime near the model changes. Therefore, for validation of the CFD results, the total forces on both disc and model should be compared with measured forces on similar components from the wind tunnel test.

6.4.1 Results of the wind tunnel test: (Wind velocity at 14.25 m/s)

Figure 46 to Figure 48 are comparing the results from CFD analysis with the results achieved by the experimental test. These graphs compare the total measured forces and moments on both the scale model and the rotating disc. As is shown all results are in agreement. This finally validates the results from the CFD simulation. It is now possible to use the results from the CFD analysis to extract the required force and moment coefficients acting on the ship's model only and use them for station keeping analysis of the full-scale ship. (See Tables 22 and 23 in Appendix 6)

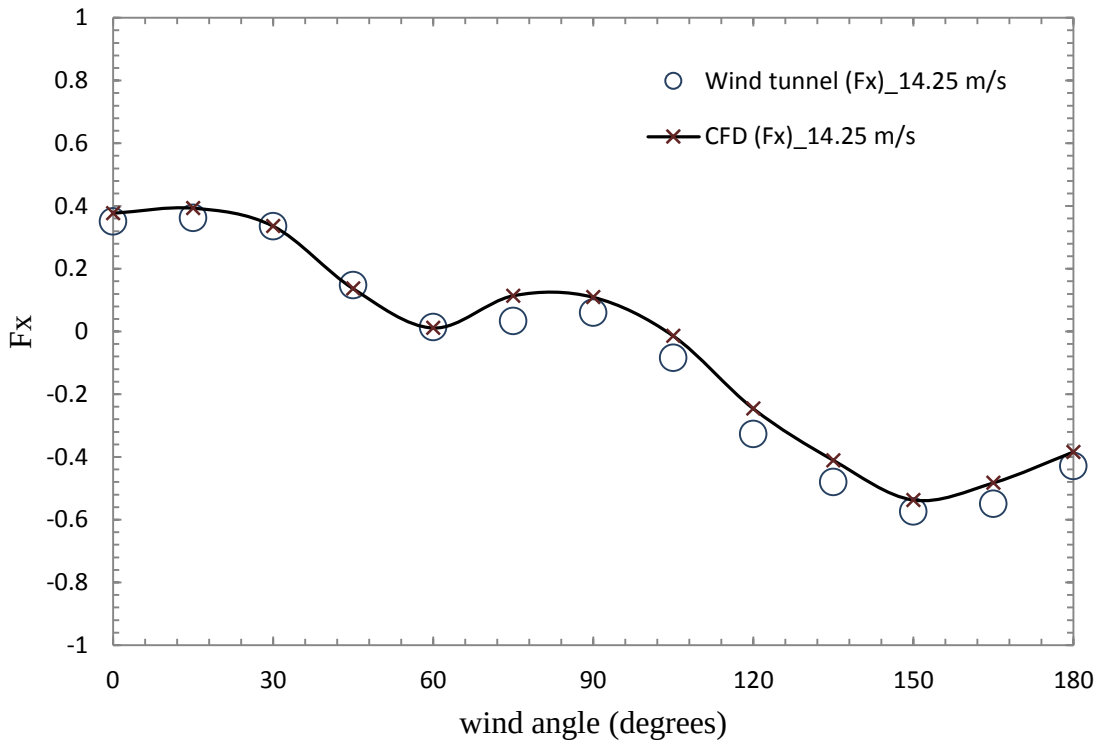

Figure 46: Comparing an experimental test in the wind tunnel with CFD analysis (F_x)

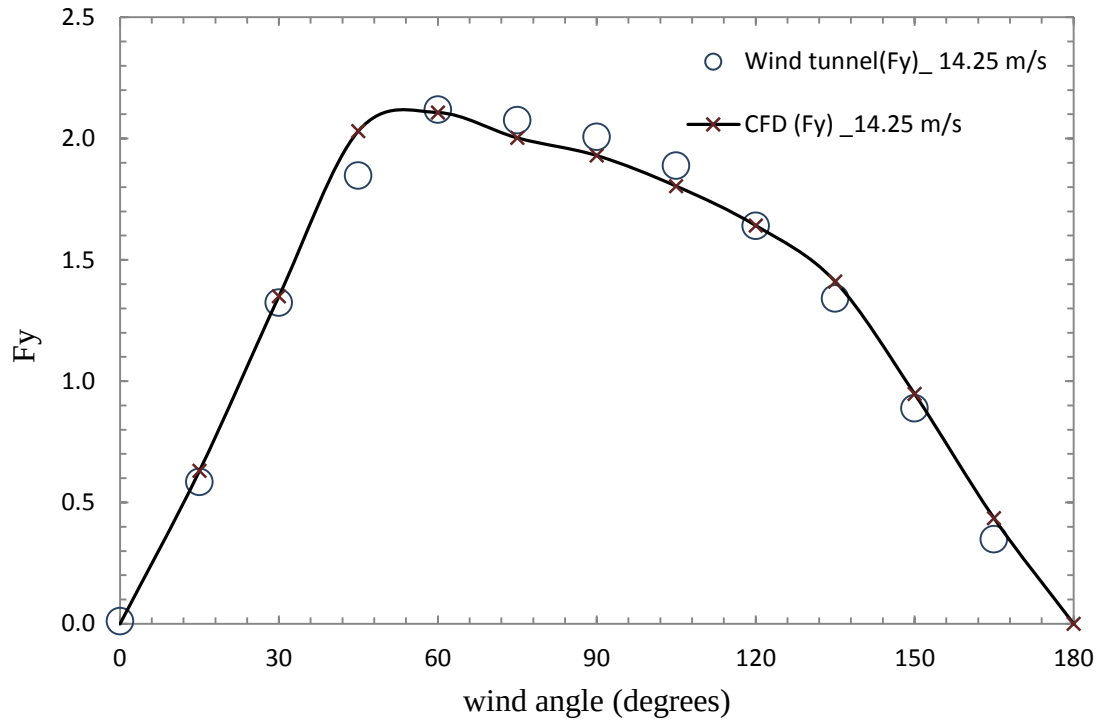

Figure 47: Comparing an experimental test in the wind tunnel with CFD analysis (F_Y)

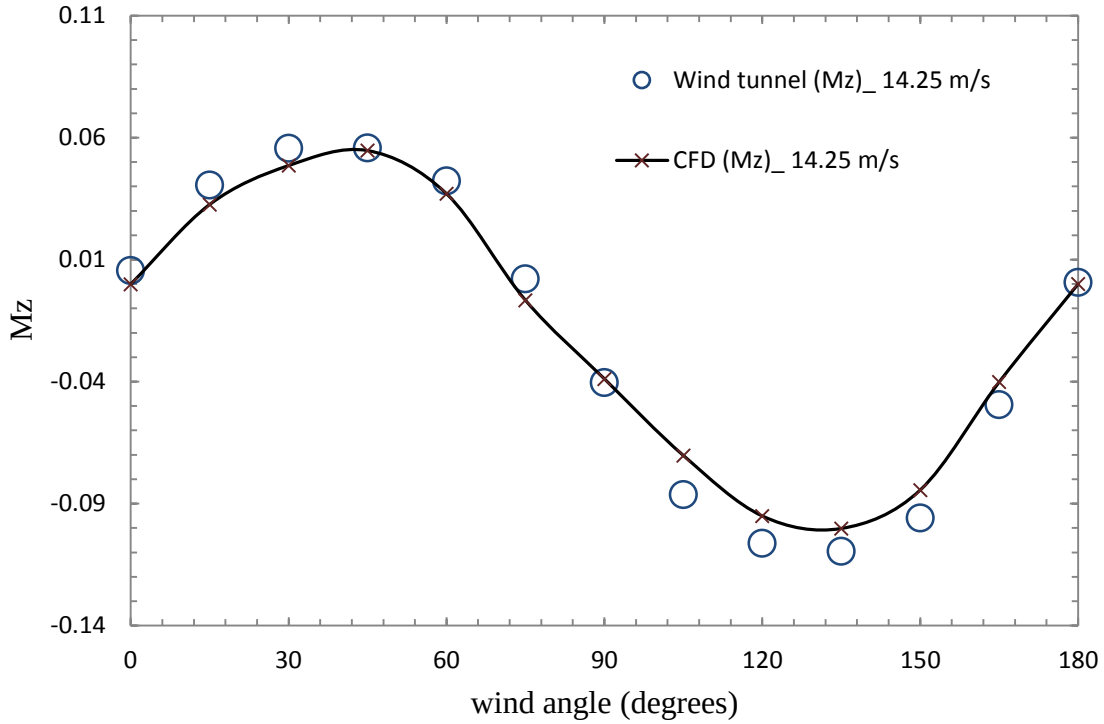

Figure 48: Comparing an experimental test in the wind tunnel with CFD analysis (Mz)

6.4.2 Comparing the results of the wind tunnel and CFD simulations in non-dimensional form (wind velocity at 14.25 m/s)

The load cell in the wind tunnel experiment measures the total forces and moments which are acting on both the scale model of the ship and the rotating disc ($f_{(ship)} + f_{(disc)}$) as these two parts are glued together. The magnitude of the force and moment acting on the rotating disc cannot be measured directly from the wind tunnel test. However, wind forces and moments acting on the rotating disc only ($f_{(disc)}$), can be measured from CFD simulations. Subtracting the above results could give the total force and moment which are acting only on the ship ($f_{(ship)}$). Found forces and moments on the ship can be non-dimensionalised and used in full station keeping analysis. (Alternatively, from CFD simulations the total force and moments acting only on the ship can be calculated directly.)

It is important to ascertain whether the contribution of the wind loading acting on the rotating disc in the total results is substantial. To find the answer, a comparison was made between the magnitude of the forces and moments acting only on the scale model (found from CFD simulations) against the magnitude of the forces and moments on both the model and the rotating disc (from the results of both CFD and wind tunnel experiments). The results from this comparison confirm that the contribution of the rotating disc on the total results is significant. This is shown in Figure 49 to Figure 51.

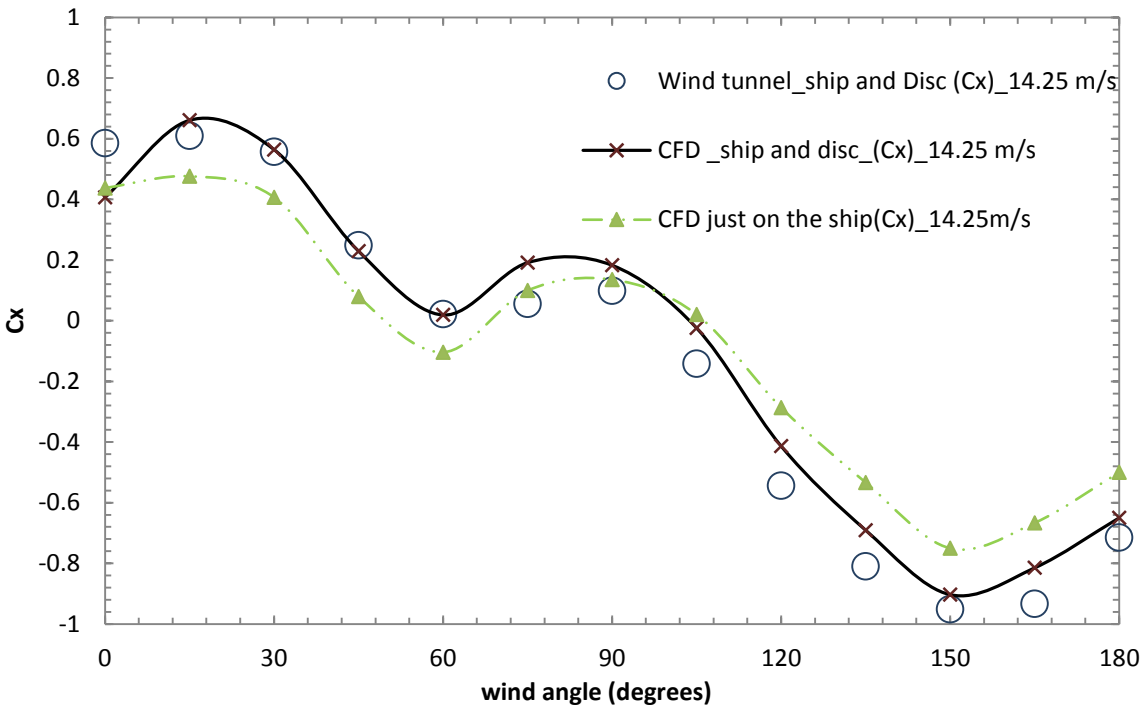

Figure 49: Comparison of the non-dimensional longitudinal force coefficients between the wind tunnel experiment and the CFD analysis on both the ship and rotating disc, and also the CFD longitudinal force coefficient on the ship only (wind angle of attack from 0 to 180°).

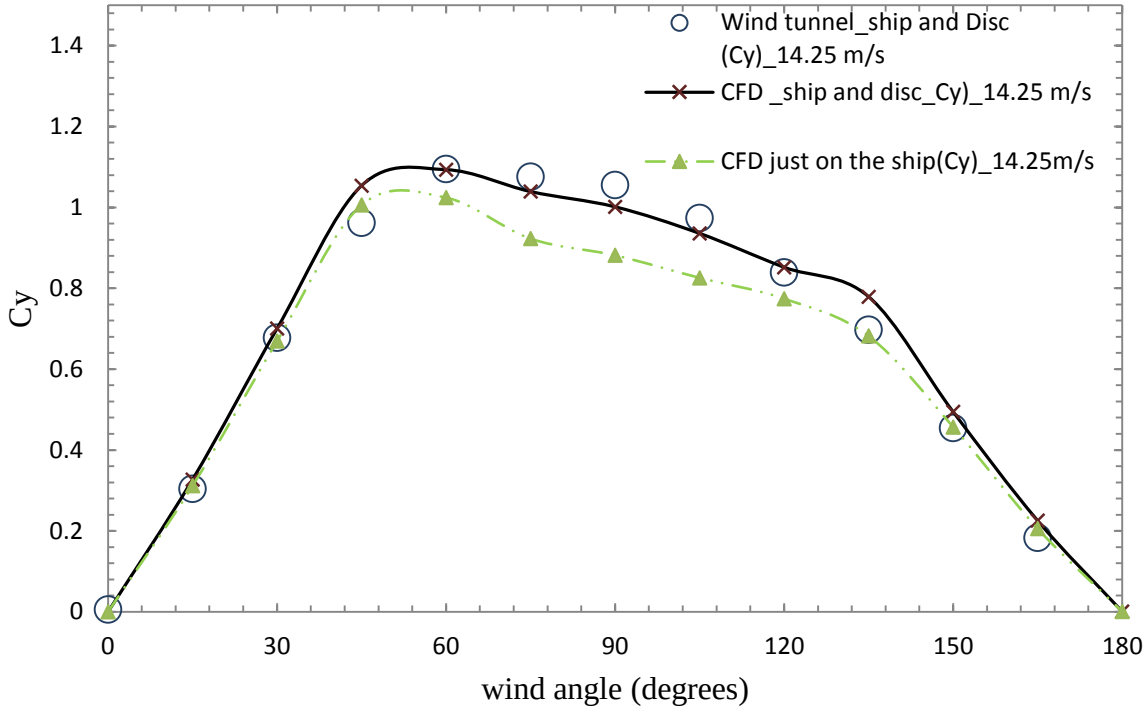

Figure 50: Comparison of the non-dimensional transversal force coefficients between the wind tunnel experiment and the CFD analysis on both the ship and the rotating disc, and also the CFD transversal force coefficient on the ship only (wind angle of attack from 0 to 180°).

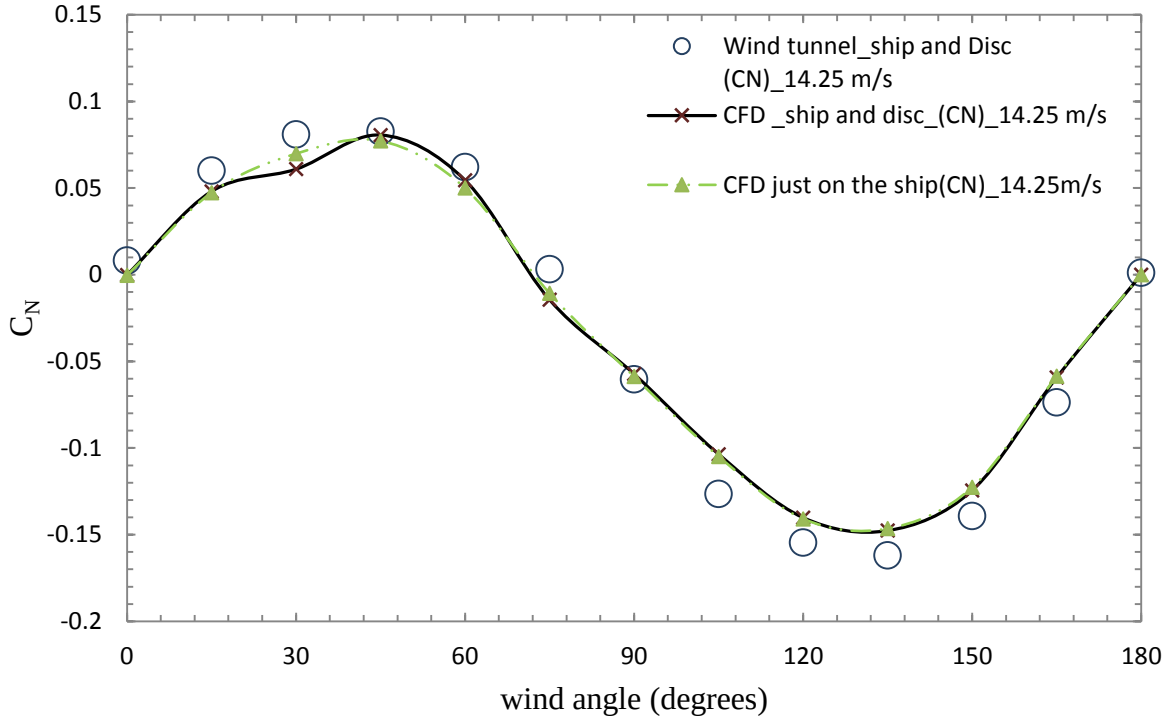

Figure 51: Comparison of the non-dimensional moment coefficient between the wind tunnel experiment and the CFD analysis on both the ship and rotating disc, and also the CFD moment coefficient on the ship only (wind angle of attack from 0 to 180°).

6.4.3 Comparing the results of the 1/300 and 1/80 scale models with Ikeda and Oura's towing tank test

Comparison between initial CFD analysis on Ikeda's experimental test on 1/80 scale model and results from CFD analysis on the 1/300 scale model can only be made if both have the same flow characteristics and boundary conditions. The original CFD analysis was first performed in a domain with the floor condition defined as slip. Defining the condition of a surface does not allow for the formation of any boundary layer on that surface. However, the floor condition in the CFD simulation on the 1/300 scale model is defined as non-slip.

In addition, the distance of the inlet boundary to the model in the next set of analysis on the 1/80 scale model, when the floor of the domain was defined as non-slip, was much greater than that which was set in the CFD analysis on the 1/300 scale model. This means that the 1/80 scale model was experiencing a completely different flow from the 1/300 scale model due to the formation of a larger boundary layer. Thus, the boundary conditions between the 1/300 CFD model and the 1/80 scale model are different and, therefore, their results are not totally comparable.

However, as a point of interest, the results from Ikeda and Oura's experiment and the results from CFD simulation on the 1/300 scale model are compared and shown in Figure 52 to Figure 54. As is shown, similarly to the previous CFD simulations (on the 1/80 scale model), the results are different.

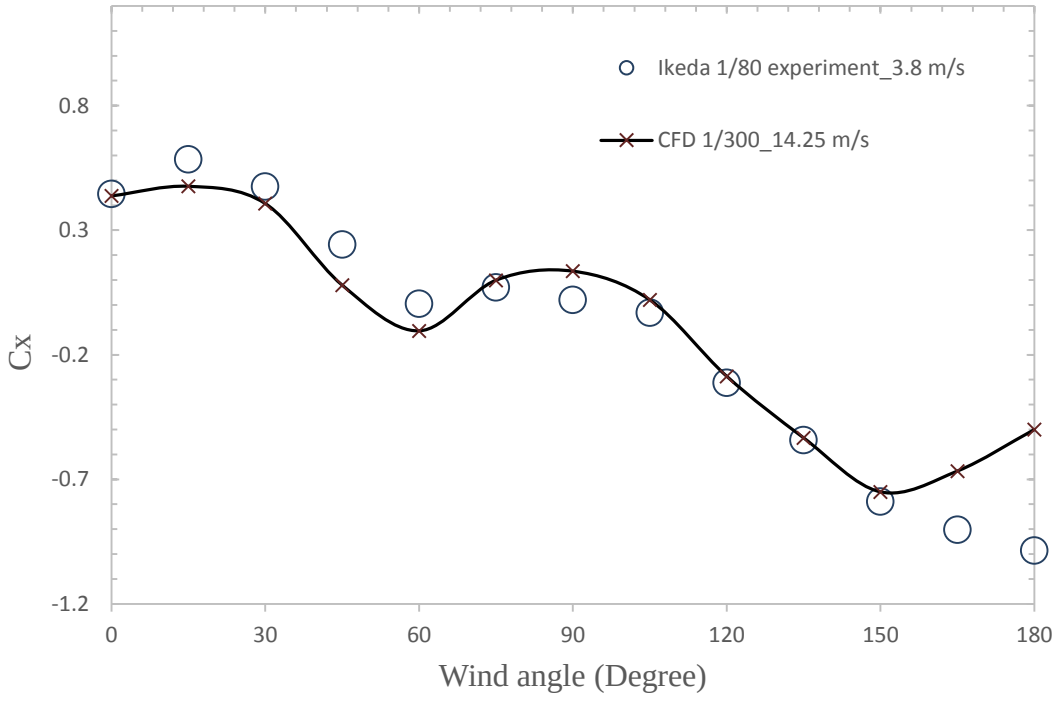

Figure 52: Comparison between CFD and Ikeda's experimental results on 1/80 scale model vs results from CFD analysis on 1/300 model. Longitudinal force coefficients (Cx)

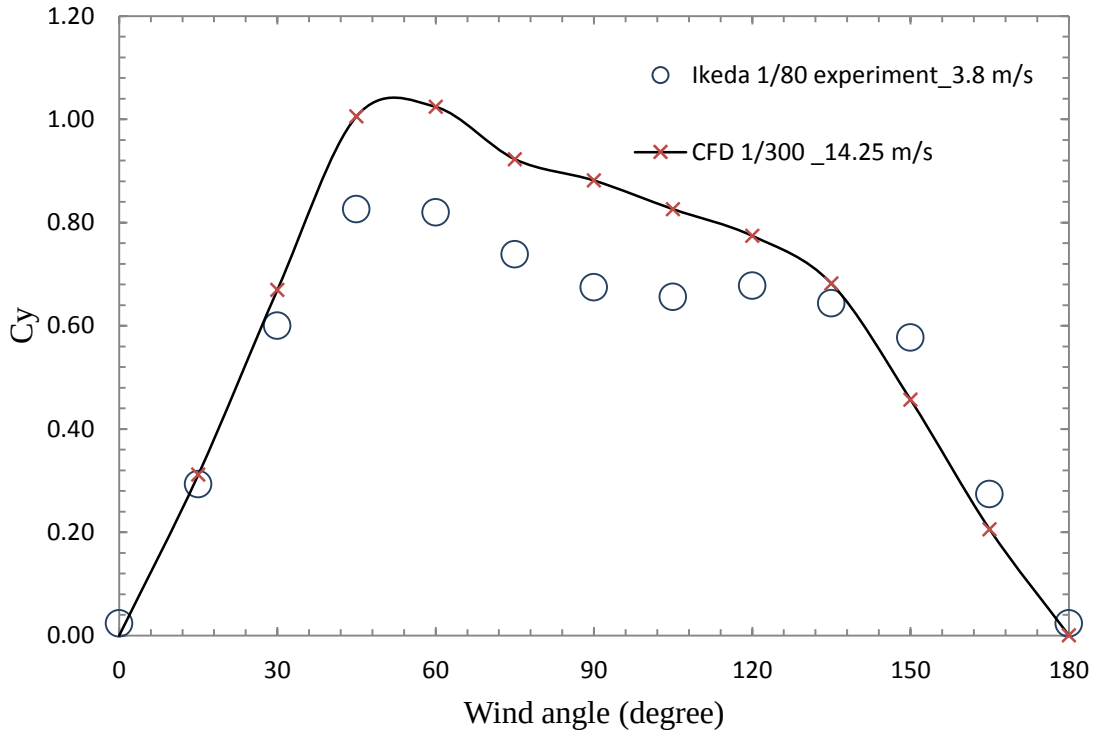

Figure 53: Comparison between CFD and Ikeda's experimental results on the 1/80 scale model vs results from CFD analysis on the 1/300 model. Transverse force coefficients (Cy)

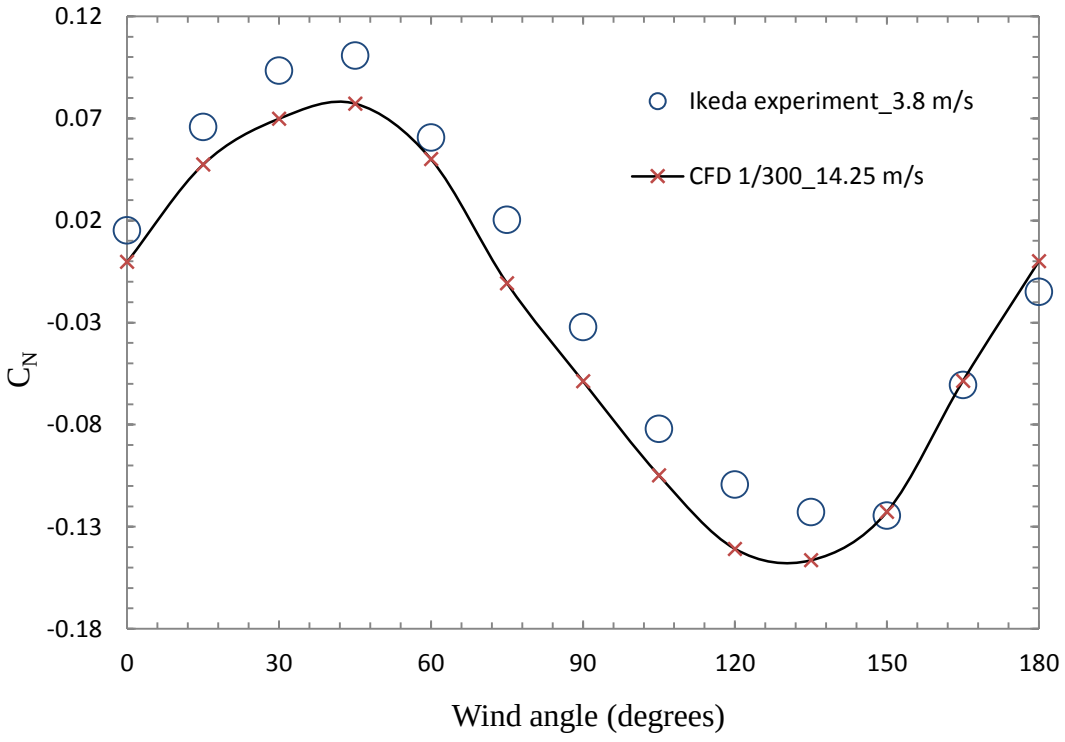

Figure 54: Comparison between CFD and Ikeda's experimental results on the 1/80 scale model vs results from CFD analysis on 1/300 model. Yaw moment coefficients (C_N)

Appendix 8, also compares the CFD results of 1/300 and 1/80 scale model to Ikeda's experiment on 1/80 scale model.

6.4.4 Comparing the results between all CFD models

To prove that the calculated wind force coefficients from CFD analysis (CFD simulations which were performed on the wind tunnel experiment) are accurate and can be used in station keeping analysis of a 112m catamaran ship, it is necessary to show those drag coefficients at different Reynold numbers. The turbulence intensity will stay unchanged. Therefore, further CFD analysis was performed to investigate the wind force coefficients at 20 m/s in the scale model. It was also decided to repeat all the analysis at the full scale with a much higher Reynolds number. Table 10 shows details of each CFD model:

V (m/s)	3.8	14.25	20	28.5	14.25
L (m)	1.32	0.352	0.352	0.352	105.6
Viscosity (m^2/s)	$1.57 \cdot 10^{-5}$	$1.57 \cdot 10^{-5}$	$1.57 \cdot 10^{-5}$	$1.57 \cdot 10^{-5}$	$1.57 \cdot 10^{-5}$
Re	$3.20 \cdot 10^{5}$	$3.20 \cdot 10^{5}$	$4.49 \cdot 10^{5}$	$6.40 \cdot 10^{5}$	$9.60 \cdot 10^{5}$

Table 10: Reynolds values for all models with different lengths or wind velocity

To create full scale simulations, all the CFD models of the wind tunnel experiments were scaled up to achieve the full scale geometry (both scale model of the ship and the wind tunnel domain). The domain of this full scale model still has similar geometrical boundary conditions as the wind tunnel test area. The wind velocity is set at 14.25 m/s (almost 30 knots) to achieve a more realistic result. All physic and mesh settings were retained as similar to the original CFD model which was created to simulate the wind tunnel experiment, with the exception of the use of four prism layers. This was to reduce the computational time. Minor adjustments were made in the mesh base size to retain a smooth transition between the prism and the core mesh. As before, all y^+ wall treatment was used. Figure 55, shows the y^+ plot.

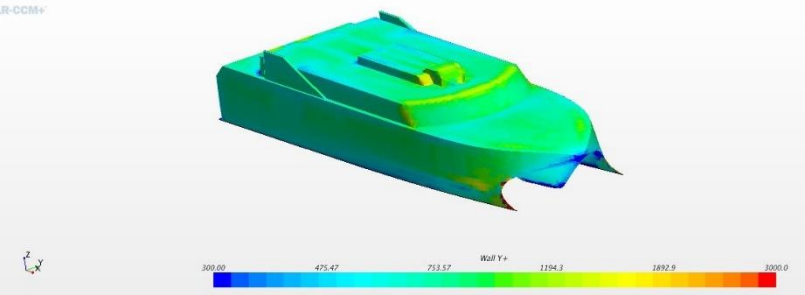

Figure 55: Wall y^+. Generally;the wall y^+ value is in the range of 300< y^+<3000.

The results from these analyses were compared with the CFD results which were originally simulated at 14.25 m/s on the 1/300 scale model. These are shown in Figure 56, Figure 57 and Figure 58.

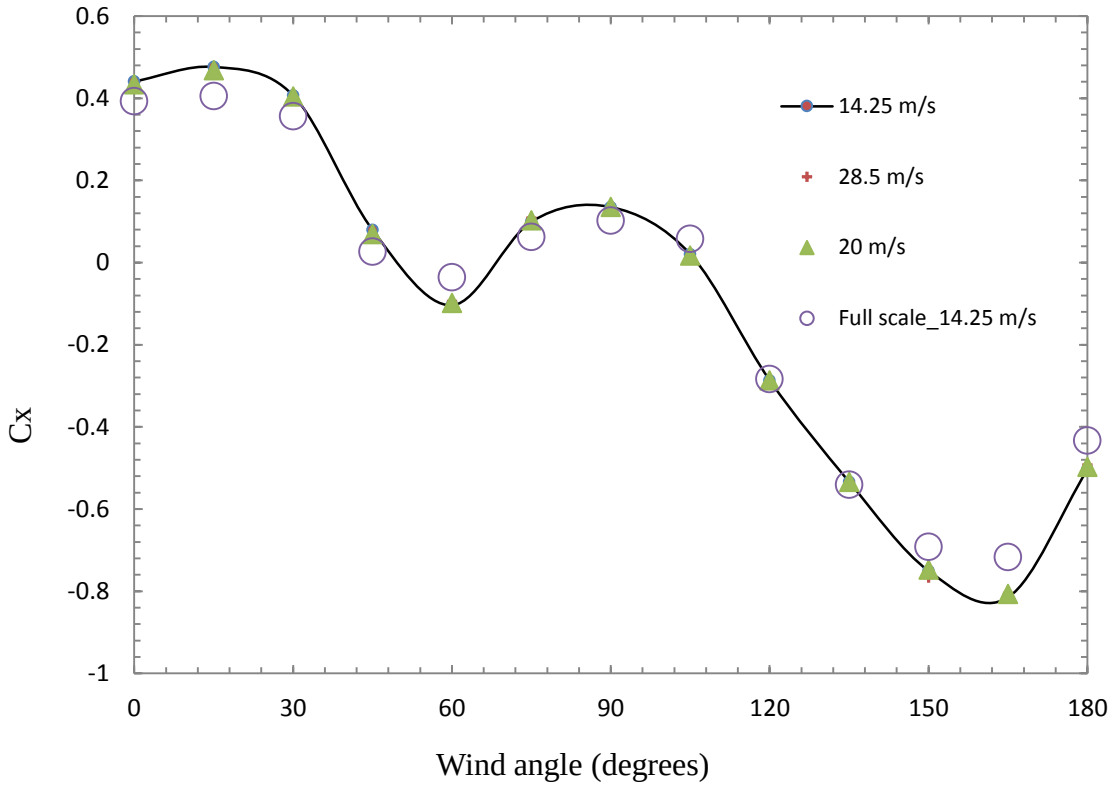

Figure 56: Comparison of the wind force coefficients at different wind velocities with full scale data(Cx)

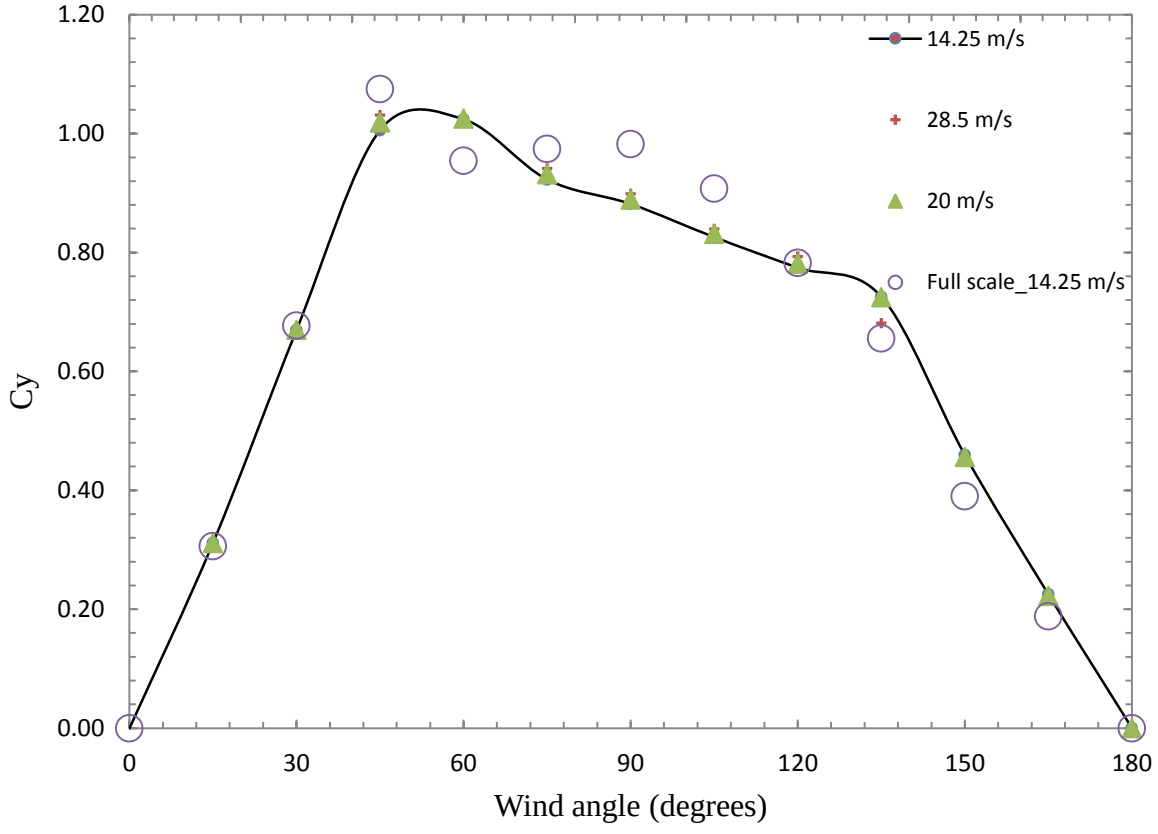

Figure 57: Comparison of the wind force coefficients at different wind velocities with full scale data (Cy)

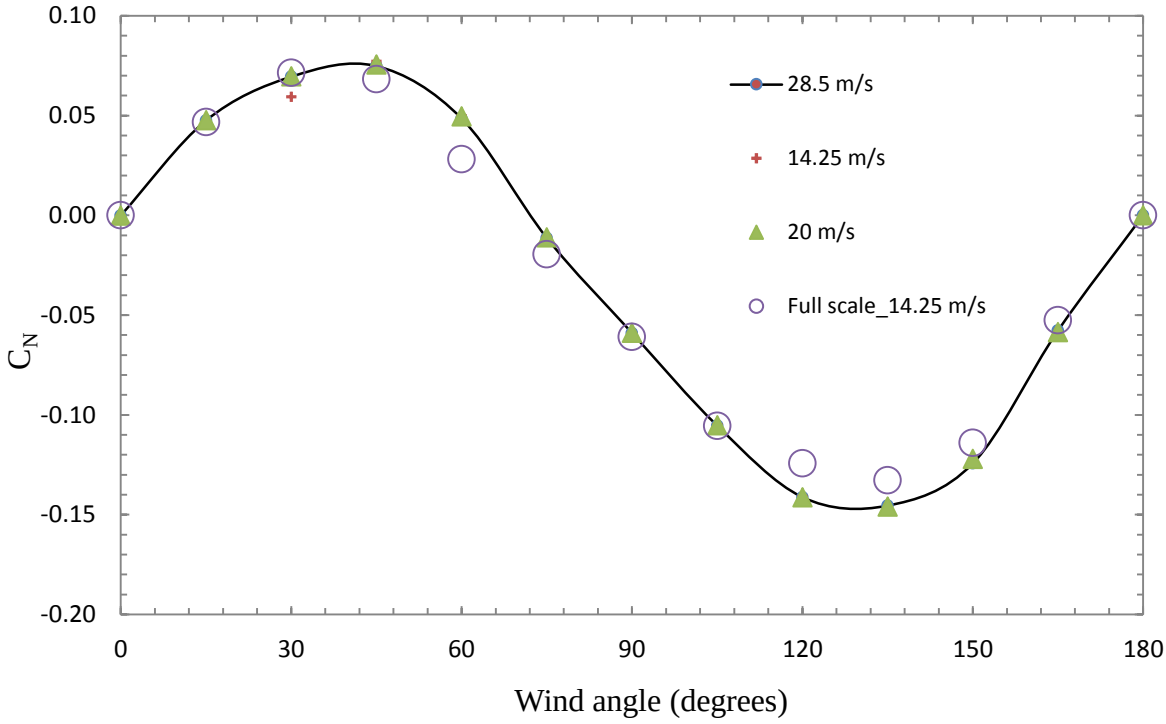

Figure 58: Comparison of the wind moment coefficients at different wind velocities with full scale data (C_N)

The above results demonstrate agreement between the full scale and the scale model CFD analysis at different wind velocities. Although the Reynolds number has been increased by a magnitude of 10^2, there are still similarities between the full and scale model results.

The various consecutive simulations with different Reynolds numbers clearly show that the scale should not be responsible for the the differences between the results. The differences between the results from the full scale ship and the scale model can be explained by closely examining the flow in the recirculation zone towards the outlet boundary. Figure 59 is the velocity vector plot at the time, when the wind angle of attack is 90° to the ship heading. As is shown, when the wind flow is passing, the ship does not get an opportunity to fully developed flow, before exiting the outlet boundary. This is because the full scale simulations were analysed with a much higher Reynolds number. This simply confirms that the size of the domain in the full scale simulation should be increased as the Reynolds number is increasing. The outlet boundary in the full scale model simulation needs to be a lot further away from the ship to allow the chaotic flow in the recirculation zone downwind of the ship to get fully developed before exiting the outlet boundary. Also, for full scale analysis, the density of mesh both in the prism and in the core layer should be carefully designed to reduce errors and approximation. It is recommended that for the full scale simulations, Large Eddy Simulation (LES) to be used. This method models the large eddies exactly but approximates the small ones, which allows for much greater accuracy.

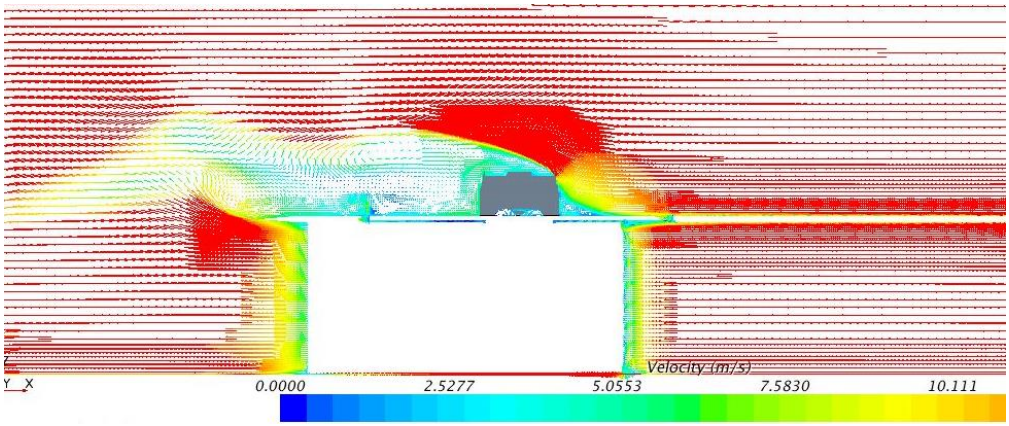

Figure 59: Full scale model velocity plot. The wind angle of attack is at 90°.

6.5 Discussion of the results

It is shown how the high velocity region behind the model changes and enlarges as the ship is heading into the wind approaches to 45°. This high velocity region generates a lift force which adds up to the total wind loadings acting on the ship. It is shown that when the wind angle of attack increases and approches 60°, the size of this region slowly decreases as the wind flow starts to separate more from the ship. By the time the wind angle of attack reaches 75°, this region completely disappears. Therefore, the maximum transverse force should be expected when the ship is facing the wind at a 45° angle. The magnitude of this force can be used in station keeping analysis of the ship which potentially identifies the required size of thrusters for the ship.

The results from CFD analysis correspond well with the results from the experimental test in the wind tunnel. This is showing that results from CFD are now validated. The results from full scale CFD analysis showed reasonable agreement with that which was measured in the scale model. However, further analysis with much higher mesh resolution and a larger domain are required to gain accurate values for a full scale station keeping study of high speed catamarans. This proves that CFD analysis can be used as a supplement to other experimental tests, such as towing tank, basin or wind tunnel tests, in order to provide reliable data for all design purposes.

It is shown that there is good agreement between CFD analysis in both the 1/80 and 1/300 scale models. This is when both results from the CFD simulations are different from results from Ikeda and Oura's experimental test. The results from the new experimental test on the 1/300 scale model, which was performed in UTAS's (Hobart) wind tunnel laboratory, and the results from a new set of CFD analysis, which was performed to replicate the above experiment, are in agreement. Implementing the outcomes of preliminary CFD analysis in design and assembly of the wind tunnel experiment resulted in a remarkable outcome.

CFD simulation showed how to minimise the effect of the side walls on the air flow inside the domain. This shows that a correct approach to a new experimental test would eliminate the need to use correction factors (referring to the study of Andersen (2012a), Janssen *et al.* (2017)) to adjust the final results when blockage effects are present.

Chapter 7 Conclusion

The manoeuvrability and station keeping of a high speed catamaran in rough weather is important to fast ferry operators, especially when the ship is travelling at low speed and is subjected to strong wind. This type of vessel experiences significant forces from wind which act on the large cross-sectional area above the waterline. Their shallow draft and light displacement can only generate a small resistance force from the water to counteract those aerodynamic forces which effect the superstructure. Catamarans have superior station keeping compared with monohulls due to a longer distance between the waterjets located in two separate hulls. Nevertheless, even catamarans with water jets may not have sufficient station keeping for the wind speeds during which they are operated. The station keeping study of these vessels determines, if their propulsion machineries (for example, water jets) are sufficient for manoeuvring the vessel or if additional equipment (for example, thrusters) are required to be installed on the ships, in order to increase their abilities to sail on the intended course with better manoeuvrability, especially at lower speed.

Knowledge of the station keeping ability of a ship is essential in order to increase the safety of that ship during docking in or departing from the harbour or while cruising at sea. For this reason, the station keeping of high speed catamarans should be taken into consideration while the ship is still in its preliminary design stage. Maybe this should be considered even before the contract, as adding any extra machineries, such as thrusters, could change the shape of the hull below the waterline, which affects the performance and cost of the ship. Wind forces and rotational moment for a particular vessel should be known within 0 to 180° of wind headings, prior to station keeping calculations. They can be found from a wind tunnel test or CFD computations (Sadovnikov 2009).

One of the goals of this study was to demonstrate that Computational Fluid Dynamics (CFD) can be used as efficient, fast and reliable data for station keeping of the ship in conjunction with validation data from the traditional experimental methods in wind tunnels or towing tanks. To show that CFD solutions are credible, it is necessary to demonstrate that results are comparable with the results from a similar experimental test. To find such an experiment, a number of experimental tests which were performed on ships, either in a wind tunnel or towing tank, was reviewed. It was found that a limited number of models of modern ferries has been tested in wind tunnels over recent years and results of these tests are mostly confidential (Sadovnikov 2009). Many wind tunnel and towing tank studies are not public open resources (Janssen *et al.* 2017). Therefore, those experiments could not be used for validation of CFD simulations.

However, a towing tank test which was performed by Ikeda and Oura on a 112m high speed catamaran was found to be an exception. Their published paper contained sufficient information for it to be replicated in CFD. That study was performed in Osaka Prefecture University in Japan in a towing tank facility (Oura & Ikeda 2007). Their experimental test was on a 1/80 scale model of a 112m Incat built catamaran in order to obtain the criterion of the wind speed for the vessel to sail in a straight direction while travelling at a constant speed.

They measured the wind force and moment coefficients by changing the attack angle of the wind by 15° from 0 to 180°. Therefore, for validation purposes, this experiment was modelled and analysed in CFD.

It is shown that the results from the CFD simulations did not support Ikeda and Oura's experimental results. It is clear that there should not be any side load and moment on the scale model when the wind is blowing directly into its bow (wind angle of attack is zero degrees), as the scale model has a symmetrical shape. However, the results from Ikeda's experiment are showing values which are not zero. It is also shown that the calculated longitudinal force coefficient (C_x) by Ikeda and Oura, especially in the quarter and following wind (between 135° to 180°), are greater than the ones measured by CFD and a wind tunnel test. The calculated transverse force coefficient (C_y) are lower than the ones measured in CFD between 0 to 135° headings. The calculated yaw moment (C_N) is generally higher than the predicted results from CFD and experimental results.

The effect of the side walls on the wind field was also found in other studies, such as Andersen (2012a) and Janssen *et al.* (2017) and this influenced the accuracy of their results. Reviewing those studies provided valuable information about the behaviour of wind around the test model in smaller domains, such as that seen in the wind tunnel. This shows that, in order to achieve accurate and useful aerodynamic assessments of a ship, it is necessary to perform the test in a domain with realistic boundary conditions.

Due to lack of access to another detailed published study, it became clear that performing a new experimental test was the only way to produce reliable information. This information could then be used to validate the CFD simulations. This experiment could be performed either in a towing tank or in a wind tunnel. Compared with performing a test in a towing tank or basin, a wind tunnel test seemed to be a better option as it provides more control over the variables in the test environment. Additionally, the cost of manufacturing a model for the test in a wind tunnel was less than making one for the towing tank. Therefore, the wind tunnel in the School of Engineering at the University of Tasmania (UTAS) was chosen to perform this experiment.

One of the most important requirements of scale model testing is that the obtained results reflect an accurate picture of the prototype's behaviour. It is therefore of fundamental importance that scale model testing does not introduce any factors which could corrupt the test data (Lutz 1997). For this reason, preliminary CFD analysis was performed to ensure that the generated boundary layer on the surfaces and other geometrical constraints of the wind tunnel (the size and shape of the wind tunnel cross sectional area) does not introduce any blockage in the mass flow of air during the test.

The results from CFD analysis showed that a 1/300 scale model of the 112m catamaran is the most suitable size that can be fitted in the wind tunnel, as a smaller model could cause a blockage in the air flow between the demi hulls of the model. Further CFD studies showed that, in order to minimise the effect of the side walls on the flow field, the model needed to be positioned in the widest part of the wind tunnel. Therefore, the model was raised from the floor of the wind tunnel and mounted on a new platform. This new platform created a new boundary

layer. The profile and the thickness of this boundary layer could be controlled which allowed the mounting of the scale model at a position in which the shape of the boundary layer velocity profile is similar to the natural velocity profile on the ocean's surface.

CFD simulations assisted in identifying the maximum wind forces acting on the model. This information was utilised in choosing the correct strain gauges to be used in the construction of a new load cell for the wind tunnel experiment. It is shown that, how CFD is used as an effective tool in designing the shape of the leading and trailing edges of the new platform. A similar shape as a NACA foil, was also used for the design of a new structure, in order to protect the strut against any wind loading. CFD simulations also assisted in choosing the most suitable location (downstream from the inlet) where, the velocity profile at that point was similar to the natural velocity profile on the ocean surface.

All of the above led to the design and build of a new test rig on which a new aerodynamic test on the 1/300 scale model of a 112m catamaran in the UTAS wind tunnel laboratory was performed. A six degree of freedom load cell was used to measure forces and moments acting on the scale model and the rotating disc. Next, a complete set of CFD analysis was performed to replicate this new wind tunnel experiment. (Care was taken to ensure that the exact geometrical domain of the wind tunnel test area was modelled in CFD.) The measured forces and moments in the wind tunnel were compared with that which was measured in CFD with the same components. The results corresponded very well. Agreement between the experiment and CFD results validated the CFD simulations and proved that CFD can be used to supplement other experimental methods in quantifying the magnitude and effects of wind loading on a high speed catamaran. After validation of CFD results the force and moments which were acting only on the scale model could easily be extracted from CFD models and used for further station keeping analysis of the ship. (As mentioned, the load cell in the wind tunnel measures the forces and moments acting on both the scale model and the rotating disc. It is shown that the effect of the rotating disc on the total measured force of the load cell is significant and cannot be neglected). It is also shown that CFD complements experimental and analytical approaches by providing an alternative and cost-effective means of simulating real fluid flows, reducing lead times and costs in design and production, prior to the wind tunnel experimental test.

The results from CFD analysis show an increase in the velocity magnitude behind the ship and through the ship's tunnel. These effects are more evident when the wind angle of attack changes from 15° to 60° heading. This behaviour can be explained because of the aerodynamic shape of the high speed catamaran generating additional lift force to the wind loading. It is shown that this high velocity region changes and enlarges as the ship's heading approaches 45°. It is shown that, beyond this point and when the ship's heading nears 60°, the size of this region slowly decreases. This is due to an increase in the separation of the wind flow from the ship. By the time the wind angle of attack is at 75°, this high velocity zone completely disappears. Therefore, the maximum transverse force should be expected when the ship is facing the wind at a 45° angle.

The results from the preliminary CFD simulations which were performed for designing the test area of the wind tunnel experiment helped to achieve agreement between CFD and

experimental results. This study shows that CFD can be used as a reliable tool in the design of an engineering experiment and also as an alternative method to calculate the wind and current forces on scale model ships. It is proven that the calculated wind force and moment coefficients from experimental tests and CFD analysis in scale models are accurate and can be used in further station keeping studies of that particular ship.

The capability of CFD in predicting wind loading on scale models shows that CFD can be also used to predict the wind loadings on a full scale ship. This should eliminate the need to use any scaling factors and formulae which are commonly used in full scale station keeping studies. Unfortunately, due to the time limitations of this research, only a few, very basic full scale CFD analyses were performed. It was also found that the distance of the model from the inlet and outlet boundaries was not chosen properly. The shape of the velocity profile at the location of the ship did not match with the natural velocity profile on the ocean's surface. The outlet boundary was not far enough from the ship to allow the flow to fully develop before reaching the outlet boundary. The results from these analyses displayed the need to increase the size of the computational domain and refine the grid settings in order to capture large eddies in the recirculation zone behind the ship. Perhaps Large Eddy Simulation (LES) could be the best approach for full scale analysis, even though it may increase the time and computational expenses.

Despite all of the above, the results from the full scale analysis were shown to have a similar trend to the results from the scale model analysis. The magnitude of the estimated results from the wind force and moments on the full scale ship were very close to that which was measured in the scale model. However, in order to achieve total confidence in these results, further analysis should be performed.

It is shown that CFD can play an important role in the understanding of the complex flow of wind forces on catamarans, at a variation of scales, and their assessment. It is shown that this study attained all its research goals.

Chapter 8 Recommendations

This research showed that there are always limitations in any experimental study. Those limitations should not be lightly assessed or ignored. Therefore, it is recommended that those limitations are eliminated, if possible. This should minimise the need to use correction factors to compensate for any blockage or other interference. Care should be taken when applying simplified equations for blockage correction.

It is recommended that CFD analysis of full-scale ships is continued, with particular attention being paid to mesh refinement in recirculation zones, in order to reduce the errors and large approximation. It is recommended for full scale simulation that LES is used. This method models the large eddies exactly but approximates the small ones which allows for greater accuracy. The analysis should be also performed in a correct sized domain, in which the ship can be placed at a correct distance from both the inlet and outlet boundaries.

It is also recommended that this study is continued to find effective methods (for example, thrusters, wider beam, and so on.) to reduce the effect of strong winds on larger high speed catamarans, especially when they are travelling at low speed and in harbour. This is to increase their manoeuvrability and to ensure a safer departure and docking in crowded harbours.

References

Aage, C, Hvid, SL, Hughes, PH & Leer-Andersen, M 1997, 'Wind loads on ships and offshore structures estimated by CFD', in JH Vughts (ed.), *8th International Conference on the Behaviour of Offshore Structures, BOSS'97*, Elsevier Science Ltd., Pergamon, Delft, vol. 2.

Aktas, B, Pirini, F & Benson, S 2017, 'Full-scale unsteady RANSE CFD seakeeping simulations of a high-speed craft', in *20th Numerical Towing Tank Symposium*, Maritime Research Institute Netherlands (MARIN), The Netherlands, pp. 16-21.

Andersen, IMV 2012a, 'Wind-tunnel investigation of wind loads on a post-panamax container ship as a function of the container configuration on deck', in *International Marine Design Conference 2012*.

Andersen, IMV 2012b, 'Wind forces on container ships', *Mercator*, no. Marts.

Bardera Mora, R 2012, 'An experimental helicopter wind envelope for ship operations', *World Academy of Science, Engineering and Technology*, vol. 68, pp. 1362-1369.

Broglia, R, Bouscasse, B, Jacob, B, Olivieri, A, Zaghi, S & Stern, F 2011, 'Calm water and seakeeping investigation for a fast catamaran', in *Proceedings of the 11th international conference on fast sea transportation (FAST2011), Honolulu*.

Cannavacciuolo, C 2014, *How the wave damping length influence the domain and wake refinements in a hull performance analysis*, Siemens, viewed 10 January 2015, <https://thesteveportal.plm.automation.siemens.com/>.

CD_ Adapco 2011, *The HRIC Convection Discretization Scheme*, Siemens, viewed 15 May 2015, <https://thesteveportal.plm.automation.siemens.com/>.

CD_ Adapco 2012, *How Do I Choose Between Steady and Unsteady?*, Siemens, viewed 2 August 2016, <https://thesteveportal.plm.automation.siemens.com/>.

CD_ Adapco 2015a, *Spotlight on Turbulence* Siemens, viewed 11 November 2014, <https://thesteveportal.plm.automation.siemens.com/>.

CD_ Adapco 2015b, *What is the vof multiphase model?*, Siemens, viewed 15 September 2014, <https://thesteveportal.plm.automation.siemens.com/>.

CD_Adapco 2012, *Running a Steady State Analysis*, Siemens, viewed 10 January 2015, <https://thesteveportal.plm.automation.siemens.com/>.

Cengel, YA & Cimbala, JM 2013, *Fluid mechanics fundamentals and applications*, 3rd SI edn, McGraw-Hill Publication, Singapore.

Cozzi, O 2010, 'Free surface flow simulation: correcting and benchmarking the ALE method in Code_Saturne', Master of Philosophy, School of Mechanical, Aerospace and Civil Engineering thesis, University of Manchester.

Cummins, K 2010, *The rise of additive manufacturing*, The engineer, viewed 10 August 2018, <https://www.theengineer. co.uk/issues/24-may-2010/the-rise-of-additive-manufacturing/>.

Forrest, JS & Owen, I 2010, 'An investigation of ship airwakes using Detached-Eddy Simulation', *Computers & Fluids*, vol. 39, no. 4, pp. 656-673.

Frank, J, Hellsten, A, Schlünzen, H & Carissimo, B 2007, 'Best practice guideline for the CFD simulation of flows in the urban environment. COST action 732', *Quality Assurance and Improvement of Meteorological Models. University of Hamburg, Meteorological Institute, Center of Marine and Atmospheric Sciences*.

Fujiwara, T, Ueno, M & Nimura, T 1998, 'Estimation of wind forces and moments acting on ships', *Journal-Society of Naval Architects of Japan*, vol. 183, pp. 77-90.

Greenwell, D & Barret, R 2006, *Control of Ship Air Wakes using inclined screens*, viewed 1 January 2018, <https://dspace-erf.nlr.nl/>.

Hsu, S, Meindl, EA & Gilhousen, DB 1994, 'Determining the power-law wind-profile exponent under near-neutral stability conditions at sea', *Journal of Applied Meteorology*, vol. 33, no. 6, pp. 757-765.

Iaccarino, G, Ooi, A, Durbin, P & Behnia, M 2003, 'Reynolds averaged simulation of unsteady separated flow', *International Journal of Heat and Fluid Flow*, vol. 24, no. 2, pp. 147-156.

Ikeda, Y 2008, 'A Method to Determine Safe seakeeping Limitations of a High-Speed Craft by Comparative studies of Model Experimental Results', in *The 6th Osaka Colloquium on Seakeeping and Stability of Ships, 2008*, pp. 189-194.

Janssen, WD, Blocken, B & van Wijhe, HJ 2017, 'CFD simulations of wind loads on a container ship: Validation and impact of geometrical simplifications', *Journal of Wind Engineering and Industrial Aerodynamics*, vol. 166, pp. 106-116.

Kashiwagi, M & Toda, Y 2008, 'Testing and Extrapolation Methods: General Guidelines for Uncertainty Analysis in Resistance Towing Tank Tests', in M Kashiwagi & Y Toda (eds), *25th*

International Towing Tank Conference : Proceedings, September 14-20, 2008, Japan Society of Naval Architects and Ocean Engineers, Fukuoka, Japan.

Larsson, L & Raven, H 2010, *Ship resistance and flow*, Society of Naval Architects and Marine Engineers, Jersey City, New Jersey.

Larsson, L, Stern, F & Bertram, V 2003, 'Benchmarking of computational fluid dynamics for ship flows: the Gothenburg 2000 workshop', *Journal of Ship Research*, vol. 47, no. 1, pp. 63-81.

Lloyd, A 1989, *Seakeeping, Ship Behaviour In Rough Weather*, A R J M Lloyd, 26 Spithead Avenue, Gosport, Hampshire, United Kingdom.

Lubitz, W & White, B 2004, 'Atmospheric boundary layer wind tunnel applications in wind turbine siting', *Department of Mechanical and Aeronautical Engineering, University of California, Davis*.

Luttrell, A 2017, '112m catamaran [Photograph]', *The Mercury (Hobart)*, <https://www.themercury.com.au/news/tasmania/king-island-freight-and-tourism-plan/news-story/271330e589c3ea4f8372540aab78d2c6>.

Lutz, T 1997, 'The effect of the boundary layer present in wind tunnels on the aerodynamic drag of a model truck', University of Cape Town.

Martin, L 1980, 'Ship manoeuvring and control in wind, Paper presented at the N.A.M.E Society Annual Meeting, 13-15 November', in New York, p. 22.

Matsumoto, K 2003, 'Reduction of wind force acting on ships', *Journal of the Kansai Society of Naval Architects*, vol. 240, pp. 115-121.

Molland, A & Barbeau, T-E 2003a, 'An investigation into the aerodynamic drag on the superstructures of fast catamarans', *Transactions of the Royal Institution of Naval Architects. Part A: International Journal of Maritime Engineering*, vol. 145, no. 1, pp. 29-39.

Nihei, Y, Li, Q & Ikeda, Y 2010, 'An experimental study on wind loads acting on a trimaran PCC', *Journal of Marine Science and Application*, vol. 9, no. 2, pp. 121-128.

Nihei, Y, Li, Q, Nakashima, T & Ikeda, Y 2010, 'A Basic Study on Wind Pressure Characteristics of a Trimaran PCC', in *ASME 2010 29th International Conference on Ocean, Offshore and Arctic Engineering*, pp. 311-318.

Oura, T & Ikeda, Y 2007, 'Maneuverability of a Wavepiercing High-Speed Catamaran at Low Speed in Strong Wind', paper presented to 2nd International Conference on Marine Research and Transportation, June 28th to June 30th 2007, Ischia, Naples, Italy.

Pettinelli, C 2013, 'How can I reduce or dampen the force oscillations in ship or boat calm water simulation? ', *CD Adapco_Steve portals*.

Polsky, S 2002, 'A computational study of unsteady ship airwake', in *40th AIAA Aerospace Sciences Meeting & Exhibit*, p. 1022.

Pope, SB 2001, *Turbulent flows*, IOP Publishing, Cambridge; New York: Cambridge University Press.

Rae, W & Pope, A 1984, *Low-speed wind tunnel testing, 1984*, John Wiley, New York.

Raven, H, Van der Ploeg, A & Eça, L 2006, 'Extending the benefit of CFD tools in ship design and performance prediction', in *Proceedings of the seventh ICHD international conference on hydrodynamics, University of Naples ''Federico II'', Ischia*, pp. 573-580.

Reichardt, K 2014, *Wall function and wall treatment*, CD Adapco_Steve Portal, Siemens, viewed 20 February 2015, <https://thesteveportal.plm.automation.siemens.com/>.

Ross 2013, *Recommendtaion for domain size for an aerodynamic test*, CD Adapco_Steve, Portal, Siemens, viewed 20 February 2015, <https://thesteveportal.plm.automation.siemens.com/>.

Rozati, A 2014, *Do I need prism layers? How many should I use?* , Siemens, viewed 12 February 2015, <https://thesteveportal.plm.automation.siemens.com/>.

Sadovnikov, D 2009, 'Station keeping of high speed ferries', in *International Conference on Innovation in High Speed Marine Vessels*, Fremantle, Australia, pp. 39-48.

Sezer-Uzol, N, Sharma, A & Long, L 2005, 'Computational fluid dynamics simulations of ship airwake', *Proceedings of the Institution of Mechanical Engineers, Part G: Journal of Aerospace Engineering*, vol. 219, no. 5, pp. 369-392.

Tasumi, H & Ikeda, Y 1999, 'Maneuverability of a high-speed catamaran running at low speed in strong wind', *The Japan-Korean Joint workshop on ship and marine hydrodynamics*.

Tominaga, Y, Mochida, A, Yoshie, R, Kataoka, H, Nozu, T, Yoshikawa, M & Shirasawa, T 2008, 'AIJ guidelines for practical applications of CFD to pedestrian wind environment around

buildings', *Journal of Wind Engineering and Industrial Aerodynamics*, vol. 96, no. 10-11, pp. 1749-1761.

Tu, J, Yeoh, GH & Liu, C 2013, *Computational fluid dynamics: a practical approach*, 2nd edn, Butterworth-Heinemann, Waltham, MA.

Van He, N, Mizutani, K & Ikeda, Y 2016, 'Reducing air resistance acting on a ship by using interaction effects between the hull and accommodation', *Ocean Engineering*, vol. 111, pp. 414-423.

Vogt, JW, Bovio, M & Mallol, B 2017, *Validation of Wind Loads on a Slender Vessel using CFD*, NUMECA International, viewed 1 July 2018, <https://www.numeca.com/>.

Wnęk, A, Paço, A, Zhou, X & Soares, CG 2010, 'Numerical and experimental analysis of the wind forces acting on LNG carrier', in *V European Conference on Computational Fluid Dynamics, Lisbon, Portugal*.

Yen, T 2012, *Please explain the DFBI setup and the terminology used in 6-DOF*, Siemens, viewed 10 February 2015, <https://thesteveportal.plm.automation.siemens.com/>.

Yen, T 2014, *How to determine the time step size*, Siemens, viewed 22 March 2015, <https://thesteveportal.plm.automation.siemens.com/>.

Zha, R-s, Ye, H-x, Shen, Z-r & Wan, D-c 2015, 'Numerical computations of resistance of high speed catamaran in calm water', *Journal of Hydrodynamics, Series. B*, vol. 26, no. 6, pp. 930-938.

Zhang, Z-r, Hui Liu, Song-ping Zhu & Zhao., F 2006, 'Application of CFD in ship engineering design practice and ship hydrodynamics.', *Journal of Hydrodynamics*, vol. 18, no 1, pp. 308-322

Appendix 1 Sinkage and trim analysis

To calculate the wind force coefficients the correct area above and below the waterline need to be calculated. To do so, the correct draft waterline should be identified.

Sinkage and trim analysis are types of simulation which is usually performed when the correct draft waterline and correct Centre of gravity (COG) of the model are unknown, or they are known but are unconfirmed. In this case, the correct draft waterline was unknown and needed to be identified. The correct waterline defines the correct area above and below the waterline. The procedure for this type of analysis is explained in detail in this appendix.

Creating CFD model:

The next few sections of this appendix highlight the steps which are required to set up a CFD model for sinkage and trim analysis. These sections describe why Star CCM$^+$ was chosen for modelling the free surface (VOF) and what other settings such as determining the domain size, the prism layer setting, the time step and boundary conditions, and selecting the type of mesh are important in performing a CFD analysis.

Detail of the model used in experimental test:

Table 11 specifies the principal particulars of the 112m WPC Incat ship which were used by Ikeda and Oura for their experiment.

Gross tonnage	L OA	Length of demi hull	Width of the demi hull	Breadth	Draft	Maximum speed	Main Engine	Water jets thrust (x4)
8000 Ton	112.6 m	105.6 m	5.8 m	30.50 m	3.7 m	40 knots	9000 KW/ 1000 RPM (x4)	303 KN (x4)

Table 11: Principal particulars of 112 m catamaran (Oura & Ikeda 2007)

The specified draft waterline at level trim in the above table is 3.7m but it does not seem to be correct as it is not matching the design waterline of any 112m ships built by Incat (The average draft waterline is around 4m). In addition, the location of the centre of gravity (COG) is not specified. Identifying correct waterline and correct COG are necessary for the calculation of drag and moment coefficients.

Ikeda and Oura have used a 1/80 scale of the 112m Incat ship. The mass of this scale model is 5.86 kg (confirmed by Professor Ikeda in one of his correspondences). The solid computer model which they used in their experimental test was provided by Incat Tasmania and was used in this research as well.

CFD software:

STAR CCM+ is the software which was used for CFD modelling in this research. It is a finite, volume-based program package for the modelling of fluid flow problems and is developed by the computer software company CD-Adapco. It solves the Navier-Stokes equations with a segregated, algebraic multigrid solver using the Rhie & Chow interpolation for pressure-

velocity coupling. Furthermore, the SIMPLE algorithm is applied to control the overall solution. For free surface flows, STAR CCM+ uses the Volume of Fluid (VOF) approach (Cozzi 2010).

Model coordinate system:

The coordinate system is a standard Cartesian right handed coordinate system fixed to the ship as shown in Figure 60.

The **x**-axis is positive forward.

The **y**-axis is positive to port.

The **z**-axis is positive upward.

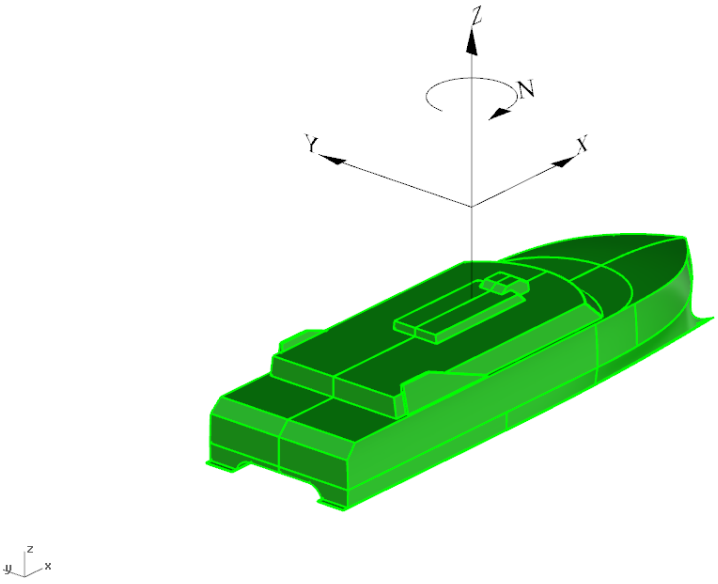

Figure 60: Ship coordinates

Domain shape and size:

The shape of the domain for this experiment is a cuboid and has the following measurements:

$X_{max} = 11.8\,m$ (9L) $\quad X_{min} = -11.8\,m$ (9L)

$Y_{max} = 11.8\,m$ (9L) $\quad Y_{min} = 11.8\,m$ (9L)

$Z_{max} = 4.5\,m$ (3.4L) $\quad Z_{min} = 4.5\,m$ (3.4L)

The transom of the model test is set at the centre of this domain which is at 0,0,0. The domain is shown in Figure 61.

The domain dimensions are set to ensure the domain is large enough to allow the flow to develop before reaching the test model and the boundaries are set far enough from the test

model to ensure that there is no edge or blockage effect influencing the flow in the domain. Domain size should be large enough to give solution independence. Domain size, like mesh size, should be treated as a variable. This means that a domain size sensitivity analysis should be performed to prove the results are independent from the domain size. Also, the width and the length of the model was chosen in a way that one wave damping length would be applicable in all directions.

During sinkage and trim analysis, the ship is set free to translate in z direction and rotate around its y axis. The movement of the ship causes waves to be generated. The generated waves move towards the domain boundaries and after reaching them, they tend to reflect back into the domain. To avoid any unphysical reflections these waves needed to be damped.

It is important to understand how the wave damping length influences the dimension of the computational domain and the wake refinement sizes. The first thing to have in mind is that the wave damping option is used to dampen the waves that are produced by the interactions between the free surface and the hull, and to avoid any unphysical reflections. Those reflections are mainly due to two reasons:

1. interaction between the waves and the edges where the mesh size suddenly changes (that is, the border of two different yet adjacent volumetric mesh refinements), and
2. interaction between the waves and the boundaries of the computational domain.

In STAR-CCM+ it is possible to set only one wave damping length. This length is then applied to all the boundaries where the wave damping option is ticked (Cannavacciuolo 2014).

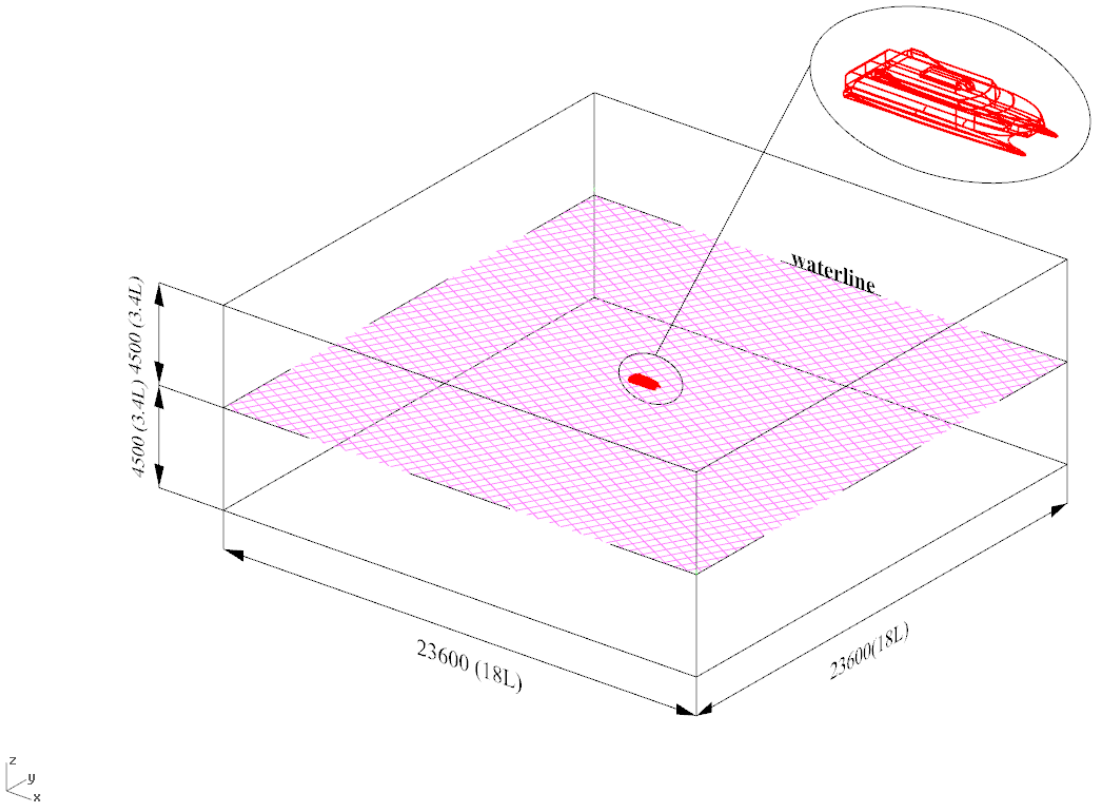

Figure 61: Computational domain dimensions. The transom of the test model is set at the centre of this domain which is at 0,0,0.

Mesh:

Trimmer mesh is a better choice than polyhedral mesh and was used throughout this research. It allows mesh alignment with a user defined coordinate system or mesh alignment with the direction of the flow. It also allows refinement in wake and other local areas.

Prism layer consideration:

Wherever there is a need to capture the flow and temperature field in the near wall region, the use of a prism layer is recommended. The number of prism layers that are required, and their spacing, varies depending on the type of flow and physics selected. For laminar flows, boundary layer thickness can be calculated with developed equations in various textbooks that are based on the free stream Reynolds number and length scale. In general, 5-20 prism layers are required within the thickness of the prism layer.

For turbulent flows, the wall treatment being applied also governs the number of prism layers required, both to resolve the boundary layer adequately, while maintaining the height of the first cell next to the wall within the acceptable y^+ values.

- If "High y^+" wall treatment is used, then one to two prism layers can be sufficient, as long as the near wall cell is being maintained at y^+ values from 30 through 300, although some best practices prefer lowering this limit to 150.
- If a "low y^+" wall treatment is used, then 10-20 prism layers can be utilised, and the y^+ must be around one (Rozati 2014).
- The all-y^+ wall treatment is a hybrid treatment that attempts to emulate or blend the high-y^+ wall treatment for coarse meshes, and the low-y^+ wall treatment for fine meshes.

For sinkage and trim analysis there is no need to capture the flow near the wall region in detail. Therefore, there is no need to have a very refined prism layer. This means high y^+ or two layer all wall y^+ wall treatment can be used and two prism layers are sufficient. Therefore, for sinkage and trim analysis two layer all y^+ wall treatment is used. Figure 62 shows the general arrangement of the CFD models. Table 12 represents the detail of the mesh and prism layer settings.

Type of mesh	Number of cells	Prism layer thickness	Number of layers	Prism layer stretching	Water density	Air density
trimmer	5110774	10 mm	2	2	997.561 kg/m^3	1.18415 kg/m^3

Table 12: Mesh setting particulars

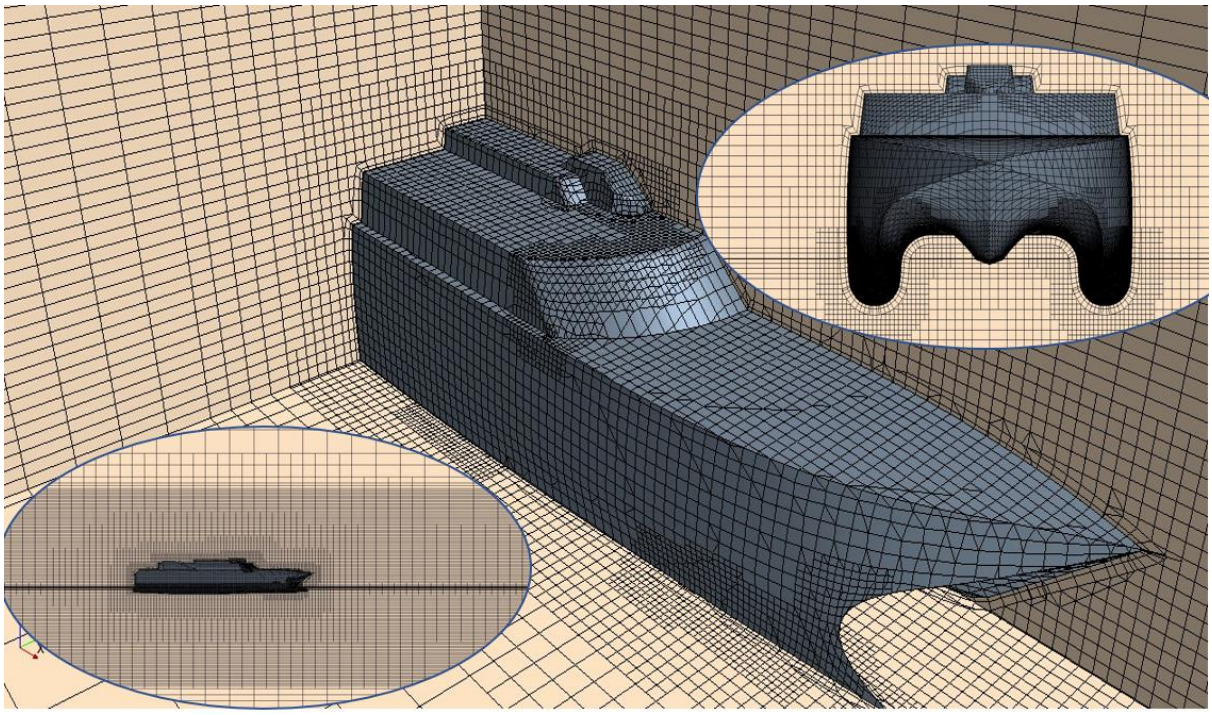

Figure 62:General mesh arrangment and prism layer

Boundary condition:

During analysis the scale model is kept stationary at the designed waterline for a short period of time (ramping time). Then the model is released into the water. The model will sink because of its own weight until the buoyancy forces push the scale model up. This sequence will be

repeated a number of times until the total buoyancy forces become equal to the gravitational forces and results converge. During the sinkage and trim analysis, a single phase flow of waves will be generated. These waves will propagate towards the domain's boundaries in all directions and in a plane perpendicular to the model ship. For this reason, all sides (except the top and bottom) of the domain are set as the pressure outlet. The top and bottom are specified as the velocity inlet (Although they can also be specified as symmetrical). The ship's surfaces are specified as non-slip.

Physics

Choosing turbulence model and wall treatment:

Both SST K-omega and Realisable K-epsilon two-layer turbulent models are suitable for this type of analysis. Initially the Realisable K-epsilon two-layer turbulent model with implicit unsteady and two layer all y^+ wall treatment was used in analysis. Then the analysis was repeated with SST K-omega to ensure the results were independent from the type of turbulence models. Wall treatments are a set of near wall modelling assumptions used to close the turbulence model in wall bounded flows. In the presence of a wall, the flow becomes more complex because of the non-slip wall condition. Turbulence models need modifications or bridging functions to deal with non- slip walls. The available wall treatments are high y^+, low y^+ and all y^+ (CD_ Adapco 2015a).

Two layer all y^+ wall treatment is formulated with the desirable characteristic of producing reasonable answers for meshes of intermediate resolution (that is, when the wall cell centroid falls within the buffer region of the boundary layer). It blends the near wall to the outer flow and removes the need for near wall dampening (Reichardt 2014).

VOF:

Eulerian multiphase is used to define the VOF (volume of fluid) in two regions of air and water. Gravity is also invoked. To model the free surface flow, Star CCM+ uses volume of fluid (VOF). The free surface is where the interaction between air and water is and can often become unstable. Therefore, an appropriate technique needs to be used to make sure it models this interface correctly. Since this a multiphase situation, the best approach is the coupled volume of fluid (VOF) method. This is an excellent way of modelling ships that produce breaking waves because it can be used for two immiscible fluids when the interface position of these fluids is required to be calculated throughout the simulation (Zhang *et al.* 2006). The volume fraction is used to calculate the value of alpha. For values of alpha = 0, the fluid is air and for values of 1, the fluid is water. Anything between this is a mixture of the two and hence there will be an interface. The continuity equation for alpha is used to locate the interface by determining where alpha is changing at the fastest rate (Zhang *et al.* 2006). Volume of Fluid (VOF) is a simple multiphase model. It is suited for simulating flows of several immiscible

fluids on numerical grids capable of resolving the interface between the phases of the mixture (CD_ Adapco 2015b).

VOF damping length:

Typically, when simulating a boat or ship motion in calm water, the forces can show marked oscillations, with a main period being a few seconds. This behaviour is due to the impulsive start of the body, which in turn causes a low frequency pressure wave to be transmitted in the domain. Due to the absence of a non-reflective boundary condition for the VOF multiphase model, this pressure wave reflects at the boundaries and bounces back into the domain. If not properly damped, this oscillation can last up to hundreds of seconds of simulated time. There are two main mechanisms to dampen the wave, and they work best when used in conjunction:

1. Activation of VOF damping
2. Progressive mesh coarsening towards the boundaries (Pettinelli 2013)

Setting the correct damping coefficient for this type of analysis is important. Figure 63 shows the distance from the side wall boundary to where the first mesh refinement close to the ship changes its density. This distance should be used as the damping length which, in this case, is 9.0 m. There are additional settings in Star CCM+ which can help to reduce the excessive oscillation of the model during the analysis. One of them is to assign damping force or damping moment. In this set of analyses, additional damping force equivalent to 1000N –s/m is added to Dynamic Fluid Body Interaction (DFBI) setting.

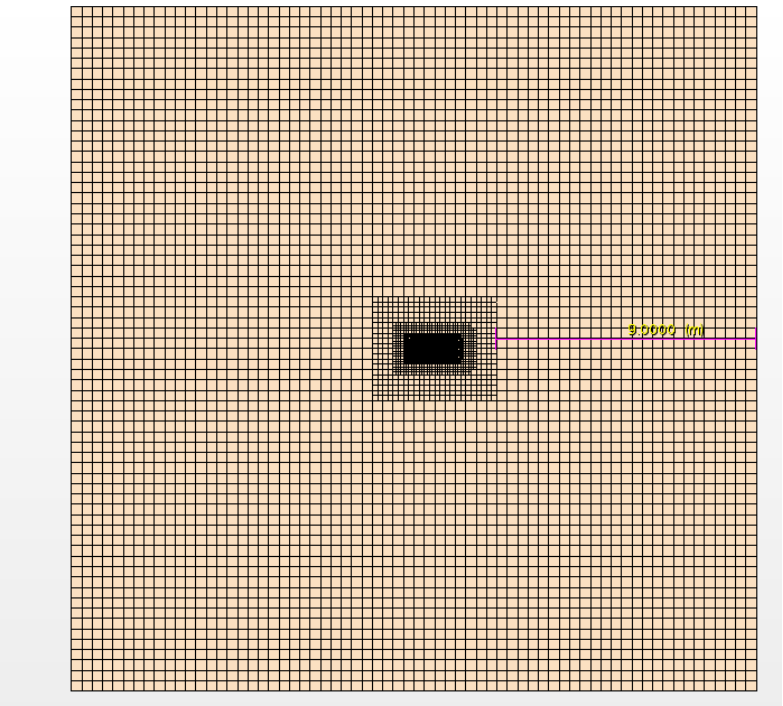

Figure 63: Depicts the distance from the wall boundary to where the mesh density changes

Steady or unsteady analysis:

It is important to establish if the simulation is steady or unsteady as unsteady simulations demand more CPU and take a longer time to converge. Simulations that are time-dependent and, hence, require the unsteady model include:

- time-varying boundary conditions;
- sliding or deforming mesh problems;
- free surface (VOF) problems, and
- transient heat transfer (CD_ Adapco 2012).

Care must be taken when there is a possibility of the presence of vortex shedding in a flow. If that is the case, then the flow is not statistically stationary and unsteady RANS computation should be employed (Iaccarino *et al.* 2003). The random field $U(x, t)$ is statistically stationary if all statistics are invariant under a shift in time (Pope 2001). Therefore, it can be concluded that the flow field is not statistically stationary. Hence, unsteady simulation should be used.

Time step:

For typical external, or immersed, flows around a body, the time-step size should be chosen to resolve the convective time scale of the body. If the body has a length L and it is travelling at a speed U, then the characteristic time scale of this body would by $T = \frac{L}{U} \cdot A$ good place to start would be to resolve this characteristic time scale in 10–20 increments so that the time-step size $\Delta t = 0.1 \cdot T$ or 0.05 T.

For free-surface applications, an important issue is to maintain a favourable convective Courant number, also known as the Courant-Friedrichs-Levy (CFL) number, in order for the high-resolution interface capturing (HRIC) scheme to track accurately the free surface position. The CFL number is defined as $= U \cdot \Delta t/\Delta x$, where Δx is the associated grid spacing; in the case of free-surface flows, the vertical mesh spacing is critical. By default, the HRIC method is optimised for free surfaces operating at CFL<0.5. The time-step size can be determined based on the mesh spacing. If the time-step size is too restrictive, the mesh can be coarsened but it can result in a loss of resolution (Yen 2014). In general, time step should be treated as a variable. This means that the analysis should be repeated with a different setting of time step to make sure the results do not change and are independent from time step.

The time step for sinkage and trim analysis was calculated based on the recommendation of ITTC. The recommendation by ITTC (Practical Guidelines for Ship CFD application, page 11) states: For standard pseudo-transient resistance computations, use $\Delta t = 0.005 \sim 0.01 \cdot L/U$ (Kashiwagi & Toda 2008). In this case, the L =1.32m and U = 3.8 m/s, then $\Delta t = 0.001$.

The HRIC Convection Discretisation Scheme:

An important quality of an immiscible phase mixture (for example, air and water) is that the fluid components always remain separated by a sharp interface. The High-Resolution Interface Capturing (HRIC) scheme is designed to mimic the convective transport of immiscible fluid components, resulting in a scheme that is suited for tracking sharp interfaces (CD_ Adapco 2011).

Setting the CFL-l (lower Courant number) and CFL-u (upper Courant number) to high values ensures that HRIC is always used and this allows the use of higher time step in analysis. In general, to estimate the time step, the target should be set to a Courant number equal to 1. For this Sinkage and trim analysis, CFL-l is set at 50 and CFL-u= 100.

Calculating the diagonal components of the moment of inertia (1/80 scale model):

Mass of the model = 5.86 kg, therefore, the mass of the ship from scaling rules is:

Model mass $= \frac{\rho m}{\rho s \cdot R^3}$ · ship mass (Lloyd 1989) which gives the mass of the ship = 3075.30 tonnes.

When ρm is fresh water density = 1025 kg/m^3, ρs is the salt water density = 1000 kg/m^3

R= 80 scaling factor

A finite element model of one of the 112m ships was used and the total mass was scaled to a total of 3075.302 tonnes. The moment of inertia for this model was:

I_{xx}	$3.05 \cdot 10^{11}$
I_{yy}	$2.32 \cdot 10^{12}$
I_{zz}	$2.51 \cdot 10^{12}$

Calculating the model test radius of gyrations:

Using the above information and knowing R=$\sqrt{\frac{I}{M}}$, the radii of gyration of the actual ship can be calculated as:

R_x	9.961
R_y	27.46
R_z	28.57

And from that the radii of the gyration of the model after scaling will be:

	radius of gyration of model
r_x	0.124
r_y	0.343
r_z	0.357

Knowing the mass of the model is 5.86 kg, it is now possible to calculate the moment of inertia of the test model using the same formula of R= $\sqrt{\frac{I}{M}}$ but this time Rx, Ry and Rz plus the mass are known and the calculation is for finding I.

The results are shown in Table 13.

I_{xx} of model	0.091
I_{yy} of the model	0.691
I_{zz} of the model	0.748

Table 13: Diagonal components of moment of inertia

The above information is needed to define DFBI (Dynamic Fluid Body Interaction) which is the process by which the rigid body motion is calculated as a response to computed forces on a specified body due to some or all of the following: its mass in a gravitational field, moments of inertia, forces due to integrated fluid pressure, specified forces and moments, and reaction forces due to body couplings such as moorings and springs (Yen 2012). The following describes the concept of solid and wake blockages and also the concept of boundary layer profiles, both on the ocean and in the wind tunnel test domain.

Procedure for performing the sinkage analysis to find correct waterline:

Sinkage and trim analysis is based on the Archimedes' principle. The Archimedes' principle states that when an object is partially submerged in a fluid, the sum of the gravity forces should be equivalent to the buoyancy forces. This law also states that when a body is partially or completely immersed in a fluid, it experiences an apparent loss in weight which is equal to the weight of the fluid displaced by the immersed part of the body.

It should be noted that there is no initial wind or current involved when undertaking sinkage and trim analysis. Both current and wind velocities are set at zero. The model will be analysed only with gravity. It is good practice to begin the analysis and run it for a while before the model is released to translate and rotate under its own weight in liquid. The release time can

be set for a few seconds after the analysis is started. When the test model is released, it will start to sink because of gravity. The buoyancy forces which are counteracting the gravity force eventually exceed the gravity force and push the model upward. This results in the test model oscillating for a while until it finds its equilibrium. At this point a single-phase flow of waves starts to be generated. These waves will propagate towards the domain's boundaries. To capture the complete movement of the test model in water the waterline interface needs to be adequately refined. The refinement should cover the entire waterline in all x and y directions and also far enough in z direction, both above and below the waterline. This is shown in Figure 66.

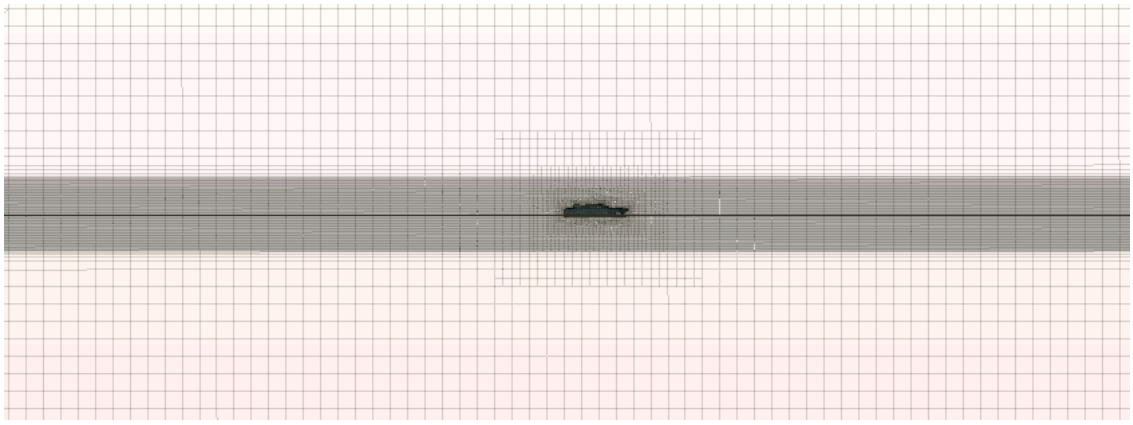

Figure 64_ Required mesh refinement in z direction

The fully displaced 112m catamaran has a waterline of around 4m. Therefore, to start the analysis, the waterline is set in VOF (volume of fluid), at (0, 0, 50 mm) in a laboratory global coordinate. 50mm is a linear scale of 1/80 of the full draft of the actual ship at 4m. This would be a good starting point. However, the waterline can be set at any other height. The model is analysed with just the gravity load and the waterline is defined at 0.050m. After convergence the force report is to be checked. The total upright force from the defined waterline should be equivalent to the total downward force which is from the mass of the model at 5.86 kg or 57.48N. If the upright buoyancy force is not equal to the mass of the model test, the waterline should be adjusted and the model re-analysed with a newly defined waterline. The analysis should be repeated until the total forces are in equilibrium. At that point, the defined waterline is the correct waterline for the model test.

After achieving convergence, the force report and moment were inspected. In the first run, the force report was not equal to the mass of the model (5.86kg or, 57.48 N). Therefore, the waterline was adjusted and the model was re-analysed. These steps were repeated until the force report was showing the total of 57.48 N. At that point the waterline was set at 0.055m. (Difference = 0.001)

With this waterline and by using Rhino, the area above the waterline for the side and front of the test model was calculated as:

Area above waterline side view 0.223 m^2

Front above waterline area 0.069 m^2

Procedure for performing the trim analysis to find the correct location of COG:

To start, a location (x, y, z) for COG a DFBI (Dynamic Fluid Body Interaction) setting is assigned. The location of the longitudinal centre of gravity (LCG) can be defined at the midship as a starting point. Transversal centre of gravity (TCG) should be set at zero, as the model is symmetrical. For the calculation of Vertical centre of gravity (VCG), a finite element model of 112m ship can be used. Knowing the model test has a mass of 5.86 kg and using the scaling rule formula for mass, the mass of the ship can be calculated as:

Ship mass $= \frac{\rho_m}{\rho_s \cdot R^3}$ = 3075.3 tonnes (Lloyd 1989).

Next, the finite element model mass is scaled to arrive at the above mass. From that, the VCG of the ship can be identified. (The assumption is made that the global FEA model has its normal fully loaded condition. It should be noted that the position of the VCG is not crucial for this set of analyses but it is good practice to be as accurate as possible to the actual value). Then the VCG of the ship is scaled to get the VCG of the test model. From the above, the VCG of the test model is calculated to be 0.112m.

1. Analyse the model and check for convergence.
2. Run a moment report about the **y** axis and the midship.
3. Check to see if there is any significant positive or negative moment.
4. Adjust the LCG accordingly in x direction and re-analyse the model.
5. Redo steps 2 to 4 until the calculated moment is almost zero.

At this time, the LCG is in the correct location and the level trim is achieved.

Following the above procedure and, after some trial and error, the level trim was achieved. At that moment the position of COG was measured at [0.526, 0.0, and 0.112] m, m, m. The sinkage and trim analysis was repeated with SST K- ω turbulence model to check the results are independent of the type of the turbulence models.

Figure 65 shows the final sinkage plot when the model is set at its correct waterline. The value of the total sinkage, when the gravity and buoyancy forces are the same, is only 0.55mm. This shows the correct waterline for the 1/80 scale model, which has the total mass of 5.86 kg, is 0.055 m. Therefore, this value will be used from now on in all calculations. Figure 66 shows the vessel at its level trim after convergence. The total amount of turning moment about the y axis (roll) is 0.000 N/m, which indicates that the position of COG in CFD model is correct.

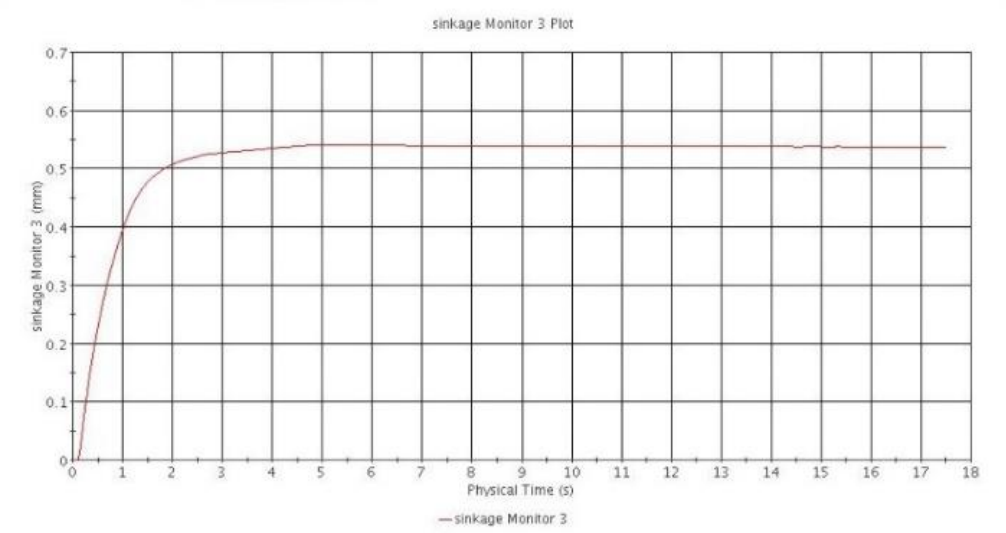

Figure 65: Results from sinkage analysis converged at new waterline of 0.055 m

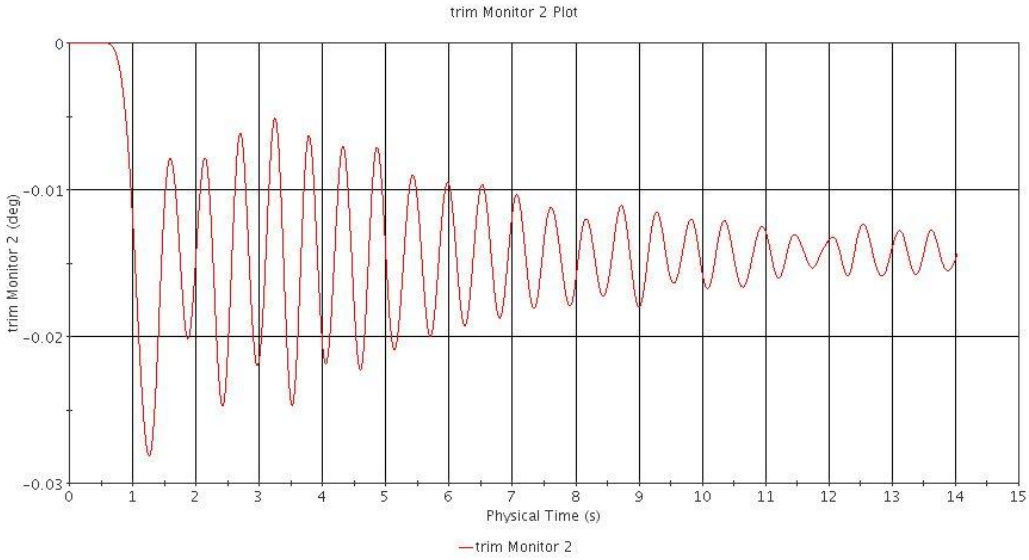

Figure 66: Results from trim analysis. Converged to -0.015 degree

The sinkage and trim analysis was repeated with the SST K- ω turbulence model to check the results are independent from the type of turbulence models. Figure 67 shows the results from the SST K- ω turbulence model when the second order of analysis was used.

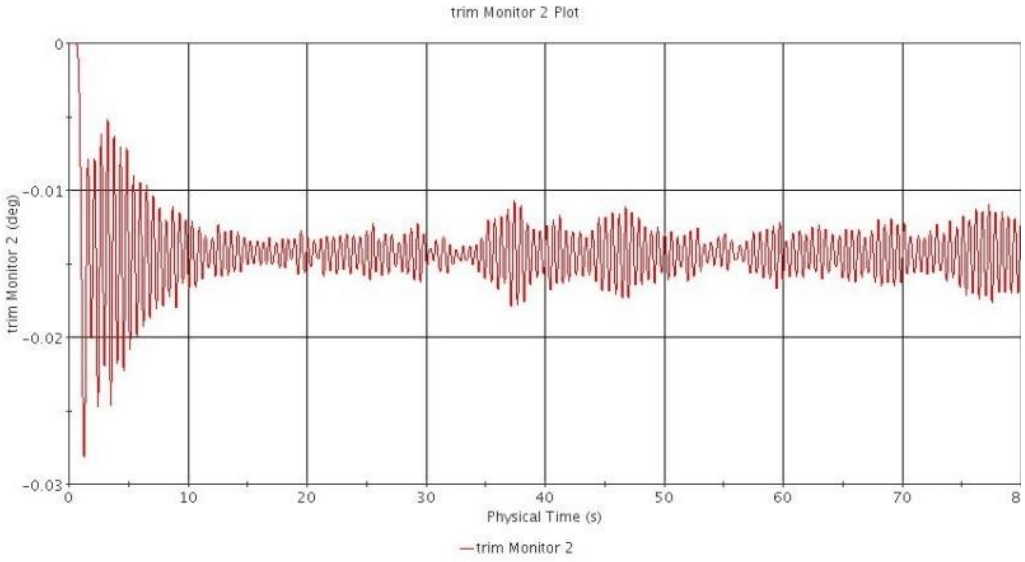

Figure 67: Trim plot from the second order analysis using SST K- ω.

Summary of the results:

The results from sinkage and trim analysis confirm that the correct waterline for the 1/80 scale model of the 112m catamaran is 0.055m and the correct COG is at [0.526, 0.0, 0.112] m, m, m.

Appendix 2 Domain Size Sensitivity Analysis

Performing domain size sensitivity analysis:

By reducing the size of the domain, the number of cells will reduce, which consequently reduces computational time and expenses. Therefore, it is necessary to ascertain the optimum domain size for CFD analysis. To do this the original model was used as a benchmark. Then, by scaling the domain in all different directions, the effect of the side walls on the final results was studied. Figure 68 shows the original computational domain which is used for the domain size sensitivity study. This model is when the ship is at 45° heading into the wind. The aim of this study is to find out how much the size of the domain can be reduced without having any influence in the flow field around the scale model or changing the final results. Therefore, the original domain was systematically scaled down. Each time, the results were compared with the original results. Table 14 shows that scaling the domain down to 25% of its original size did not have any effect on the final results. This means that the results are independent from the domain size.

Figure 69 to Figure 72 are showing the pressure plots of those different domains. It is shown that, by reducing the domain sizes, the pressure fields extend to either the inlet, the side boundaries or the outlet. However, the overall results in Table 14 indicate that this effect does not have a major impact on wind force coefficients.

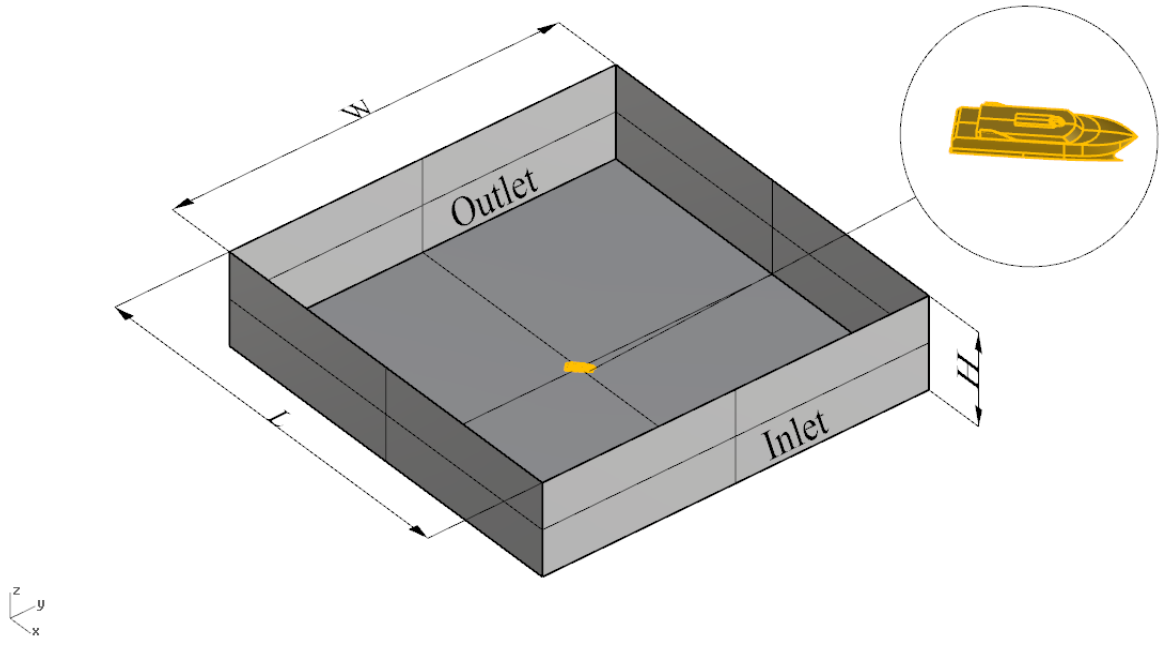

Figure 68: Domain isometric view. Domain dimensions (L = 21.76m, W = 21.76m, H = 5.12m)

Original Domain:

The original domain dimensions are:

L = 21.76m, W = 21.76m, H = 5.12m

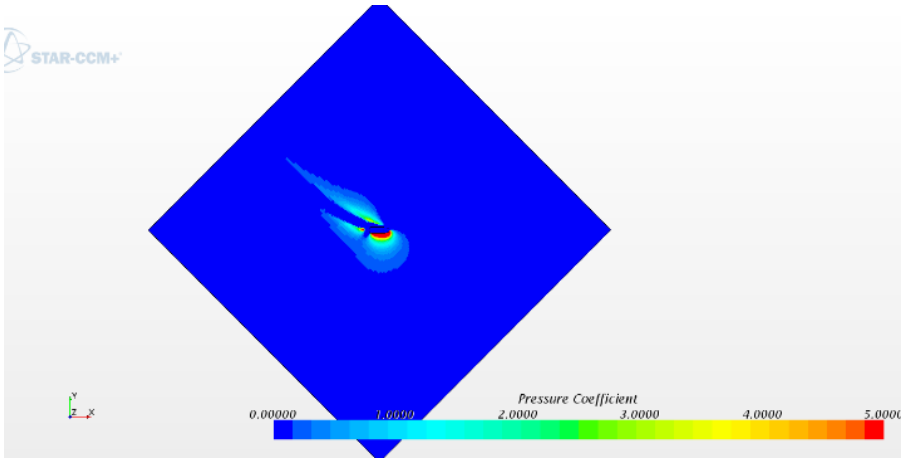

Figure 69: Pressure field plot. This plot shows that the side walls have no effect on the flow around the model. Also, both inlet and outlet boundaries are located at a distance, far enough from the model, allowing for flow to be fully developed before reaching the model and exiting from the domain outlet.

Domain size was reduced 50% in x and y and z:

L =10.88m, W =10.88m, H = 2.56m

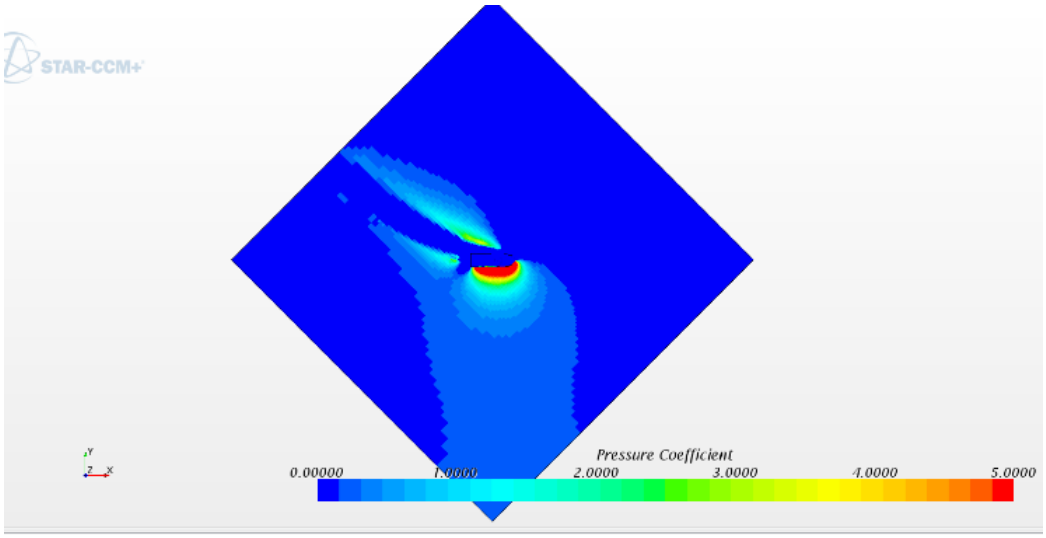

Figure 70_ Pressure field plot. Domain size is reduced by 50%.

Domain size was reduced 50% in x & 25% in y direction:

L = 10.88m, W = 5.44m, H = 2.56m

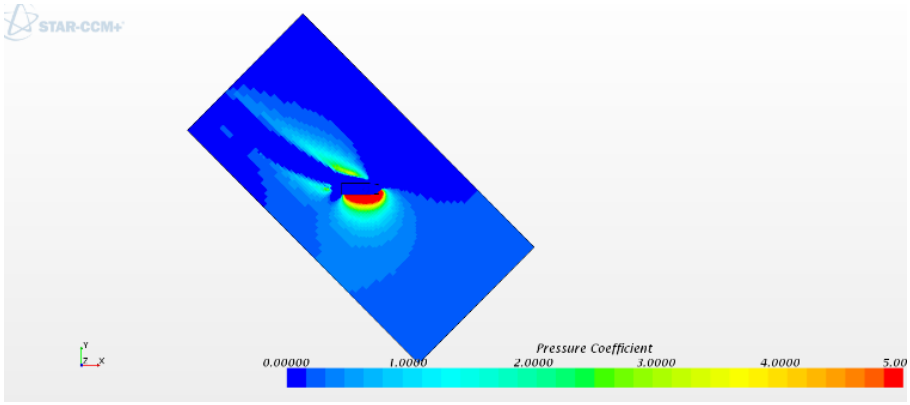

Figure 71: Pressure field plot

Domain size reduced to 25% both in x and y:

L = 5.44m, W= 5.44m, H = 2m

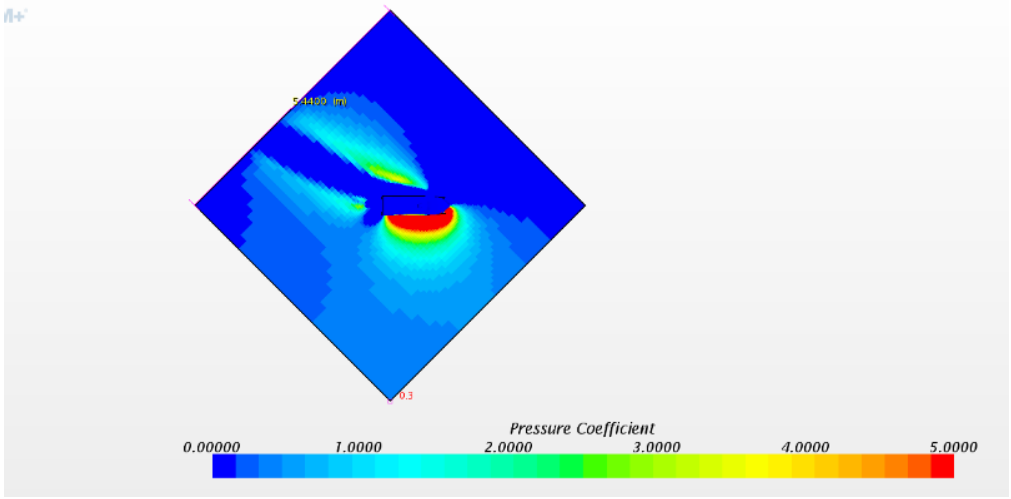

Figure 72: Pressure field plot

Domain size (L x W x H)	C_x	C_y	C_N
21.76 x 21.76 x 5.12	0.117	0.954	0.146
10.88 x 10.88 x 2.56	0.1168	0.923	0.141
10.88 x 5.44 x 2.56	0.117	0.927	0.1417
5.44 x 5.44 x 2	0.122	0.929	0.142

Table 14: Comparing the results of the same model with different domain sizes

Appendix 3 Replicating Ikeda and Oura's experiment

Domain size:

The suggested domain size (minimum requirements) to perform an aerodynamic analysis on an object in an open space by CD. Adapco is shown in Figure 73.

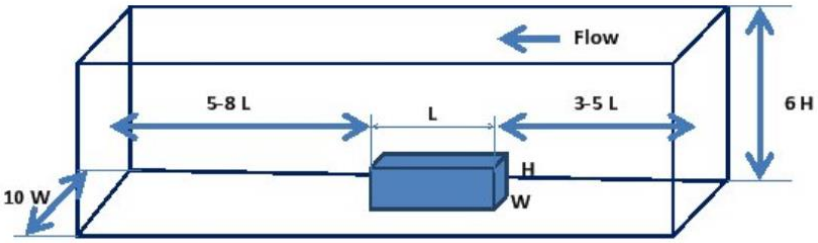

Figure 73: Recommended for domain size for an aerodynamic test on a car in an open space (Ross 2013)

In general:

- Domain size should be large enough so that any minor changes in size do not have any effect or influence on the flow or the results from the analysis.
- The inlet has to be far enough from the test model so the flow can develop properly, prior reaching to the region of interest.
- The outlet boundary should also be far enough from the model so that it has no effect on upstream flow. The outlet boundary must be placed as far away as possible from the region of interest and should be avoided in regions of strong geometrical changes or in wake regions with recirculation (Tu *et al.* 2013).

The length of the waterline of the 112m catamaran was defined as 105.6 m. (Refer to Table 11, Appendix 1) Therefore, the waterline of the 1/80 scale model is 1.32m.

Initial domain size is set at (L = 21.76 m, W = 21.76 m, H = 5.12 m) and the point of origin (0,0,0) was set at midship and on its centreline. Figure 74 shows the computational domain with the model centred on the floor of the domain.

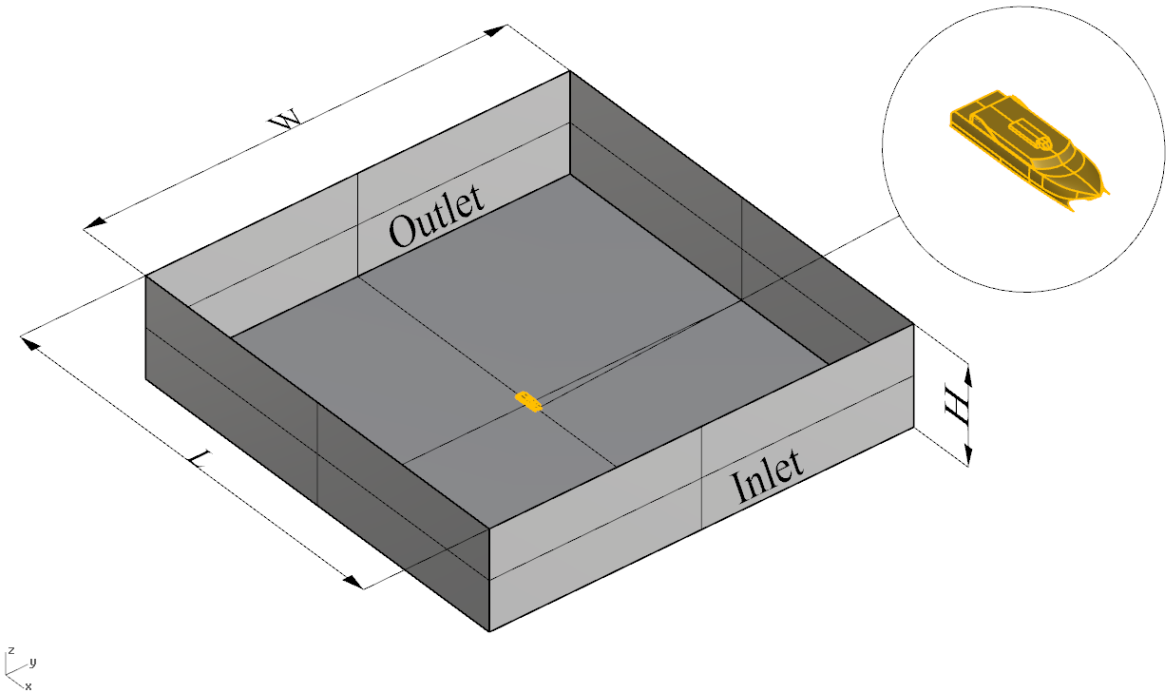

Figure 74: Computational domain only above the waterline with the wind angle of attack at zero 0°. The scale model is on the floor, centre of the domain at (0,0,0).

The first CFD model was created while the test model was aligned with wind directly blowing at 0° from the bow. This is when the local coordinate of the test model was set to be aligned with the global coordinate. The wind velocity was set at 3.8 m/s. The mid ship of the model (point at centreline of the model and half the length between perpendiculars ($L_{pp}/2$) on its waterline) was set at the centre of the domain's floor (0,0,0).

Choosing correct turbulence model:

There are a number of ways in which errors can be introduced in CFD analysis. These errors can be from the computational domain, the level of convergence, physical modelling or human error. It is always necessary to check the solutions to ensure that the results can be trusted. It is also important to check the correct turbulence physic model is used and that the results are independent from mesh and domain sizes. Turbulence modelling and the choice of wall treatment are linked. It is necessary to choose one based on the other (Tu *et al.* 2013).

In general, the standard K-epsilon model works sufficiently in free stream to solve the Reynolds average Navier-Stokes equations. However, this turbulence model fails in solving those equations at the near wall layer. Additionally, the calculation of the shear stresses in adverse gradient flows are often over predicted. On the other hand, K-omega works very well close to the wall but it is not that sensitive in free stream. That is why the K-omega model was replaced by the shear stress transport (SST) model. This model is a combination of K-epsilon which does a good job in the outer part of the boundary layer, and K-omega which is more accurate in the near wall region.

The preferred turbulence model to solve the Reynolds Average Navier-Stokes equations in CFD models for the first part of Ikeda's experiment is the SST K- ω with two layers all y^+ wall treatment. Knowing that each turbulence model has its own formulation to solve and approximate the Reynolds Average Navier-Stokes equations, CFD analysis should be repeated with at least one other turbulence model to ensure the approximated results are closer to their exact value and that the solution is independent from the specific turbulence model (for example, the Realisable K-epsilon turbulence model and two layers all y^+ wall treatment).

Similarly, a check should be performed on the chosen type of wall treatment. The fact that even the two-layer all y^+ wall treatment does a decent job in solving the Navier -Stokes equations in the buffer layer region is not sufficient. It is still important to make sure the calculated y^+ does not fall in the buffer layer region, especially if we are dealing with unsteady flow, where the flow can be characterised as statically not stationary or if we have VOF. An email (Kynan Maley, personal communication, 12th March 2015) confirms, that two layer all y^+ wall treatment does a reasonable job in region of buffer layer but it is not recommended.

In summary the best practice is to make sure the y plus value is either $y^+ > 30$ or $y^+ < 5$. However, if the value of $5 < y^+ < 30$, then further analysis is required to make sure the results are still valid. This can be done by refining the prism layer to get y^+ value in the region which is desired (e.g. < 5 or >30). Then the analysis should be repeated and the results compared. This assures that results are independent from the type of wall treatments.

Type of mesh:

Polyhedral meshing has the advantage of smooth growth away from the body, while trimmed meshes tend to be more efficient at placing cells in the desired refinement areas. The polyhedral volume mesher is directly dependent on the quality of the starting surface triangulation. In other words, a poor quality starting surface will lead to a poor quality volume mesh. The trimmer model is not directly dependent on the surface quality of the starting surface and, as such, is more likely to produce a good quality mesh for most situations. The trimmed cell mesher provides a robust and efficient method of producing a high-quality grid for both simple and complex mesh generation problems. It combines a number of highly desirable meshing attributes in a single meshing scheme:

•predominantly hexahedral mesh with minimal cell skewness;

•refinement that is based upon surface mesh size and other user-defined refinement controls;

•surface quality independence, and

•alignment with a user specified coordinate system.

Therefore, the trimmer mesh is the preferred type of mesh and is used for these sets of analysis. The mesh refinement is set to be aligned with the direction of the wind flow. This can be achieved by creating a new Cartesian coordinate system which is used to define both mesh refinement and wind direction.

Calculation of prism layer thickness and y^+:

The prism layer mesh model is used with a core volume mesh to generate orthogonal prismatic cells next to wall surfaces or boundaries. This layer of cells is necessary to improve the accuracy of the flow solution.

A prism layer is defined in terms of:

- It's thickness;
- the number of cell layers within it;
- the size distribution of the layers, and
- the function that is used to generate the distribution either by geometric or hyperbolic tangent.

The analysis can start with a coarse mesh and an average y^+ of 30, with using two layers all $\mathbf{y^+}$ wall treatment. This ensures that, even when the y^+ value falls within the buffer layer, the results from analysis are still reasonably valid. After the first set of analysis, a mesh sensitivity analysis should be performed for y^+ value < 5 and results should be compared. Table 15 shows general mesh particulars for CFD models. Figure 75 and Figure 76 display the grid density in the model.

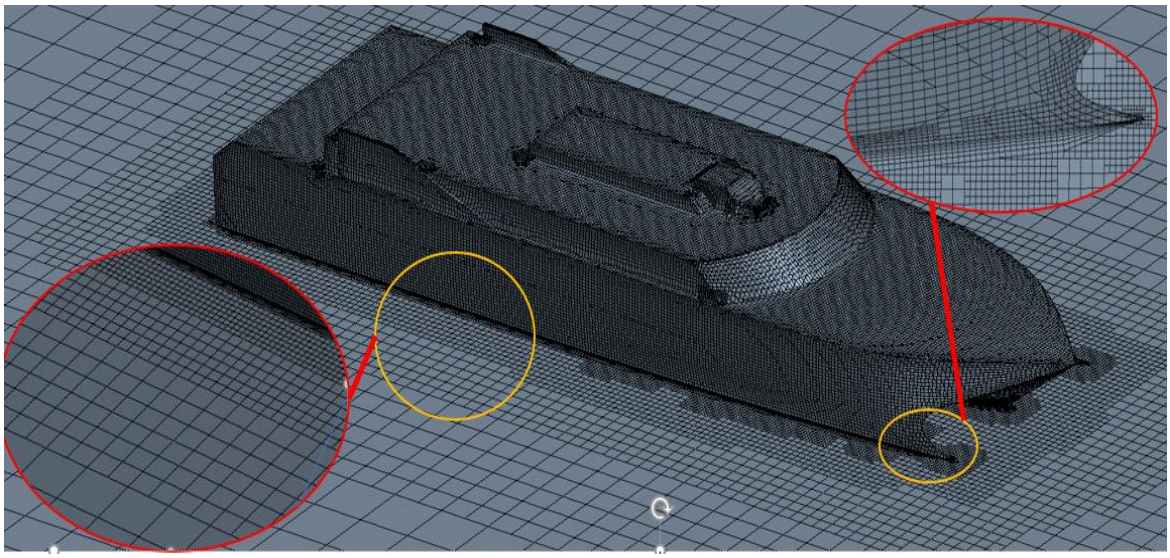

Figure 75: Progression of the mesh refinement from prism layer to core mesh around the ship. Mesh is partially magnified for clarity.

Type of mesh	Number of cells	Prism layer thickness	Number of layers	Prism layer stretching	Water density	Air density
trimmer	710,000 plus	14 mm	6	1.3	997.561 kg/m^3	1.18415 kg/m^3

Table 15: General grid specification

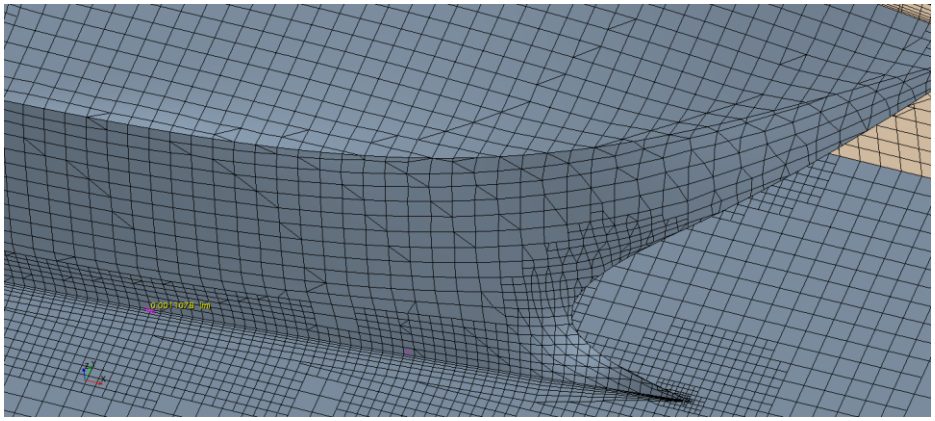

Figure 76: Prism layer with six cells

Steady or unsteady analysis:

It is important to establish if the simulation is steady or unsteady as the unsteady simulations demand more CPU and take longer time to converge.

Simulations that are time-dependent and therefore require the unsteady model include:

- time-varying boundary conditions;
- sliding or deforming mesh problems;
- free surface (VOF) problems, and
- transient heat transfer (CD_ Adapco 2012).

Care must be taken when there is a possibility of the presence of vortex shedding in flow. If that is the case, then the flow is not statistically stationary and unsteady RANS computation should be employed (Iaccarino *et al.* 2003).

The type of flow in the first part of Ikeda's experiment does not have time variant boundary conditions and there is no VOF. Therefore, the flow field is statistically stationary. Hence, steady simulation can be used. This will save a lot of computational time and CPU, and assist in quicker convergence.

Time step:

In general, The Courant Number (CFL) is used only by the coupled (steady/unsteady) solver, to control the size of the local time-steps that are used in the time-marching procedure. For steady simulations, the local time-step is used by the pseudo time-step associated with the iterations. For a steady-state simulation, a larger CFL number increases the local pseudo-time step size and produces faster convergence.

For steady simulations, the coupled solver in STAR-CCM+ employs a time marching scheme to drive the unsteady form of the governing equations to a steady state. In this case, a pseudo-

transient term replaces the physical time derivative. The solution advances in pseudo-time to drive this term to zero. The solution in each cell is advanced independently with an optimal pseudo-time step computed locally according to stability constraints. In this way, convergence to steady state is achieved in the most efficient manner (CD_Adapco 2012). Therefore, in steady analysis, there is no need to set the time step. The first model is created for when the wind velocity is at 3.8 m/s and is directly blowing to the bow at 0°. The model test and domain are aligned with the x global co-ordinate.

Boundary conditions:

The sides and top boundary were set as symmetry. Inlet was set as velocity inlet. Outlet was set as pressure outlet. The surface of the ship test model was set as non-slip wall and the bottom boundary was set as slip wall. Assigning the slip wall as the condition for the bottom boundary is not correct. However, it was confirmed by Professor Ikeda that, at the time of performing the test, there no ripples or waves were generated on the towing tank water surface.

Note: as a point of interest, this set of analysis was repeated with the same boundary conditions but with the exception of making the bottom boundary as a non-slip wall. The results are included at the end of this appendix. The analysis is in steady state and there is no VOF. Therefore, there is no requirement for setting VOF damping length.

Results from analysis:

Realisable K-epsilon with two layers all y^+ wall treatment was used for modelling the turbulence. Using all y^+ wall treatment ensures the results are still valid even if the y^+ value falls in the buffer layer. The wind angle of attack was set at 0° and the wind velocity was set at3.8 m/s. Figure 77 to Figure 79 are showing the plots of force and moment coefficients after convergence was achieved. Table 16 shows the results of the first set of analysis when the wind angle of attack is at 0°. Figure 80 displays the wall y^+ value. As is shown, the results are between 5 and 30 (buffer layer zone). The size of the very first cell near the wall is measured at 1.1mm.

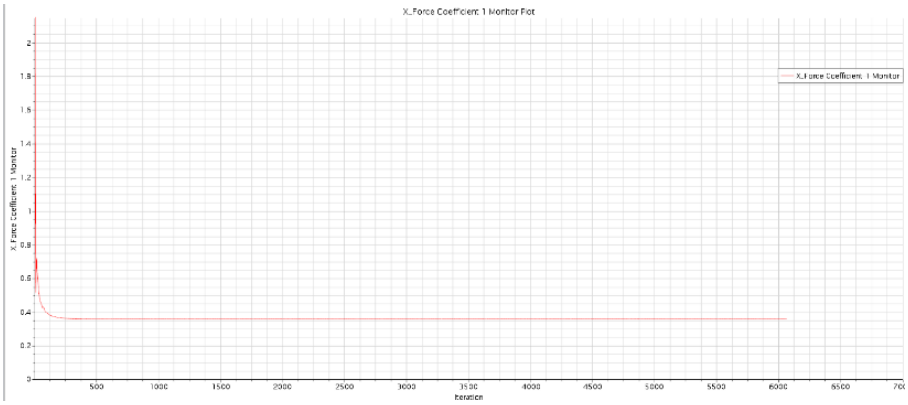

Figure 77: X_force coefficient plot

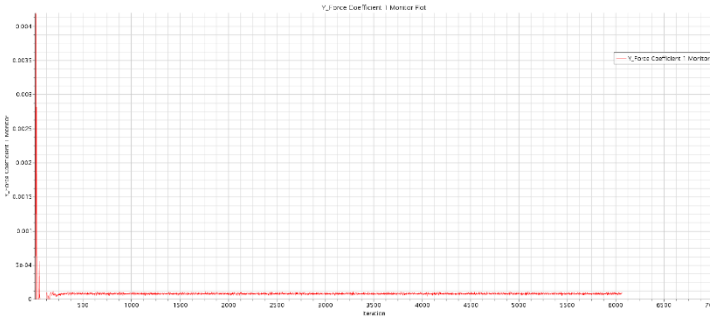

Figure 78: Y_force coefficient plot

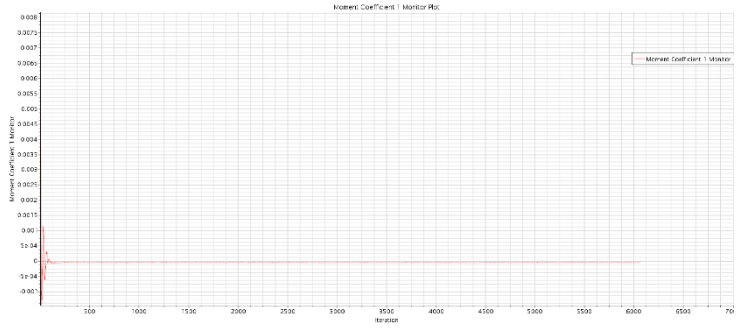

Figure 79: Moment coefficient plot

K_ zero			7000	iterations
		Cx	Cy	C_N
	CFD	0.361	0.000	0.000
	Exp (Ikeda)	0.44561	0.023	0.015

Table 16: Results when angle of wind attack is 0° into the bow and wind velocity is 3.8 m/s

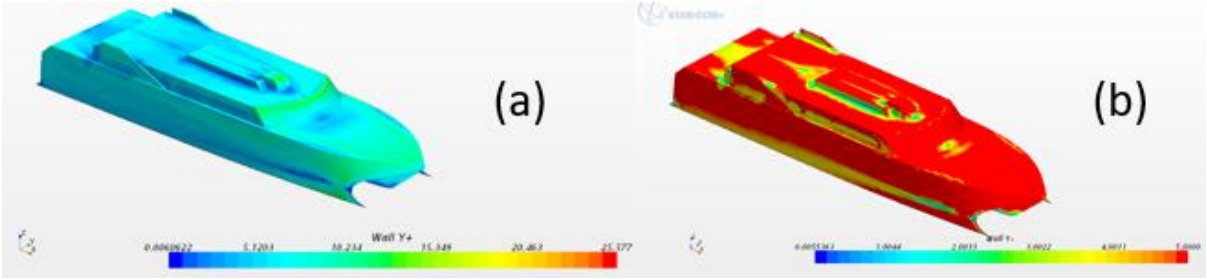

Figure 80: (a) y^+ plot with the range of 1< y^+ < 30. Most of the y^+ is in buffer layer. (b)To show this, the upper limit was reduced to show the reason for using all y+ wall treatment.

Appendix 4 Grid sensitivity analysis

This appendix is the continuation of Appendices 1 and 2. In this part the CFD models are checked to ensure all results are independent from grid, time step, prism layer, physics, and so on.

Y^+:

Checking the y^+ value for all the above models confirmed that the y^+ value was mostly in the range of 5 to 30. This is the range of y^+ for the buffer layer. It is recommended that the size of the first cell near the wall should be set in such a way as to avoid the value of the y^+ fall in this region. Therefore, the prism layer mesh was refined to achieve the $y^+ < 5$ which defines the region of viscous sub layer.

Mesh refinement for $y^+ < 5$:

The analysis was repeated with Realisable K-epsilon with two layers all y^+ wall treatment for a better y^+. The prism layer was refined to have 11 layers and the very first cell has a size of 0.00025 m. Table 17 displays the meshing particulars of the CFD model. Figure 81 shows the transition between the prism layer and the core mesh. In this CFD model, the wind angle of attack is set at 0°. Figure 82 shows the value of y^+ is mainly below 5 (It is usual to have poor y^+ around leading edges and corners due to poor mesh but this does not affect the accuracy of results). Table 18 display the results of CFD analysis with a higher mesh resolution in both the prism layer and the core area for this CFD model.

Prism layer and mesh sensitivity analysis:

Next, a complete set of CFD analysis was performed with both six and eleven prism layer settings. Each time, the analysis was repeated after changing the wind angle of attack by 15° from to 180°. Figure 83 to Figure 85 show the results from Ikeda's experiment against the CFD results from models using Realisable K-epsilon to solve the Reynolds Average Navier-Stokes equations with two layers all y^+ wall treatment. Both results from CFD models with 6 and 11 prism layers are shown. As is shown in the above, the results from models with 11 cells in the prism layer and the one with 6 cells in the prism layers are very close. More study was performed by changing the grid size in the core area. This was done by increasing the maximum cell size. Once again, the results were similar. This proves that analysis results are independent from the mesh resolution and it is grid independent.

Type of mesh	Number of cells	Prism layer thickness	Number of layers	Prism layer stretching	Water density	Air density
Trimmer	1,300,000 plus	14 mm	11	1.3	997.561 kg/m^3	1.18415 kg/m^3

Table 17: Meshing particulars of refined model

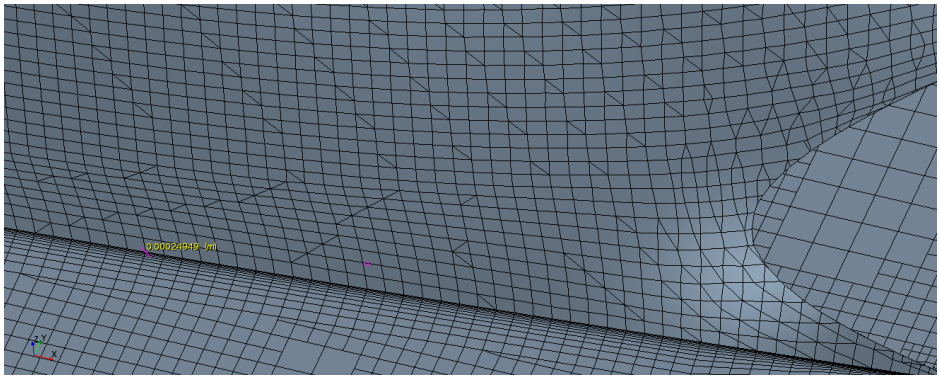

Figure 81: Total of 11 cells in prism layer

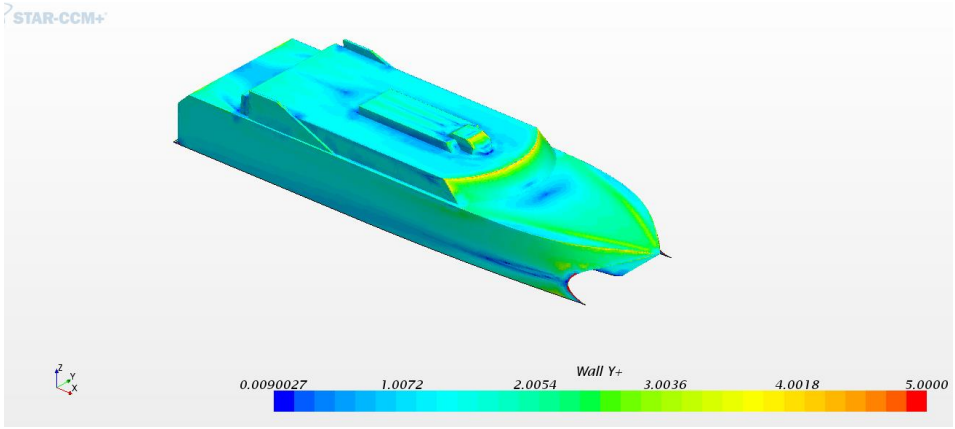

Figure 82: More refinement in prism layer to achieve better y^+ .

K_ zero	1374697 cells		3300	Iterations
		Cx	Cy	C_N
	CFD	0.365	0.000	0.000
	Exp (Ikeda)	0.445	0.023	0.015

Table 18: Wind angle of attack is 0° (directly into the bow). 11 cell prism layer-Realisable K_epsilon

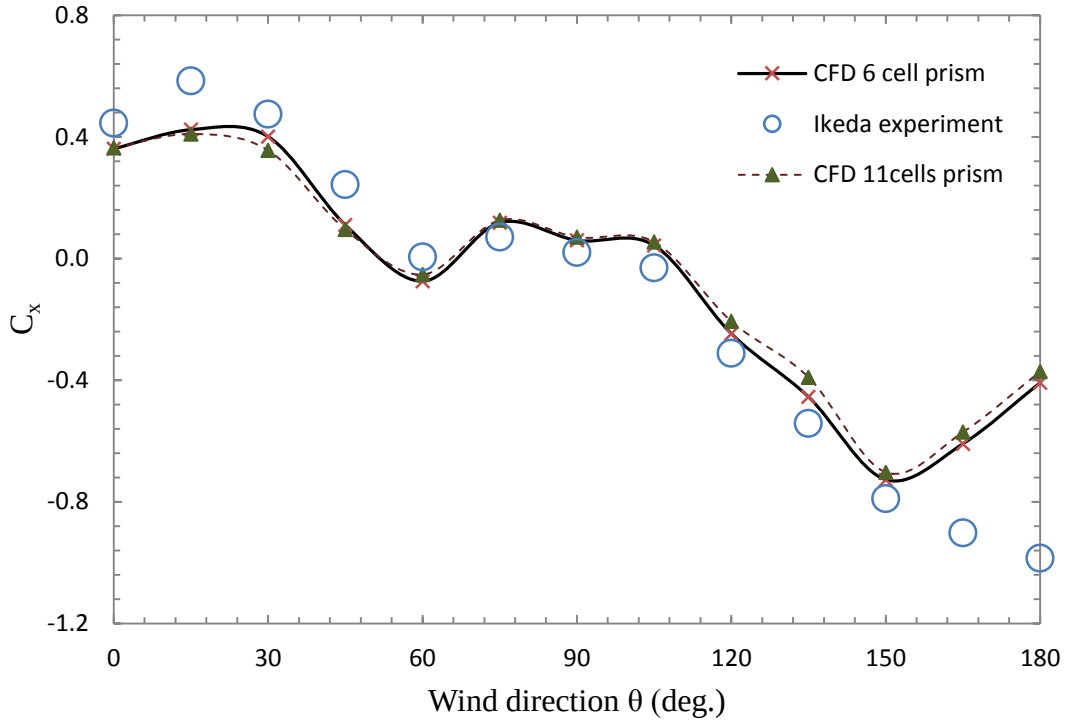

Figure 83: (1/80 scale model) CFD (6 and 11 cells prism layers) vs Ikeda's experimental results, longitudinal force coefficient (C_x). The measured longitudinal force coefficients from results in Ikeda's experiment are higher than those calculated in CFD.

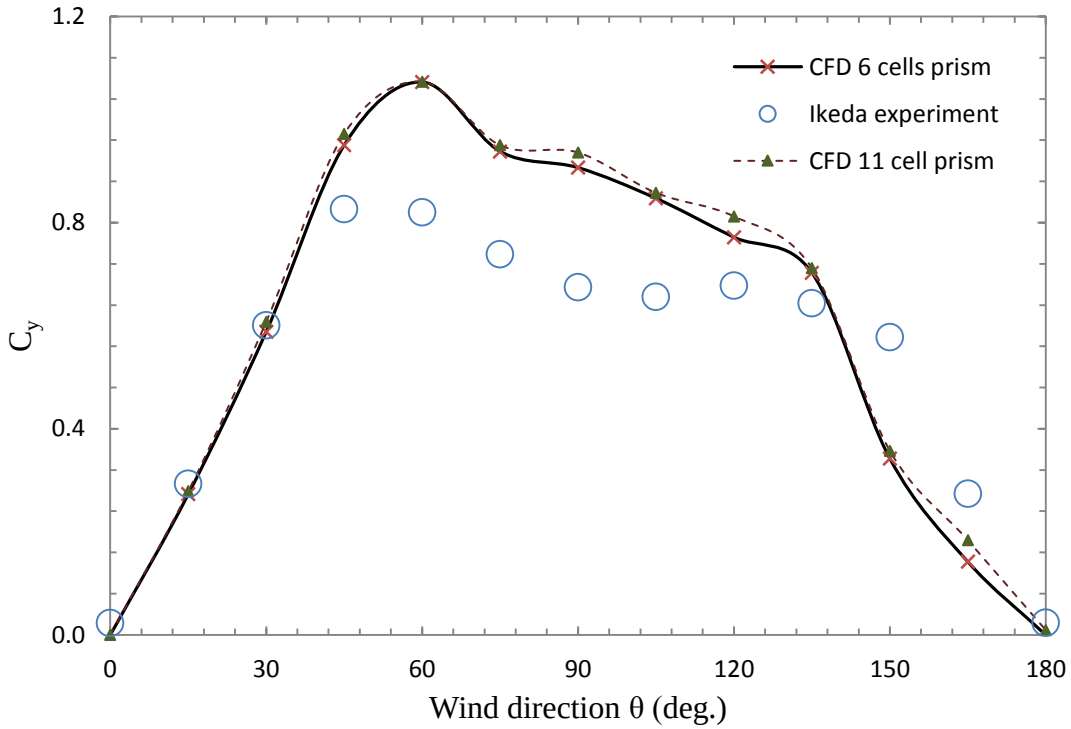

Figure 84: (1/80 scale model) CFD (6 and 11 cells prism layers) vs Ikeda's experimental results, transverse force coefficient (C_y). The measured transverse force coefficients from Ikeda's experimental results are generally lower than CFD results.

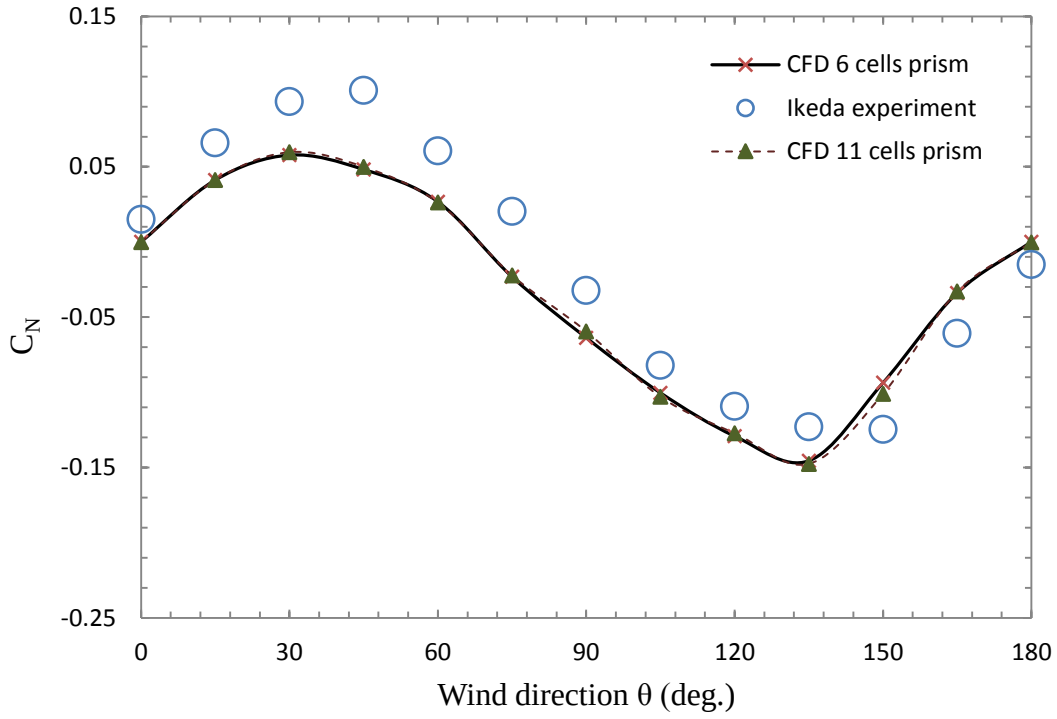

Figure 85: (1/80 scale model) CFD (6 and 11 cells prism layers) vs Ikeda's experimental results, yaw moment coefficient (C_N). Calculated moment coefficients by Ikeda are generally higher than those measured in CFD.

Turbulence modelling study:

To ensure the results are also independent of specific turbulence models, all analysis was repeated but this time using SST K- ω**,** as the preferred turbulence model. Figure 86 to Figure 88 are comparing the results from CFD analysis with Realisable K-epsilon with the results from the SST K- ω**.** All settings between the models, including having two layers all y^+ wall treatment and 11 cell prism layers, are the same.

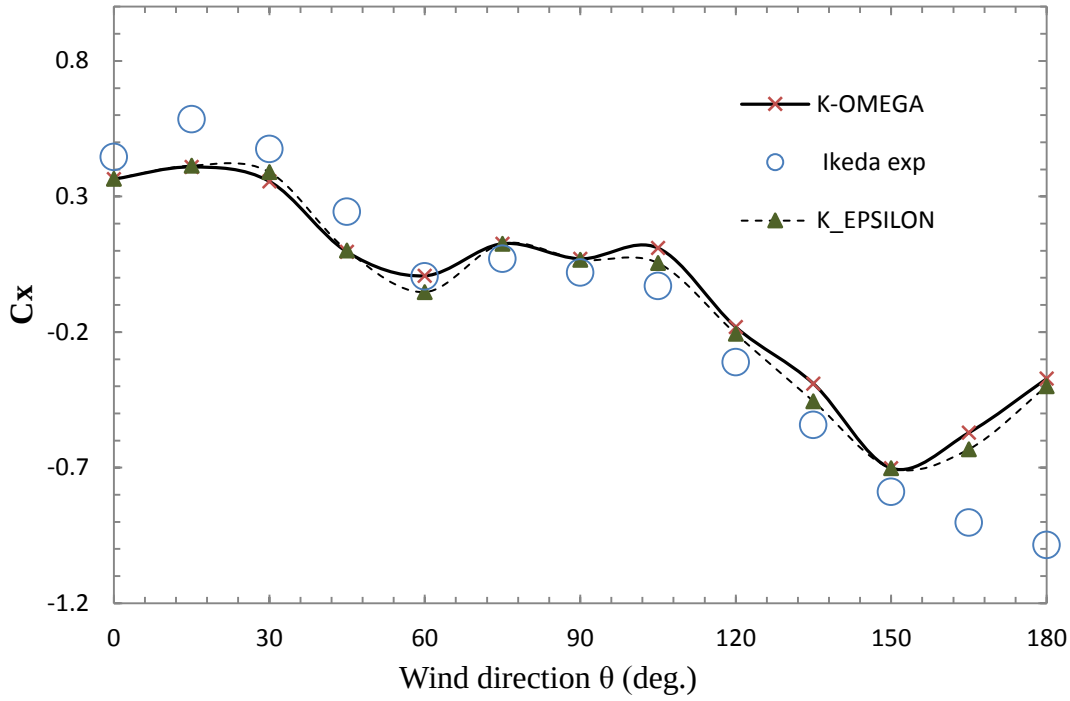

Figure 86: CFD (K-omega and K-epsilon) vs Ikeda's experimental results (C_x). The measured longitudinal force coefficients from results in Ikeda's experiment are higher than those calculated in CFD.

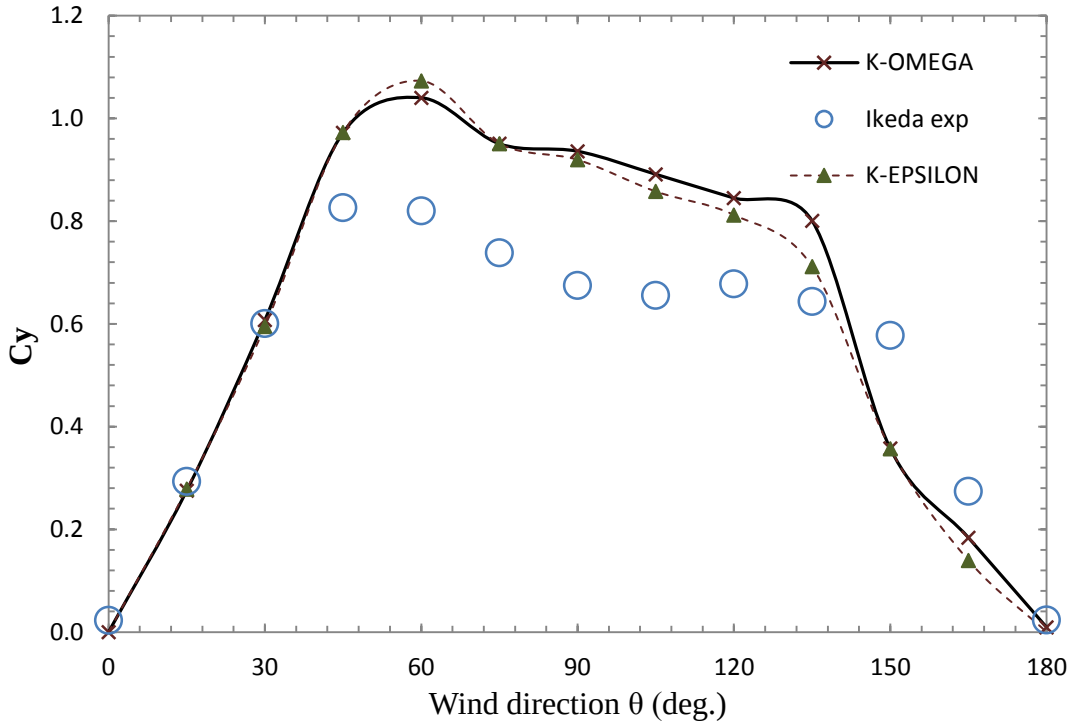

Figure 87: CFD (K-omega and K-epsilon) vs Ikeda's experimental results, transverse force coefficient (C_y). The measured transverse force coefficients from Ikeda's experimental results are generally lower than CFD results.

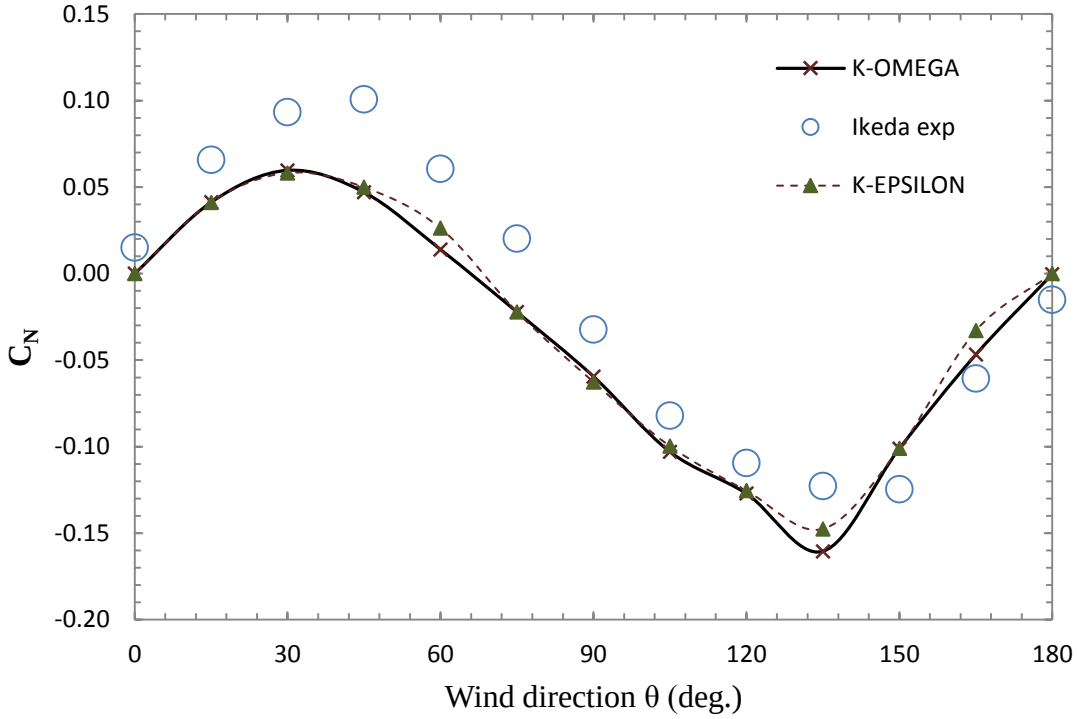

Figure 88: CFD (K-omega and K-epsilon) vs Ikeda's experimental results, yaw moment coefficient (C_N). Calculated moment coefficients by Ikeda are generally higher than those measured in CFD.

Comparison of force and moment coefficients for different wind velocities:

Further studies were performed on all CFD models by increasing the wind velocity from 3.8 m/s to 5.7 m/s and then 7.6 m/s. The non-dimensionalised coefficients (C_x, C_y and C_N) were compared. Comparing the results showed that changing the wind velocity does not have any effect on the magnitude of the forces and moment coefficients. This means that the effect of changing the wind velocity by a factor of two also changes the magnitude of the forces and moment by four. This is because the coefficients remain the same. This is shown in Figure 89 to Figure 91.

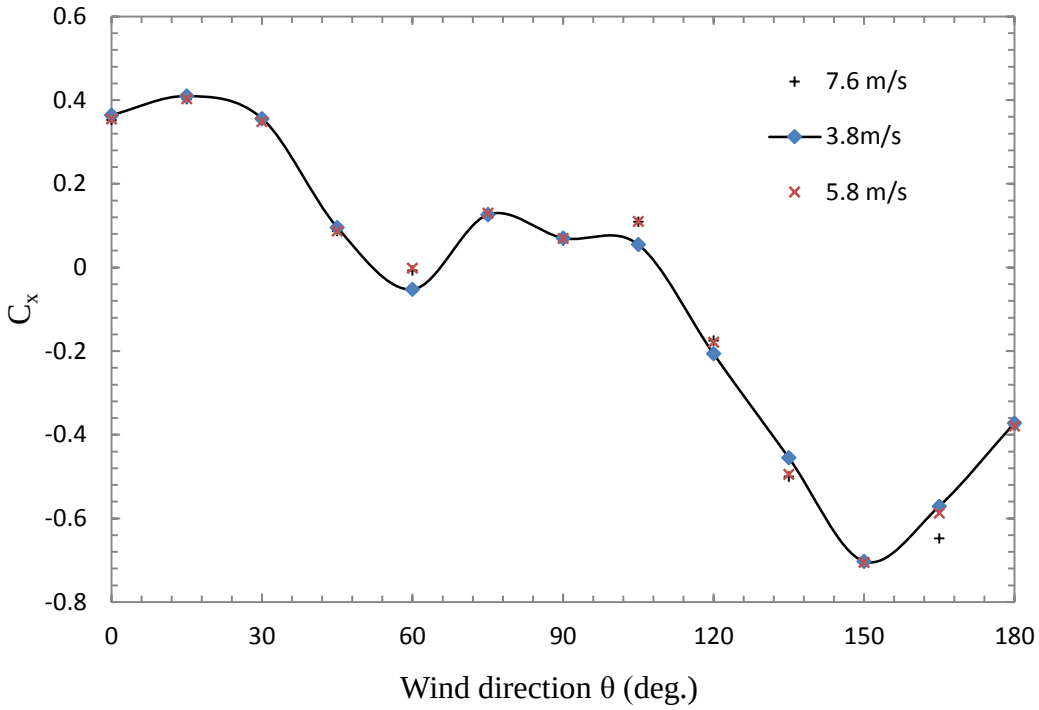

Figure 89: C_x results for different wind velocities (CFD)

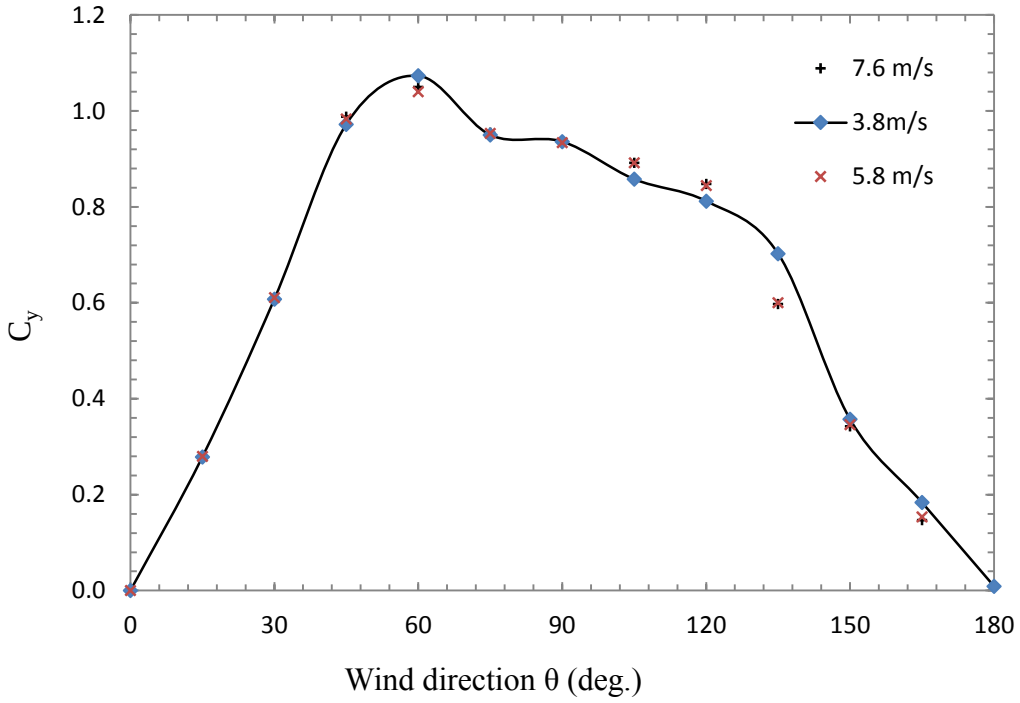

Figure 90: C_y results for different wind velocities (CFD)

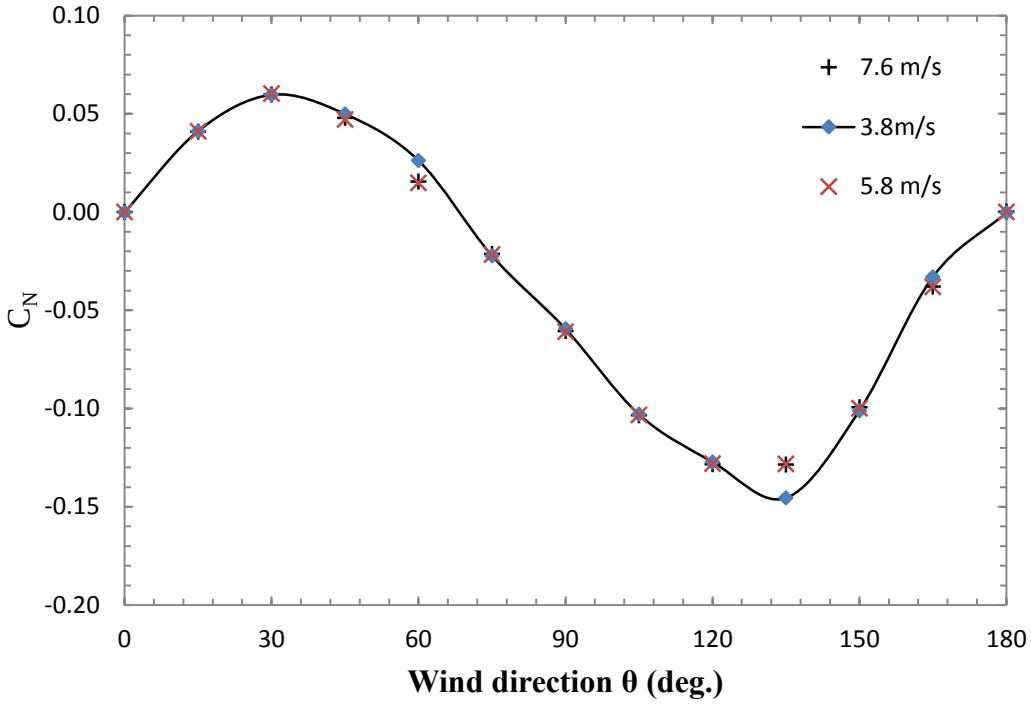

Figure 91: C_N results for different wind velocities (CFD)

Changing the floor condition to nonslip:

Finally, the bottom boundary of the domain was defined as non-slip. It can be seen that the results from having the floor condition as slip is closer to the experimental results compared with having the condition of the floor as non-slip. This is once again showing limitations in Ikeda's experiment. It is clear that in real life there is always a boundary profile existing on the ocean's surface. This means that the floor condition should be set as nonslip. However, the results from the above analysis indicate the opposite. This can only show that the wind generated by fans during Ikeda's test was not set uniformly all the way to the water surface. The results from analysis are compared with the models, and with the bottom boundary defined as slip, and are shown in Figure 92 to Figure 94.

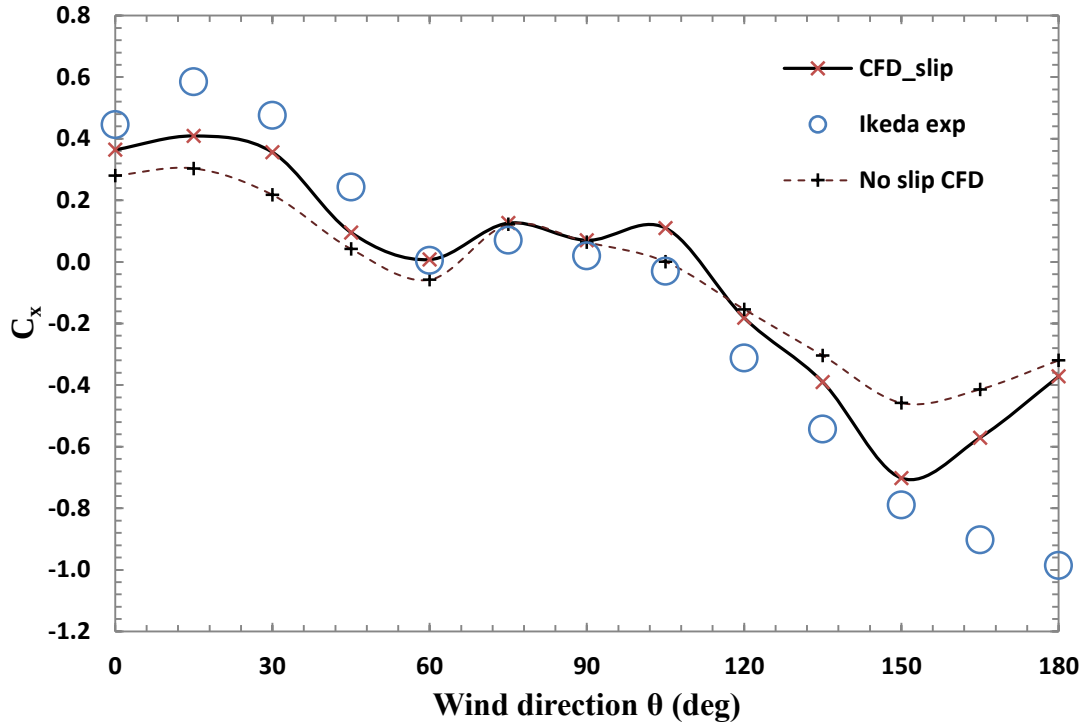

Figure 92: Comparison of force coefficient (in x direction) between slip and non-slip bottom boundaries in CFD vs Ikeda's experimental results

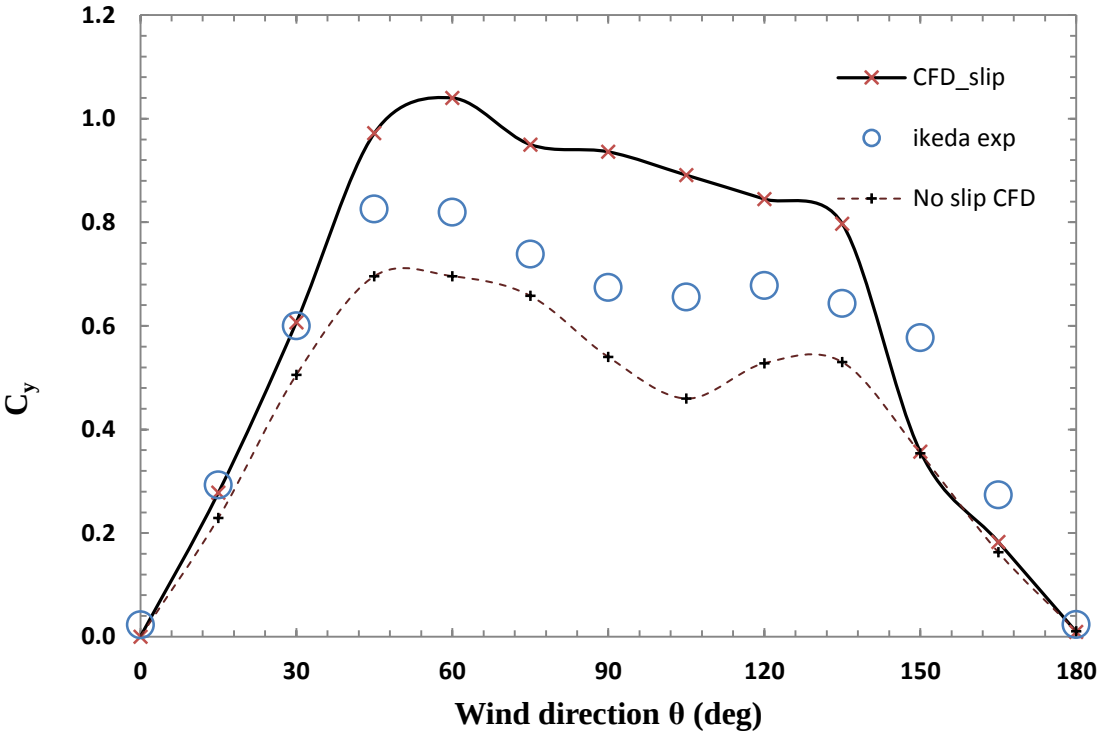

Figure 93: C_y plot. Comparison of force coefficient (in y direction) between slip and non-slip bottom boundaries in CFD vs Ikeda's experimental results

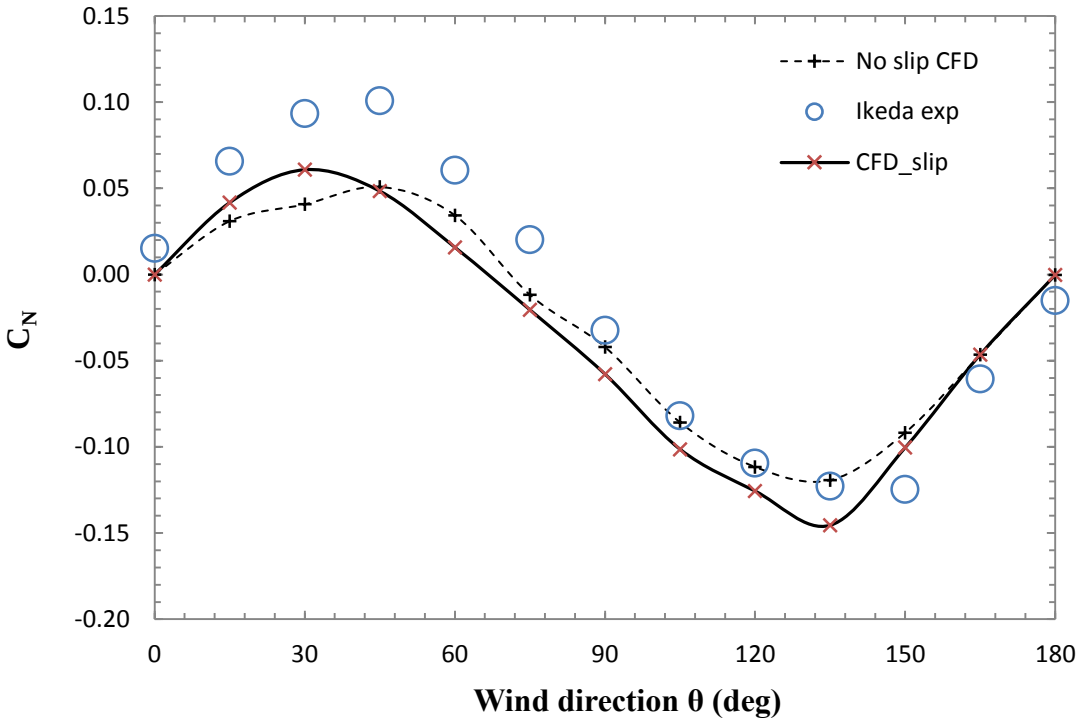

Figure 94: C_N plot. Comparison of moment coefficient results between slip and non-slip bottom boundaries in CFD vs Ikeda's experimental results

Appendix 5 Design and assembly of the wind tunnel test area

This appendix describes in detail the steps which were taken for the design of the wind tunnel assembly.

Figure 95 and Figure 96 show the new platform which is designed to stop the effect of any wind load on the underside of the rotating disc. This platform will be bolted to the side walls of the wind tunnel to create two separate regions in the test area.

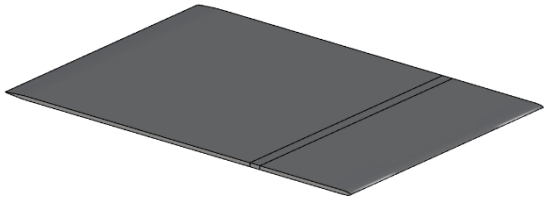

Figure 95: The platform which is designed to eliminate the wind loads on the underside of the test model. This platform will be glued to the side walls of the test section of the wind tunnel.

The rotating disc on which the ship's model is mounted should be protected in order to avoid any additional lift or drag force. This can be achieved by inserting this rotating disc inside the new platform which is shown in Figure 121.

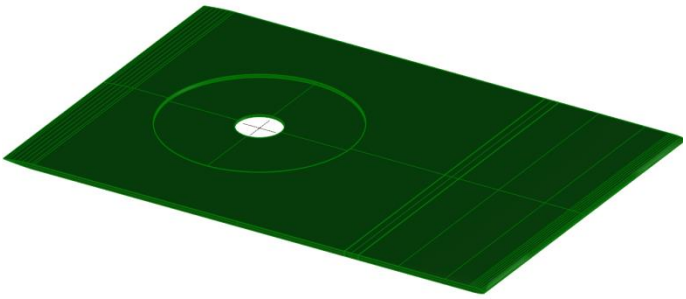

Figure 96: The platform with a machined section to accommodate the rotating disc. This will eliminate the wind load on the rotating disc.

Figure 96 shows a section of the platform which is machined out to allow the rotating disc to be fitted inside. The depth of the machined section is defined in such a way that, at the time of final assembly, the top surface of the rotating disc is level with the top surface of the platform, while the bottom surface has enough clearance from the top surface of the machined section of the platform. This clearance should be large enough to make sure that when the rotating disc translates around its y axis during the test and while it is under the wind load, the two surfaces would not come in contact. With this arrangement the platform eliminates any unwanted wind force on the test model and rotating disc.

The length of this platform is carefully calculated so that the generated boundary layer profile on the length of this platform where the ship model is mounted, has a similar shape to the natural boundary profile on the ocean. The final length of the platform also had an impact on positioning the outlet boundary for the CFD domain. These are explained in detail further in this appendix.

Design of leading and trailing edge of the platform:

The leading and trailing edge of the platform are designed in such a way as to minimise the flow separation and disturbance in the test area. The best shape for the leading edge and trailing edge of the raised platform is the shape of a NACA foil. This shape was originally designed for foils and is shown in Figure 97. The leading edge of the new platform should have a similar shape to the front part of the NACA foil. Similarly, the trailing edge of the platform should have the same shape as the trailing edge of the NACA foil.

Figure 97: The shape of NACA foil was used in the design of both the leading and trailing edges of the platform.

Design of a shell to protect the strut again the wind flow during the test:

The strut, which is connecting the rotating disc (where the model is mounted) to the load cell, is subject to the air flow during the test. This introduces errors to the results by increasing the forces on the load cell. Also, the strut has a circular cross section. This means that the strut could be subjected to vortex shedding during the test which could cause extreme vibration in the test assembly. Therefore, a protective cover was designed to eliminate any effect of the wind flow on the strut during the test. The cross section of this cover has the shape of NACA foil. This part is shown in Figure 98.

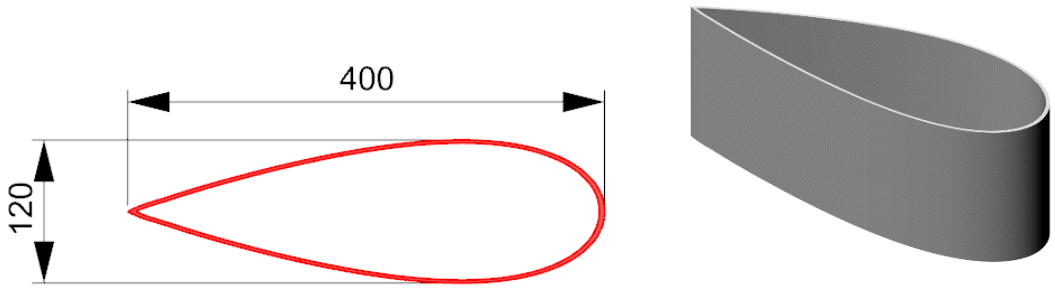

Figure 98: Design configuration of a protective cover to stop the wind load having any effect on the strut. The cross section of this cover has the shape of a NACA profile. This is to minimise the flow separation.

Wind tunnel simulation of the atmospheric boundary layer:

The next step is to find the most suitable location for the scale model in the test area. Positioning the model in place in the wind tunnel should be carefully determined.

Creating a combined wind field in any wind tunnel is very difficult. However, it is possible to perform the test in such a way that the test model is located far enough from the wind tunnel inlet that the vertical velocity profile at that location is similar to the natural atmospheric profile of the ocean.

When air flows over the ocean surface from any direction, a natural boundary layer is formed. This means that the wind velocity at the surface is zero and increases with higher altitude. The local wind field caused by the movement of the ship does not have a boundary layer and is homogenous as illustrated in Figure 99. The actual wind field encountered by the part of the ship above the water surface is thus a combination of the wind field with a boundary layer and the homogenous wind field caused by the ship's forward speed (Andersen 2012b).

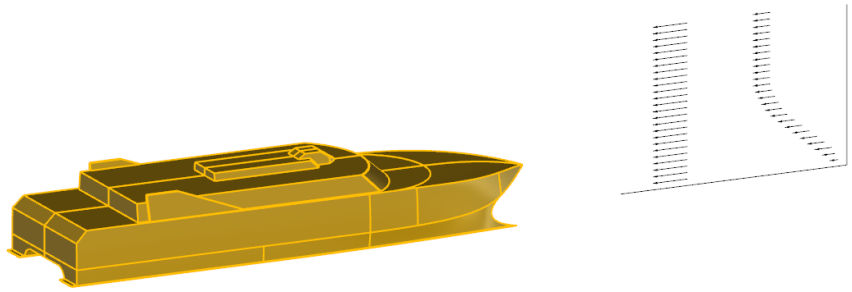

Figure 99: Local wind field caused by the ship and the natural velocity profile at sea

Identifying the best location for the scale mode:

CFD was used to find the ideal location for mounting the model in the wind tunnel. The velocity profile in the different location of the wind tunnel was measured by using line probes in the CFD domain. From the CFD results it became evident that, at 700mm downstream from the leading edge of the platform, the velocity profile has the closest trend to the natural velocity profile driven by power-law for atmospheric boundary layer on the ocean’s surface. Therefore, the midship of the scale model should be positioned at this point. This is explained in more detail below.

Generally, the wind velocity on the ocean is measured at 10m height (Larsson & Raven 2010). This height for the scale of 1/300 is about 33mm above the waterline. The following figure shows the magnitude of the velocity at different locations in the wind tunnel; this was measured by line probes. It can be seen that the velocity at 200 mm away from the midship (just before

the nose of the model ship) is dropping to 14.25 m/s, after accelerating at the leading edge of the platform which is 700mm away from the midship. Figure 100 displays the vertical velocity profile measured at different locations of the test area by using line probes.

The wind flow does speed up while it is passing the leading edge of the platform but, later as shown above, it slows down to be the same as the wind tunnel inlet speed which is 14.25 m/s. The midship of the scale model is at 0,0,0. The line probes are at 200mm, 400mm and 700 mm from the midship. Figure 100 shows that the wind speed at 200mm from the midship and at 33mm above the platform (or 10m at full scale) is 14.25m/s. This means that the model does experience the design wind speed for the analysis.

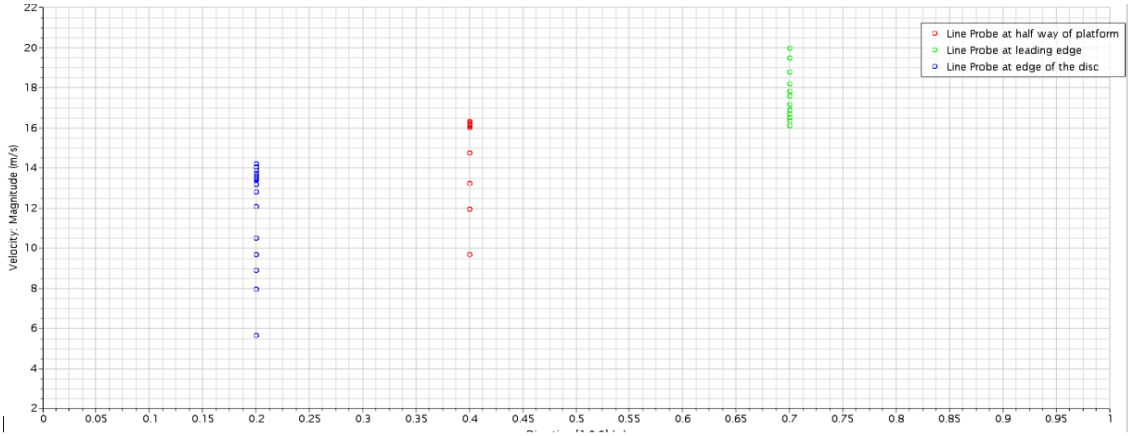

Figure 100: Vertical velocity profile at different locations of the test area. The magnitude of the wind velocity was measured by using line probes in CFD. The mid ship is at 0,0,0

Atmospheric velocity profile on ocean:

The natural velocity profile of the wind flowing across the ocean can be described as:

$$\frac{U_H}{u_{H10}} = \left(\frac{H}{H10}\right)^{\alpha} \qquad \text{(app 5. 1)}$$

where H is the height above the sea surface in metres, H_{10} is a reference height which traditionally is 10 metres. α is the exponent representing the velocity profile. For velocity profiles over the ocean, α is usually between 0.11 and 0.14, which is then the exponent which should be approximated when wind tunnel tests of ocean structures are carried out (Andersen 2012a). Figure 101, shows the velocity profile plot for different values of α. Table 19 represents the calculated data for this plot.

The power-law exponent α defines the shape of the boundary layer velocity profile. Its value in the wind tunnel must closely match the full scale value of α. Generally, the value of α depends on the roughness of the terrain. Over open ocean, α ≈ 0.1 (Lubitz & White 2004).

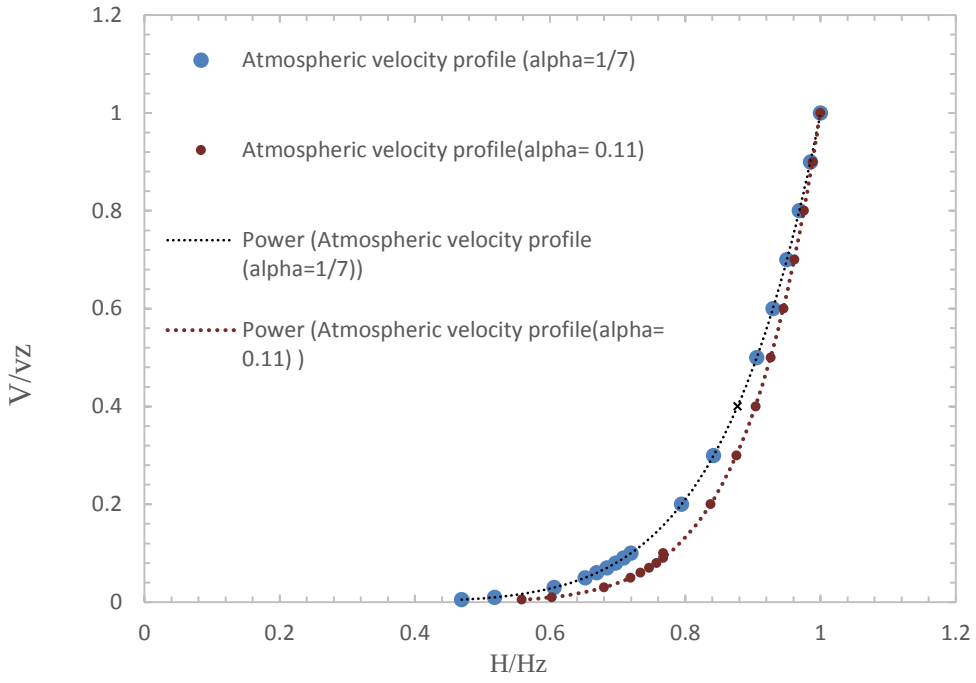

Figure 101: Velocity profile over the ocean using two different α values. Generally, the value of α over the open ocean is closer to 0.11.

alpha 1/7	alpha= 0.11	
v/vz	v/vz	z/zh
0.469117	0.558325	0.005
0.517947	0.60256	0.01
0.605963	0.67996	0.03
0.651836	0.719	0.05
0.669037	0.733832	0.06
0.683934	0.746381	0.07
0.697106	0.757425	0.08
0.708934	0.767303	0.09
0.719686	0.767303	0.1
0.794597	0.837748	0.2
0.841982	0.875958	0.3
0.877307	0.904121	0.4
0.905724	0.926588	0.5
0.929624	0.945359	0.6
0.950323	0.961525	0.7
0.968625	0.975753	0.8
0.985061	0.988477	0.9
1	1	1

Table 19: Data driven by power-law formula for the atmospheric velocity profile. Values are for alpha equal to both 0.11 and 1/7

Velocity profile on the surface of the platform:

A new CFD analysis was performed to find the most suitable location for the test model where the generated vertical velocity profile over platform is close to the natural boundary profile over the ocean. Figure 102 and Figure 103 show the location of the line probes on the top surface of the platform. Figure 104 shows the velocity profile at different locations on the platform. Table 20 shows the velocity profile data extracted from CFD line probes at different locations in the wind tunnel.

In order to compare the measured velocity profile with the atmospheric velocity profile on ocean, the measured data from CFD being non-dimensionalised. Figure 105 shows plots of the non-dimensionalised velocity profile on the platform at different distances from the leading edge (These results are extracted from CFD analysis). These profiles are compared with the desired atmospheric boundary layer plot (driven from the power-law equation with α equal to 0.11). This showed that the best location for positioning the test model in the wind tunnel is at about 700 mm from the leading edge of the platform. The midship of the model will be located at this point.

Figure 102: The distance of the line probes at different distances from the leading edge of the platform. The tunnel is empty.

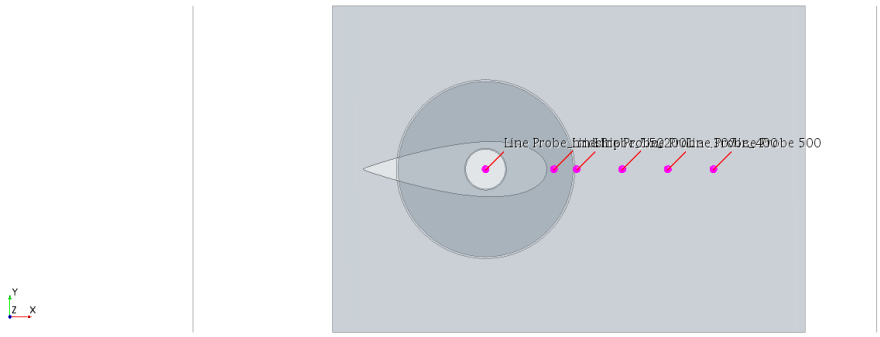

Figure 103: Location of line probes. These lines are used to investigate the velocity profile at different distances from the leading edge of the platform. (plan view)

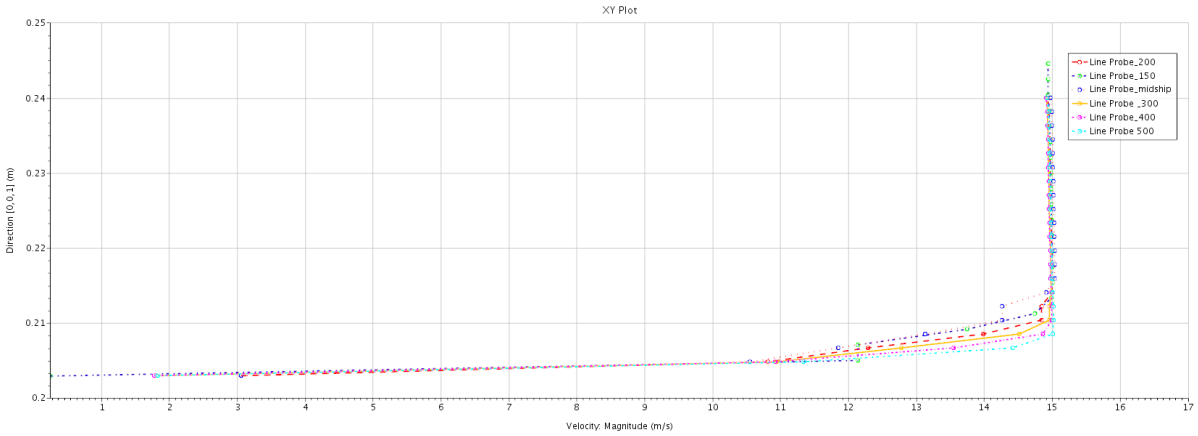

Figure 104: Velocity profile at different locations of the wind tunnel using line probe in CFD

Line Probe_midship: Velocity: Magnitude (m/s)	Line Probe_midship: Direction [0,0,1] (m)	Line Probe_200: Velocity: Magnitude (m/s)	Line Probe_200: Direction [0,0,1] (m)	Line Probe_400: Velocity: Magnitude (m/s)	Line Probe_400: Direction [0,0,1] (m)
3.047867413	0.203	3.045053648	0.203	1.766896249	0.203
9.72088936	0.204	9.941849205	0.204	9.886055006	0.204
10.53936611	0.205	12.28012357	0.205	13.54077946	0.205
11.83932904	0.206	12.28012357	0.206	13.54077946	0.206
11.83932904	0.207	12.28012357	0.207	13.54077946	0.207
13.12177708	0.208	13.97885123	0.208	14.85375226	0.208
13.12177708	0.209	13.97885123	0.209	14.85375226	0.209
13.12177708	0.210	14.83475128	0.21	14.98610739	0.21
14.256444	0.211	14.83475128	0.211	14.98610739	0.211
14.256444	0.212	14.83475128	0.212	14.98610739	0.212
14.9076352	0.213	14.98810523	0.213	14.98169893	0.213
14.9076352	0.214	14.98810523	0.214	14.98169893	0.214
14.9076352	0.215	14.99261999	0.215	14.96659831	0.215
15.02693197	0.216	14.99261999	0.216	14.96668039	0.216
15.02693197	0.217	14.99261999	0.217	14.96668039	0.217
15.02693197	0.218	14.99284512	0.218	14.96668039	0.218
15.02693197	0.219	14.99284512	0.219	14.96668039	0.219
15.02693197	0.220	14.98229407	0.22	14.95285586	0.22
15.01908986	0.221	14.98229407	0.221	14.95285586	0.221
15.01908986	0.222	14.98229407	0.222	14.95285586	0.222
15.01908986	0.223	14.98229407	0.223	14.95285586	0.223
15.01908986	0.224	14.98229407	0.224	14.95285586	0.224
15.00823658	0.225	14.9706223	0.225	14.9428091	0.225
15.00823658	0.226	14.9706223	0.226	14.9428091	0.226
15.00823658	0.227	14.9706223	0.227	14.9428091	0.227
15.00823658	0.228	14.9706223	0.228	14.9428091	0.228
15.00823658	0.229	14.9706223	0.229	14.9428091	0.229
14.99799992	0.230	14.9706223	0.23	14.9428091	0.23
14.99799992	0.231	14.95945447	0.231	14.93281042	0.231
14.99799992	0.232	14.95945447	0.232	14.93281042	0.232
14.99799992	0.233	14.95945447	0.233	14.93281042	0.233
14.99799992	0.234	14.95945447	0.234	14.93281042	0.234
14.98639275	0.235	14.94666619	0.235	14.92058612	0.235
14.98639275	0.236	14.94666619	0.236	14.92058612	0.236

Table 20: Value of the velocity profile at different locations of the wind tunnel. The top surface of the platform is 203 mmm above the origin. Each line probe has a height of 33mm.

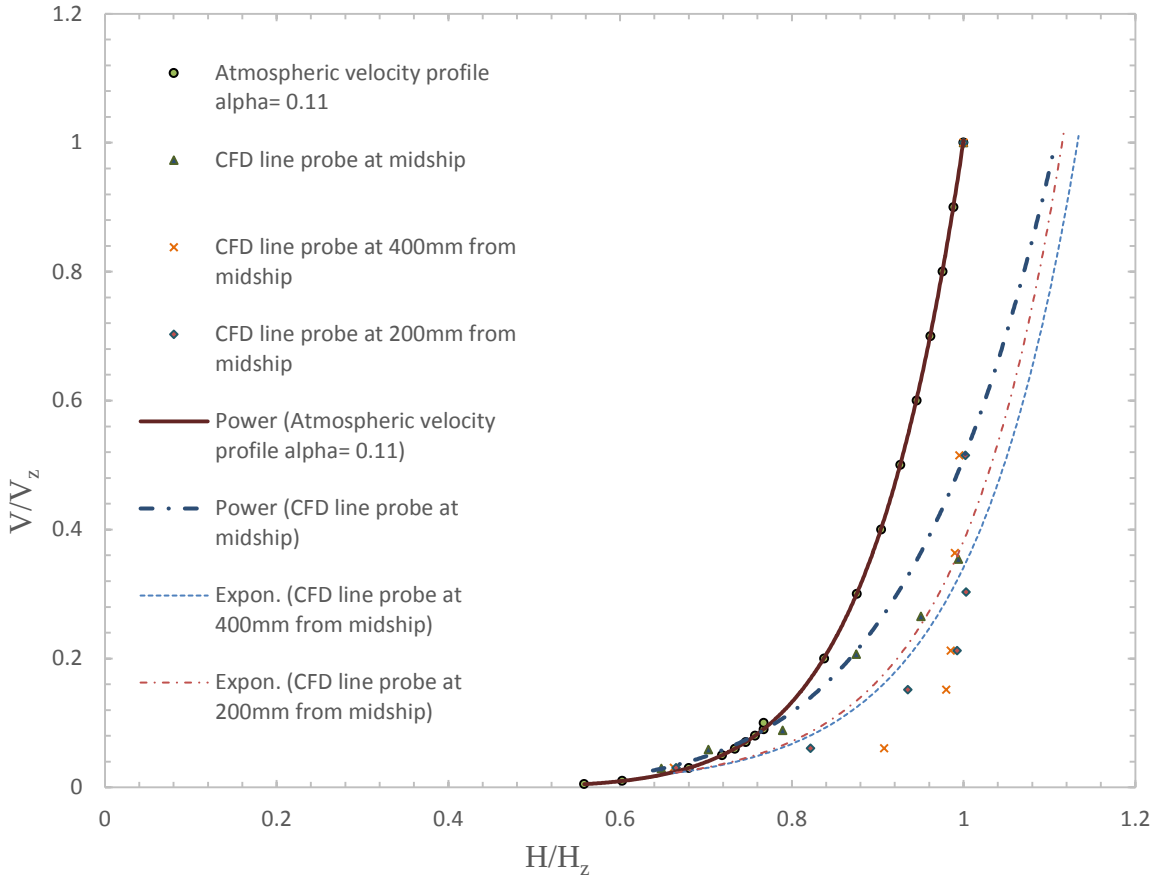

Figure 105: Velocity profiles measured by line probes in CFD at different locations on the platform inside the wind tunnel vs the atmospheric velocity profile on the ocean. The closest shape is from the line probe which is at 700mm from the leading edge of the platform; this is called midship.

Wind tunnel experiment results:

A similar approach was undertaken in the wind tunnel and the velocity profile at different locations of the platform surface was measured. Table 21 shows the measured data in the wind tunnel. The measured velocity profile at 700mm from the leading edge of the platform, both from CFD and the experiment is non-dimensionalised and compared with the measured profile from CFD and the atmospheric profile. This is shown in Figure 106.

results from wind tunnel experiment

velocity at midship		
	velocity (m/sec)	height (mm)
ho	8.309	0
h1	9.904	1
h2	10.718	2
h3	11.395	3
h4	11.951	4
h5	12.387	5
h6	12.836	6
h7	13.184	7
h8	13.525	8
h9	13.804	9
h10	14.023	10
h11	14.146	11
h12	14.215	12
h13	14.273	13
h14	14.291	14

velocity at 200 mm from midship		
	velocity (m/sec)	height (mm)
ho	4.561	0
h1	8.473	1
h2	12.447	2
h3	13.919	3
h4	14.169	4
h5	14.261	5
h6	14.273	6
h7	14.292	7
free flow	14.31	8
free flow	14.31	14
free flow	14.31	14

velocity at 400 mm from midship		
	velocity (m/sec)	height (mm)
ho	4.369	0
h1	7.832	1
h2	12.691	2
h3	14.151	3
h4	14.302	4
h5	14.296	5
h6	14.314	6
free flow	14.294	7
free flow	14.294	14
free flow	14.294	14

velocity at 700 mm from midship		
	velocity (m/sec)	height (mm)
ho	10.106	0
h1	14.184	1
h2	14.306	2
h3	14.304	3
h4	14.304	4
free flow	14.304	7
free flow	14.304	14
free flow	14.304	14

Table 21: Measured velocity profile in wind tunnel by using pitot tube at different part of the platform

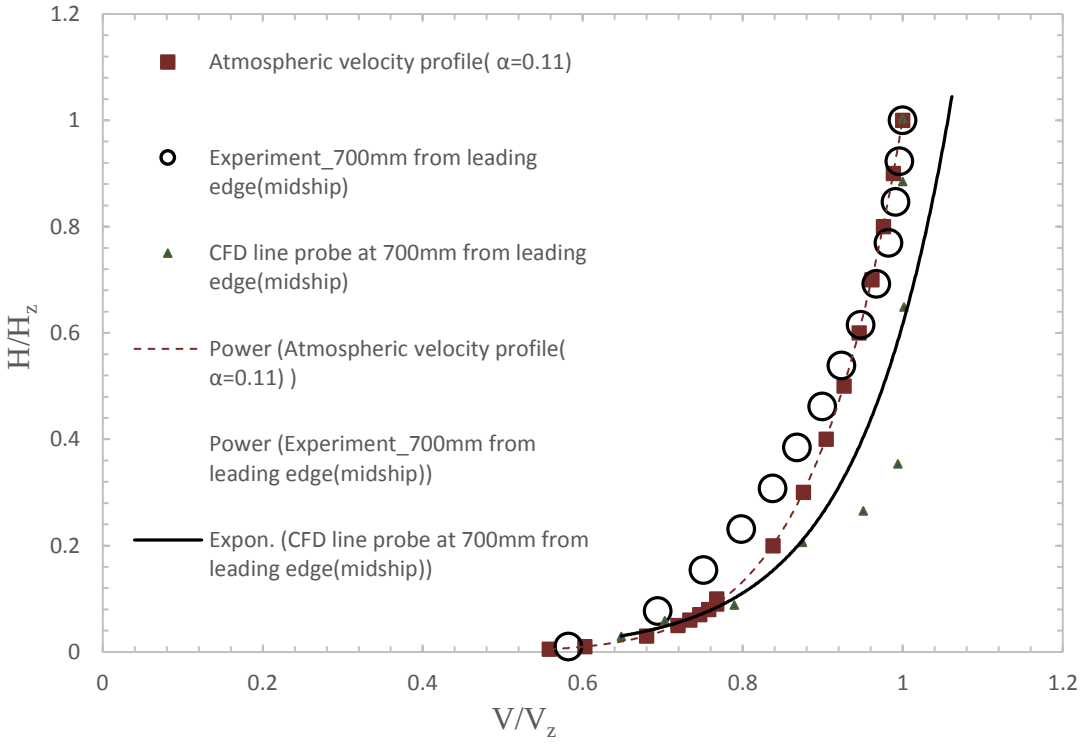

Figure 106: Velocity profile plot at 700 mm from the leading edge, from both the CFD and the experiment vs the natural atmospheric profile with values of alpha at 0.11

Due to the limitation in length of the UTAS wind tunnel, this point cannot be pushed any further towards the outlet boundary. Otherwise the model and rotating disc will be pushed outside of the test area. The results from both CFD analysis and the wind tunnel experiment confirm that the model should be located at a distance of 700 mm from the leading edge of the raised platform.

Appendix 6 Comparison of results (Wind tunnel vs CFD)

The non-dimensional measured forces and moment coefficients in the wind tunnel experiment (acting on both scaled model and rotating disc as is shown in figure 107) are compared with the results from CFD analysis and are shown in Table 22.

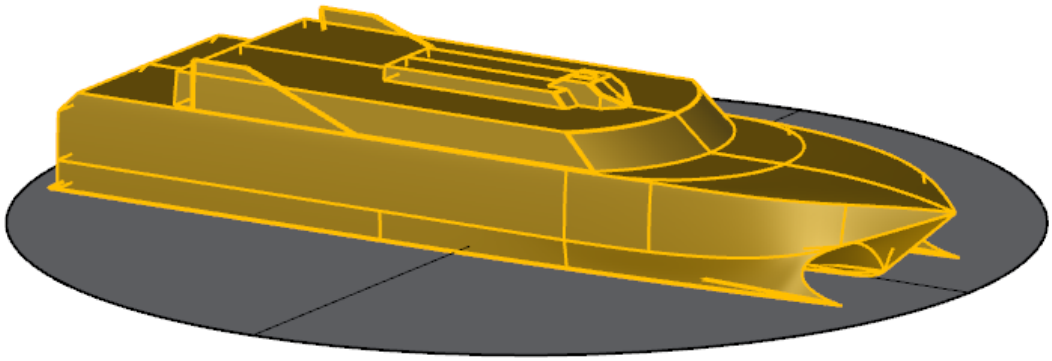

Figure 107: Measured forces and moment acting on both the model and the rotating disc in wind tunnel

	wind tunnel experiment results					CFD results on 1/300 scale model		
wind angle	f x (wt_exp)	f y (wt_exp)	mz (wt_exp)		wind angle	Fx_cfd (1/300)	Fy_cfd (1/300)	Mz_cfd (1/300)
0	0.350	0.011	0.006		0	0.377	-0.001	0.000
15	0.361	0.584	0.041		15	0.393	0.630	0.033
30	0.335	1.324	0.056		30	0.336	1.350	0.049
45	0.147	1.847	0.056		45	0.136	2.031	0.055
60	0.013	2.119	0.042		60	0.011	2.107	0.037
75	0.033	2.075	0.002		75	0.114	2.003	-0.007
90	0.059	2.007	-0.040		90	0.109	1.930	-0.039
105	-0.085	1.888	-0.086		105	-0.014	1.804	-0.070
120	-0.328	1.640	-0.106		120	-0.246	1.642	-0.095
135	-0.481	1.340	-0.110		135	-0.411	1.411	-0.100
150	-0.574	0.888	-0.096		150	-0.537	0.948	-0.084
165	-0.550	0.349	-0.049		165	-0.483	0.435	-0.040
180	-0.430	-0.114	0.001		180	-0.384	0.001	0.000

Table 22: Measured forces and moment in wind tunnel vs results from CFD analysis on 1/300 scale model of the 112 m catamaran

The non-dimensional measured forces and moment coefficients in the wind tunnel experiment (acting on scaled model only as is shown in figure 108) extracted from CFD analysis and are shown in Table 22. These values can be used in station keeping analysis of the 112m high speed wave piercing catamaran.

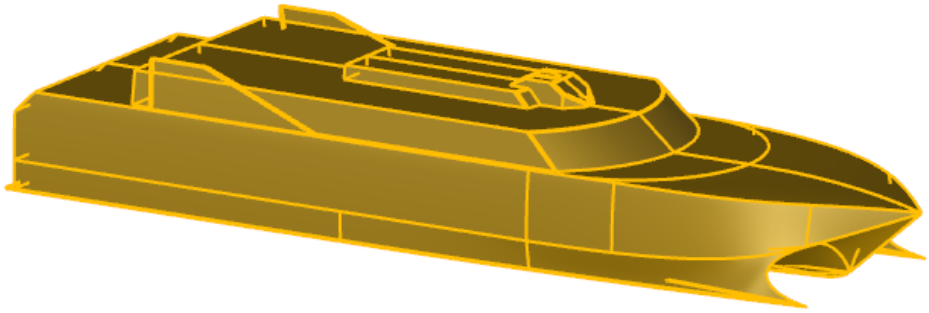

Figure 108: Measured forces and moment (extracted from CFD analysis) acting on the model only in wind tunnel

	results from CFD 1/300 scale		
θ(deg.)	C_x	C_y	C_N
0	0.438	0.000	0.000
15	0.476	0.311	0.047
30	0.407	0.669	0.070
45	0.079	1.006	0.077
60	-0.104	1.024	0.050
75	0.099	0.923	-0.011
90	0.136	0.881	-0.059
105	0.021	0.826	-0.105
120	-0.286	0.774	-0.141
135	-0.534	0.682	-0.146
150	-0.750	0.457	-0.123
165	-0.667	0.206	-0.059
180	-0.500	0.000	0.000

Table 23: Non-dimensional force and moment coefficients on scale model only. These results can be used for station keeping analysis of the 112m high speed catamaran.

Appendix 7 Location of the outlet boundary

The length of the glassed section of the wind tunnel test area is 1200 mm long. The side walls of this test area are fixed and will be modelled in the CFD domain exactly where they are. This is because, for calculation of the flow blockage, the actual size of the wind tunnel cross section should be used. The location of the inlet boundary is also set at the start of the glassed section of the test area. This is where the air enters the domain as a uniform flow at the desired velocity. However, the location of the outlet boundary does not necessarily need to be set at the end of the wind tunnel's glassed section. The end of the glassed section of the test area coincides with the end of the trailing edge of the platform.

When the wind flow hit the scale model, air flow separates at the model edges, generating recirculation zones over downwind surfaces (roof, side and downwind walls) and extends into the downwind wake. The size and intensity of the recirculation zone depends on the wind angle of attack and ship's heading. The velocity profile in recirculation zone does constantly changes in the flow direction while is constantly expanding. This significantly affects the recirculation vortex and subsequently the re-attachment length. At the trailing edge the flow from below the platform adds to the intensity of the flow in this region. Therefore, for CFD analysis, the outlet boundary should not be set at this location as the flow in this region is still developing. The other reason for not setting the outlet boundary in this location is due to the existence of the reverse flow where the wind flow re-enters the domain and cause progressive instability of the numerical procedure to the extent of resulting in a wrong solution.

The outlet boundary initially was set at 200mm aft of the trailing edge. However, it is necessary to demonstrate that the results from the analysis are unaffected by the location of the outlet location. This can be done by carrying out a sensitivity analysis of the effects of different downstream distances from the flow development region after passing the model ship.

To find out if the location of the outlet boundary has any effect on the final results, the location of the outlet boundary was moved to 600mm aft of the platform's trailing edge and the analysis was repeated as shown in Figure 109. The results are compared with the CFD results when the outlet boundary was set at 200 away from the trailing edge of the platform and they are shown in Table 24. As is shown, the results are very close. When the wind passes, the model forms a recirculation zone. This zone gets larger as the test model rotates and approaches 90 degrees heading. However, this recirculation zone soon disappears when it reaches the trailing edge of the platform, due to the interference of the flow which is running below the platform surface and mixing with the flow which runs on the top of the platform. This eliminates the effect of the shear drag on final results downstream of this point.

Figure 110 is displaying the scalar plot of the wind velocity for the model which is at 90° heading into the wind. Figure 111 is the vector plot of the wind velocity which shows how the flow from the underside of the platform reduces the length of the recirculating zone behind the model at the trailing edge of the platform. Therefore, it can be concluded that having a smaller

domain, in which the outlet boundary is set at 200mm from the trailing edge of the platform, is sufficient. This should save a lot of computational time and expense because of fewer cells being in the domain.

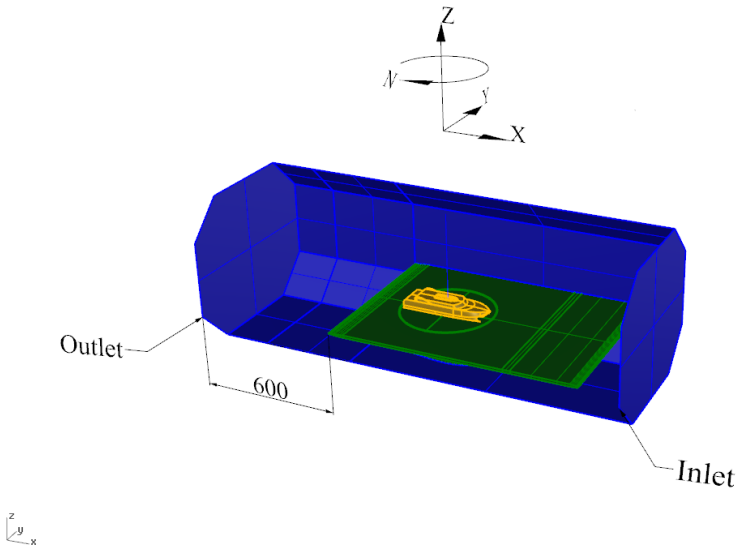

Figure 109: The CFD domain when the outlet boundary moved to 600mm aft of the trailing edge of the platform

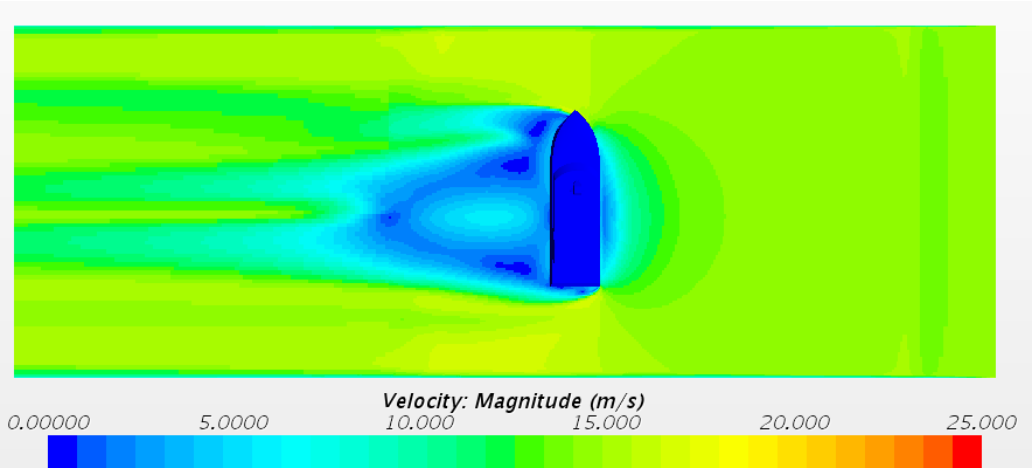

Figure 110: Scalar plot of the wind velocity

		Longer domain		Shorter domain
Fx		-0.098		-0.109
Fy		1.86		1.93
Mz		-0.038		-0.038
X coef		0.132		0.135
Y coef		0.877		0.881
M coef		-0.058		-0.058

Table 24: Comparison between the results from the CFD analysis with the domain outlet set at 200 and 600 mm aft of the trailing edge of the platform. The results are showing that moving the outlet further away from the test model has minimal effect on results.

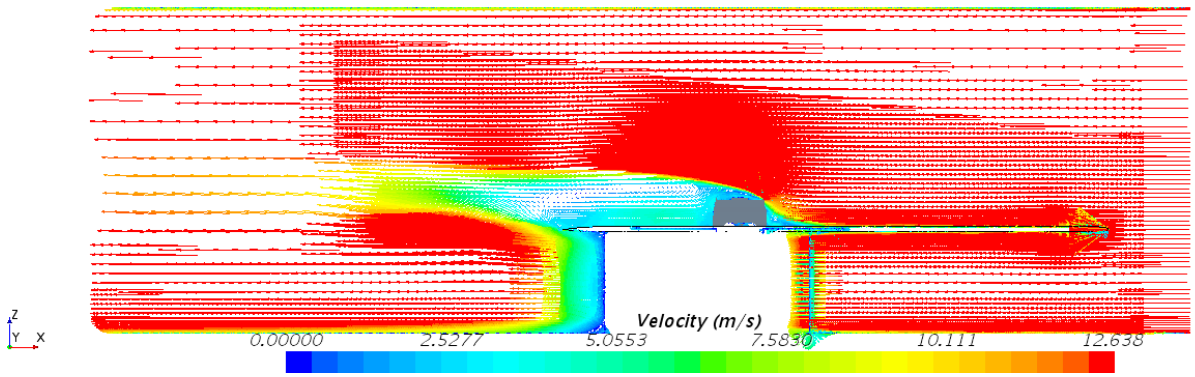

Figure 111: Vector plot of the wind velocity. It is showing how the flow from below the platform disturbs the recirculation zone which is generated behind the ship.

Appendix 8 Comparison of the results (1/300 and 1/80 CFD vs the 1/80 scale Ikeda and Ours experiment)

Comparison between the initial CFD analysis on Ikeda's experimental test on the 1/80 scale model and results from CFD analysis on the 1/300 scale model can only be made if both have the same flow characteristics and boundary conditions. The original CFD analysis was first performed in a domain with the floor condition defined as slip. Defining the condition of a surface does not allow any boundary layer to be formed on that surface. However, the floor condition in CFD simulation of the 1/300 scale model was non-slip.

Also, the distance of the inlet boundary to the model in the next set of analyses on the 1/80 scale model, when the floor of the domain was defined as non-slip, was much greater than that which was set in the CFD analysis of the 1/300 scale model. This means that the 1/80 scale model was experiencing a completely different flow field from that of the1/300 scale model due to the formation of a larger boundary layer. This means that the boundary conditions between the 1/300 CFD model and the 1/80 scale model are different and, therefore, direct comparison between their results cannot be made.

Table 25 shows data from Ikeda and Oura's experiment and CFD analysis on the 1/300 and 1/80 scale models. The CFD 1/80 scale model has the floor as slip and Table 26 shows the results of the CFD (1/80 scale model) with the floor condition as non-slip. As a point of interest, the results are plotted against each other and are shown in Figure 112 to Figure 114. It is shown that there is better agreement of the CFD analysis between the 1/80 and 1/300 scale models when the floor of the domain is defined as slip. Regardless, all results are different from the results of Ikeda and Oura.

	(floor cocndition_no-slip)										
		results from CFD			Ikeda results				results from CFD		
		1/300 scale			1/80 scale				1/80 scale	(floor cocndition_slip)	
	C_x	C_y	C_N		Cxwin	Cywin	Cmwin		Cx	Cy	Cn
0	0.438	0.000	0.000	0	**0.446**	**0.023**	**0.015**	0	0.364	0.000	0.000
15	0.476	0.311	0.047	15	**0.585**	**0.293**	**0.066**	15	0.410	0.236	0.042
30	0.407	0.669	0.070	30	**0.475**	**0.600**	**0.093**	30	0.356	0.607	0.061
45	0.079	1.006	0.077	45	**0.243**	**0.826**	**0.101**	45	0.077	1.009	0.048
60	-0.104	1.024	0.050	60	**0.005**	**0.820**	**0.060**	60	0.008	1.040	0.016
75	0.099	0.923	-0.011	75	**0.070**	**0.738**	**0.020**	75	0.126	0.951	-0.020
90	0.136	0.881	-0.059	90	**0.020**	**0.674**	**-0.032**	90	0.070	0.936	-0.058
105	0.021	0.826	-0.105	105	**-0.030**	**0.656**	**-0.082**	105	0.110	0.891	-0.101
120	-0.286	0.774	-0.141	120	**-0.312**	**0.678**	**-0.109**	120	-0.181	0.845	-0.126
135	-0.534	0.682	-0.146	135	**-0.543**	**0.643**	**-0.123**	135	-0.390	0.801	-0.159
150	-0.750	0.457	-0.123	150	**-0.789**	**0.577**	**-0.125**	150	-0.703	0.357	-0.100
165	-0.663	0.206	-0.058	165	**-0.902**	**0.274**	**-0.061**	165	-0.571	0.184	-0.046
180	-0.500	0.000	0.000	180	**-0.986**	**0.023**	**-0.015**	180	-0.372	0.009	0.000

Table 25: Force and moment coefficients data from the CFD analysis on the 1/80 and 1/300 scale models of the 112m catamaran at different wind angle attacks. Results from Ikeda's experiment are also shown.

	results from CFD		
	1/80 scale (floor cocndition_no-slip)		
	cx	cy	cn
0	0.280	0.000	0.000
15	0.304	0.229	0.031
30	0.218	0.506	0.041
45	0.042	0.696	0.051
60	-0.058	0.696	0.034
75	0.122	0.658	-0.012
90	0.064	0.540	-0.042
105	0.000	0.460	-0.086
120	-0.154	0.528	-0.112
135	-0.304	0.530	-0.119
150	-0.458	0.354	-0.092
165	-0.414	0.163	-0.047
180	-0.320	0.010	0.000

Table 26: Force and moment coefficients data from CFD analysis on the 1/80 scale model with the floor of the domain defined as non-slip

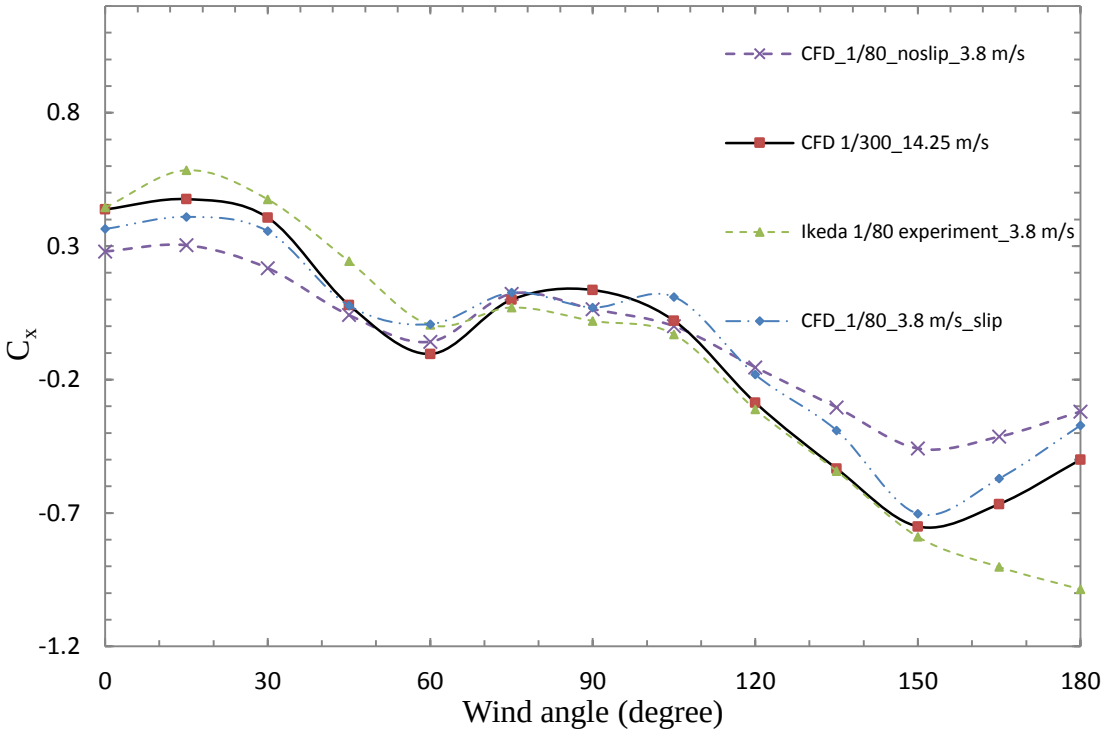

Figure 112: Comparison between CFD and Ikeda's experimental results on the 1/80 scale model vs results from CFD analysis on the 1/300 model. (Cx)

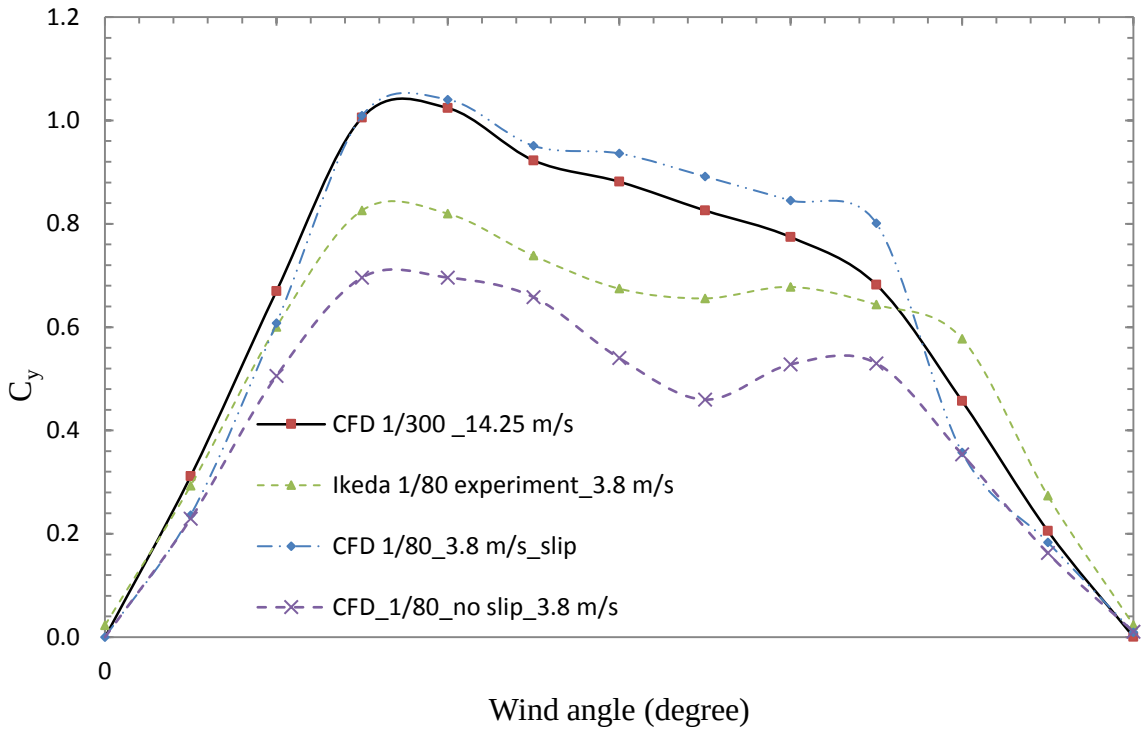

Figure 113: Comparison between CFD and Ikeda's experimental results on 1/80 scale model vs results from CFD analysis on 1/300 model (Cy)

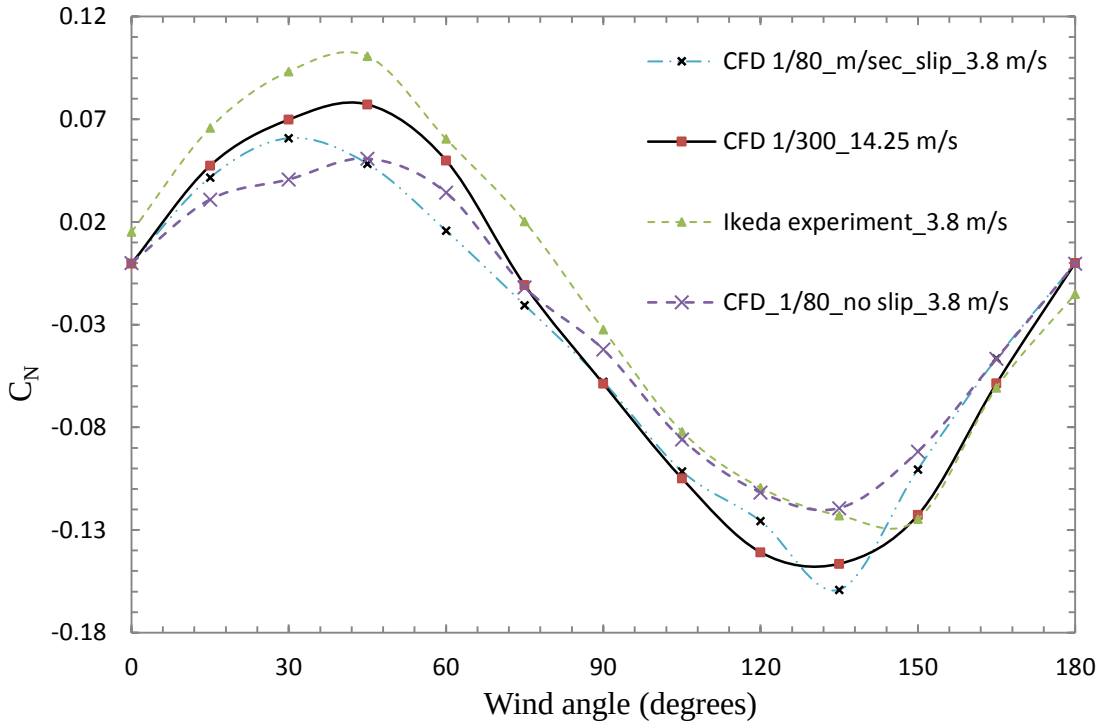

Figure 114: Comparison between CFD and Ikeda's experimental results on 1/80 scale model vs results from CFD analysis on 1/300 model. (C_N)

Appendix 9 Detailed drawings for the assembly of the wind tunnel

Figure 115 to Figure 121 are presenting all detailed drawings which were submitted to the UTAS laboratory for production and assembly of the wind tunnel test area.

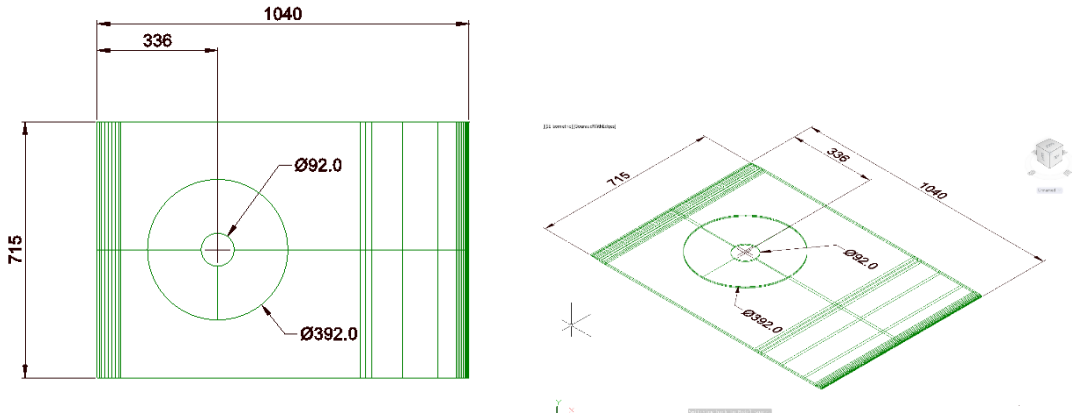

Figure 115: Detailed drawings of the platform. Top left (plan view). Top right (isometric view)

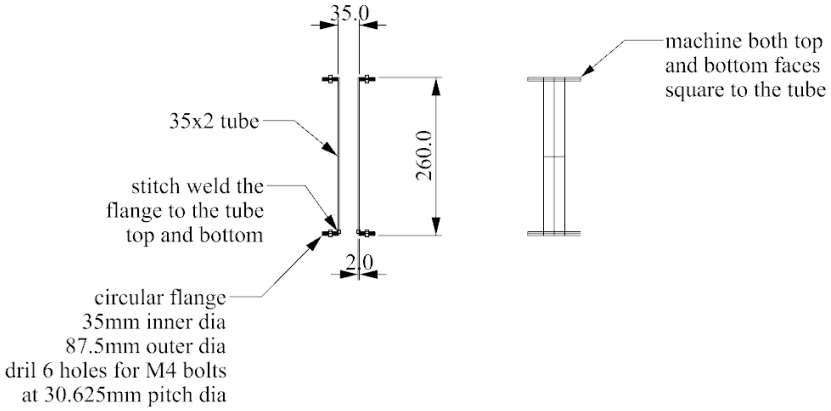

Figure 116: Strut detail drawing

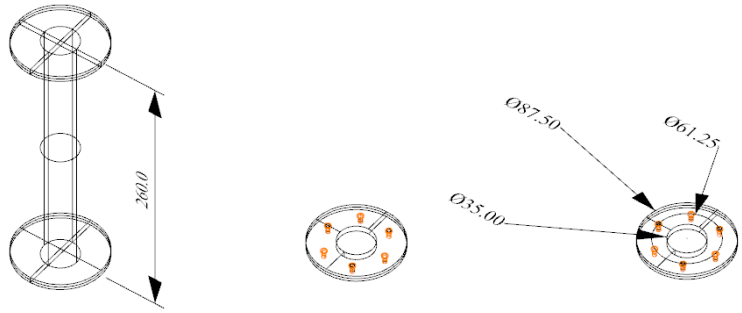

Figure 117: Isometric view of the strut assembly with flange attachment

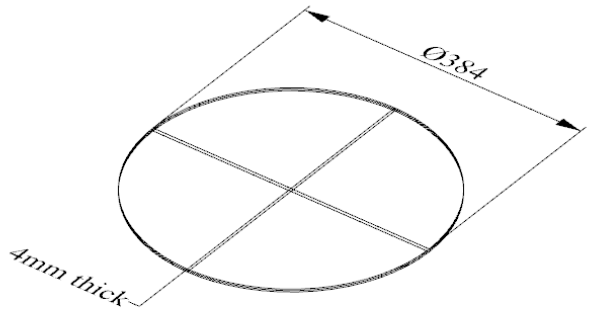

Figure 118: Rotating disc details

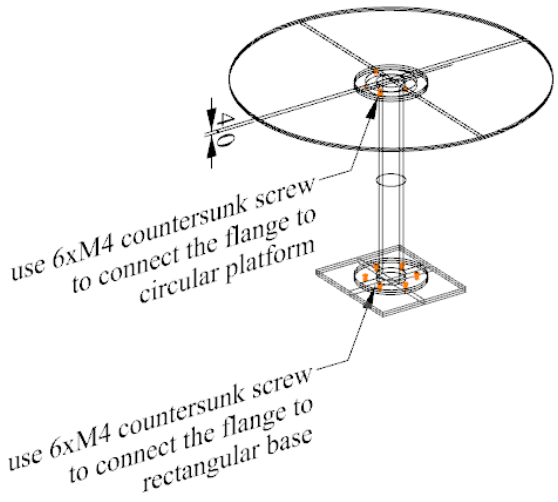

Figure 119: Rotating disc and strut assembly

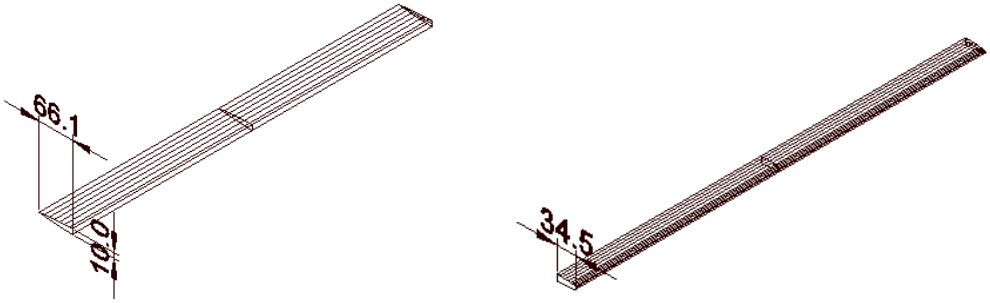

Figure 120: Detail of leading and trailing edges of the platform

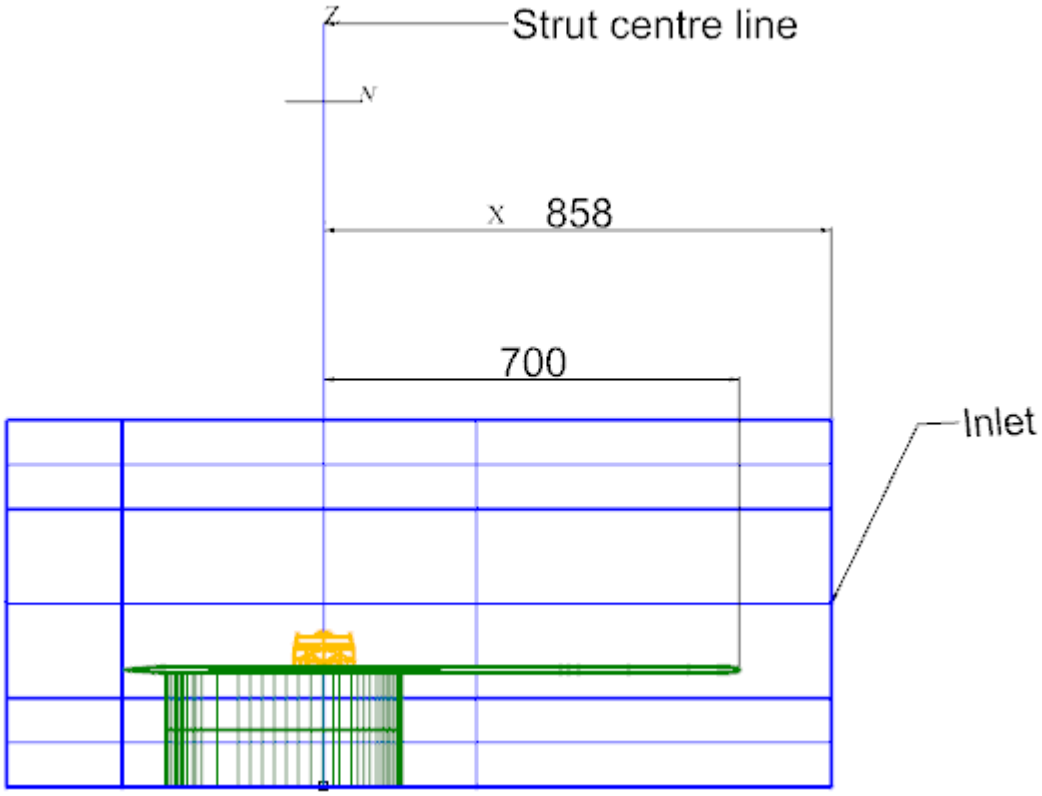

Figure 121: Final assembly of the wind tunnel test area

Appendix 10 Boundary layer thickness at midship (experiment)

Table 27 shows the measurements which were taken by Pitot tube to measure the total boundary layer thickness at the midship of the scale model. These measurements were taken in an empty tunnel (without the presence of the scale model).

	experimental data					wind tunnel results					
This was the very first boundary layer traverse, midship.											
Pressure [	Temperat	Pitot Pres	Air Densit	Height (m	Air Veloci	Fx [N]	Mx [N•mr	Fy [N]	My [N•mr	Fz [N]	Mz [N•mm]
985.799	22.319	39.883	1.156	0.25	8.309	-0.907	-39.908	-0.175	-82.304	0.879	-8.986
985.683	22.337	56.658	1.155	1.25	9.904	-0.656	-37.229	0.043	-67.388	1.312	-1.181
986.077	22.305	66.387	1.156	2.25	10.718	-0.687	-38.045	0.047	-69.022	1.305	-1.044
987.311	22.301	75.136	1.157	3.25	11.395	-0.722	-39.187	0.064	-72.115	1.312	-1.051
986.965	22.19	82.659	1.157	4.25	11.951	-0.689	-36.234	0.052	-70.397	1.322	0.274
986.344	22.276	88.722	1.156	5.25	12.387	-0.707	-37.852	0.061	-71.781	1.323	0.835
986.516	22.258	95.294	1.157	6.25	12.836	-0.73	-38.229	0.057	-72.963	1.325	0.232
986.507	22.269	100.531	1.157	7.25	13.184	-0.739	-38.976	0.067	-73.535	1.325	0.545
986.353	22.249	105.799	1.157	8.25	13.525	-0.734	-37.668	0.096	-73.447	1.327	0.564
986.464	22.226	110.233	1.157	9.25	13.804	-0.746	-38.657	0.082	-74.034	1.333	0.246
986.361	22.245	113.74	1.157	10.25	14.023	-0.745	-39.133	0.087	-73.948	1.324	-0.059
986.34	22.169	115.784	1.157	11.25	14.146	-0.737	-37.766	0.099	-73.734	1.329	-0.009
986.096	22.181	116.886	1.157	12.25	14.215	-0.71	-37.025	0.082	-72.161	1.317	0.56
985.904	22.171	117.823	1.157	13.25	14.273	-0.686	-36.499	0.085	-70.53	1.322	1.892
985.89	22.127	118.149	1.157	14.25	14.291	-0.696	-43.515	0.043	-73.568	1.239	0.998
986.004	22.082	118.643	1.157	15.25	14.319	-0.708	-43.675	0.05	-73.341	1.256	-0.126
985.579	21.957	118.322	1.157	16.25	14.299	-0.699	-40.748	0.066	-72.496	1.25	0.196

Table 27: Data measurement taken by pitot tube to measure the boundary layer thickness developed on the platform during the test. (The above data was taken in an empty tunnel.)

Appendix 11 Calibration of the load cell

An email (Calvary Gerard, personal communication, 25th January 2018) detailing the method used for calibration of the load cell and is described here.

A nylon fishing line was fixed at a known height above the datum (taken as the top side of the lower load cell plate). A magnetic base and post were used to attach the fishing line. The fishing line was aligned with principal axes to ensure the correct application of the load (level and parallel to a principal axis). The other end of the fishing line was fixed around a ball bearing pulley and had a weight carrier attached. Data acquisition was commenced, zero the six load cell outputs, and observed for stability. The zero point was recorded onto an XY chart in LabVIEW. 200 grams incremental loads were applied from zero to 1kg. After each increment, stability was monitored. Each point was recorded onto the XY chart. LabVIEW was stopped and the XY chart observed for linearity. If linear, the data should be exported to Excel. If not, it was investigated and re-done. The fishing line was reattached to a higher point on the magnetic base post. The above loading and recording steps were repeated, and the data exported into Excel. And then another step was undertaken at a higher point.

The six output signals each have two components: one due to the load parallel to the axis (this should be the same magnitude for each test height) and one due to the bending moment around the base plate. The last component should increase linearly as test height increases. Therefore, subtracting one set of test results from another set taken at a different height will eliminate the common component (principal axis load component) and the difference will be due to a change of the bending moment around the base. This component will be proportional to the height difference between the two tests, and will be so for each height and weight increment.

This method enables the finding of each load cell's output for the bending moment around the base plate and around each axis. Four different heights were used and the spreadsheet demonstrates consistent values (mV/N•mm) for each load cell and axis. Then back calculation, subtracting the bending component of load cell output from each set of test results (according to test height) will expose the constant component of the outputs, in each set of results, due to the principal axis load components. This too is demonstrated accurately in the spreadsheet.

Next, the output of each of the six load cells for axial and bending loads around each axis (mV/N & mV/N•mm) was achieved. From here the equations to calculate a 6x6 matrix to convert from mV to N &N.mm could be written. Thus, the LabVIEW measures six voltages and outputs principal loads and bending moments directly, referring to the top side of the load cell base plate. To demonstrate the calibration linearity, some screenshots of the LabVIEW during a calibration were taken. Those shots are showing how it can be seen, in real time, whether a calibration is going well (or not!). The final results were ready to be exported to Excel.

Figure 122 is one of the screen shots during the calibration process:

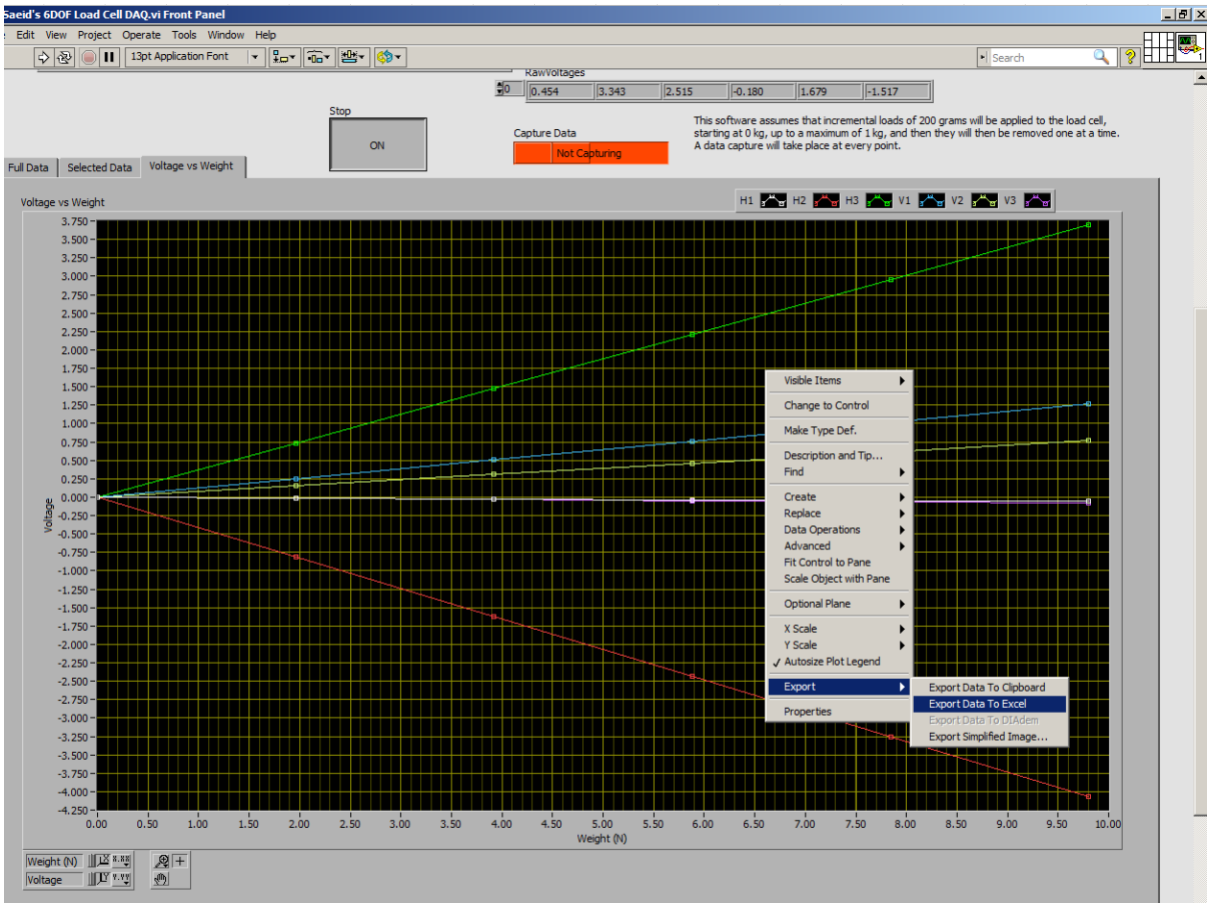

Figure 122: Load cell (design and calibration)

Appendix 12 Wind tunnel test results

Table 28 displays the results from the wind tunnel experiment while the wind velocity was set at 14.25 m/s. The load cell measures forces and moments which are acting on both the scale model and the rotating disc. Next, the experiment was repeated but this time the wind velocity was set at 28.5 m/s. The results of this section are shown in the Table 29. Figure 123 to Figure 125 compare the forces and moments measured in the wind tunnel experiment with that which was measured in CFD while the wind velocity was set at 28.5 m/s. Figure 126 to Figure 128 are comparing the force and moment coefficients between the wind velocity of 28.5 m/s and 14.25 m/s.

Test at 14.25 m/s (while rotating the model from zero to 180°):

This file was originall	Saeid's Test Data (Wed 14 Mar 2018_11_10_48 AM).csv											
0												
Time [s]	Relative H	Pressure [	Temperat	Pitot Pres	Air Densit	Air Veloci	Fx [N]	Mx [N•mr	Fy [N]	My [N•mr	Fz [N]	Mz [N•mm]
11:12:17 AM	49.802	1013.672	21.549	121.069	1.193	14.249	0.011	189.011	0.3	1.33	3.418	-5.593
15												
Time [s]	Relative H	Pressure [	Temperat	Pitot Pres	Air Densit	Air Veloci	Fx [N]	Mx [N•mr	Fy [N]	My [N•mr	Fz [N]	Mz [N•mm]
11:20:13 AM	49.718	1013.536	21.576	119.871	1.192	14.18	0.584	180.866	0.361	200.046	3.615	-40.551
30												
Time [s]	Relative H	Pressure [	Temperat	Pitot Pres	Air Densit	Air Veloci	Fx [N]	Mx [N•mr	Fy [N]	My [N•mr	Fz [N]	Mz [N•mm]
11:24:29 AM	49.823	1013.401	21.603	121.863	1.192	14.299	1.324	137.352	0.335	436.613	4.204	-55.676
45												
Time [s]	Relative H	Pressure [	Temperat	Pitot Pres	Air Densit	Air Veloci	Fx [N]	Mx [N•mr	Fy [N]	My [N•mr	Fz [N]	Mz [N•mm]
11:33:56 AM	49.668	1013.251	21.496	119.828	1.192	14.178	1.847	51.402	0.147	589.126	4.886	-55.824
60												
Time [s]	Relative H	Pressure [	Temperat	Pitot Pres	Air Densit	Air Veloci	Fx [N]	Mx [N•mr	Fy [N]	My [N•mr	Fz [N]	Mz [N•mm]
11:37:13 AM	49.353	1013.326	21.536	120.739	1.192	14.232	2.119	21.733	0.013	629.603	5.237	-42.3
75												
Time [s]	Relative H	Pressure [	Temperat	Pitot Pres	Air Densit	Air Veloci	Fx [N]	Mx [N•mr	Fy [N]	My [N•mr	Fz [N]	Mz [N•mm]
11:51:46 AM	48.846	1013.312	21.614	120.318	1.192	14.209	2.075	88.504	0.033	571.627	4.832	-2.155
90												
Time [s]	Relative H	Pressure [	Temperat	Pitot Pres	Air Densit	Air Veloci	Fx [N]	Mx [N•mr	Fy [N]	My [N•mr	Fz [N]	Mz [N•mm]
8:25:23 AM	48.982	991.834	21.914	118.647	1.165	14.27	2.077	79.66	0.026	610.393	3.77	40.426
105												
Time [s]	Relative H	Pressure [	Temperat	Pitot Pres	Air Densit	Air Veloci	Fx [N]	Mx [N•mr	Fy [N]	My [N•mr	Fz [N]	Mz [N•mm]
12:01:57 PM	48.393	1013.089	21.669	120.96	1.191	14.249	1.888	-29.903	-0.085	536.44	4.566	86.31
120												
Time [s]	Relative H	Pressure [	Temperat	Pitot Pres	Air Densit	Air Veloci	Fx [N]	Mx [N•mr	Fy [N]	My [N•mr	Fz [N]	Mz [N•mm]
12:06:14 PM	48.3	1013.104	21.715	121.946	1.191	14.308	1.64	-163.111	-0.328	444.576	5.011	106.317
135												
Time [s]	Relative H	Pressure [	Temperat	Pitot Pres	Air Densit	Air Veloci	Fx [N]	Mx [N•mr	Fy [N]	My [N•mr	Fz [N]	Mz [N•mm]
12:10:15 PM	48.141	1013.045	21.765	119.934	1.191	14.191	1.34	-233.21	-0.481	372.914	5.034	109.592
150												
Time [s]	Relative H	Pressure [	Temperat	Pitot Pres	Air Densit	Air Veloci	Fx [N]	Mx [N•mr	Fy [N]	My [N•mr	Fz [N]	Mz [N•mm]
12:15:48 PM	47.939	1013.003	21.817	121.865	1.191	14.307	0.888	-313.599	-0.574	260.008	4.936	95.848
165												
Time [s]	Relative H	Pressure [	Temperat	Pitot Pres	Air Densit	Air Veloci	Fx [N]	Mx [N•mr	Fy [N]	My [N•mr	Fz [N]	Mz [N•mm]
12:21:01 PM	47.555	1012.748	21.881	118.99	1.19	14.14	0.349	-354.252	-0.55	100.416	4.765	49.485
180												
Time [s]	Relative H	Pressure [	Temperat	Pitot Pres	Air Densit	Air Veloci	Fx [N]	Mx [N•mr	Fy [N]	My [N•mr	Fz [N]	Mz [N•mm]
12:23:54 PM	47.37	1012.753	21.841	121.466	1.19	14.285	-0.114	-321.593	-0.43	-43.252	4.644	-0.727

Table 28: Complete results from the wind tunnel test while the wind velocity at inlet is approximately 14.25 m/s

Repeating the test at 28.5 m/s (while rotating the model from zero to 180°):

This file was o	Saeid's Test Data (Mon 19 Mar 2018_8_53_33 AM).csv											
		0										
Time [s]	Relative H	Pressure [	Temperat	Pitot Pres	Air Densit	Air Veloci	Fx [N]	Mx [N•mr	Fy [N]	My [N•mr	Fz [N]	Mz [N•mm]
8:54:01 AM	50.445	991.912	22.195	472.454	1.164	28.492	-0.001	599.158	1.214	23.292	12.185	-23.119
15		15										
Time [s]	Relative H	Pressure [	Temperat	Pitot Pres	Air Densit	Air Veloci	Fx [N]	Mx [N•mr	Fy [N]	My [N•mr	Fz [N]	Mz [N•mm]
9:01:06 AM	50.06	992.097	22.168	474.01	1.164	28.535	2.623	598.309	1.41	861.934	13.543	-162.657
30		30										
Time [s]	Relative H	Pressure [	Temperat	Pitot Pres	Air Densit	Air Veloci	Fx [N]	Mx [N•mr	Fy [N]	My [N•mr	Fz [N]	Mz [N•mm]
9:07:23 AM	49.47	992.176	22.274	475.292	1.164	28.577	5.454	385.116	1.22	1771.013	16.872	-221.948
45		45										
Time [s]	Relative H	Pressure [	Temperat	Pitot Pres	Air Densit	Air Veloci	Fx [N]	Mx [N•mr	Fy [N]	My [N•mr	Fz [N]	Mz [N•mm]
9:13:16 AM	49.156	992.518	22.341	473.49	1.164	28.521	7.397	158.668	0.457	2382.974	18.492	-230.669
60		60										
Time [s]	Relative H	Pressure [	Temperat	Pitot Pres	Air Densit	Air Veloci	Fx [N]	Mx [N•mr	Fy [N]	My [N•mr	Fz [N]	Mz [N•mm]
9:18:15 AM	49.412	992.734	22.337	473.405	1.164	28.515	7.834	43.815	-0.119	2432.524	20.015	-167.295
75		75										
Time [s]	Relative H	Pressure [	Temperat	Pitot Pres	Air Densit	Air Veloci	Fx [N]	Mx [N•mr	Fy [N]	My [N•mr	Fz [N]	Mz [N•mm]
9:25:04 AM	49.699	992.498	22.406	474.044	1.164	28.542	6.969	355.124	0.195	1997.844	19.362	-11.12
90		90										
Time [s]	Relative H	Pressure [	Temperat	Pitot Pres	Air Densit	Air Veloci	Fx [N]	Mx [N•mr	Fy [N]	My [N•mr	Fz [N]	Mz [N•mm]
9:30:23 AM	49.297	992.751	22.492	472.713	1.164	28.502	5.556	99.004	0.004	1578.098	18.111	166.829
105		105										
Time [s]	Relative H	Pressure [	Temperat	Pitot Pres	Air Densit	Air Veloci	Fx [N]	Mx [N•mr	Fy [N]	My [N•mr	Fz [N]	Mz [N•mm]
9:37:18 AM	48.115	992.958	22.64	474.794	1.164	28.568	5.155	-262.903	-0.403	1533.378	17.861	340.425
120		120										
Time [s]	Relative H	Pressure [	Temperat	Pitot Pres	Air Densit	Air Veloci	Fx [N]	Mx [N•mr	Fy [N]	My [N•mr	Fz [N]	Mz [N•mm]
9:41:58 AM	47.301	993.131	22.767	474.807	1.163	28.571	4.666	-610.147	-1.131	1273.973	19.029	431.017
135		135										
Time [s]	Relative H	Pressure [	Temperat	Pitot Pres	Air Densit	Air Veloci	Fx [N]	Mx [N•mr	Fy [N]	My [N•mr	Fz [N]	Mz [N•mm]
9:46:26 AM	46.657	993.027	22.818	472.162	1.163	28.495	4.129	-864.909	-1.654	1159.664	19.052	423.11
150		150										
Time [s]	Relative H	Pressure [	Temperat	Pitot Pres	Air Densit	Air Veloci	Fx [N]	Mx [N•mr	Fy [N]	My [N•mr	Fz [N]	Mz [N•mm]
9:51:32 AM	45.501	992.916	22.884	472.145	1.163	28.497	3.102	-1140.63	-2.003	912.762	17.729	357.699
165		165										
Time [s]	Relative H	Pressure [	Temperat	Pitot Pres	Air Densit	Air Veloci	Fx [N]	Mx [N•mr	Fy [N]	My [N•mr	Fz [N]	Mz [N•mm]
9:54:48 AM	44.738	992.94	22.918	473.218	1.163	28.53	1.25	-1257.31	-2.011	322.354	17.15	187.108
180		180										
Time [s]	Relative H	Pressure [	Temperat	Pitot Pres	Air Densit	Air Veloci	Fx [N]	Mx [N•mr	Fy [N]	My [N•mr	Fz [N]	Mz [N•mm]
10:05:03 AM	43.597	993.562	23.015	469.478	1.163	28.411	-0.018	-1082.03	-1.438	-88.273	16.897	25.408

Table 29: Results from the wind tunnel experiment while the wind velocity at inlet is 28.5 m/s

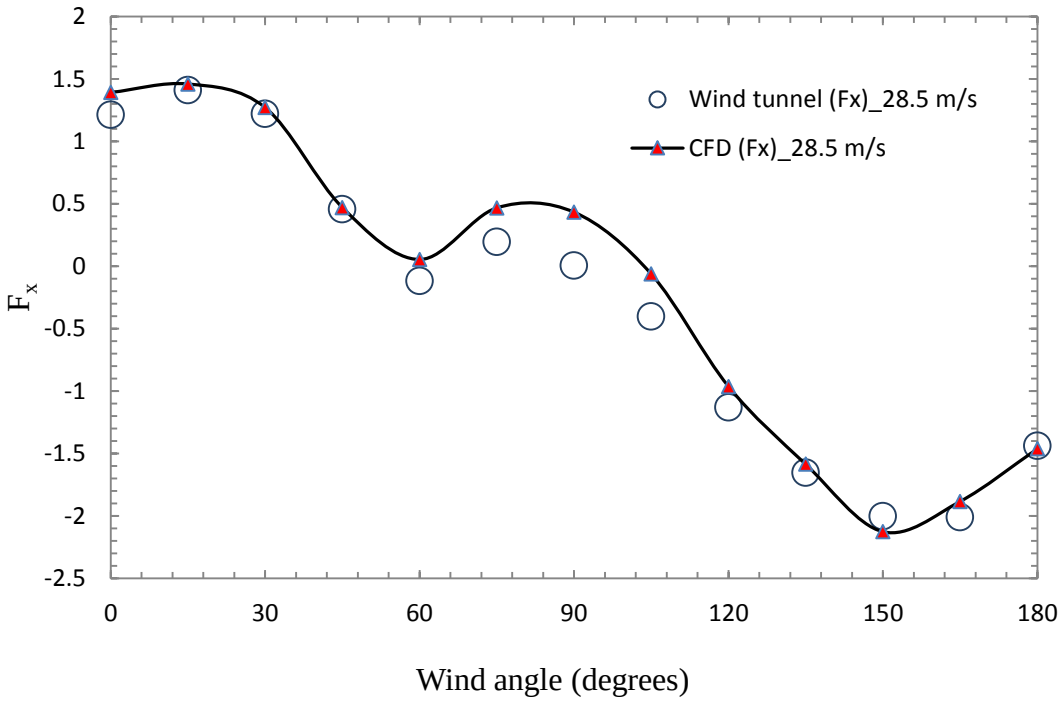

Figure 123: Comparing the experimental test in the wind tunnel with CFD analysis (F_x) (wind velocity of 28.5 m/s)

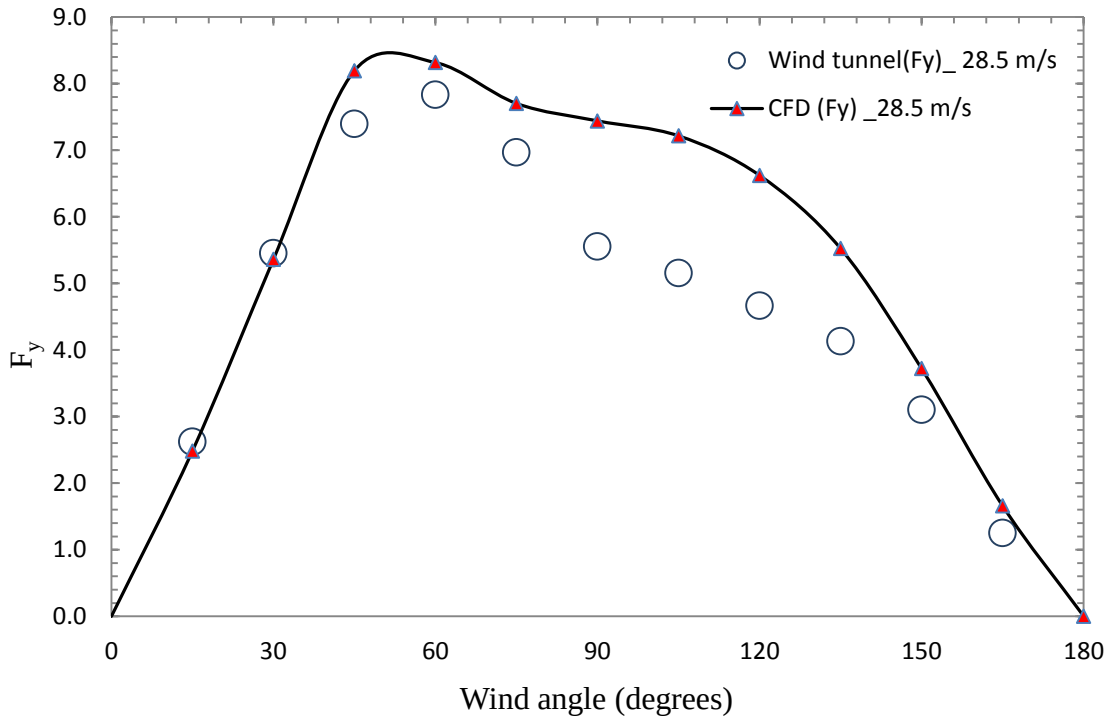

Figure 124: Comparing the experimental test in the wind tunnel with CFD analysis (F_y) (wind velocity of 28.5 m/s)

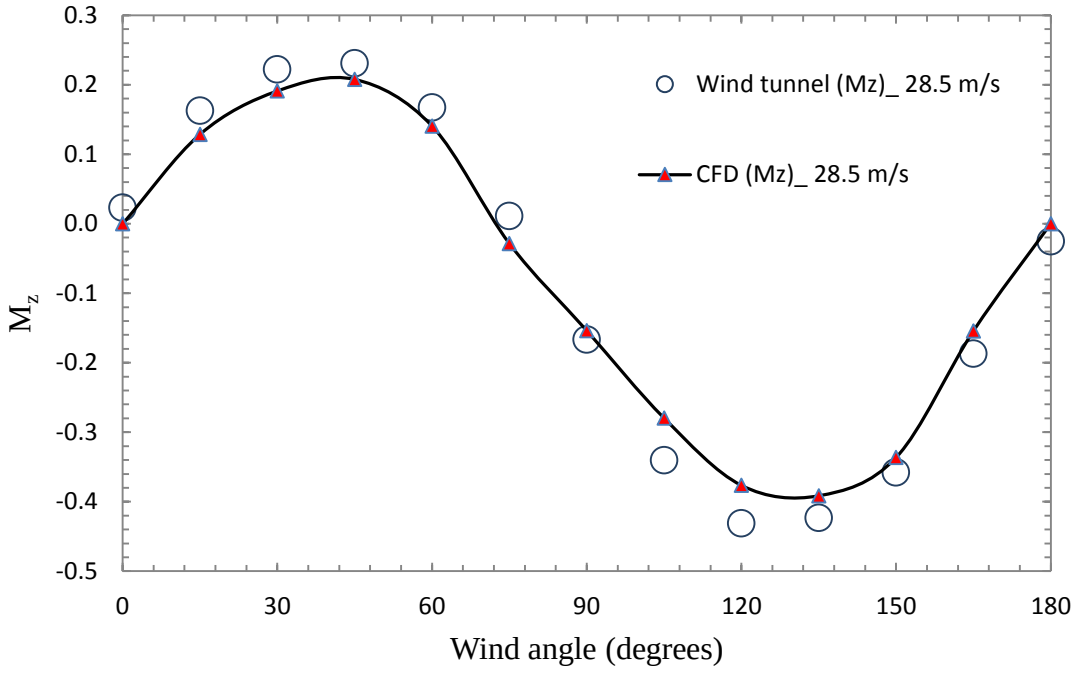

Figure 125: Comparing the experimental test in the wind tunnel with CFD analysis (Mz); (wind velocity of 28.5 m/s)

Comparing force and moment coefficients results (CFD) (wind velocity 28.5 m/s vs 14.25 m/s):

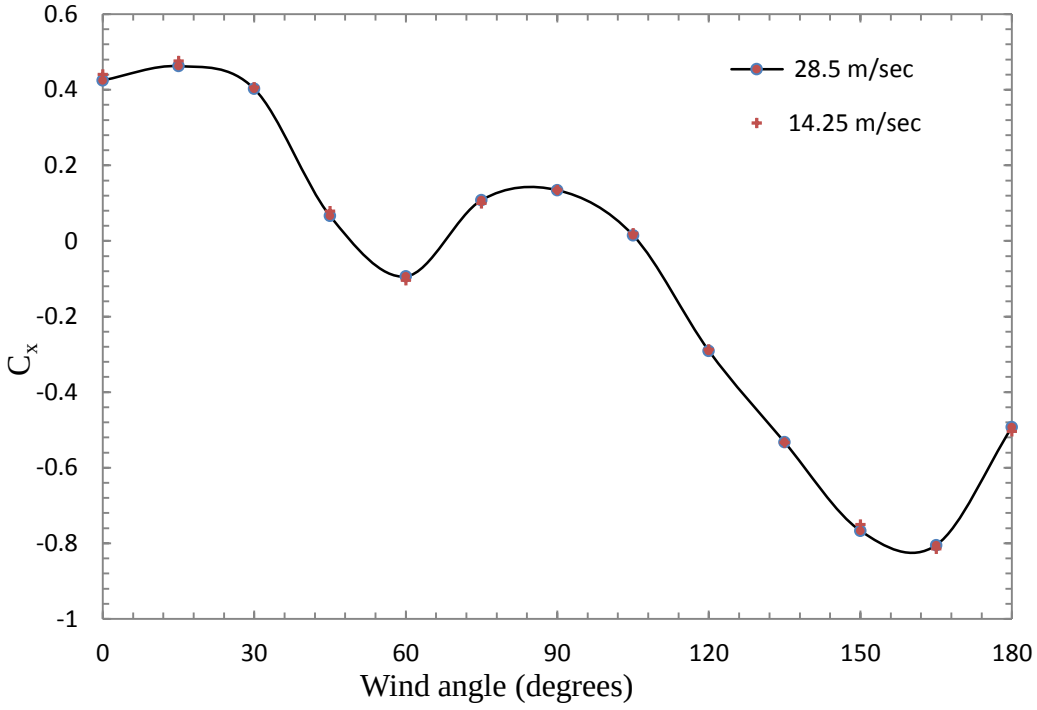

Figure 126: Wind force coefficient measured at wind velocity of 14.25 m/s vs wind velocity of 28.5 m/s (Cx)

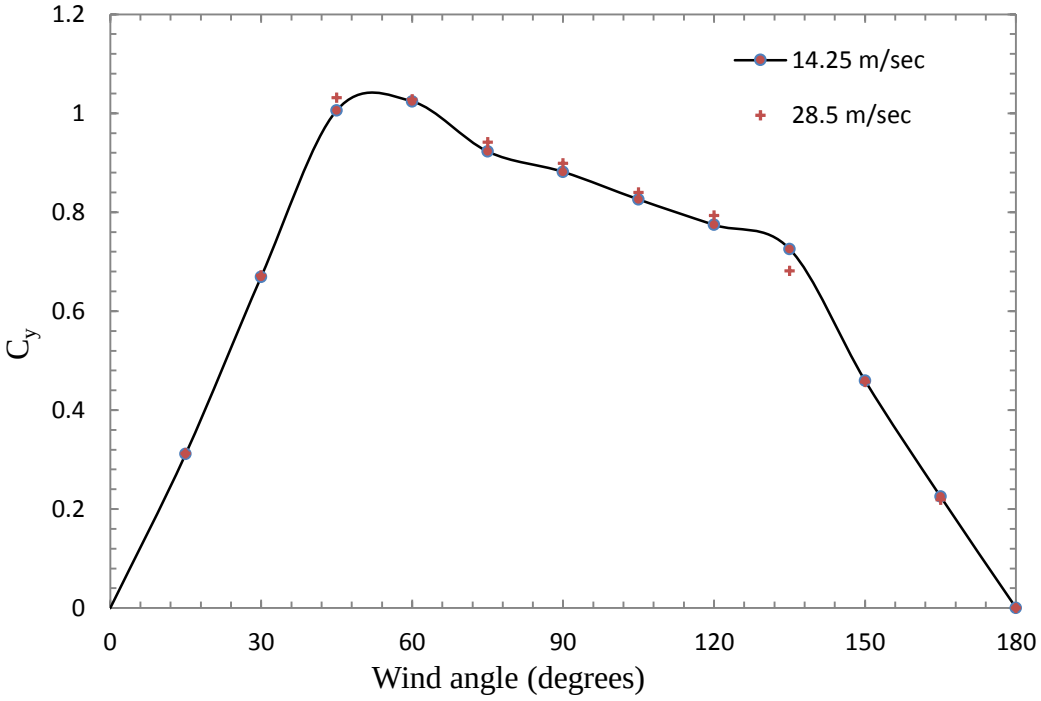

Figure 127: Wind force coefficient measured at wind velocity at 14.25 m/s vs wind velocity of 28.5 m/s (Cy)

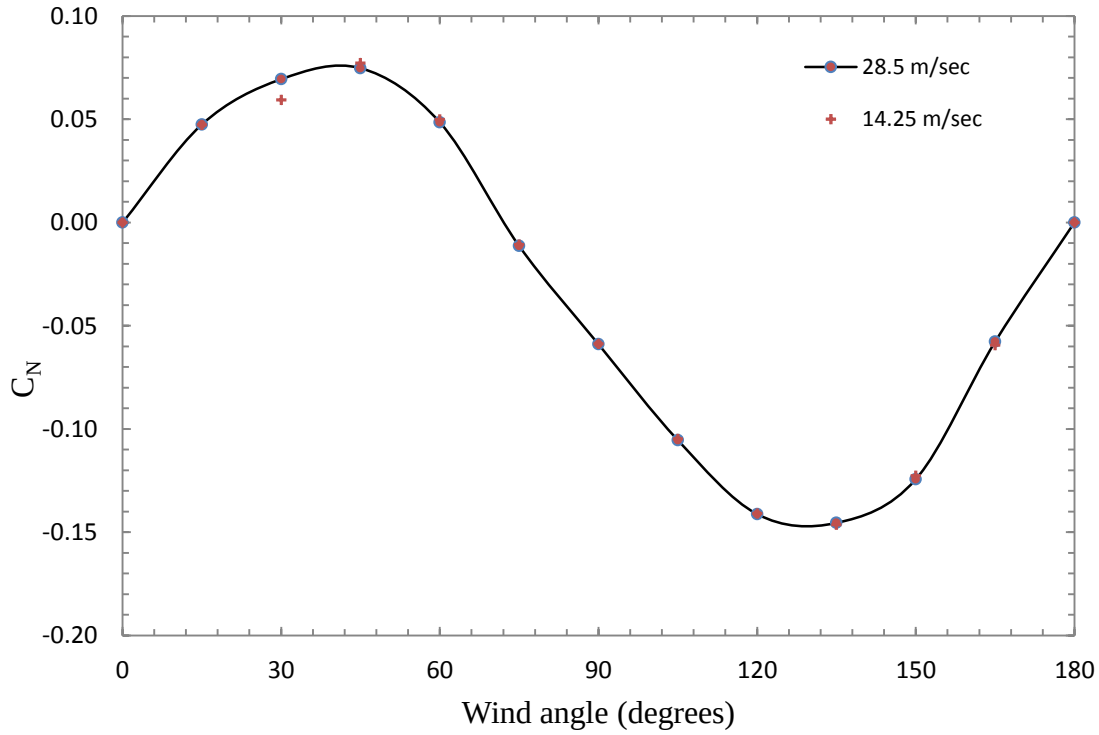

Figure 128: Wind moment coefficient measured at wind velocity of 14.25 m/s vs wind velocity of 28.5 m/s (C_N)

Appendix 13 Velocity and pressure contours for all headings

Velocity contours (wind velocity at 14.25 m/s; wind angle of attack 0°):

The x axis of the model is aligned with the wind tunnel's longitudinal axis when wind is blowing directly to the bow.

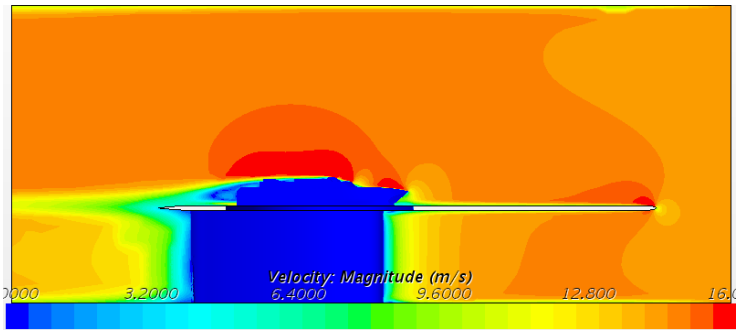

(a)

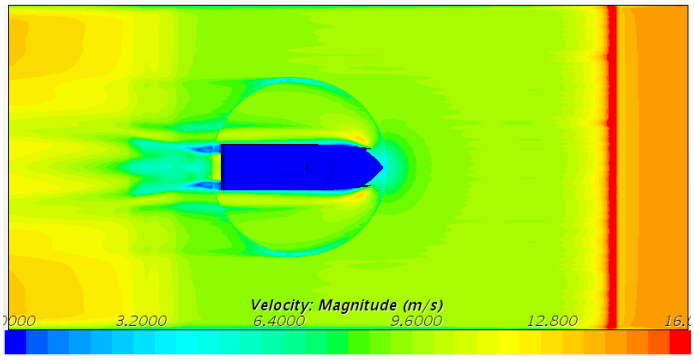

(b)

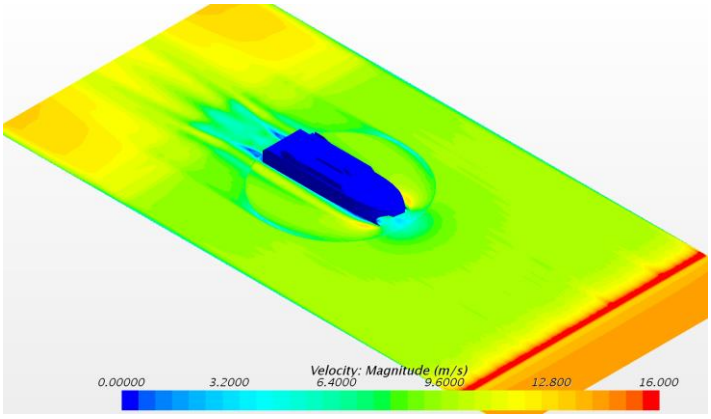

(c)

Figure 129: CFD velocity contours for a wind speed of 14.25 m/s and wind angle of attack at 0°. (a) elevation at centreline of the domain, (b) plan view at waterline level, (c) isometric view at waterline level

Pressure contours (wind velocity at 14.25 m/s; wind angle of attack is 0°):

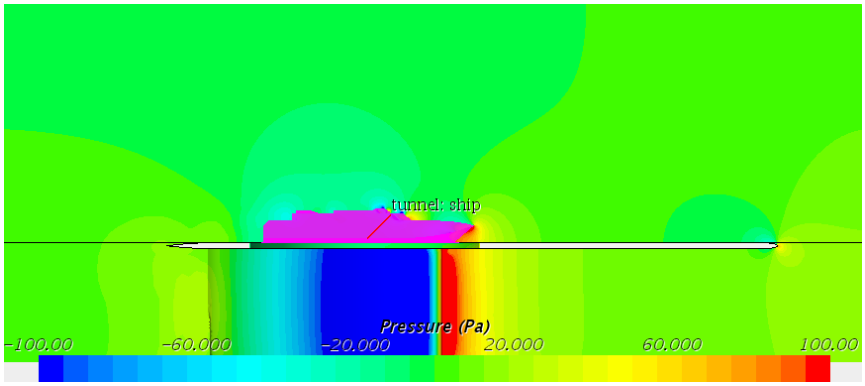

(d)

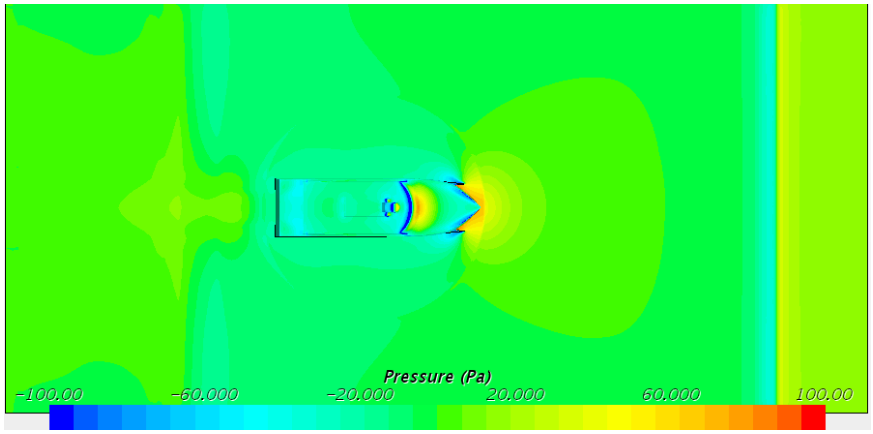

(e)

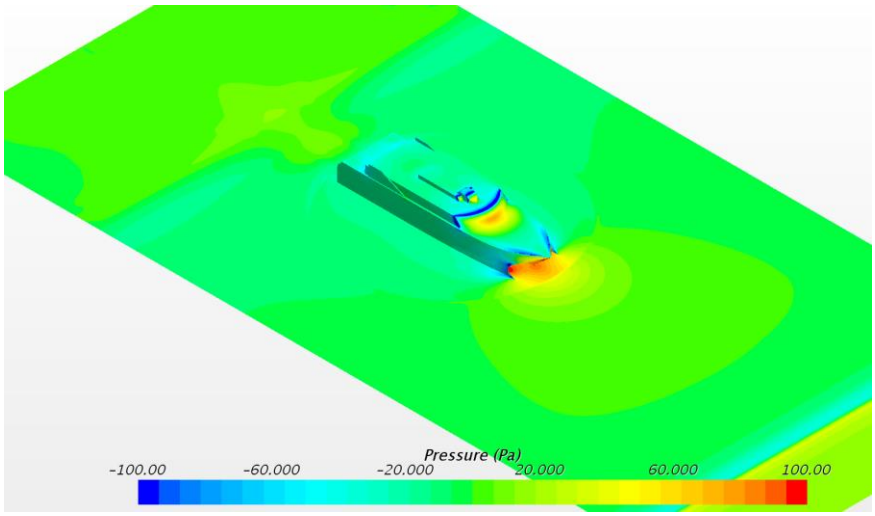

(f)

Figure 130: CFD pressure contours for a wind speed of 14.25 m/s and wind angle of attack at 0°. (a) elevation at centreline of the domain, (b) plan view at waterline level, (c) isometric view at waterline level

Velocity contours (wind velocity at 14.25 m/s; wind angle of attack is 15°):

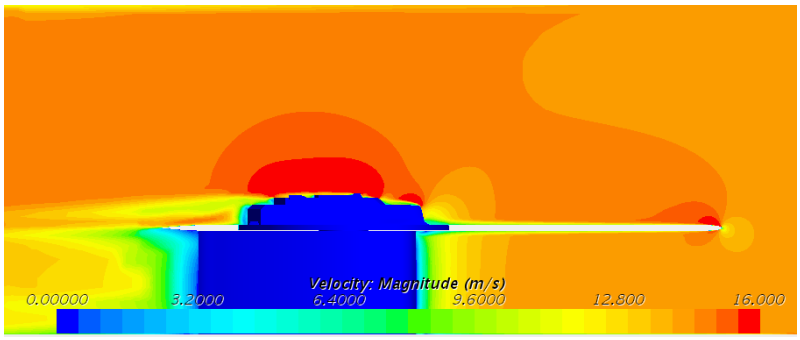

(a)

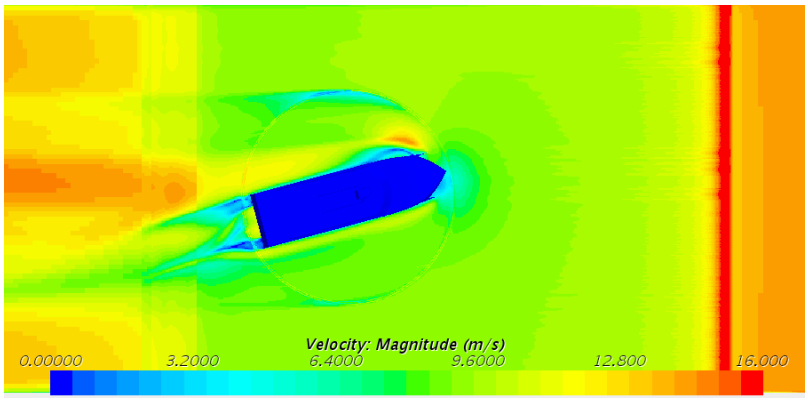

(b)

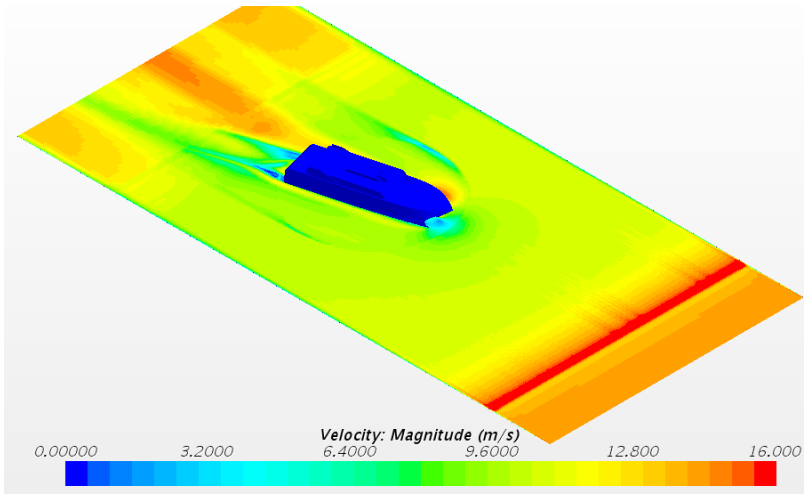

(c)

Figure 131: CFD velocity contours for a wind speed of 14.25 m/s and wind angle of attack at 15°. (a) elevation at centreline of the domain, (b) plan view at waterline level, (c) isometric view at waterline level

Pressure contours (wind velocity at 14.25 m/s; wind angle of attack is 15°):

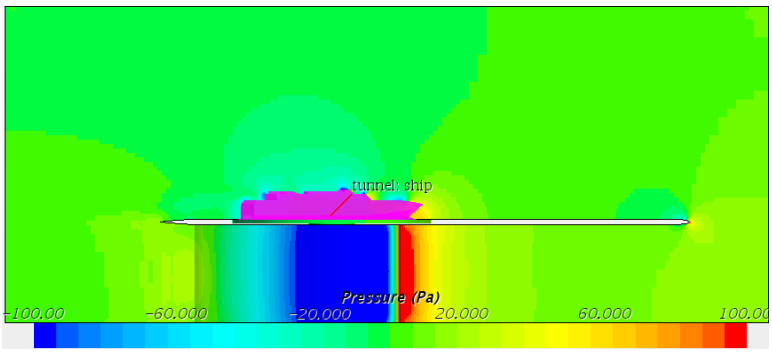

(d)

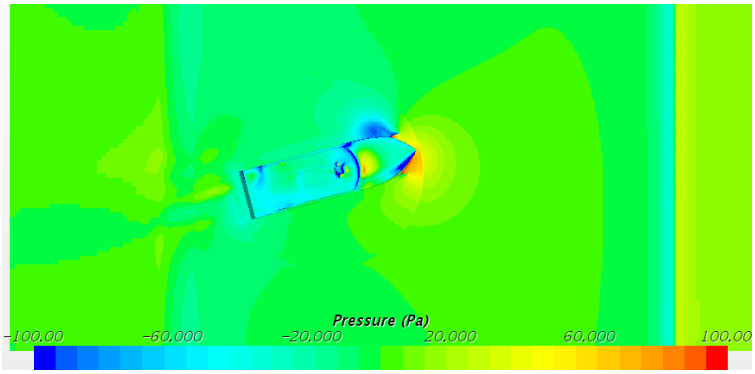

(e)

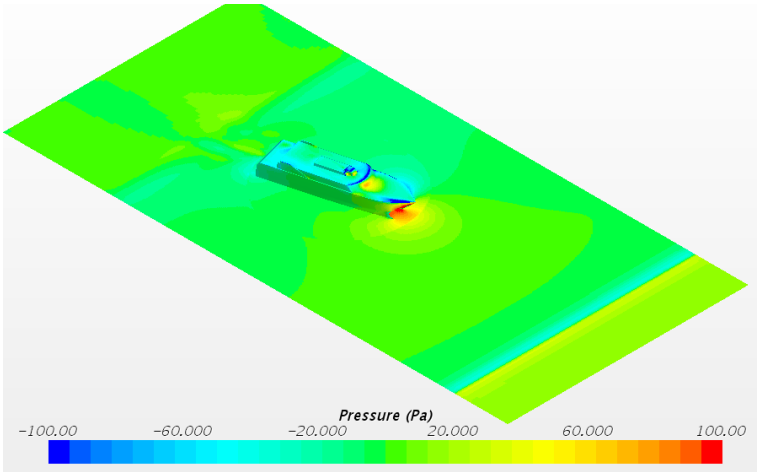

(f)

Figure 132: CFD pressure contours for a wind speed of 14.25 m/s and wind angle of attack at 15°. (a) elevation at centreline of the domain, (b) plan view at waterline level, (c) isometric view at waterline level

Velocity contours (wind velocity at 14.25 m/s; wind angle of attack is 30°):

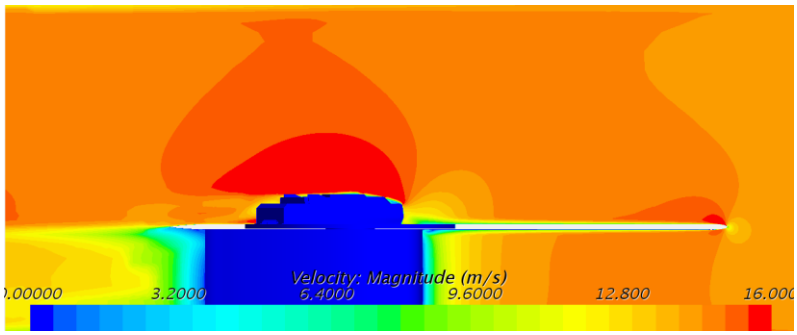

(a)

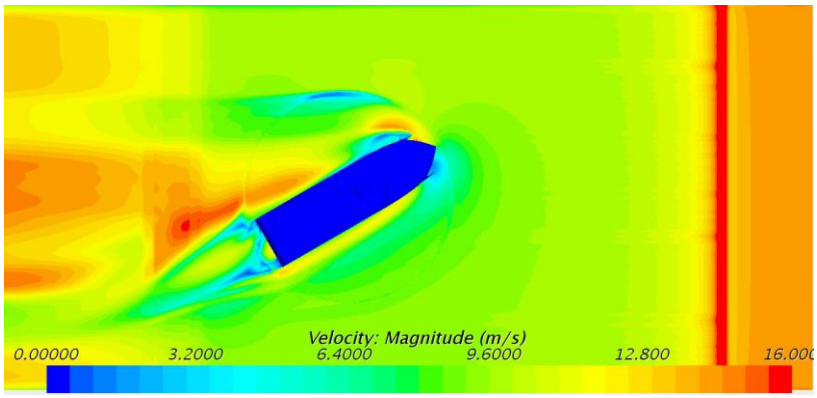

(b)

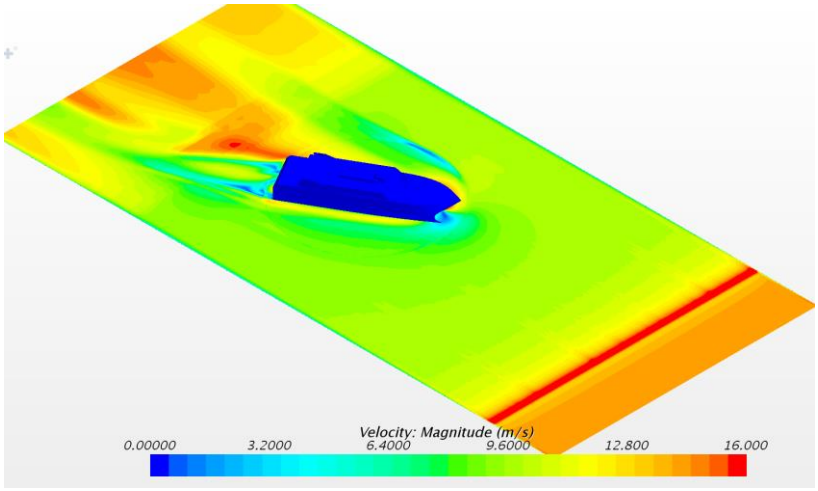

(c)

Figure 133: CFD velocity contours for a wind speed of 14.25 m/s and wind angle of attack at 30°. (a) elevation at centreline of the domain, (b) plan view at waterline level, (c) isometric view at waterline level

Pressure contours (wind velocity at 14.25 m/s_wind angle of attack is 30°):

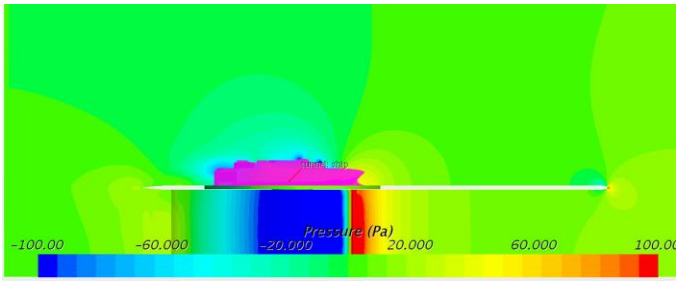

(d)

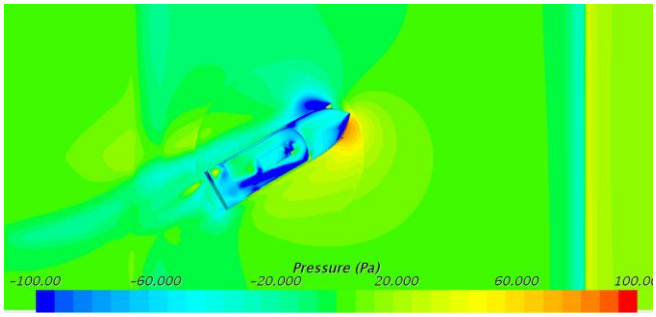

(e)

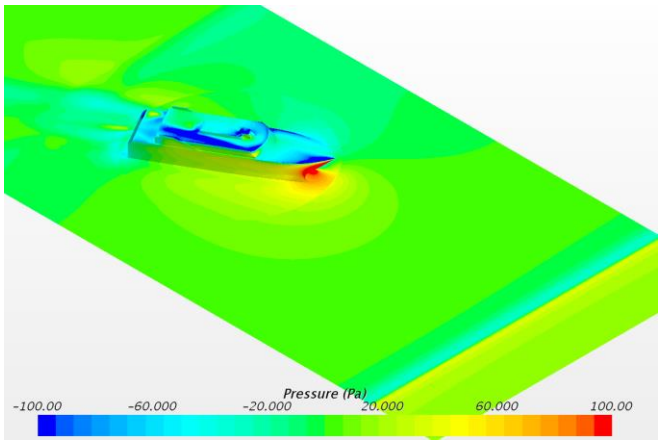

(f)

Figure 134: CFD pressure contours for a wind speed of 14.25 m/s and wind angle of attack at 30°. (a) elevation at centreline of the domain, (b) plan view at waterline level, (c) isometric view at waterline level

Velocity contours (wind velocity at 14.25 m/s; wind angle of attack is 45°):

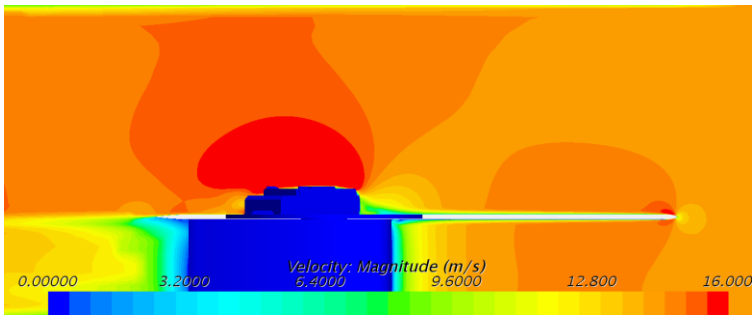

(a)

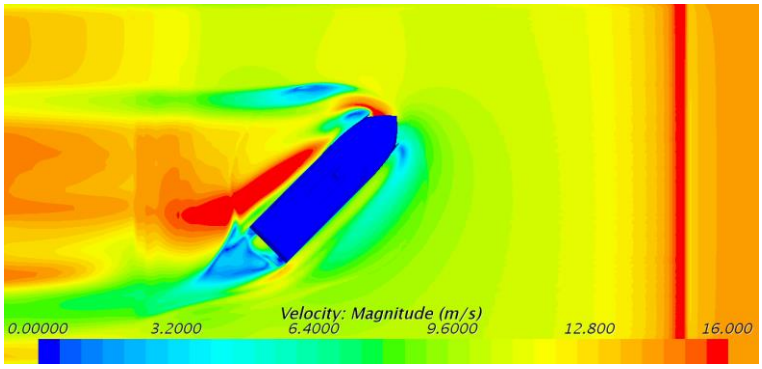

(b)

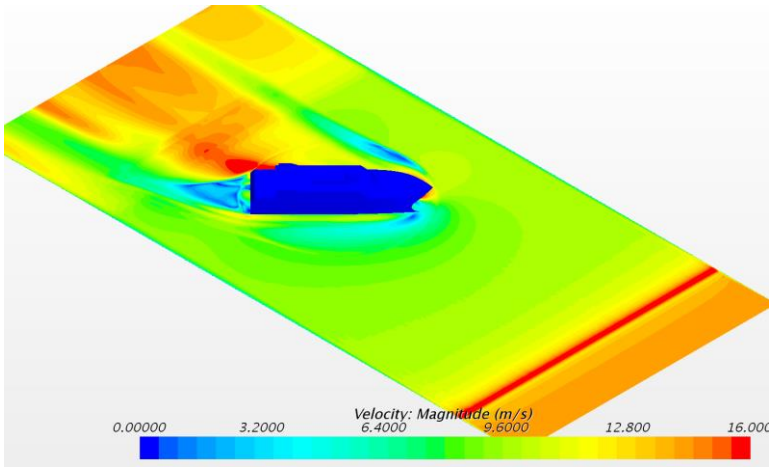

(c)

Figure 135: CFD velocity contours for a wind speed of 14.25 m/s and wind angle of attack at 45°. (a) elevation at centreline of the domain, (b) plan view at waterline level, (c) isometric view at waterline level

Pressure contours (wind velocity at 14.25 m/s; wind angle of attack is 45°):

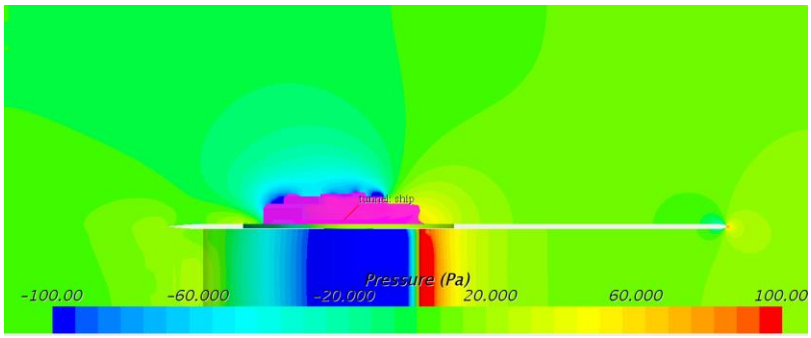

(d)

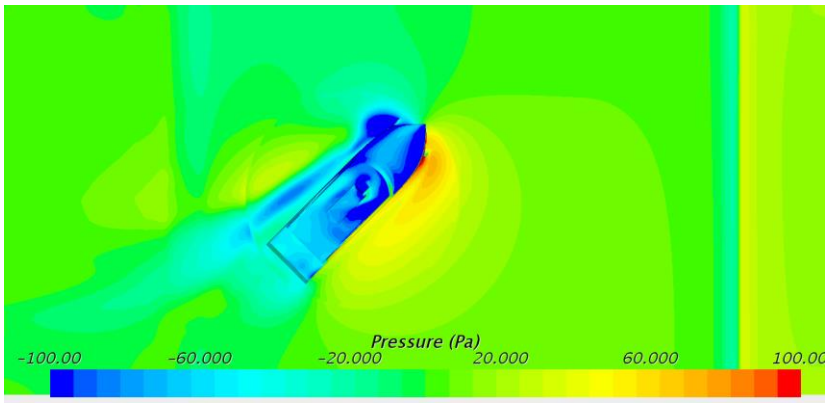

(e)

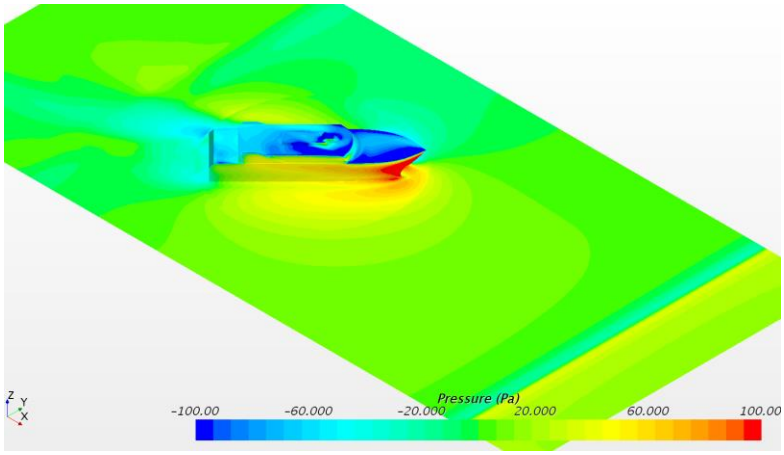

(f)

Figure 136: CFD pressure contours for a wind speed of 14.25 m/s and wind angle of attack at 45°. (a) elevation at centreline of the domain, (b) plan view at waterline level, (c) isometric view at waterline level

Velocity contours (wind velocity at 14.25 m/s; wind angle of attack is 60°):

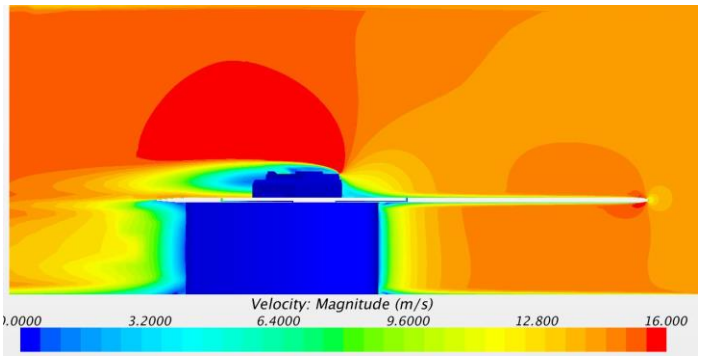

(a)

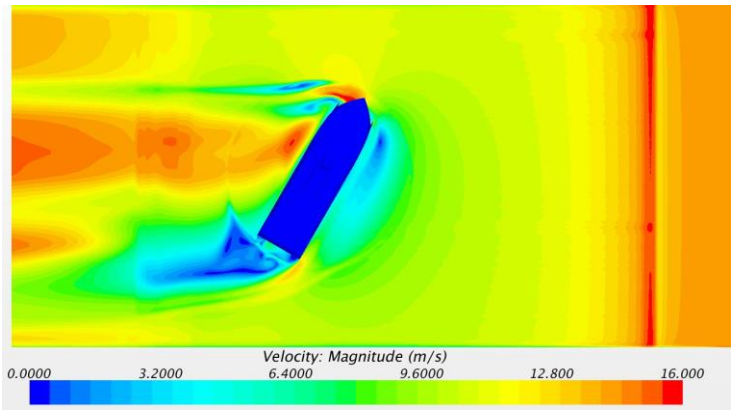

(b)

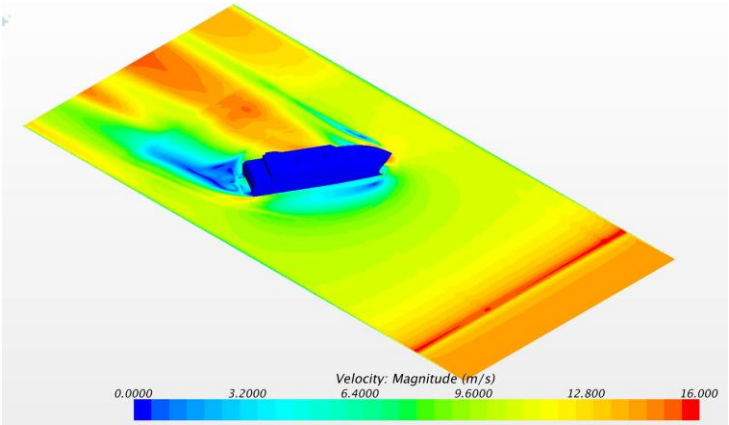

(c)

Figure 137: CFD velocity contours for a wind speed of 14.25 m/s and wind angle of attack at 60°. (a) elevation at centreline of the domain, (b) plan view at waterline level, (c) isometric view at waterline level

Pressure contours (wind velocity at 14.25 m/s; wind angle of attack is 60°):

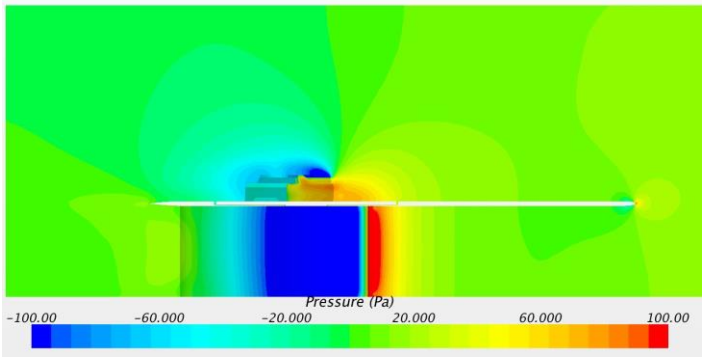

(d)

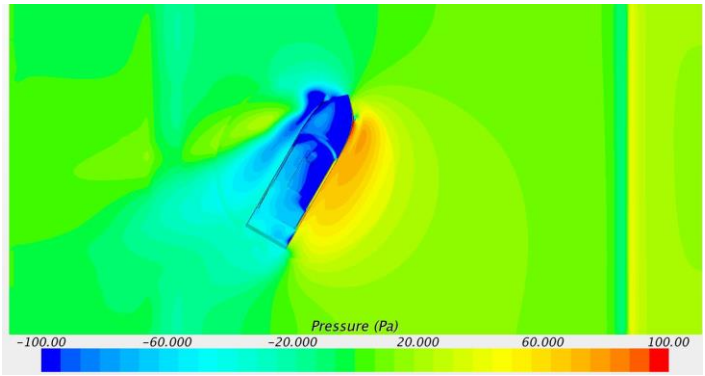

(e)

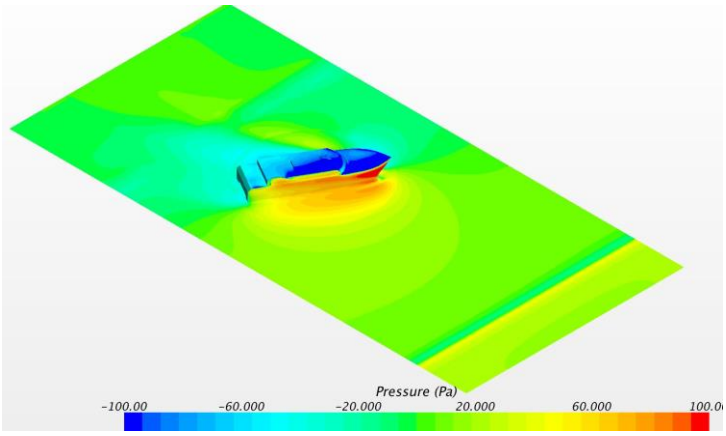

(f)

Figure 138: CFD pressure contours for a wind speed of 14.25 m/s and wind angle of attack at 60°. (a) elevation at centreline of the domain, (b) plan view at waterline level, (c) isometric view at waterline level

Velocity contours (wind velocity at 14.25 m/s; wind angle of attack is 75°):

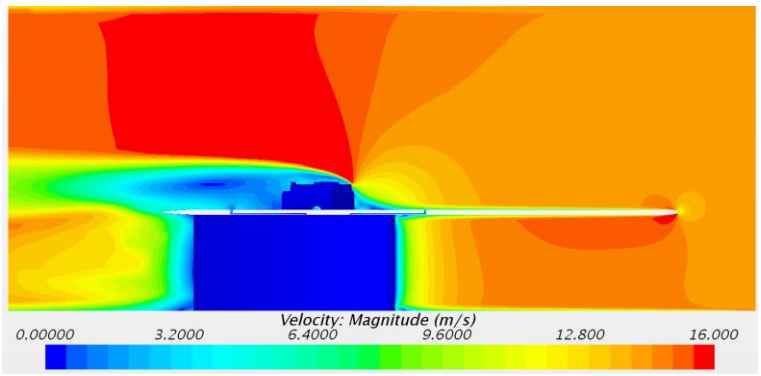

(a)

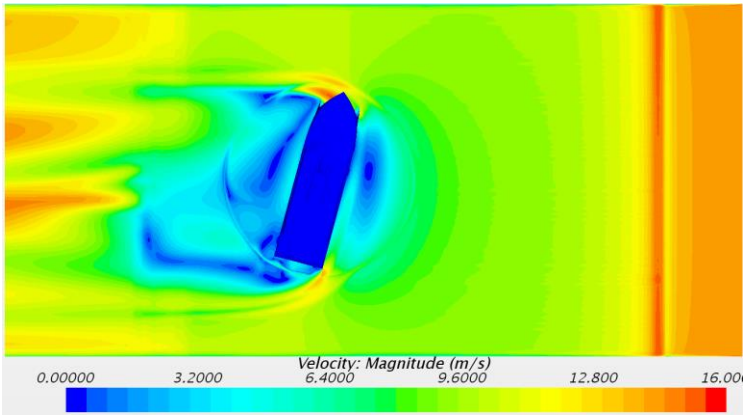

(b)

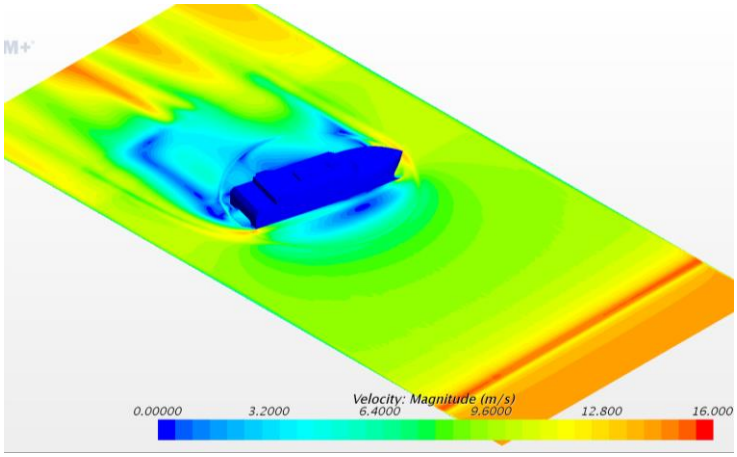

(c)

Figure 139: CFD velocity contours for a wind speed of 14.25 m/s and wind angle of attack at 75°. (a) elevation at centreline of the domain, (b) plan view at waterline level, (c) isometric view at waterline level

Pressure contours (wind velocity at 14.25 m/s_wind angle of attack is 75°):

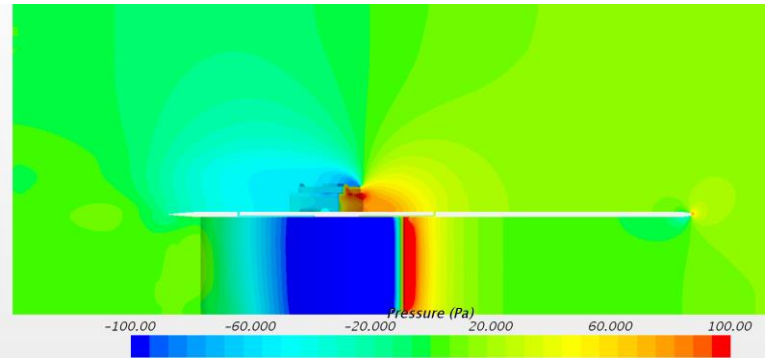

(d)

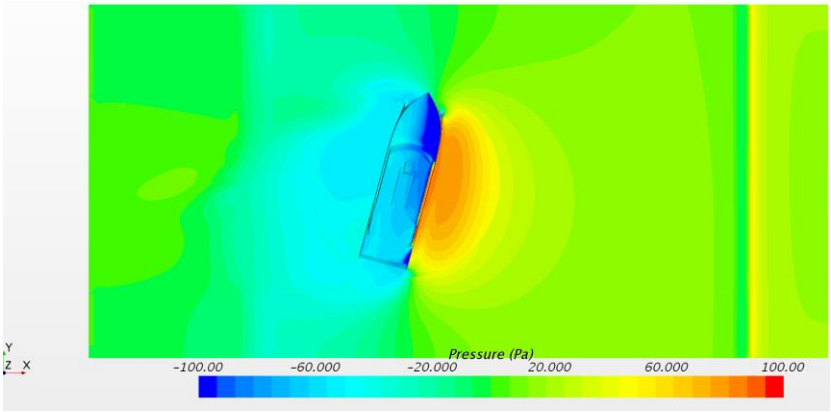

(e)

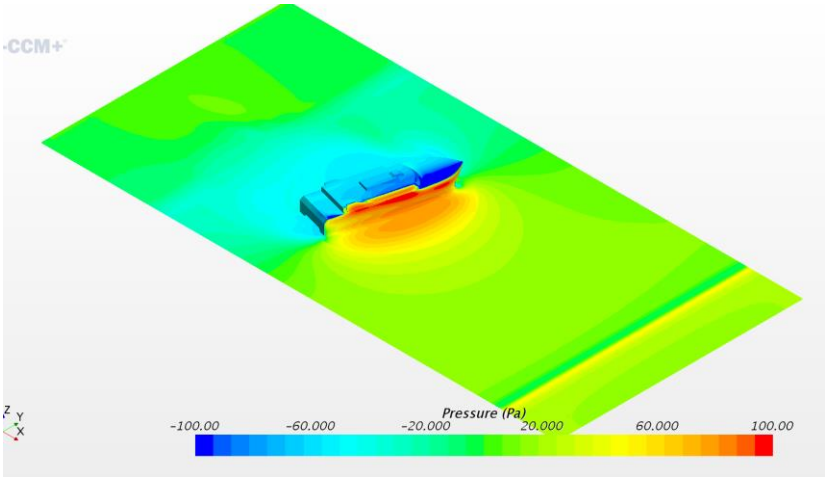

(f)

Figure 140: CFD pressure contours for a wind speed of 14.25 m/s and wind angle of attack at 75°. (a) elevation at centreline of the domain, (b) plan view at waterline level, (c) isometric view at waterline level

Velocity contours (wind velocity at 14.25 m/s; wind angle of attack is 90°):

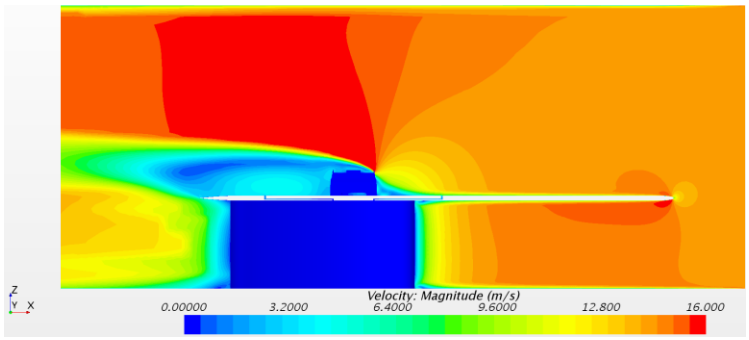

(a)

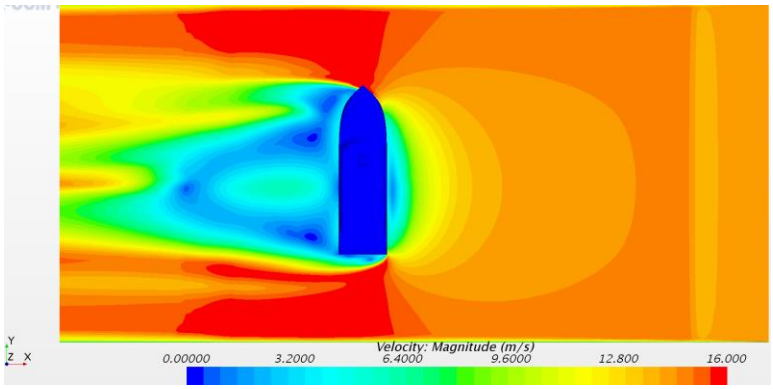

(b)

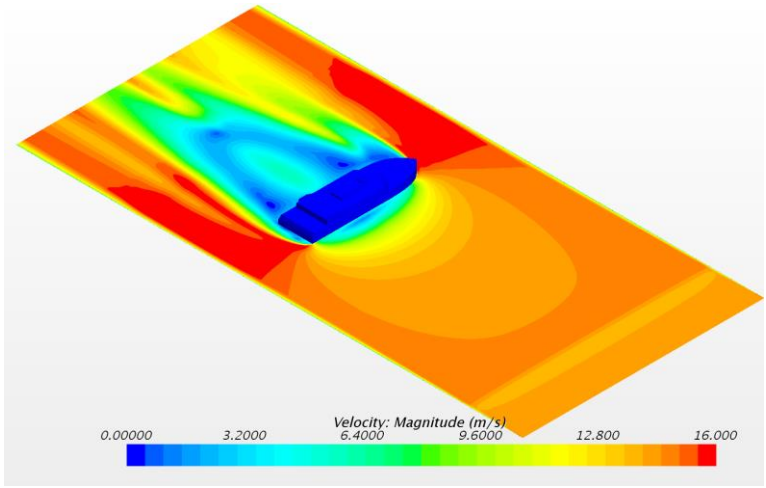

(c)

Figure 141: CFD velocity contours for a wind speed of 14.25 m/s and wind angle of attack at 90°. (a) elevation at centreline of the domain, (b) plan view at waterline level, (c) isometric view at waterline level

Pressure contours (wind velocity at 14.25 m/s; wind angle of attack is 90°):

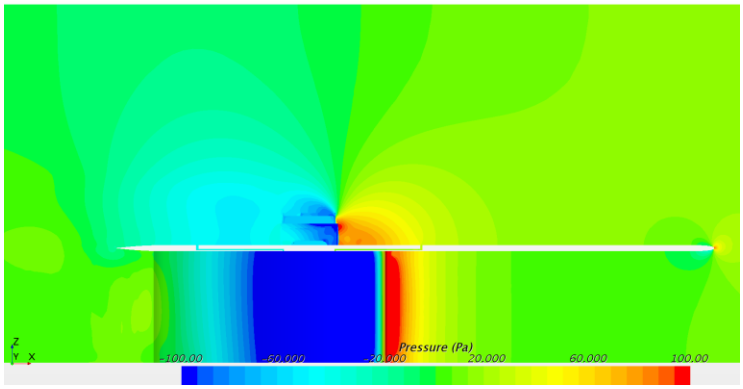

(d)

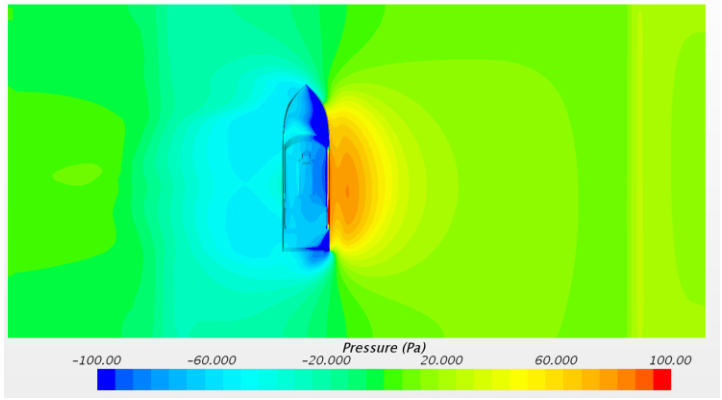

(e)

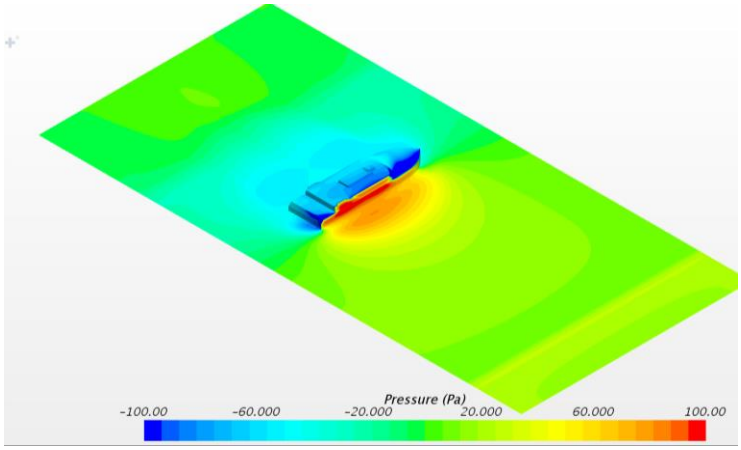

(f)

Figure 142: CFD pressure contours for a wind speed of 14.25 m/s and wind angle of attack at 90°. (a) elevation at centreline of the domain, (b) plan view at waterline level, (c) isometric view at waterline level

Velocity contours (wind velocity at 14.25 m/s; wind angle of attack is 105°):

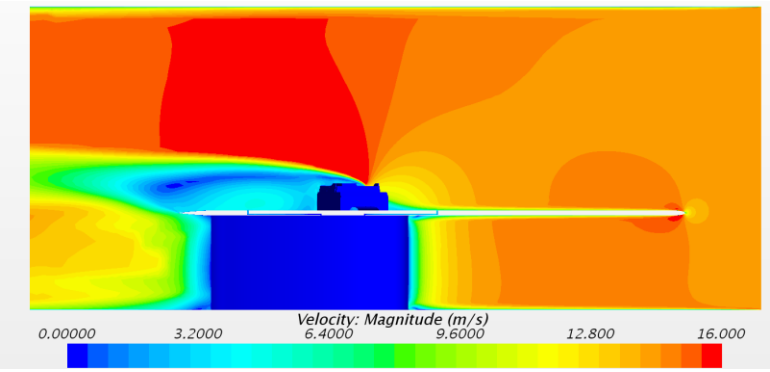

(a)

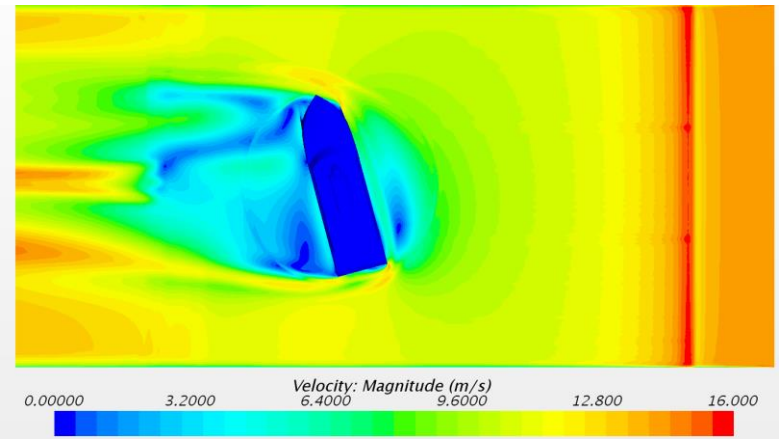

(b)

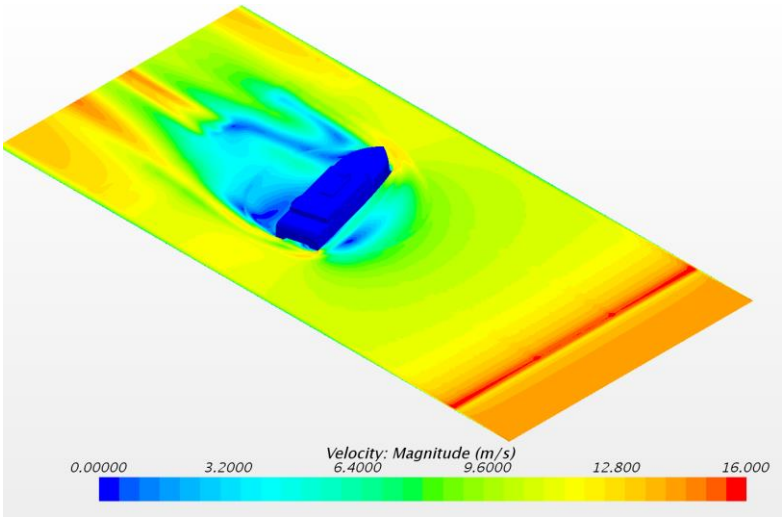

(c)

Figure 143: CFD velocity contours for a wind speed of 14.25 m/s and wind angle of attack at 105°. (a) elevation at centreline of the domain, (b) plan view at waterline level, (c) isometric view at waterline level

Pressure contours (wind velocity at 14.25 m/s; wind angle of attack is 105°):

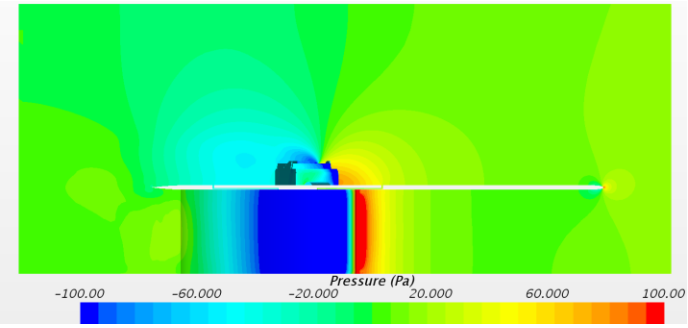

(d)

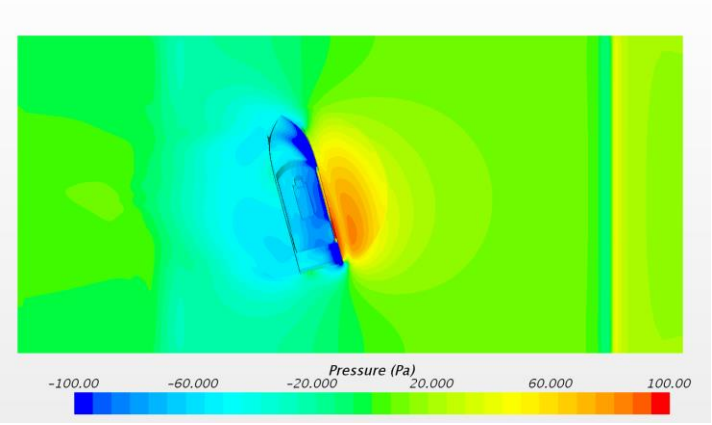

(e)

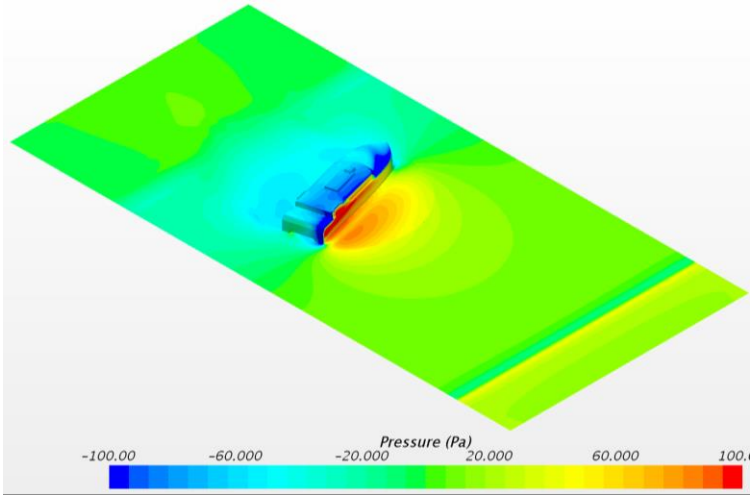

(f)

Figure 144: CFD pressure contours for a wind speed of 14.25 m/s and wind angle of attack at 105°. (a) elevation at centreline of the domain, (b) plan view at waterline level, (c) isometric view at waterline level

Velocity contours (wind velocity at 14.25 m/s; wind angle of attack is 120°):

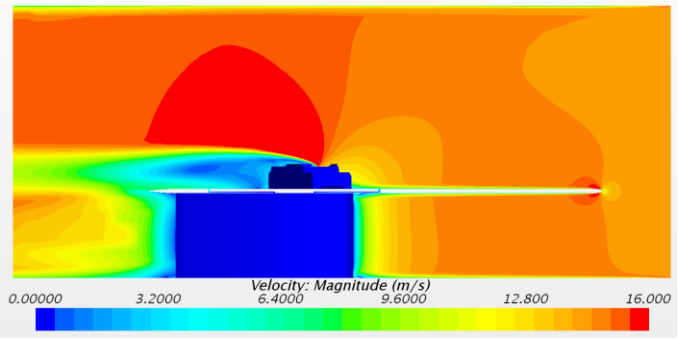

(a)

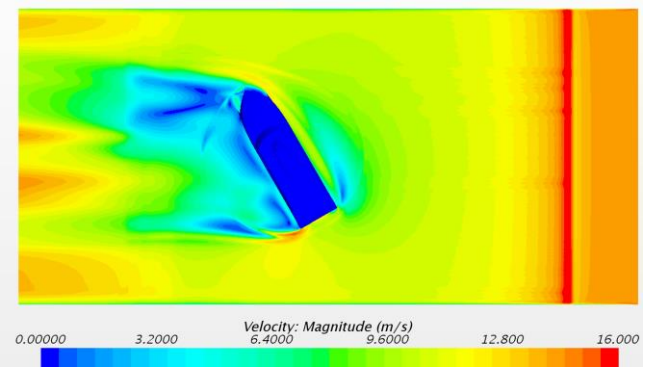

(b)

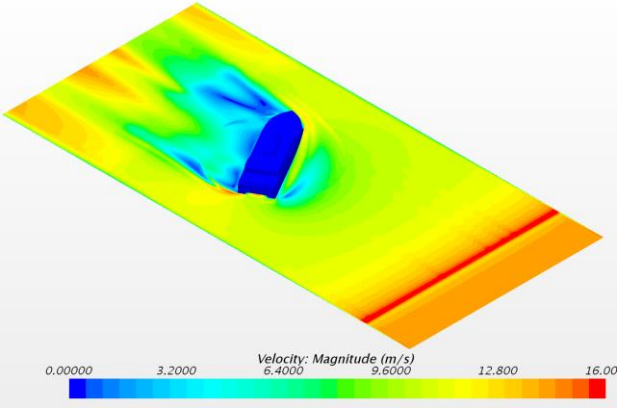

(c)

Figure 145: CFD velocity contours for a wind speed of 14.25 m/s and wind angle of attack at 120°. (a) elevation at centreline of the domain, (b) plan view at waterline level, (c) isometric view at waterline level

Pressure contours (wind velocity at 14.25 m/s; wind angle of attack is 120°):

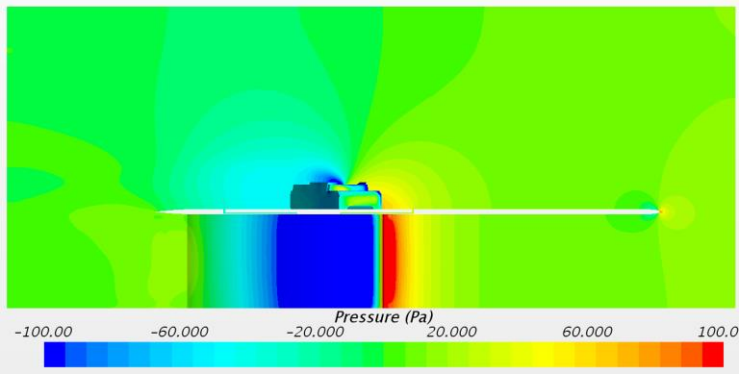

(d)

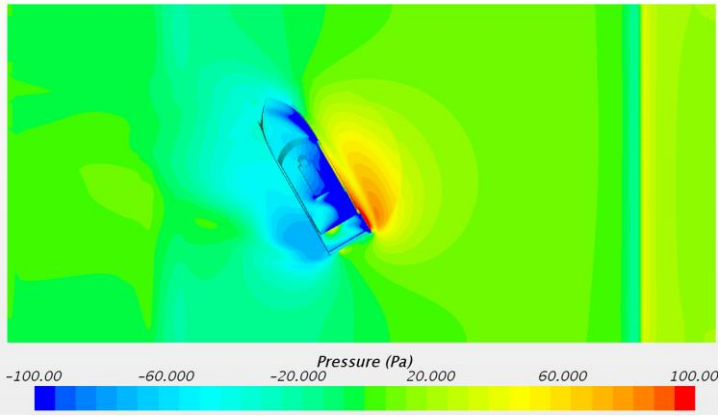

(e)

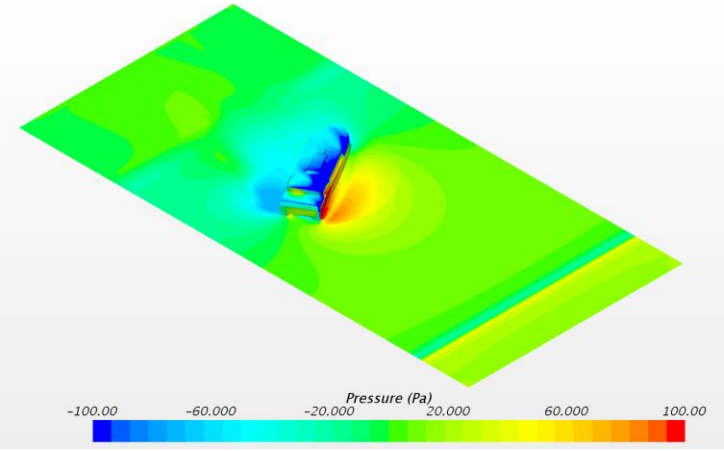

(f)

Figure 146: CFD pressure contours for a wind speed of 14.25 m/s and wind angle of attack at 120°. (a) elevation at centreline of the domain, (b) plan view at waterline level, (c) isometric view at waterline level

Velocity contours (wind velocity at 14.25 m/s; wind angle of attack is 135°):

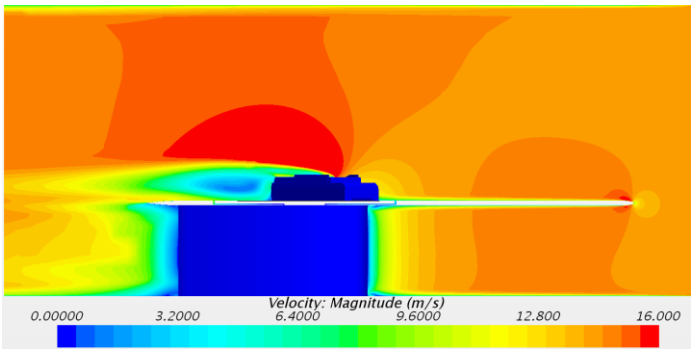

(a)

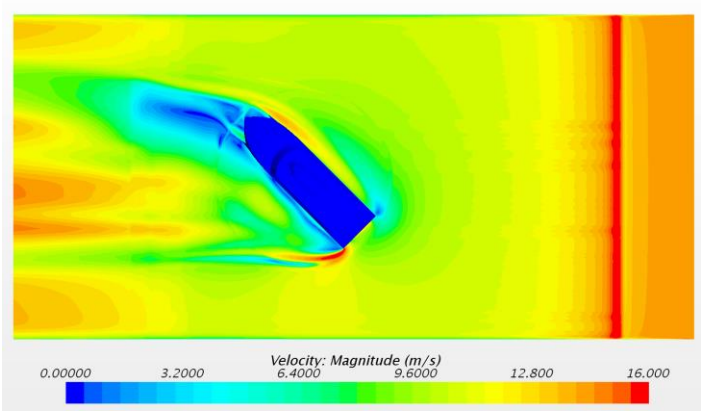

(b)

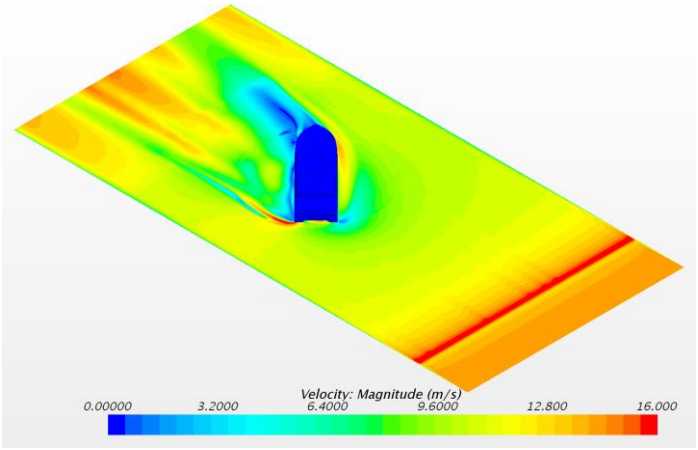

(c)

Figure 147: CFD velocity contours for a wind speed of 14.25 m/s and wind angle of attack at 135°. (a) elevation at centreline of the domain, (b) plan view at waterline level, (c) isometric view at waterline level

Pressure contours (wind velocity at 14.25 m/s; wind angle of attack is 135°):

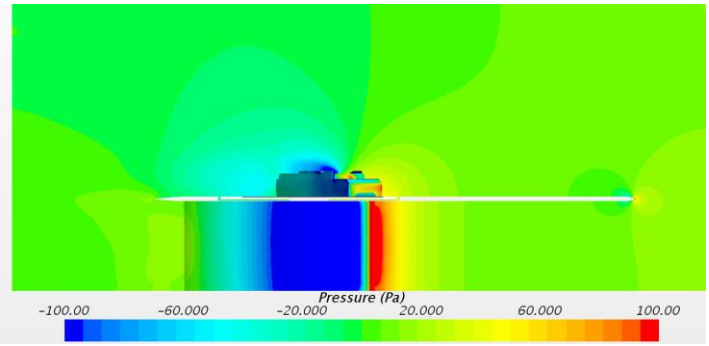

(d)

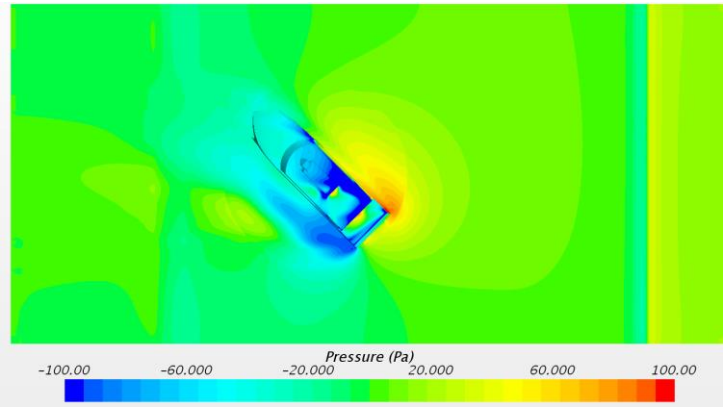

(e)

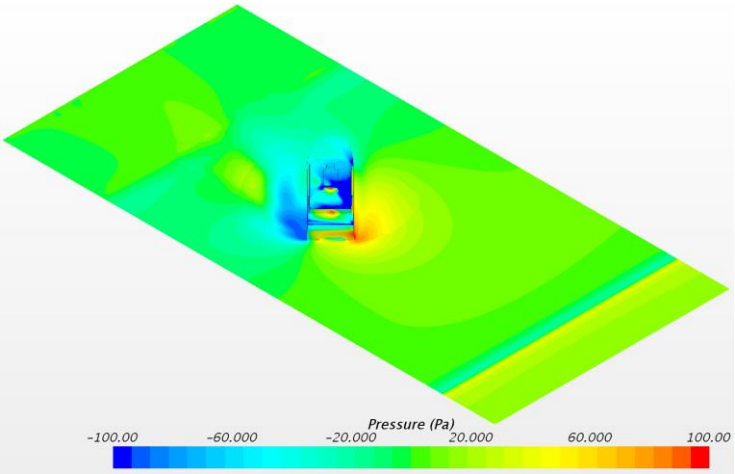

(f)

Figure 148: CFD pressure contours for a wind speed of 14.25 m/s and wind angle of attack at 135°. (a) elevation at centreline of the domain, (b) plan view at waterline level, (c) isometric view at waterline level

Velocity contours (wind velocity at 14.25 m/s; wind angle of attack is 150°):

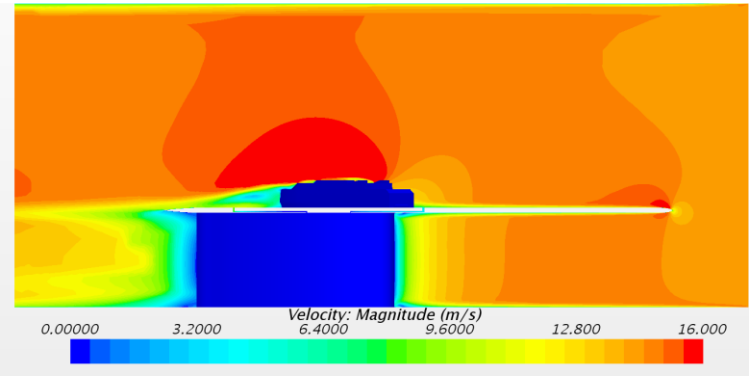

(a)

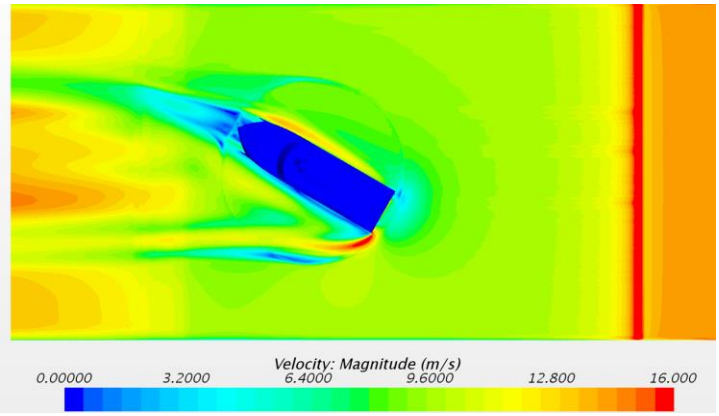

(b)

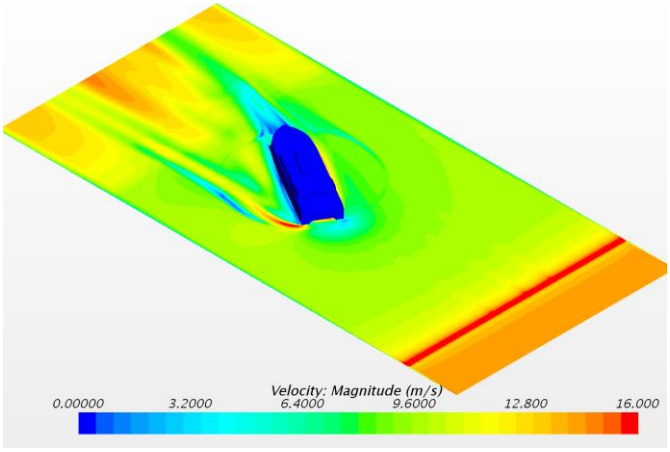

(c)

Figure 149: CFD velocity contours for a wind speed of 14.25 m/s and wind angle of attack at 150°. (a) elevation at centreline of the domain, (b) plan view at waterline level, (c) isometric view at waterline level

Pressure contours (wind velocity at 14.25 m/s; wind angle of attack is 150°):

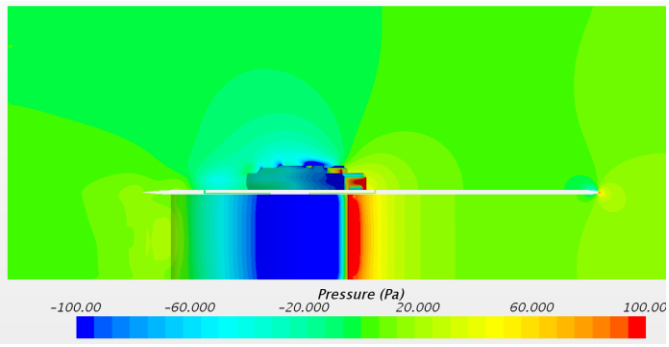

(d)

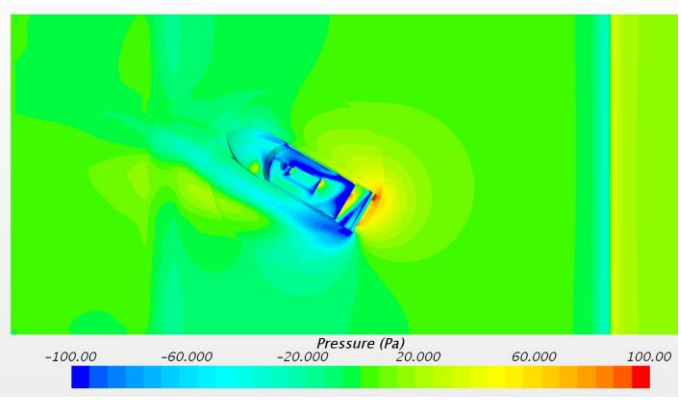

(e)

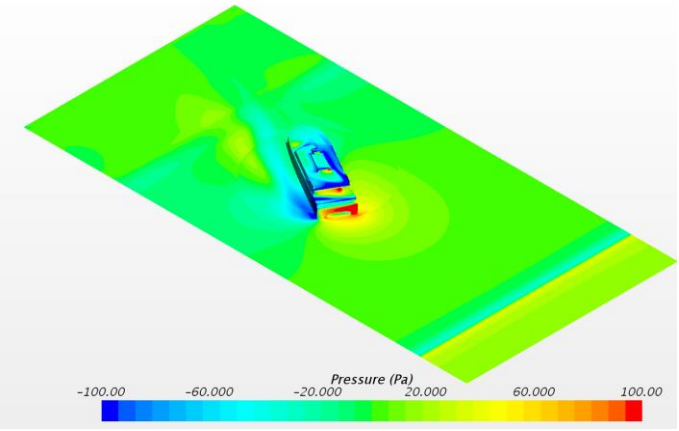

(f)

Figure 150: CFD pressure contours for a wind speed of 14.25 m/s and wind angle of attack at 150°. (a) elevation at centreline of the domain, (b) plan view at waterline level, (c) isometric view at waterline level

Velocity contours (wind velocity at 14.25 m/s; wind angle of attack is 165°):

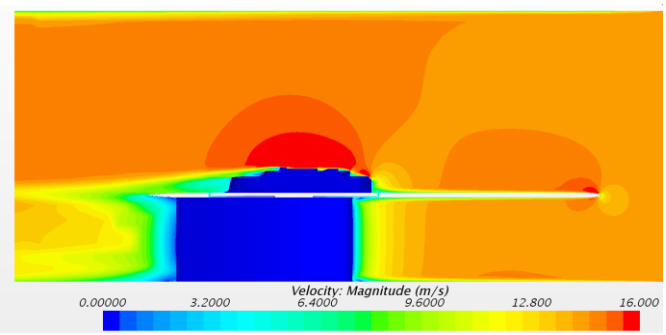

(a)

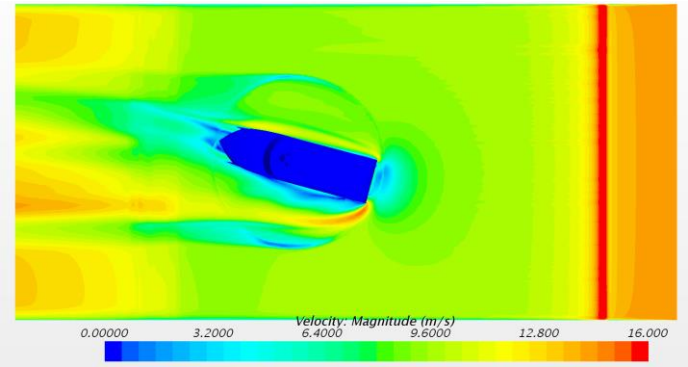

(b)

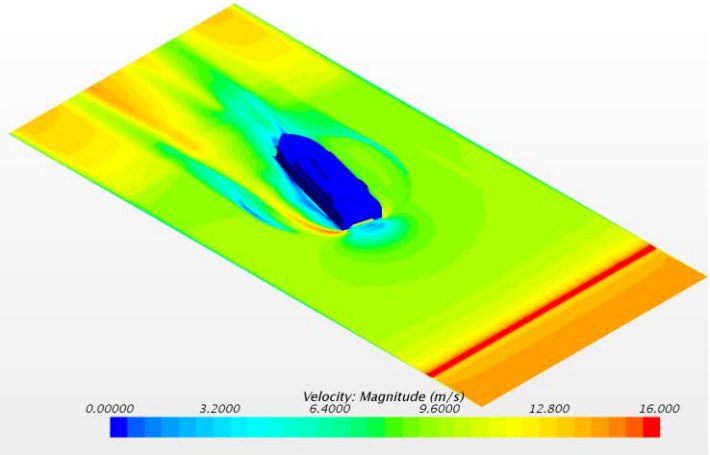

(c)

Figure 151: CFD velocity contours for a wind speed of 14.25 m/s and wind angle of attack at 165°. (a) elevation at centreline of the domain, (b) plan view at waterline level, (c) isometric view at waterline level

Pressure contours (wind velocity at 14.25 m/s; wind angle of attack is 165°):

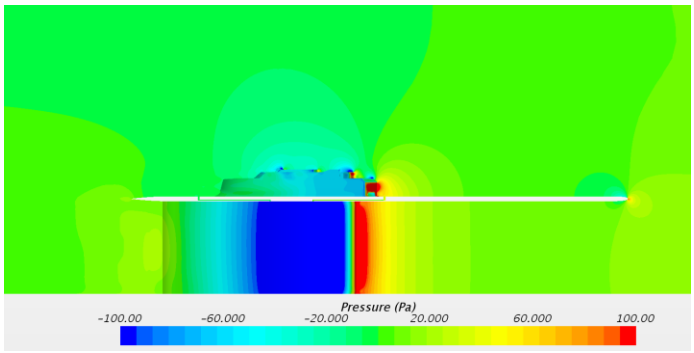

(d)

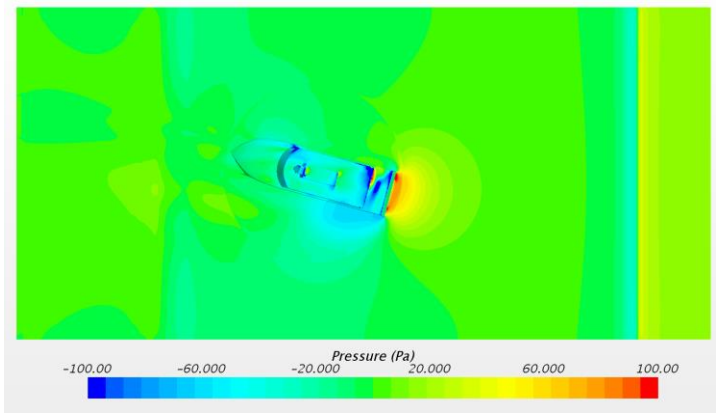

(e)

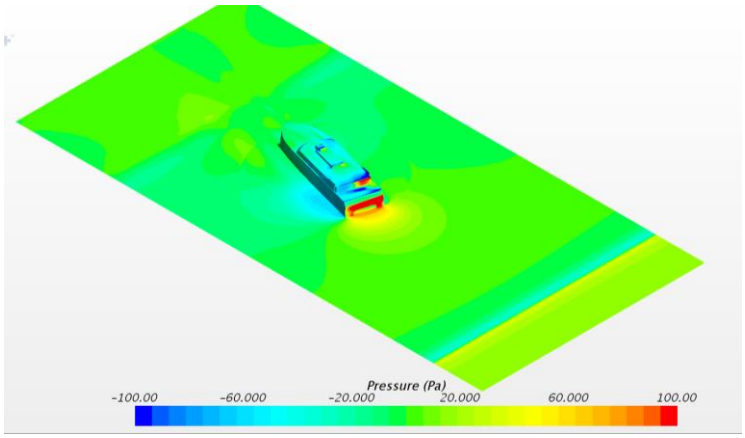

(f)

Figure 152: CFD pressure contours for a wind speed of 14.25 m/s and wind angle of attack at 165°. (a) elevation at centreline of the domain, (b) plan view at waterline level, (c) isometric view at waterline level

Velocity contours (wind velocity at 14.25 m/s; wind angle of attack is 180°):

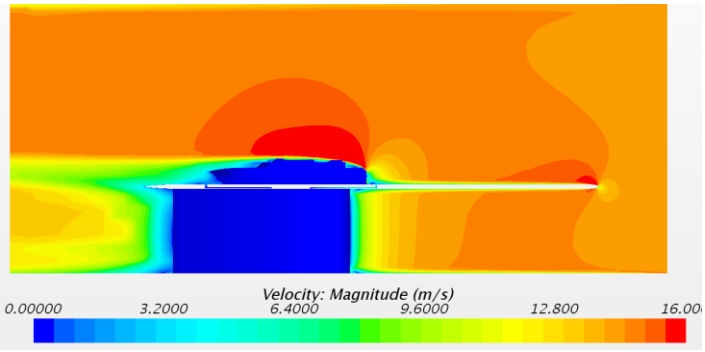

(a)

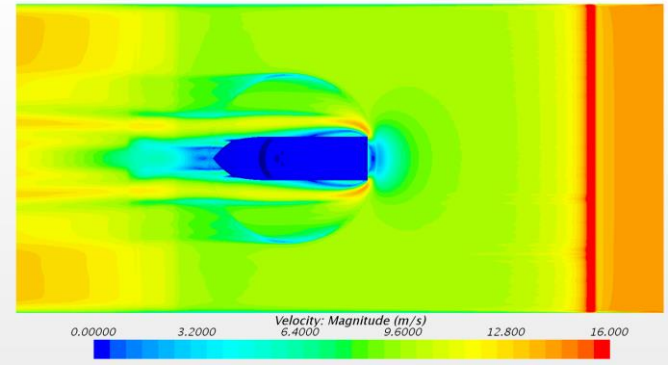

(b)

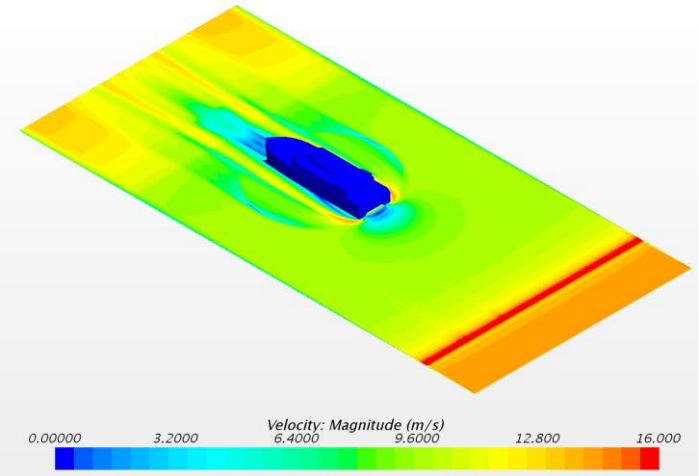

(c)

Figure 153: CFD velocity contours for a wind speed of 14.25 m/s and wind angle of attack at 180°. (a) elevation at centreline of the domain, (b) plan view at waterline level, (c) isometric view at waterline level

Pressure contours (wind velocity at 14.25 m/s; wind angle of attack is 180°):

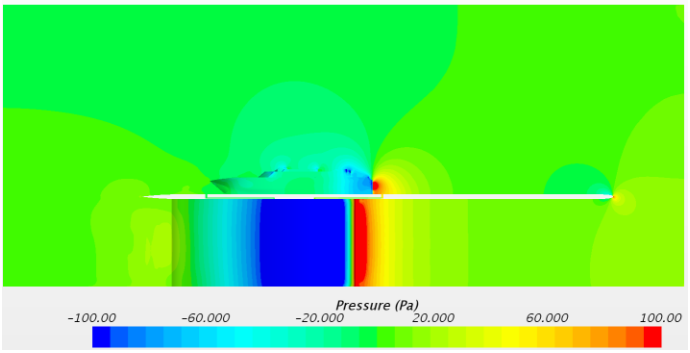

(d)

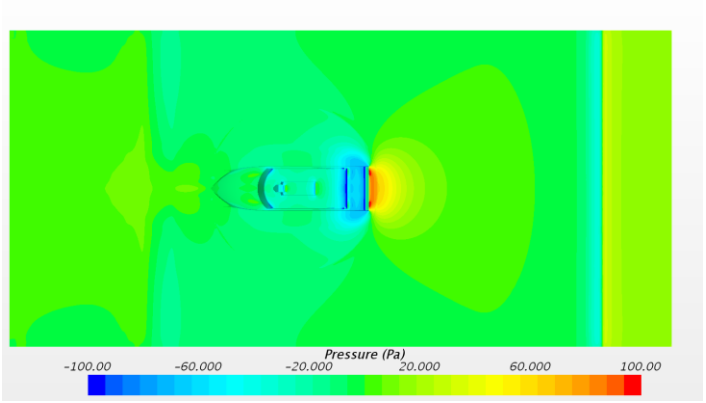

(e)

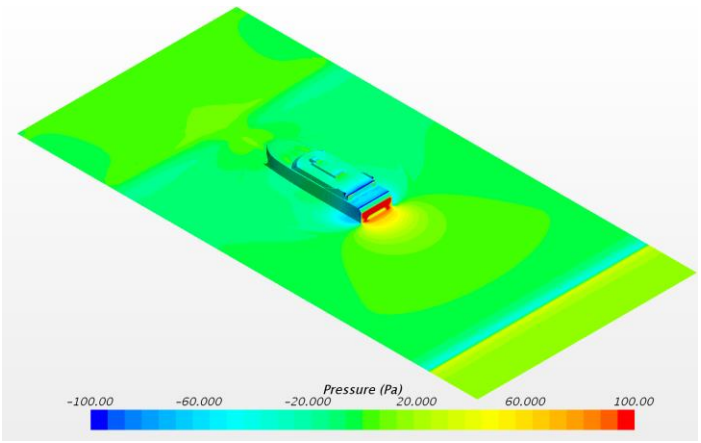

(f)

Figure 154: CFD pressure contours for a wind speed of 14.25 m/s and wind angle of attack at 180°. (a) elevation at centreline of the domain, (b) plan view at waterline level, (c) isometric view at waterline level

.